Sub-Doppler spectroscopy of alkali vapors confined in nanometric and micrometric thin cells

Rodolphe Momier

To cite this version:

Rodolphe Momier. Sub-Doppler spectroscopy of alkali vapors confined in nanometric and micrometric thin cells. Physics [physics]. Université Bourgogne Franche-Comté; Institute for Physical Research of the National Academy of Sciences of Armenia, 2024. English. NNT : 2024UBFCK030 . tel-04866189

HAL Id: tel-04866189
https://theses.hal.science/tel-04866189v1

Submitted on 6 Jan 2025

HAL is a multi-disciplinary open access archive for the deposit and dissemination of scientific research documents, whether they are published or not. The documents may come from teaching and research institutions in France or abroad, or from public or private research centers.

L'archive ouverte pluridisciplinaire **HAL**, est destinée au dépôt et à la diffusion de documents scientifiques de niveau recherche, publiés ou non, émanant des établissements d'enseignement et de recherche français ou étrangers, des laboratoires publics ou privés.

THESE DE DOCTORAT DE L'UNIVERSITÉ BOURGOGNE FRANCHE-COMTÉ

PRÉPARÉE AU LABORATOIRE INTERDISCIPLINAIRE CARNOT DE BOURGOGNE (UMR CNRS 6303)

Département Interactions et Contrôle Quantiques (ICQ)

École doctorale n° 553
CARNOT-PASTEUR

Doctorat de Physique

par

M. MOMIER Rodolphe

Spectroscopie sous-Doppler de vapeurs alcalines confinées dans des cellules minces nanométriques et micrométriques

Thèse présentée et soutenue à Ashtarak le 17 septembre 2024

Composition du Jury :

Mme BEKHTEREVA Elena	Professeure de Physique Université Polytechnique de Tomsk, Russie	Examinatrice Présidente du Jury
M. BUDKER Dmitry	Professeur de Physique Helmholtz-Institute, Mayence, Allemagne	Rapporteur
M. ULENIKOV Oleg	Professeur de Physique Université Polytechnique de Tomsk, Russie	Rapporteur
M. AUZINSH Marcis	Professeur de Physique Université de Lettonie	Examinateur
M. SARGSYAN Armen	Chargé de recherche, Institute for Physical Research, Arménie	Co-directeur de thèse
M. PAPOYAN Aram	Professeur de Physique, Institute for Physical Research, Arménie	Directeur de thèse
M. LEROY Claude	Professeur de Physique, Laboratoire ICB, Université de Bourgogne, France	Directeur de thèse

UNIVERSITÉ BOURGOGNE FRANCHE-COMTÉ
Laboratoire Interdisciplinaire Carnot de Bourgogne - UMR CNRS 6303

NATIONAL ACADEMY OF SCIENCES OF ARMENIA
Institute for Physical Research

Sub-Doppler spectroscopy of alkali vapors confined in nanometric and micrometric thin cells

by

M. Rodolphe MOMIER

A Thesis in Physics
Submitted for the Degree of Doctor of Philosophy

Date of defense: September 17, 2024

Members of the Jury:

Mrs. BEKHTEREVA Elena	Professor of Physics Tomsk Polytechnic University, Russia	Examiner President of the jury
Mr. BUDKER Dmitry	Professor of Physics Helmholtz-Institute Mainz, Germany	Referee
Mr. ULENIKOV Oleg	Professor of Physics Tomsk Polytechnic University, Russia	Referee
Mr. AUZINSH Marcis	Professor of Physics University of Latvia	Examiner
Mr. SARGSYAN Armen	Doctor of Physics Institute for Physical Research, Armenia	Co-supervisor
Mr. PAPOYAN Aram	Professor of Physics Institute for Physical Research, Armenia	Supervisor
Mr. LEROY Claude	Professor of Physics Laboratoire ICB, Dijon, France	Supervisor

Laboratoire Interdisciplinaire Carnot de Bourgogne - UMR CNRS 6303, Université de Bourgogne, 9 Avenue A. Savary, 21078 Dijon, France

Institute for Physical Research of the National Academy of Sciences of Armenia, Ashtarak-2, 0203 Armenia

À la mémoire de ma grand-mère qui ne se lassait jamais de vanter les exploits de son petit-fils…
À la mémoire de mon père qui n'aura pas vécu assez longtemps pour en faire autant.

Remerciements

Tout ce voyage a débuté par un simple stage d'une semaine en dernière année de Licence. Il y a ensuite eu un projet de recherche en 1ère année de Master, un semestre de recherche en Arménie en 2ème année... et voilà où j'en suis. Alors, comme vous vous en doutez, il y a du monde à remercier. Pas mal de monde, en fait. Laissez-moi prendre un moment pour remercier les personnes qui ont contribué de près ou de loin à toute cette entreprise. These acknowledgments will be written in a mix of English and French; sorry in advance.

Je tiens tout d'abord à exprimer ma plus profonde gratitude à mes trois directeurs de thèse qui ont formé une équipe de choc et m'ont apporté un soutien sans faille tout au long de ce travail. Je souhaite exprimer tout ma reconnaissance au Pr. **Claude Leroy**, directeur de thèse "côté français". Claude, merci d'avoir cru en moi depuis la Licence et de m'avoir accompagné tout au long de ce chemin. Votre expertise, votre pédagogie et vos conseils (toujours avisés, parfois difficiles à entendre...) ont sans aucun doute été essentiels à la réussite de ce projet de thèse. Les nombreuses heures que vous avez consacrées à la relecture de mes travaux et à nos discussions ont été d'une valeur inestimable. Merci d'avoir été si présent et patient tout au long de ce parcours, que ce soit pour discuter de physique ou faire le tour des caves à vin.

I also wish to express my heartfelt thanks to Prof. **Aram Papoyan**, my thesis supervisor from the Armenian side. Aram, thank you for being so pedagogical and available during my visits to Armenia despite your busy schedule. The days (and evenings...) spent with you and Svetlana in the lab were undoubtedly very educational. Thank you for allowing me to see my work from a different perspective and instilling in me the curiosity and creativity necessary for any good scientist.

I sincerely thank Dr. **Armen Sargsyan** for his participation in supervising this work. Armen, thank you for bringing your expertise in nanocells and for introducing me to experiments from my very first visit to Armenia, even before the start of this thesis. Thank you for taking me under your wing. I will always be immensely grateful for all the help you provided, both scientifically and personally. I wish you all the best for the future, to you, Gayane, Tigran, and Daniel.

Of course, I also thank Prof. **David Sarkisyan** for contributing to this work through his experimental expertise and for providing valuable critical insights. I thank all the researchers and staff I met at the Institute for Physical Research (**Ara**, **Hrant**, **Levon**, **Pavel**, **Emil**, **Lusine**, **Paytsar**) and the others for their hospitality and kindness.

I would like to express my utmost gratitude to Prof. **Elena Bekhtereva**, Prof. **Dmitry Budker**, Prof. **Oleg Ulenikov** and Prof. **Marcis Auzinsh** for agreeing to be part of my jury and taking time to read this (long) manuscript.

Je remercie vivement **Fred Chaussard** et **Christophe Finot** de m'avoir permis d'enseigner l'optique, la mécanique des fluides, l'électromagnétisme et les mesures physiques à leurs côtés au cours de mon doctorat. Les nombreuses heures d'enseignement effectuées avec vous ont été un excellent exercice et m'ont conforté dans mon projet de carrière. Je remercie également **Grégoire Guillon** et **Pierre Mathey** que j'ai eu grand plaisir à cotoyer durant ces heures d'enseignement.

Je tiens également à remercier le service des Relations Internationales de l'Université Bourgogne Franche-Comté, et plus particulièrement Dr. **Yevgenya Pashayan-Leroy**, pour avoir geré d'une main de maître les financements de mes nombreux déplacements à l'étranger. Mes plus sincères remerciements vont également au Service Administratif et Financier du Laboratoire ICB, et plus particulièrement à **Ibtissam Bourdadi - El Bakkouchi**, pour m'avoir accompagné dans la préparation de tous mes déplacements et d'avoir toujours répondu à mes questions, aussi bêtes soient-elles. Merci également à **Pierre Guichard** (Rotary Dijon Ducs de Bourgogne) d'avoir supporté ma 1ère mobilité internationale. Enfin, merci à tout le personnel du laboratoire ICB à qui j'ai pu avoir affaire, notamment les collègues de l'équipe **SMPCA** puis **MARS** (**Vincent**, **Cyril**, ...) pour la bonne humeur permanente règnant dans l'étage et un colloque HRMS 2023 mémorable.

Le doctorat est une épreuve qu'il serait bien triste de mener à terme seul. Je tiens à remercier mes collègues (amis?) doctorants du bureau D115B et plus largement du 1er étage pour avoir fait de ces années les meilleures - et je pèse mes mots - de ma vie[1]. **Astgh**, "honey!", merci d'avoir empli les murs du bureau de tant de fou-rires et de blagues au sens parfois plus que douteux (that's what she said!). **Gog**, merci d'avoir toujours répondu "yes!" à chaque fois que le mot "coffee?" était prononcé. Au delà d'être d'excellentes amies, je ne doute pas que vous deviendrez d'éminentes chercheuses. Je vous souhaite à toutes les deux une belle vie parisienne et j'ai hâte de vous retrouver, en France, en Arménie ou ailleurs! **Pierrot**, président adjoint du CAFD115B (le comité autoproclamé des fêtes du bureau D115B), merci pour tes imitations, tes pranks a répétition et le nombre incalculable de parties de Battleground ou tu étais, je dois l'avouer, bien meilleur que moi. J'espère que tu ne regrettes pas trop d'avoir rejoint ce bureau. J'aurais beaucoup aimé le partager avec toi quelques années supplémentaires. **Жора**, merci d'avoir contribué à ma productivité scientifique de la pire manière possible en me faisant régulièrement réinstaller World of Warcraft et Factorio. **Maxime**, toujours avec un nouveau jeu de société à proposer en soirée! Merci de toujours avoir eu un sachet de thé a dépanner... et d'avoir fini par m'offrir une T-box et une bouilloire, fidèles compagnons des sessions d'écriture de ce manuscrit. **Étienne**, qui dit début en même temps et fin en même temps dit mêmes galères : merci pour le soutien, particulièrement pendant ma (notre) phase de rédaction. Merci au reste du groupe, cotoyé pendant plus ou moins longtemps, d'avoir été présent[2]: **Colm**, **Raef**, **Owen**, **Siggi**, **JJ**, **Benjamin**, **Maria**, **Artur**, **Aleksei**. Les nombreuses soirées resto - bar - jeux de société avec vous tous ont constitué un excellent échappatoire et votre présence continue m'a permise de réaliser cette thèse dans les meilleures conditions possibles. Merci à vous tous, du plus profond de mon cœur.

Victoire, à mes côtés depuis mon entrée à la fac (enfin presque), qui aurait cru qu'on attaquerait une thèse dans le même labo en même temps ? Je crois qu'on se doit beaucoup. Avoir une amie avec qui se serrer les coudes quotidiennement a été un atout non négligeable. Merci d'avoir ensoleillé mes journées (pas toutes faciles, il faut l'avouer) au labo. Maintenant que tes piles fonctionnent, j'attends que tu révolutionnes la chimie. **Julien**, "michlimam", toujours disponible pour un appel impromptu malgré la distance, pour tabasser un boss dans Zelda ou bien capturer des pokémons que je n'ai pas dans ma version... Merci à vous deux d'avoir été de si bons copains et d'être toujours présents après toutes ces années. Je vous souhaite à tous les deux une excellente fin de thèse et bon courage pour la rédaction.

J'aimerais glisser un mot pour Julien "agent J". **Julien**, je te dois une grosse partie de ma passion pour la physique. Merci d'avoir été un si bon binôme de TP pendant les premières années de mon cursus. Merci également aux deux autres formant le quatuor des "machines" : **Gaël** et **Max-Tobias**. Évidemment, **Mickaël**, **Alexandre**, **Yan**, je peux en dire tout autant de vous. Je ne compte même plus les heures passées à la BU à bucher sur nos examens communs. Même si nous avons tous choisis des voies différentes, je suis ravi d'avoir fait ce gros bout de chemin avec vous et j'espère que vous vous épanouissez tous au mieux dans vos domaines respectifs.

Alex, ma chère colocataire, merci pour ton soutien indéfectible et ta compréhension tout au long de ces cinq dernières années. Que ce soit en offrant une oreille attentive lors des nombreux moments de doute ou en "embellissant" mon quotidien en dehors du travail, tu as sans aucun doute joué un rôle crucial dans la réussite de cette thèse et même de mon master. Merci de m'avoir soutenu dans les moments difficiles, de m'avoir permis de trouver un équilibre entre le travail et la vie personnelle. Avec le recul, vivre avec moi n'a vraiment pas dû être de tout repos. Merci d'avoir participé à ma déconstruction ! J'espère que mes futurs colocs seront aussi cools que toi (mais j'en doute fort), sinon la vie sera bien ennuyante.

À mes amis de longue - voire très longue - date : **Loïc**, **Laura**, **Marion**, **Ludo** : vous savez déjà tout, on s'est déjà tout dit. Merci d'être vous. Ne changez pas. Je vous aime d'amour.

Merci à tous les membres de ma famille : mon oncle et ma tante **Marie-France** et **Hervé**, mes cousins **Enzo**, **Tom** et **Émile**, leurs conjointes **Claire** et **Léa**, mon frère **Benoit** et tous les autres, pour m'avoir soutenu même malgré la distance et pour certains de même faire le déplacement au bout du continent pour la soutenance.

---

[1] Afin d'éviter tout conflit, cette liste n'est *pas* classée par ordre de préférence.

[2] Cette liste non plus.

Maman, merci de m'avoir accompagnée dès le jour ou je t'ai annoncé que je m'engageais dans un si long parcours universitaire même si tu n'étais pas très (du tout) rassurée. Ta force et ta persévérance m'ont toujours inspirés à donner le meilleur de moi-même. Merci d'avoir toujours été derrière moi malgré les épreuves que nous avons pu traverser. Ta présence constante à mes côtés a été une source inépuisable de force et de réconfort. Tes encouragements, tes sacrifices et ton soutien sans faille m'ont permis de surmonter les défis et de persévérer dans les moments les plus difficiles. Encore une fois, félicitations pour ton diplôme. Tu n'imagines pas à quel point je suis fier de toi. Je t'aime.

Bon, ça fait déjà un sacré pavé, je vais m'arrêter ici[3]. Que tous ceux que j'ai cotoyé ces dernières années ne doutent pas de l'impact positif qu'ils ont eu de près ou de loin sur ma santé mentale et sur ce travail, que vous figuriez ou non dans cette liste. Je pars heureux vers de nouveaux horizons et je n'oublierai jamais ces 8 années passées à Dijon. Si vous avez besoin de vous aérer, ma porte à Mayence ou ailleurs sera toujours ouverte.

May all those I have interacted with over the past few years never doubt the positive impact they have had, whether directly or indirectly, on my mental health and this work, whether you are mentioned in this list or not. I leave happily for new horizons and will never forget these eight years spent in Dijon. If you ever need a change of scenery, my door in Mainz or elsewhere will always be open.

Merci à tous, sincèrement.
Rodolphe

R.N.

This project is supported by: The NATO Science for Peace and Security Programme

---

[3] Pour ceux qui auront lu jusqu'ici, le plus important : https://www.youtube.com/watch?v=NfF3bTh0W0Q

Abstract

This thesis explores various aspects of sub-Doppler spectroscopy, ranging from fundamental studies of the Zeeman effect to coherent pumping processes. It provides a general overview of past and present advancements using thin spectroscopic cells of nanometric and micrometric thickness. From a theoretical perspective, we recall the model describing the interaction between a laser and a vapor confined in a thin cell. We present a comprehensive theoretical description of the behavior of a sodium vapor under magnetic fields up to 10 000 G. Additionally, we develop a complete theoretical framework for dipole moment cancellation and calculate the magnetic field values at which Zeeman transitions of alkali atoms are canceled. These values depend solely on physical constants and can serve as standards for calibrating magnetometers. We also present a magnetometer scheme utilizing thin potassium cells allowing to measure magnetic fields with high spatial resolution, potentially beneficial for magnetometry in challenging environments. The formation of EIT resonances in strong magnetic fields is investigated both theoretically and experimentally, showing promise for laser frequency locking on strongly detuned frequencies. Lastly, we explore the formation of narrow N-resonances and examine the effect of additional buffer gas on their width and contrast. N-resonances are promising candidates for atomic frequency standards that can be achieved with commercially available diode lasers.

Keywords: atomic spectroscopy ; alkali ; Zeeman effect ; magnetometry ; magneto-optical processes

Résumé

Cette thèse explore divers aspects de la spectroscopie sous-Doppler, allant des études fondamentales de l'effet Zeeman aux processus de pompage cohérent. Elle offre une vue d'ensemble des avancées antérieures et actuelles en utilisant des cellules spectroscopiques fines d'épaisseur nanométrique et micrométrique. Du point de vue théorique, nous rappelons le modèle décrivant l'interaction entre un laser et une vapeur confinée dans une cellule fine. Nous présentons une description théorique complète du comportement d'une vapeur de sodium dans un champ magnétique allant jusqu'à 10 000 G. De plus, nous développons un cadre théorique complet pour l'annulation du moment dipolaire et calculons les valeurs de champ magnétique pour lesquelles les transitions Zeeman des atomes alcalins sont annulées. Ces valeurs dépendent uniquement de constantes physiques et peuvent servir de références pour l'étalonnage de magnétomètres. Nous présentons également un schéma de magnétomètre utilisant de fines cellules de potassium permettant de mesurer les champs magnétiques avec une haute résolution spatiale, potentiellement bénéfique pour la magnétométrie dans des environnements difficiles. La formation de résonances EIT dans des champs magnétiques forts est étudiée théoriquement et expérimentalement, montrant une faisabilité pour le verrouillage de la fréquence laser sur des fréquences fortement décalées. Enfin, nous explorons la formation de résonances N étroites et examinons l'effet d'un gaz tampon supplémentaire sur leur largeur et leur contraste. Les résonances N sont des candidates prometteuses pour des étalons de fréquence atomique pouvant être réalisés avec des lasers à diode disponibles dans le commerce.

Mots-clés : spectroscopie atomique ; alcalins ; effet Zeeman ; magnétométrie ; procédés magnéto-optiques

Contents

Introduction **1**
- 1 Motivation . . . 2
- 2 Outline of the thesis . . . 3
  - 2.1 Chapters . . . 3
  - 2.2 Appendices . . . 4
- 3 Outcome . . . 5
  - 3.1 Published articles . . . 5
  - 3.2 Unpublished articles . . . 6
  - 3.3 Dissemination at international conferences . . . 6

1 Nanometric-thin cell spectroscopy **7**
- 1.1 Introduction . . . 7
- 1.2 Nanometric-thin cells . . . 8
  - 1.2.1 Manufacturing and structure of the cell . . . 9
  - 1.2.2 Brief comparison to other experimental techniques . . . 10
- 1.3 Fabry-Pérot nanocavity model . . . 11
  - 1.3.1 Propagation equation . . . 11
  - 1.3.2 Reflected and transmitted signals . . . 13
  - 1.3.3 Derivation of the macroscopic polarization . . . 15
  - 1.3.4 Linear regime of interaction approximation . . . 16
  - 1.3.5 Lineshape analysis . . . 18
  - 1.3.6 Ensemble of two-level systems . . . 20
- 1.4 Atom-surface interactions . . . 22
  - 1.4.1 Van der Waals effect . . . 22
  - 1.4.2 Experimental setup . . . 24
  - 1.4.3 Van der Waals effect on Cs and Rb D_1 lines . . . 24
  - 1.4.4 Retardation of the van der Waals (vdW) effect . . . 27
- 1.5 Conclusion . . . 28

2 Alkali vapors in a magnetic field **29**
- 2.1 Introduction . . . 29
- 2.2 The Dirac equation, hyperfine structure and Zeeman effect . . . 30
  - 2.2.1 General overview . . . 30
  - 2.2.2 Fine structure . . . 31
  - 2.2.3 Zeeman effect . . . 32
- 2.3 Spectra of alkali D lines in a magnetic field . . . 35
  - 2.3.1 Energy shifts and transition frequencies . . . 35
  - 2.3.2 Transition dipole moments . . . 36
  - 2.3.3 Sodium D_1 line . . . 38
  - 2.3.4 Sodium D_2 line . . . 44
- 2.4 Magnetically-Induced Circular Dichroism in alkali metal isotopes with nuclear spin 3/2 . . . 49
  - 2.4.1 Experimental setup . . . 50
  - 2.4.2 Experimental results . . . 51
- 2.5 Conclusion . . . 54

3 Transition cancellations in all stable alkali isotopes 55
3.1 Introduction . . . 55
3.2 D_1 line: theoretical considerations . . . 56
3.2.1 Zeeman Hamiltonian . . . 57
3.2.2 Transition intensities . . . 58
3.3 Analytical treatment of D_1 and D_1 - like transitions . . . 60
3.3.1 Sodium and potassium . . . 62
3.3.2 Rubidium . . . 63
3.3.3 Cesium . . . 65
3.3.4 Experimental feasibility . . . 66
3.4 Numerical treatment of D_2 and D_2 like transitions of Rb . . . 68
3.4.1 ^{87}Rb . . . 68
3.4.2 ^{85}Rb . . . 71
3.5 Conclusion . . . 71

4 Magnetometry with thin cells 75
4.1 Introduction . . . 75
4.2 Experimental study: magnetometry with a ^{39}K nanocell . . . 76
4.2.1 Spectroscopic nanocell filled with ^{39}K vapor . . . 77
4.2.2 Experimental setup . . . 78
4.2.3 Experimental results . . . 78
4.3 Experiment: magnetometry with a ^{39}K microcell . . . 82
4.3.1 Micrometric thin ^{39}K vapor cell . . . 82
4.3.2 Experimental setup . . . 82
4.3.3 Experimental results and discussion . . . 83
4.4 Conclusion . . . 85

5 Coherent processes 87
5.1 Introduction . . . 87
5.2 Formation of EIT resonances using “forbidden” transitions in the HPB regime . . . 88
5.2.1 Probabilities and frequency shifts of the MI transitions of Cs D_2 line . . . 88
5.2.2 Theoretical description of the EIT process . . . 90
5.2.3 Experimental setup . . . 91
5.2.4 Experimental results . . . 92
5.3 Buffer gas influence on the formation of N-resonances . . . 95
5.3.1 Experiment . . . 96
5.3.2 N-resonances in a magnetic field . . . 100
5.3.3 Discussion . . . 102
5.4 Conclusion . . . 103

Conclusion and perspectives 105

Appendices 107

A Properties of the angular momentum 109
A.1 Quantification of the angular momentum . . . 109
A.1.1 Commutation relations . . . 109
A.1.2 Eigenvalues of the angular momentum operator . . . 109
A.2 Coupling of angular momenta . . . 112
A.2.1 Coupling of two angular momenta . . . 112
A.2.2 Coupling of three angular momenta . . . 114

A.3 Irreducible Tensor Operators, Wigner-Eckart theorem . . . 115
  A.3.1 Irreducible Tensor Operators . . . 115
  A.3.2 Wigner-Eckart theorem . . . 116

B Properties of alkali atoms **119**
B.1 Hyperfine structure . . . 119
B.2 Data tables . . . 120

C Semi-classical atom-light interactions **123**
C.1 Density matrix formalism . . . 123
  C.1.1 Definition . . . 123
  C.1.2 Liouville equation of motion . . . 124
  C.1.3 Building the system of equations . . . 125
C.2 Interaction with a laser field . . . 125
  C.2.1 Electric Dipole Approximation . . . 125
  C.2.2 Rotating wave approximation . . . 126
C.3 Three-level Λ system . . . 126
  C.3.1 Building the interaction Hamiltonian . . . 126
  C.3.2 Dark state, Electromagnetically-Induced Transparency . . . 128

Bibliography **143**

List of Figures

Introduction **1**

1 Number density and Doppler broadening of Li, Na, Cs and K. 2

Chapter 1 **7**

1.1 Schematic diagram of a NC 8
1.2 Front and side views of a NC 9
1.3 Experimental transmission and saturated absorption (SA) spectra of Cs 10
1.4 Scheme of a nanocell (NC) seen as a nanocavity 11
1.5 Ratio of the reflected intensities 14
1.6 Scheme of a two-level system 15
1.7 Probability density function of the Maxwell-Boltzmann distribution 16
1.8 Theoretical transmitted lineshape for an arbitrary two-level system 19
1.9 Theoretical reflected lineshape for an arbitrary two-level system 19
1.10 Typical theoretical SR ($L = 350$ nm) and transmission ($L = \lambda$) spectra obtained with a NC 21
1.11 Typical theoretical derivative of selective reflection (dSR) ($L = 350$ nm) and SD ($L = \lambda$) spectra obtained with a NC 21
1.12 Experimental and theoretical absorption spectra of Cs D_2 line 22
1.13 Transition frequency shift due to atom-surface interactions 23
1.14 Experimental setup used for the study of atom-surface interactions 24
1.15 Spectra of the $4 \longrightarrow 3', 4'$ transitions of Cs D_1 line 25
1.16 Dipole-dipole frequency shift of Cs D_1 line as a function of the atomic vapor density . 26
1.17 Spectra of the $1 \longrightarrow 1', 2'$ transitions of ^{87}Rb D_1 line 26
1.18 Van der Waals C_3 coefficients of Rb and Cs D_1 lines 27

Chapter 2 **29**

2.1 Block structure of the Zeeman Hamiltonian 34
2.2 Hyperfine structure of sodium D_1 line for weak magnetic fields 35
2.3 Hyperfine structure of sodium D_1 line 36
2.4 Zeeman spectra computation procedure 38
2.5 Possible transitions of sodium D_1 line 38
2.6 Transition dipole moments and frequencies of sodium D_1 line (π polarization) 39
2.7 Sodium D_1 line frequency shifts, π polarization 40
2.8 Absorption spectra of sodium D_1 line, π polarization 41
2.9 Absorption spectra of sodium D_1 line, π polarization, hyperfine Paschen–Back (HPB) regime 41
2.10 Transition dipole moments of sodium D_1 line (σ polarization). 42
2.11 Absorption spectra of sodium D_1 line, σ polarization 43
2.12 Absorption spectra of sodium D_1 line, σ polarization, hyperfine Paschen–Back (HPB) regime 43
2.13 Possible transitions of sodium D_2 line, π polarization 44
2.14 Transition dipole moments of sodium D_2 line, π polarization. 45
2.15 Absorption spectra of sodium D_2 line, π polarization 45
2.16 Absorption spectra of sodium D_2 line, π polarization, hyperfine Paschen–Back (HPB) regime 46
2.18 Transition dipole moments of sodium D_2 line, σ polarization. 47
2.17 Possible transitions of sodium D_2 line, σ polarization 47

2.19 Absorption spectra of sodium D_2 line, σ^- polarization 48
2.20 Absorption spectra of sodium D_2 line, σ polarization, hyperfine Paschen–Back (HPB) regime 49
2.21 Magnetically-Induced circular dichroism experimental setup 50
2.22 ^{87}Rb D_2 line transitions guiding transition (GT) and magnetically induced (MI) transitions 51
2.23 Absorption spectra of rubidium D_2 line, σ polarization. 52
2.24 GT to magnetically induced (MI) transition intensity ratios 53

Chapter 3 55
3.1 Scheme of all possible alkali D_1 lines 57
3.2 Generic D_1-type Zeeman π transitions for $m = -1$. 59
3.3 Generic D_1-type Zeeman transfer coefficients for $m = -1$ π transitions. 60
3.4 π transitions ($m = -1$) of ^{23}Na, ^{39}K and ^{41}K. 62
3.5 ^{40}K D_1 line π transitions. 63
3.6 Rubidium D_1 line π modified transfer coefficients and transition intensities. 64
3.7 Rubidium $6^2P_{1/2}$ line π modified transfer coefficients and transition intensities. 64
3.8 ^{133}Cs D_1 line π transitions. 65
3.9 derivative of selective reflection (dSR) spectra of ^{85}Rb D_1 line highlighting transition cancellations 66
3.10 Scheme of ^{85}Rb D_1 line π transitions. 66
3.11 $5^2S_{1/2} \longrightarrow 6^2P_{3/2}$ π transition modified transfer coefficients and scheme 69
3.12 ^{87}Rb $5^2S_{1/2} \longrightarrow 6^2P_{3/2}$ $\sigma^{\pm}$ modified transfer coefficients. 70

Chapter 4 75
4.1 Strongest ^{39}K D_1 line transition intensities in the hyperfine Paschen–Back (HPB) regime. 77
4.2 Diagram of the strongest ^{39}K D_1 line transitions in the hyperfine Paschen–Back (HPB) regime. 77
4.3 Nanocell-based magnetometer experimental setup 78
4.4 Theoretical and experimental spectra of ^{39}K D_1 line, $L = 385$ nm, $B = 267$ G. 79
4.5 Experimental spectra of ^{39}K D_1 line for various magnetic fields recorded with a nanocell (NC) 79
4.6 Frequency ratio between the different polarizations for the nanocell (NC) magnetometer 80
4.7 Measurement of the magnetic field gradient with the nanocell magnetometer 81
4.8 Microcell magnetometer experimental setup 82
4.9 Saturated absorption spectra of ^{39}K D_1 line recorded with a microcell. 83
4.10 Experimental spectra of ^{39}K D_1 line for various magnetic fields recorded with a microcell (MC) 84
4.11 Frequency ratio between the different polarizations for the microcell (MC) magnetometer 85

Chapter 5 87
5.1 Scheme of Cs D_2 line σ^+ Λ systems used to form EIT resonances 89
5.2 Magnetic field dependence of Cs D_2 line Zeeman MI transitions. 89
5.3 Three-level Λ-system scheme excited by a bichromatic laser field. 90
5.4 Scheme of the EIT experimental setup. 91
5.5 Probe transmission spectra of the Cs nanocell, $B = 1400$ G. 92
5.6 Probe transmission spectra of the Cs nanocell, $B = 1770$ G. 93
5.7 Probe transmission spectra of the Cs nanocell, $B = 2880$ G and comparison with theory. 94
5.8 Cs D_2 line transition frequency shifts. 94
5.9 N-resonance level diagram. 95
5.10 Scheme of the N-resonance experimental setup 96

5.11 Probe absorption spectra of ^{85}Rb D_1 line, 20 Torr Ne 97
5.12 Power dependence of the N-resonance linewidth, 6 Torr Ne, 0.8 cm cell. 98
5.13 Power dependence of the N-resonance contrast and linewidth, 6 Torr Ne, 0.8 cm cell . 98
5.14 N-resonance contrast versus buffer gas partial pressure, 0.8 cm cell and probe transmission spectra with 400 Torr Ne. 99
5.15 Pure Rb probe transmission spectra, 0.8 cm cell. 99
5.16 Probe transmission spectra for various magnetic field values, 0.8 cm cell, 20 Torr Ne. . 100
5.17 Frequency shift of the N-resonance components with respect to the magnetic field . . 101
5.18 Λ systems of ^{85}Rb D_1 line involved in N-resonance formation. 101
5.19 Splitting on an EIT and N-resonance, 0.8 cm cell, B = 3 G, 6 Torr Ne. 102

Appendix B **119**
B.1 Hyperfine structure of alkali D lines 119

Appendix C **123**
C.1 Three-level Λ system with two lasers. 127

List of Tables

Chapter 3 **55**

3.1 Hyperfine structure constants and Landé factors for various isotopes and transitions. . . 61
3.2 Magnetic field values cancelling D_1 π transitions of ^{23}Na, ^{39}K and ^{41}K. 62
3.3 Magnetic field values cancelling π transitions of ^{40}K. 63
3.4 Magnetic field values cancelling Rb π transitions. 65
3.5 Magnetic field values cancelling ^{133}Cs D_1 transitions. 65
3.6 Excited hyperfine splittings of Rb 68
3.7 Magnetic field values cancelling ^{87}Rb D_2 and $5^2S_{1/2} \longrightarrow 6^2P_{3/2}$ π transitions. 69
3.8 Magnetic field values cancelling D_2 and ^{87}Rb $5^2S_{1/2} \longrightarrow 6^2P_{3/2}$ σ^+ transitions. 70
3.9 Magnetic field values cancelling ^{87}Rb $5^2S_{1/2} \longrightarrow 6^2P_{3/2}$ σ^- transitions. 71
3.10 Magnetic field values cancelling ^{85}Rb D_2 and $5^2S_{1/2} \longrightarrow 6^2P_{3/2}$ σ^-, σ^+ and π transitions. The most imprecise values are given in red cells. 72

Appendix B **119**

B.1 Physical and optical constants of Cs. 120
B.2 Physical and optical constants of Na and K. 121
B.3 Physical and optical constants of Rb. 122

Acronyms

CG Clebsch–Gordan

CO Crossover

CW Continuous wave

DFB Distributed feedback

dSR Derivative of selective reflection

ECDL Extended cavity diode laser

EIT Electromagnetically induced transparency

FP Fabry–Pérot

FWHM Full width at half maximum

GT Guiding transition

HPB Hyperfine Paschen–Back

ITO Irreducible tensor operator

MC Microcell

MCD Magnetically induced circular dichroism

MI Magnetically induced

NC Nanocell

RWA Rotating wave approximation

SA Saturated absorption

SD Second derivative

SNR Signal to noise ratio

SR Selective reflection

vdW Van der Waals

VSOP Velocity-selective optical pumping

WE Wigner–Eckart

Introduction

Lasers [1] are pivotal in investigating quantum systems and manipulating their properties. Alkali atoms (Li, Na, K, Rb, Cs, and, to a lesser extent, Fr) are favored in atomic physics for their high atomic vapor density at low temperatures (fig. 1a) and strong optical transitions (D lines) in the visible or near-infrared spectrum, which are accessible with relatively inexpensive continuous wave (CW) lasers. Their simple energy level structure comprising a single valence electron makes them very well-documented species [2–7] and greatly simplifies theoretical calculations. Understanding magneto-optical effects in alkali metal vapors is crucial for applications such as electromagnetically induced transparency (EIT) studies [8, 9], Faraday filters [10, 11], optical magnetometry [12–17] and laser frequency stabilization [18].

In recent decades, extensive studies on alkali atoms have focused on phenomena such as the Faraday effect [19–21], Hanle effect [22–25], Dicke effect [26, 27], prolonged resonance interaction times in buffered vapor cells [28, 29], and magneto-optical processes [30–32]. These studies have paved the way for innovations like alkali vapor-based lasers [33–35], precise optical magnetometers, and advancements in quantum information technologies such as optical quantum memory devices [36, 37] and logic gates [38, 39]. Other more fundamental applications of alkali atoms include (but are not by any means limited to) the study of Rydberg states [40, 41], dipole-dipole and cooperative interactions [42, 43], atom-surface interactions [44], formation and studies of dimers [45, 46]. They were for example used in the first experimental realizations of Bose-Einstein condensates in 1995 [47, 48].

Studying atomic systems, especially their hyperfine structures, is complex. The hyperfine structure cannot be described by the Schrödinger equation alone. The influence of external magnetic and electric fields, which lead to the Zeeman [49], Paschen-Back [50], and Stark [51] effects, requires a more complex description using the Dirac equation. Additionally, the increasing precision of measurements in recent decades necessitates implementing advanced mathematical and physical tools, such as the Liouville equation or von Neumann formalism. More and more powerful computers are essential for performing numerical simulations that match the precision of these measurements.

For a vapor media, the thermal motion of atoms results in Doppler broadening (see fig. 1). A laser of frequency ω_L and wavevector $\mathbf{k}$ will be seen by an atom with a velocity $\mathbf{v}$ as $\omega = \omega_L - \mathbf{k} \cdot \mathbf{v}$, resulting in a line broadening [53]

$$\Gamma_D = \omega_0 \sqrt{\frac{8 \ln(2) k_B T}{mc^2}} \tag{1}$$

where ω_0 is the transition frequency (line center), m is the atomic mass, k_B is the Boltzmann constant and T is the temperature. This broadening inevitably leads to the overlapping of hyperfine transitions and their Zeeman components, thus limiting their spectroscopic applicability. Significant sub-Doppler narrowing of atomic transitions can be attained with the use of so-called optical nanocells (NCs) [54–56]. Being enclosed in optical cells with a thickness of the order of the resonant wavelength, alkali metal vapors become a powerful tool for the high-resolution atomic spectroscopy, opening new possibilities for studying magneto-optical processes, where spectral resolution of individual transitions between magnetic sublevels (Zeeman transitions) is essential.

Complete determination of the behavior of all the possible individual Zeeman transitions can be done using a well-known theoretical model first provided by Tremblay et al. [57]. Importantly, besides frequency splitting in a magnetic field, Zeeman transitions also undergo significant probability changes. This allows us to observe the appearance of several peculiarities, such as Guiding Transitions and two different types of so-called magnetically induced circular dichroism (MCD) [58, 59]. Several efficient techniques have been developed to enhance the spectral visibility of Zeeman transitions while preserving their relative probability scaling, such as the derivative of Selective Reflection [60] and Second Derivative of absorption [61, 62].

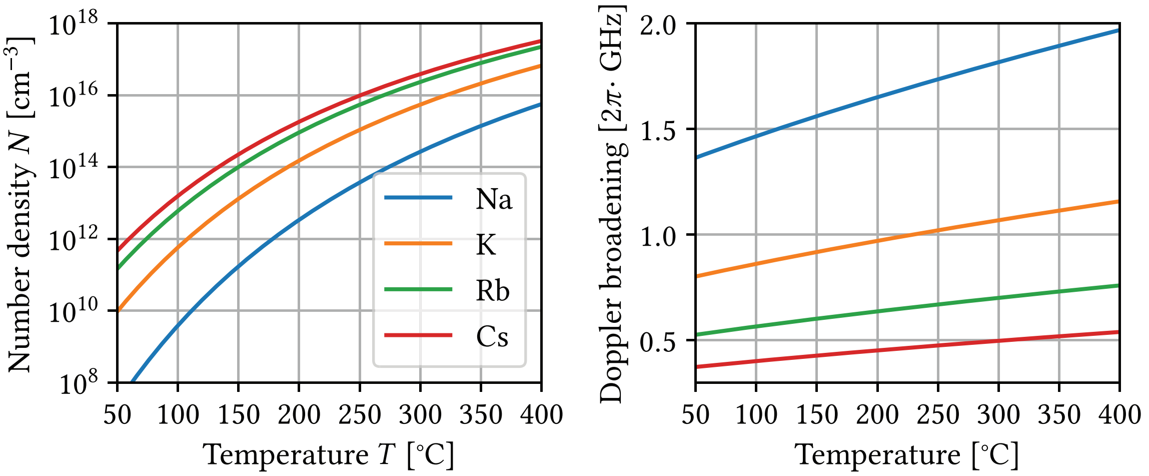

Figure 1 – a) Atomic number density N [cm^{-3}] of Na, K, Rb, and Cs as a function of the temperature, calculated according to $N = P_v/k_BT$ with $\log_{10}(P_v) \ = \ A + BT^{-1}$. The empirical parameters A and B can be found in [52]. b) Doppler broadening Γ_D of the D_1 line of Na, K, Rb, and Cs calculated according to eq. (1) with the data provided in appendix B.

In summary, alkali metal vapors offer versatile tools for exploring fundamental and applied physics, from quantum phenomena to advanced optical technologies, owing to their unique spectroscopic properties and practical advantages in experimental setups.

1 Motivation

This thesis focuses on different aspects of sub-Doppler spectroscopy, from fundamental Zeeman effect studies to coherent pumping processes. It gives a general overview of what has been done and what can be done with thin spectroscopic cells.

Chapter 2 stems from the observation that most experimental studies typically use rubidium and cesium atomic vapors due to the availability of relatively inexpensive CW diode lasers operating in their resonant wavelength range. Magneto-optical effects on sodium D lines have been much less studied. Although some information concerning Zeeman transitions of sodium exists in the literature [63–65], the available information is far from being complete. We have decided to illustrate the theoretical description of the behavior of alkali vapors in NCs, with and without applying an external magnetic field. In the meantime, we observed that several transitions got canceled for very precise values of the external magnetic field. This effect had been observed by Davis, Metcalf, and Phillips in 1979 [66]. We noticed that it was possible to derive theoretically these values. All the values have been exactly determined either by numerical simulation or analytical calculation. As they only depend on physical constants, one can envisage the reciprocal effect: the annihilation of a transition for a very precise value of the magnetic field means this value could be used as a standard for the calibration of a magnetometer. This is done in chapter 3.

Chapter 4 focuses on magnetometry applications. We have decided to use cells filled with ^{39}K, a promising candidate for table-top vapor cell magnetometry setups as its characteristic magnetic field value B_0 (determining when the nuclear spin and total electron angular momentum decouple) is substantially lower than the analogous value for Rb and Cs. Therefore, when ^{39}K atoms are placed in an external magnetic field, important specific features of the behavior of the Zeeman transitions, such as a strong change in their probability and a significant decrease in their number can be easily observed [6, 67–71] by applying a much weak magnetic field weaker than for Cs or Rb [appendix B]. Modern state-of-the-art magnetometers now achieve excellent sensitivity but are focused on the measurement of extremely low magnetic fields in shielded environments [72, 73]. Here, we choose to focus more on measurement range and spatial resolution than sensitivity. As our theory agrees very well with the experiment, experimental setups to retrieve magnetic field values can be built with good spatial resolution, with the advantage of being immune to external perturbations and thermal drift.

Chapter 5 explores coherent processes and various ways to generate narrow, all-optical resonances. This is typically done with a bichromatic laser setup, usually denoted “probe” and “coupling”. Such resonances heavily depend on the properties of Zeeman transitions, and mainly on their huge shift with respect to the magnetic field. We have noticed that by wisely choosing the probe and coupling polarizations, it was possible to form EIT resonances far detuned from the D line transition frequency of cesium (and possibly other alkali isotopes). These resonances can be used for laser frequency locking [18]. We then investigate N-resonances, which have the advantage of being even narrower. EIT and N-resonances have a significant number of important applications in a variety of fields, such as information storage, quantum communication, optical magnetometry, or metrology [74–76].

2 Outline of the thesis

This thesis is 171 pages long and contains 5 chapters, 87 figures, 13 tables, and 240 references.

2.1 Chapters

The five main chapters are organized as follows:

- In chapter 1, we explore the fundamentals and advantages of NC spectroscopy, allowing sub-Doppler resolution with a single laser. This concept was first theoretically proposed by Vartanyan and Lin [77] and further refined by Zambon and Nienhuis [78], and Dutier *et al.* [79], who considered interferometric effects within the cells, leading to asymmetrical lineshapes and coherent Dicke narrowing. We discuss the benefits of NCs over traditional techniques, such as achieving high-resolution spectra without crossover resonances using a simple experimental setup. The manufacturing process, described by Sarkisyan *et al.* [54], involves polished sapphire windows and a wedge-shaped structure, allowing precise control over the cell thickness and spectroscopic conditions. The theoretical description of NCs considers reflections at cell interfaces and solutions for lineshapes are given using Maxwell’s formalism and optical Bloch equations. Experimental studies include measurements of van der Waals (vdW) interactions for Cs and Rb atoms, revealing the retardation effect predicted by Carvalho *et al.* [80] and Laliotis *et al.* [81]. A comparison with traditional sub-Doppler techniques, like saturated absorption spectroscopy, shows that NCs offer superior resolution and simplicity. Applications of NCs in studying magneto-optical processes, molecular spectroscopy, and cooperative effects demonstrate their value in precise measurements and fundamental research.
- In chapter 2, we describe the behavior of alkali atoms in electromagnetic fields using the Dirac equation. We examine the Dirac Hamiltonian terms like kinetic energy and spin-orbit coupling. We derive the Hamiltonian for alkali atoms in a static magnetic field, discuss the hyperfine structure and the Zeeman effect, and present a theoretical model from Tremblay *et al.* [57] used to calculate alkali transition frequencies and intensities. We then apply this model to the D lines of sodium, incorporating the NC model from chapter 2. We investigate sodium vapor behavior under different magnetic fields and laser polarizations, detailing Zeeman transitions and their intensities. We analyze the effects of state mixing and selection rules, noting that high magnetic fields lead to the hyperfine Paschen–Back (HPB) regime where nuclear spin and electronic angular momentum decouple. Finally, we explore MCD in alkali metal isotopes with a nuclear spin of 3/2. We focus on forbidden transitions with $\Delta F = \pm 2$, which can have high probabilities under certain magnetic fields. We describe an experimental setup for studying the D_2 line transitions of ^{87}Rb using circularly polarized laser radiation, analyze intensity ratios of magnetically induced (MI) transitions, and highlight their potential applications in magneto-optical processes.

- In chapter 3, we develop a theoretical model to determine the magnetic field values that cancel the D_1 and $5^2S_{1/2} \longrightarrow 6^2P_{1/2}$ transitions of all stable alkali isotopes. We start with a general definition of the hyperfine structure and build Hamiltonians for the ground and excited states of each Zeeman transition in the coupled basis $|F, m\rangle$. After extensive calculations, we derive an analytical formula for the roots of specific transition intensities, revealing a symmetric "pair" behavior in some transitions. We then use this formula to identify all possible cancellation values. We review the physical constants used and the influence of their precision on the results and provide an exhaustive overview of the canceled or maximized transitions and their corresponding magnetic field magnitudes. Relevant graphs and tables are presented, and the phenomenon is illustrated using derivative of selective reflection (dSR) spectra. We also discuss the feasibility of experimentally measuring these magnetic field values. Finally, we examine the cancellation values of the D_2 and $5^2S_{1/2} \longrightarrow 6^2P_{3/2}$ lines of ^{85}Rb and ^{87}Rb. Since an analytical formula could not be derived, we determined the magnetic field values numerically. Due to the complexity of the hyperfine structure, we present the results in tables for clarity.
- In chapter 4, we present two methods that can be used to measure magnetic fields using thin cells. First, a method using a NC is presented. This approach allows for measuring magnetic fields ranging from 0.1 to 10 kG with high micrometer spatial resolution. It is particularly effective in environments where there are significant magnetic field gradients, reaching up to 3 G per micrometer. Experimental results obtained from absorption spectra measurements using the NC are compared to theoretical predictions derived from models developed in previous chapters, demonstrating excellent agreement. Secondly, a method using a micrometric-thin cell is introduced. Unlike NCs, microcells (MCs) have a thickness of around 30 μm. They are designed to produce narrow atomic lines in transmission spectra without unwanted crossover resonances. However, while microcells offer easier manufacturing compared to NCs, they provide a lower spatial resolution. Despite this limitation, microcells offer a practical solution for magnetic field measurements due to their straightforward fabrication process.
- In chapter 5, we explore two main types of coherent processes in alkali vapors. In the first part, we investigate the formation of EIT resonances using cesium's σ^+ $F = 3 \longrightarrow F = 5$ MI transitions as probe radiation in strong magnetic fields (1 - 3 kG). The experiment, conducted in a NC with a vapor column thickness corresponding to the cesium D_2 line transition, shows significant and frequency-shifted EIT resonances due to the MI transitions' steep frequency shift slope. Preliminary theoretical calculations based on Doppler-broadened three-level systems reasonably agree with experimental findings. In the second part, the study focuses on N-resonances observed in centimeter-scale vapor cells. These resonances exhibit enhanced contrast and reduced linewidths when a buffer gas (typically Neon) is introduced into the alkali vapor. Research explores various vapor cell configurations with different buffer gas pressures (0 to 400 Torr), optimizing resonance characteristics and analyzing their behavior under external magnetic fields. This research contributes to advancing precision magnetometry techniques through experimental and theoretical investigations of novel light-matter interactions.

2.2 Appendices

As an addition, three appendices containing useful theoretical complements to the work presented in this thesis are provided:

- In appendix A, we study the coupling of two and three angular momenta, necessary for the derivation of the fine and hyperfine structures. We introduce the Wigner–Eckart (WE) theorem, Clebsch–Gordan (CG) coefficients, $3j$- and $6j$-symbols, and irreducible tensor operators (ITOs).
- In appendix B, we provide a number of numerical values used in the computations performed in this thesis. These values relate to the hyperfine structure of various alkali isotopes and are all either taken from the literature or recalculated.

- In appendix C, we recall the main lines of the density matrix formalism for an ensemble of atoms interacting with a classical light field. We then build the interaction Hamiltonian of a three-level Λ-system using the dipole and rotating wave approximation (RWA) and briefly explain the phenomenon of EIT in the dark state formalism.

3 Outcome

The work presented in this thesis has been mostly published and widely disseminated at several international conferences.

3.1 Published articles

The work presented in this thesis gave rise to the publication of the following journal articles:

- R. Momier, A. Aleksanyan, E. Gazazyan, A. Papoyan, and C. Leroy. *New standard magnetic field values determined by cancellations of* ^{85}Rb *and* ^{87}Rb *atomic vapors* $5^2S_{1/2} \to 6^2P_{1/2,3/2}$ *transitions.* J. Quant. Spectrosc. Radiat. Transf. **257** (2020), p. 107371
- A. Aleksanyan, R. Momier, E. Gazazyan, A. Papoyan, and C. Leroy. *Transition cancellations of* ^{87}Rb *and* ^{85}Rb *atoms in a magnetic field.* J. Opt. Soc. Am. B **37** (11) (2020), 3504–3514
- R. Momier, A. V. Papoyan, and C. Leroy. *Sub-Doppler spectra of sodium D lines in a wide range of magnetic field: Theoretical study.* J. Quant. Spectrosc. Radiat. Transf. **272** (2021), p. 107780
- A. Sargsyan, R. Momier, A. Papoyan, and D. Sarkisyan. *Sub-Doppler Spectroscopy of Room-Temperature Cs Atomic Vapor in a 400-nm-Thick Nanocell.* J. Exp. Theor. Phys. **133** (4) (2021), pp. 404–410
- A. Sargsyan, A. Tonoyan, R. Momier, C. Leroy, and D. Sarkisyan. *Dominant magnetically induced transitions in alkali metal atoms with nuclear spin 3/2.* J. Opt. Soc. Am. B **39** (4) (2022), p. 973
- M. Auzinsh, A. Sargsyan, A. Tonoyan, C. Leroy, R. Momier, D. Sarkisyan, and A. Papoyan. *Wide range linear magnetometer based on a sub-microsized K vapor cell.* Appl. Opt. **61** (19) (2022), p. 5749
- A. Sargsyan, R. Momier, C. Leroy, and D. Sarkisyan. *Saturated absorption technique used in potassium microcells for magnetic field sensing.* Laser Phys. **32** (10) (2022), p. 105701
- A. Aleksanyan, R. Momier, E. Gazazyan, A. Papoyan, and C. Leroy. *Cancellation of* D_1 *line transitions of alkali-metal atoms by magnetic-field values.* Phys. Rev. A **105** (4) (2022), p. 042810
- A. Sargsyan, A. Tonoyan, R. Momier, C. Leroy, and D. Sarkisyan. *Formation of strongly shifted EIT resonances using "forbidden" transitions of Cesium.* J. Quant. Spectrosc. Radiat. Transf. **303** (2023), p. 108582
- A. Sargsyan, R. Momier, C. Leroy, and D. Sarkisyan. *Competing van der Waals and dipole-dipole interactions in optical nanocells at thicknesses below 100 nm.* Phys. Lett. A **483** (2023), p. 129069
- A. Tonoyan, A. Sargsyan, R. Momier, C. Leroy, and D. Sarkisyan. *Formation of Narrow Atomic Lines of Rb in the UV Region Using a Magnetic Field.* Opt. Mem. Neural Networks **32** (S3) (2023), S343–S348
- R. Momier, A. Sargsyan, A. Tonoyan, C. Leroy, and D. Sarkisyan. *Micrometric-Thin Cell Filled with Rb Vapor for High-Resolution Atomic Spectroscopy.* Opt. Mem. Neural Networks **32** (3) (2023), S349–S355

Links to the preprints can be found here.

3.2 Unpublished articles

The following article is under review (submitted to Spectrochimica Acta Part B) as of July 2024:

- A. Sargsyan, R. Momier, C. Leroy, and D. Sarkisyan. *Influence of buffer gas on the formation of N-resonances in rubidium vapors.* 2024. DOI: `10.48550/arXiv.2402.09184`. arXiv: `2402.09184 [physics]`. Pre-published

3.3 Dissemination at international conferences

All slides and posters presented at international conferences are available by clicking the links below.

- R. Momier, A. Papoyan, and C. Leroy. *Theoretical study of sodium D lines in a wide range of magnetic field with sub-Doppler resolution.* Student presentation, International Conference Laser Physics 21, Ashtarak, Armenia, Sep 21-24 2021.
- R. Momier, A. Aleksanyan, A. Sargsyan, A. Tonoyan, M. Auzinsh, D. Sarkisyan, A. Papoyan, and C. Leroy. *Magnetometry with a nanometric-thin K vapor cell.* Invited speaker, 14th European Conference on Atoms, Molecules and Photons (ECAMP 14), Vilnius, Lithuania, Jun 27 - Jul 1 2022.
- R. Momier, A. Sargsyan, A. Tonoyan, M. Auzinsh, D. Sarkisyan, A. Papoyan, and C. Leroy. *Magnetometry with a nanometric-thin K vapor cell.* Student presentation, International Conference Laser Physics 22, Ashtarak, Armenia, Sep 14-16 2022.
- R. Momier, A. Sargsyan, A. Tonoyan, M. Auzinsh, D. Sarkisyan, A. Papoyan, and C. Leroy. *Sub-Doppler spectroscopy of ^{39}K for magnetic field measurements.* Poster presentation, 54th conference of the European Group on Atomic Systems (EGAS 54), Strasbourg, France, Jun 18-22 2023.
- R. Momier, A. Sargsyan, A. Tonoyan, D. Sarkisyan, and C. Leroy. *Formation of strongly shifted EIT resonances using "forbidden" transitions of Cesium.* Poster presentation, 54th conference of the European Group on Atomic Systems (EGAS 54), Strasbourg, France, Jun 18-22 2023.
- R. Momier, A. Sargsyan, A. Tonoyan, D. Sarkisyan, and C. Leroy. *Formation of strongly shifted EIT resonances using "forbidden" transitions of Cesium.* Poster presentation, 28th Colloquium on High-Resolution Molecular Spectroscopy (HRMS), Dijon, France, Aug 28 - Sep 1 2023.
- R. Momier, A. Sargsyan, A. Tonoyan, D. Sarkisyan, and C. Leroy. *Sub-Doppler spectroscopy of ^{39}K for magnetic field measurements.* Poster presentation, 28th Colloquium on High-Resolution Molecular Spectroscopy (HRMS), Dijon, France, Aug 28 - Sep 1 2023.
- R. Momier, A. Sargsyan, A. Tonoyan, D. Sarkisyan, and C. Leroy. *Generation of EIT resonances with $\Delta F = +2$ transitions of Cs D_2 line.* Student presentation, International Conference Laser Physics 23, Ashtarak, Armenia, Sep 12-15 2023.

The results were also presented at internal seminars of the Institute for Physical Research, Ashtarak, Armenia, and of the Laboratoire ICB, Dijon, France, as well as during joint seminars between both institutions.

This thesis is intended to be as self-sufficient as possible; however, typos and/or mistakes and/or (especially) dead links may remain. If you notice any while reading the electronic version, please send me an email at `momier.rodolphe@gmail.com`. I would be grateful for any corrections.

Chapter 1

Nanometric-thin cell spectroscopy

In this chapter, we first demonstrate the advantage of nanometric-thin cells over usual spectroscopic cells. We then provide a theoretical model allowing us to compute transmission and selective reflection spectra. The spectra are in very good agreement with experimental measurements. In the last part, we use our nanometric-thin cells to measure atom-surface interaction coefficients of Rb and Cs and confirm several theoretical predictions recently performed by other groups.

Contents

1.1 Introduction **7**
1.2 Nanometric-thin cells **8**
1.2.1 Manufacturing and structure of the cell 9
1.2.2 Brief comparison to other experimental techniques 10
1.3 Fabry-Pérot nanocavity model **11**
1.3.1 Propagation equation 11
1.3.2 Reflected and transmitted signals 13
1.3.3 Derivation of the macroscopic polarization 15
1.3.4 Linear regime of interaction approximation 16
1.3.5 Lineshape analysis 18
1.3.6 Ensemble of two-level systems 20
1.4 Atom-surface interactions **22**
1.4.1 Van der Waals effect 22
1.4.2 Experimental setup 24
1.4.3 Van der Waals effect on Cs and Rb D_1 lines 24
1.4.4 Retardation of the van der Waals (vdW) effect 27
1.5 Conclusion **28**

1.1 Introduction

Thin alkali vapor cells of nanometric thickness are fascinating spectroscopic tools, gaining strong interest from the research community since the early 2000s as they allow to obtain sub-Doppler resolution easily with only one laser. Such a cell is commonly referred to as a nanocell (NC) and is commonly described as two dielectric windows enclosing an ensemble of two-level systems, where the gap between the windows is of the order of the transition wavelength λ of the system. It was first shown theoretically by Vartanyan and Lin [77] that Doppler-free resonances may occur in selective reflection (SR) spectra of NC for specific thicknesses. The symmetry properties of transmitted and reflected lineshapes have been studied again by Zambon and Nienhuis [78] where Faraday rotation and dichroism lineshape expressions were derived. However, the reflection from the second window was not taken into account. This was later done by Dutier *et al.* [79], where the cell was considered as a Fabry–Pérot (FP) cavity, taking into account the reflection from the second window. This leads to an interferometric behavior of the different fields and a significant asymmetry of the lineshapes. Moreover, it was proven that no reflected signal can be observed if the thickness of the cell is a multiple of λ, while strong narrowing of the transmission signal occurs if the thickness is a multiple of $\lambda/2$, which is a manifestation of coherent Dicke narrowing [95].

Experimental realization of such cells was first performed by Sarkisyan *et al.* at the Institute for Physical Research (Ashtarak, Armenia). In [54], they successfully reported the fabrication of a 150 - 300 nm thin NC allowing them to observe with a single beam the sub-Doppler structure of Cs D_2 line, with a linewidth an order of magnitude smaller than the room temperature Doppler-broadening. Since then, NCs have been used in a variety of studies ranging from fundamental studies of magneto-optical processes in strong magnetic fields [69] to molecular spectroscopy [96]. This chapter is aimed at recalling the basics of NC spectroscopy, and is organized as follows:

- In section 1.2, we recall the advantages of NC spectroscopy compared to other spectroscopic techniques. We describe the basic principles of sub-Doppler confinement in such cells and their manufacturing process.
- Section 1.3 is dedicated to the theoretical description of a NC, largely based on the work of Dutier *et al.* [79] and Zambon and Nienhuis [78], taking into account all the possible reflections at the different interfaces of the cell. The description of the fields in and out of the cell is performed using the Maxwell formalism coupled with the optical Bloch equations, assimilating the vapor to an ensemble of two-level systems. Analytical solutions of the lineshapes are given in the weak probe limit.
- In section 1.4 we present an experimental study of atom-surface interactions in a NC performed by recording various spectra of Cs and Rb D_1 lines. We measure the C_3 coefficient of van der Waals interaction of Cs and Rb atoms with the windows and, going to very low thicknesses ($<$ 60 nm), we highlight that this coefficient is often overestimated in the literature. We also present experimental evidence of the so-called “retardation” of the van der Waals effect predicted in recent theoretical studies [80, 81].

1.2 Nanometric-thin cells

At the Institute for Physical Research (Ashtarak, Armenia), NCs can be manufactured. As it has been first shown by Sarkisyan *et al.* in [54], such cells allow to easily record sub-Doppler spectra with a single low-power laser beam, as opposed to saturated absorption (SA) spectroscopy.

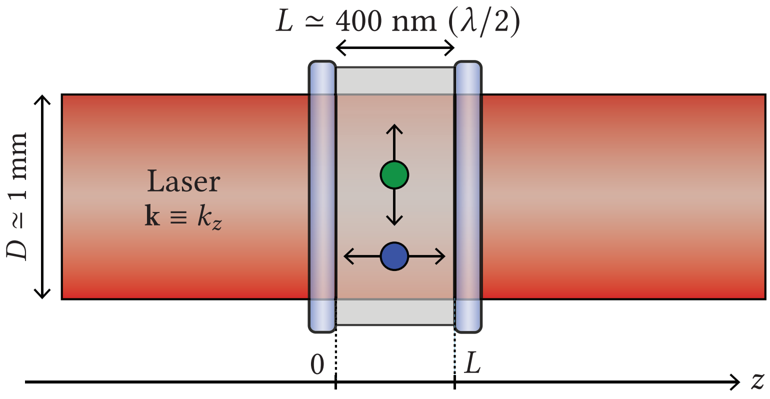

Figure 1.1 – Schematic diagram of a NC of thickness L with a laser beam propagating along z.

To put it simply, the essence of the process is the following: let us consider a 1 mm diameter laser beam propagating along the z direction hitting a NC at perpendicular incidence. The cell contains atoms moving at 300 m.s^{-1} (of the order of the typical most probable thermal velocity of alkali atoms at room temperature), and its thickness is typically around half a transition wavelength λ. If we take $L \simeq 400$ nm, the time of flight of atoms moving along the propagation direction is therefore

$$t_L = \frac{L}{v_z} = \frac{400 \cdot 10^{-9}}{300} \simeq 1.3 \text{ ns}, \tag{1.1}$$

while the time of flight of the atoms crossing (in a perfectly orthogonal way[1]) the laser beam, say along

---

[1] For the sake of simplicity of this explanation, we consider only atoms moving along x, y or z. Of course, in reality, atoms may (and do) move in other directions.

x, is

$$t_D = \frac{D}{v_x} = \frac{10^{-3}}{300} \simeq 3\ \mu\text{s}. \tag{1.2}$$

It directly comes that t_L is much smaller than the typical lifetime τ (inverse of the decay rate $\Gamma/2\pi$, typically several tens of ns) of an alkali atom while t_D is much bigger, implying that only the atoms flying orthogonally to the laser have time to be pumped and thus participate to absorption. Since for these atoms $\mathbf{k} \cdot \mathbf{v} = 0$, Doppler broadening is virtually killed simply due to the geometry of the cell. Of course, residual broadening remains due to atoms moving in other directions. This residual broadening is not significant and the typical linewidth obtained experimentally with a NC is an order of magnitude narrower than the Doppler broadening and allows to observe hyperfine transitions (between F states) separately [54] and obtain full resolution of all transitions occurring between Zeeman sublevels in a magnetic field [60] (and references therein).

1.2.1 Manufacturing and structure of the cell

In fig. 1.2, we present a schematic description of the cells manufactured in our laboratory. As seen in the front view (a), the cell consists of a sandwich of two $20 \times 30 \times 3$ mm^3 windows. The windows are usually made of sapphire (Al_2O_3) due to its chemical stability against alkali vapors. One could use windows made of glass, but they would irreversibly darken at high temperatures (the process is described for sodium in [97]). The sapphire is cut so that its natural birefringence is minimized if the cell is excited under normal incidence (i.e. the crystal c-axis is orthogonal to the window)[2]. To avoid various losses, the windows must be well polished, typically to a roughness smaller than $\lambda/10$.

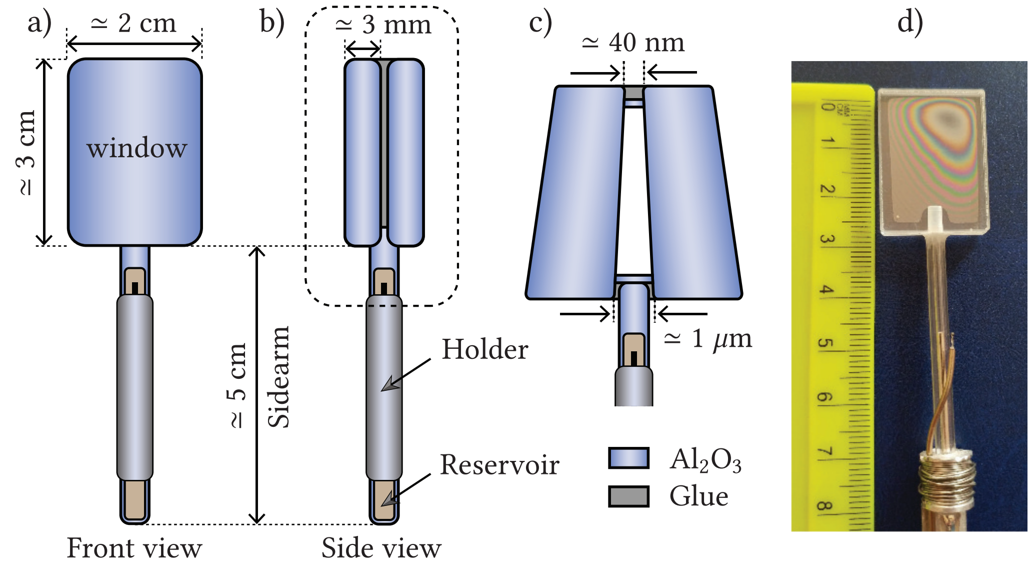

Figure 1.2 – Front (a) and side (b-c) views of a NC with typical dimensions. c) Zoom on the dashed rectangle showing the wedged structure of the cell. d) Real picture of a NC.

As can be seen on the side view (b), the windows are glued together around their perimeter. On the top and bottom, rectangular sapphire strips are created by vacuum deposition[3] to give the cell a wedge-shaped structure, see the zoom in fig. 1.4c. This allows to access different cell thicknesses during experiments, simply by adjusting the height of the cell. The width of the vapor column will typically vary between 40 nm and 1 μm or more, which can still be considered virtually uniform within a small laser beam (1 mm). On the bottom, once the windows are glued together, a hole is drilled in the glue, and a sapphire tube (sidearm, inner diameter 1 mm) containing solid alkali metal (Na, K, Rb or Cs[4]) is placed. The whole process takes place in a vacuum chamber and filling is performed like for usual glass cells.

---

[2] Sapphire may sometimes be replaced by Yttrium-Aluminium garnet (YAG, $Y_3Al_5O_{12}$). Depending on the study (requiring high laser power, for example), it may be more useful to use garnet as it has no natural birefringence.

[3] For "regular" thin cells (micrometric for example) we follow roughly the same procedure, but titanium strips are used as spacers instead of sapphire deposition. Titanium is also chemically stable against alkali vapors.

To increase the vapor density during experiments, the cell is placed in an oven. It is possible to determine the vapor density by knowing the temperature of the upper part of the metallic column in the sidearm [98]. To prevent causing damage to the windows (for example, condensation), their temperature has to be kept slightly higher than that of the sidearm. We typically use a two-section oven if the temperature is high and has to be precisely controlled, or simply use a regular oven with the sidearm out. A chromel-alumel thermocouple is soldered to the sapphire sidearm, as shown in fig. 1.2c, allowing us to retrieve the temperature of the metallic column.

1.2.2 Brief comparison to other experimental techniques

The best way of highlighting the advantage of NCs over regular sub-Doppler techniques is probably to compare spectra side to side. In fig. 1.3, we present an experimental transmission spectrum of Cs D_2 line ($3 \longrightarrow 2', 3', 4'$ transitions) recorded with a NC and a usual SA spectrum. It is clearly seen that the peaks are better pronounces in NC than in SA, and that unnecessary crossover (CO) resonances (dips located exactly between two transitions) strongly complicate the SA spectrum, without carrying relevant information on the vapor. As it has been thoroughly discussed in other works (e.g. [99] and references therein), NC spectroscopy has striking advantages compared to the use of usual cells. One can note that:

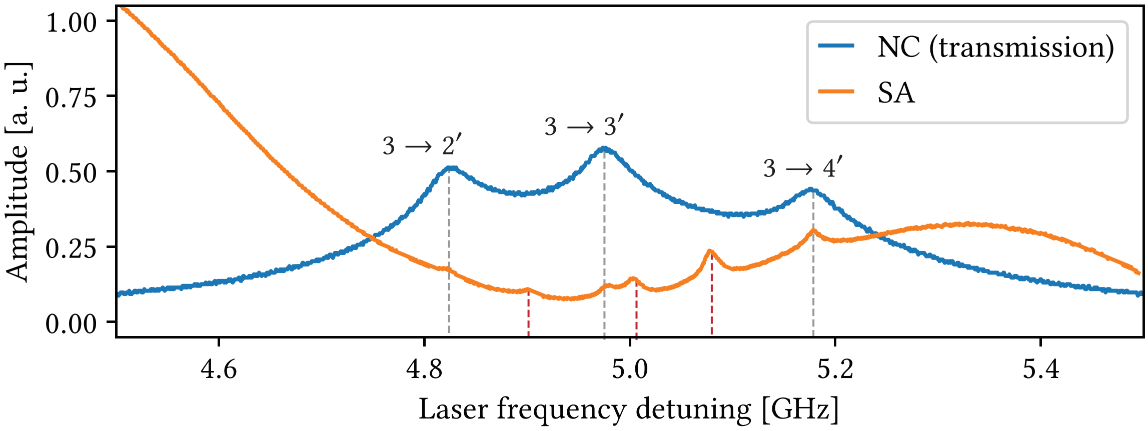

Figure 1.3 – Blue: experimental transmission spectrum of the $3 \longrightarrow 2', 3', 4'$ transitions of Cs D_2 line recorded with a NC ($L = \lambda/2$, $T = 110$ °C). Orange: SA spectrum recorded with a cm-long cell. The grey dashed lines indicate the position of the transitions and the red dashed lines indicate cross-over resonances.

- Sub-Doppler atomic lines can be observed with the use of a single low-power beam [54]. Despite the advantages, it is seen that the spectral width in the case of a NC is bigger than the spectral width of SA spectra.
- Sub-Doppler molecular spectroscopy can be performed [96],
- A very simple experimental setup is needed, only requiring an additional oven to increase the vapor density in the cell at will,
- Full resolution of hyperfine and Zeeman transitions can be achieved, thus magneto-optical processes can be precisely studied [60, 68, 69],

---

[4] We do not own a lithium cell. Due to their small size, Li atoms evaporate through the glue when the cell is heated. Cs may be liquid at room temperature (its melting point is 28.4 °C) but is in fact in a supercooled state.

- Absorption and reflection spectra (and their derivatives) have a much bigger signal-to-noise ratio than SA spectra and do not include any crossover resonances, only complicating the spectra without carrying any information on the atomic vapor [55, 61],
- It is possible to investigate cooperative effects and atom-surface interactions due to the small thickness of the cell [44, 100–102].

1.3 Fabry-Pérot nanocavity model

1.3.1 Propagation equation

We will now focus on the theoretical description of the fields reflected and transmitted by the cell. Let us consider a cavity made of two dielectric windows of refractive indices n_1 and n_2 separated by a distance L, enclosing a dilute[5] atomic vapor. Any effect that could be caused by the windows such as birefringence and diffraction are neglected. The windows are considered to be parallel and transparent (neither absorption nor scattering losses are taken into account). The system is represented in fig. 1.4.

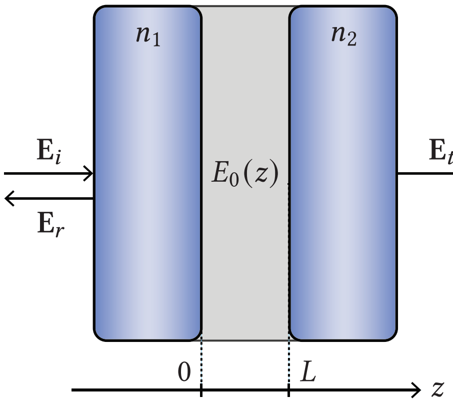

Figure 1.4 – Scheme of a cavity of thickness L made of two windows of refractive indices n_1 and n_2, with the incident ($\mathbf{E}_i$), transmitted ($\mathbf{E}_t$) and reflected ($\mathbf{E}_r$) laser fields. The reflected laser field $\mathbf{E}_r$ accounts for reflections at the air-window, window-vapor, vapor-window, and window-air interfaces, omitted in this figure for the sake of clarity.

We focus here on a purely one-dimensional problem (polarization effects are neglected), where the atomic medium is excited under normal incidence by an incident plane wave $\mathbf{E}_i$ of wavevector $\mathbf{k}$ and angular frequency ω:

$$\mathbf{E}_i(z,t) = \frac{1}{2}E_i \exp\left[-i(\omega t - kn_1 z)\right] \cdot \mathbf{e}_i + \text{c.c.}, \tag{1.3}$$

where $k = \omega/c$ and $\mathbf{e}_i$ is a unit vector denoting an arbitrary polarization. The portion of the field transmitted through the vapor and the second window is of the form

$$\mathbf{E}_t(z,t) = \frac{1}{2}E_t \exp\left[-i(\omega t - kn_2 z + \phi)\right] \cdot \mathbf{e}_t + \text{c.c.}, \tag{1.4}$$

while the reflected field, taking into account various reflections such as the air-window, window-vapor, vapor-window, and window-air interfaces can be written

$$\mathbf{E}_r(z,t) = \frac{1}{2}E_r \exp\left[-i(\omega t + kn_1 z)\right] \cdot \mathbf{e}_r + \text{c.c.}. \tag{1.5}$$

In eqs. (1.3) to (1.5), the amplitudes E_r and E_t are constant and E_i is assumed to be real. The goal of this chapter is to express the amplitude of the reflected and transmitted fields. The field $\mathbf{E}_0$ inside the atomic medium (between 0 and L) and the atomic response $\mathbf{P}_0$ can be described by[6]

---

[5] The refractive index of the vapor can be neglected.

$$\mathbf{E}_0(z,t) = \frac{1}{2}E_0(z)\exp\left[-i(\omega t - kz)\right] + \text{c.c.} \tag{1.6}$$

$$\mathbf{P}_0(z,t) = \frac{1}{2}P_0(z)\exp\left[-i(\omega t - kz)\right] + \text{c.c.}. \tag{1.7}$$

To express the reflected and transmitted amplitudes, we use the electromagnetic continuity relations for the fields at each interface, coupled with the Maxwell equations describing the propagation of the field in the atomic medium. At $z = 0$ and $z = L$, these relation respectively read

$$\begin{cases} E_i + E_r = E_0(0) \\ in_1k(E_i - E_r) = ikE_0(0) + \frac{\partial}{\partial z}E_0(0) \end{cases} \quad \text{and} \quad \begin{cases} E_0(L) = E_t \\ ikE_0(L) + \frac{\partial}{\partial z}E_0(L) = in_2kE_t \end{cases}. \tag{1.8}$$

Inside the vapor, under stationary continuous wave (CW) excitation, the field satisfies the propagation equation

$$\frac{\partial^2}{\partial z}E_0(z) + 2ikE_0(z) = -\frac{k^2}{\epsilon_0}P_0(z), \tag{1.9}$$

or, more conveniently:

$$\frac{\partial}{\partial z}\left[\exp(2ikz)\frac{\partial E_0(z)}{\partial z}\right] = -\frac{k^2}{\epsilon_0}P_0(z)\exp(2ikz). \tag{1.10}$$

Assuming the atomic response is known (we will derive it later in this chapter), one can integrate eqs. (1.9) and (1.10) between 0 and L to get

$$\frac{\partial E_0(L)}{\partial z} - \frac{\partial E_0(0)}{\partial z} + 2ik\left[E_0(L) - E_0(0)\right] = -\frac{k^2}{\epsilon_0}\int_0^L P_0(z)\mathrm{d}z \tag{1.11}$$

$$\frac{\partial E_0(L)}{\partial z}\exp(2ikL) - \frac{\partial E_0(0)}{\partial z} = -\frac{k^2}{\epsilon_0}\int_0^L P_0(z)\exp(2ikz)\mathrm{d}z. \tag{1.12}$$

Equations (1.11) and (1.12) can be written

$$\frac{\partial E_0(L)}{\partial z} - \frac{\partial E_0(0)}{\partial z} + 2ik\left[E_0(L) - E_0(0)\right] = 2ikI_f \tag{1.13}$$

$$\frac{\partial E_0(L)}{\partial z}\exp(2ikL) - \frac{\partial E_0(0)}{\partial z} = 2ikI_b, \tag{1.14}$$

where the so-called forward and backward integrals of the atomic response I_f and I_b were defined as follows:

$$I_f = \frac{ik}{2\epsilon_0}\int_0^L P_0(z)\mathrm{d}z \tag{1.15}$$

$$I_b = \frac{ik}{2\epsilon_0}\int_0^L P_0(z)\exp(2ikz)\mathrm{d}z. \tag{1.16}$$

In the limit $L \longrightarrow \infty$, these integrals are respectively associated with the usual long cell transmission and SR signals [103, 104]. From this point, it is possible to solve the linear system of equations consisting in eqs. (1.8), (1.13) and (1.14) with respect to the transmitted and reflected amplitudes E_t and E_r. We obtain the following solution:

$$E_t = t_{02}t_{10}E_i/F + t_{02}\left(I_f - r_1I_b\right)/F = E_t^{\text{FP}} + E_t^{\text{R}} \tag{1.17}$$

$$E_r = \left[r_1 - r_2\exp(2ikL)\right]E_i/F + t_{01}\left[I_b - r_2I_f\exp(2ikL)\right]/F = E_r^{\text{FP}} + E_r^{\text{R}}, \tag{1.18}$$

---

[6] To possibly take into account inhomogeneities that could occur along the propagation axis (saturation, pumping, transient effects due to atomic motion or atom-surface interactions), no assumptions are made regarding the form of the amplitudes $E_0(z)$ and $P_0(z)$.

where E_t^{FP} and E_r^{FP} are the solutions that would be obtained in the case of an empty FP cavity, ie. if $I_b = I_f = 0$, and E_t^{R} and E_r^{R} are resonant contributions induced by the excitation of the atomic medium. In eqs. (1.17) and (1.18), $F = 1 - r_1 r_2 \exp(2ikL)$ is the quality factor of the FP cavity, r_1 and r_2 are the reflection coefficients of each window, and t_{01}, t_{10} and t_{02} are the transmission coefficients at each interface:

$$r_i = \frac{n_i - 1}{n_i + 1} \qquad t_{0i} = \frac{2}{n_i + 1} \qquad t_{10} = \frac{2n_1}{n_1 + 1}. \tag{1.19}$$

It is clear from eqs. (1.17) and (1.18) that the backward integral of atomic response I_b cannot be neglected in transmission spectra, even with an antireflection coating[7] on the second window. If an antireflection coating was applied to the first window, I_b would vanish. However in that case no reflection signal can be detected. Analogously, the forward response cannot be neglected in the reflection spectrum and would vanish only in the presence of an antireflection coating on the second window. If none of the windows are coated, it is necessary to take into account both forward and backward responses when computing spectra of vapors contained in thin cells. In longer cells, I_b can be safely neglected as it has a rather small coherence length (one optical wavelength). As we will see later, I_b will have a strong influence on the line shape compared to absorption (or reflection) lines recorded in longer cells.

1.3.2 Reflected and transmitted signals

We will now express the intensities of the transmitted and reflected signals as this is what is recorded during experiments. The intensity of an electric field reads in general as follows:

$$I = \frac{1}{2}\epsilon_0 c E E^* \propto |E|^2 . \tag{1.20}$$

As shown in eqs. (1.17) and (1.18), E_r and E_t are in fact superpositions of two fields. We can write

$$|E_t|^2 = \left|E_t^{\mathrm{FP}}\right|^2 + \left|E_t^{\mathrm{R}}\right|^2 + 2\,\mathrm{Re}\left[E_t^{\mathrm{FP}} E_t^{\mathrm{R}}\right] \tag{1.21}$$

$$|E_r|^2 = \left|E_r^{\mathrm{FP}}\right|^2 + \left|E_r^{\mathrm{R}}\right|^2 + 2\,\mathrm{Re}\left[E_r^{\mathrm{FP}} E_r^{\mathrm{R}}\right] . \tag{1.22}$$

Calculating each term separately, we obtain the transmitted and reflected intensities

$$|E_t|^2 = \underbrace{\frac{t_{02}^2 t_{10}^2}{|F|^2} E_i^2}_{\text{Empty FP signal}} + \underbrace{\frac{t_{02}^2}{|F|^2}\left(\left|I_f\right|^2 + r_1^2 \left|I_b\right|^2 - 2r_1\,\mathrm{Re}\left[I_f^* I_b\right]\right)}_{\text{Signal re-emitted by the vapor}} + \underbrace{2\frac{t_{02}^2 t_{10}}{|F|^2}\,\mathrm{Re}\left[I_f - r_1 I_b\right]}_{\text{Homodyne beating} \propto \mathrm{Re}\left[E_t^{\mathrm{FP}} E_t^{\mathrm{R}}\right]} \tag{1.23}$$

$$|E_r|^2 = \underbrace{\frac{E_i}{|F|^2}\left[r_1^2 + r_2^2 - 2r_1 r_2 \cos(2kL)\right]}_{\text{Empty FP signal}} + \underbrace{\frac{t_{01}^2}{|F|^2}\left(\left|I_b\right|^2 + r_2^2 \left|I_f\right|^2 - 2r_2\,\mathrm{Re}\left[I_f I_b^* \exp(2ikL)\right]\right)}_{\text{Signal re-emitted by the vapor}} \tag{1.24}$$

$$+ \underbrace{2\frac{E_i t_{01}}{|F|^2}\,\mathrm{Re}\left[\{r_1 - r_2 \exp(-2ikL)\}\left\{I_b - r_2 \exp(2ikL) I_f\right\}\right]}_{\text{Homodyne beating} \propto \mathrm{Re}\left[E_r^{\mathrm{FP}} E_r^{\mathrm{R}}\right]} . \tag{1.25}$$

Each signal has three contributions: an empty FP signal that can be seen as background since in most experiments the scanning range of the laser is much smaller than the free spectral range of the cavity, a contribution re-emitted by the vapor, and a contribution that may be interpreted as a homodyne beating with the transmitted (or reflected) field of an empty FP cavity. One can finally show that, in the case of a dilute vapor, since $E_t^{\mathrm{FP}} \gg E_t^{\mathrm{R}}$ and $E_r^{\mathrm{FP}} \gg E_r^{\mathrm{R}}$, it is possible to express the recorded transmitted and reflected signals S_t and S_r with the following simple expressions:

---

[7] An antireflection coating on one of the windows (or both) can be taken into account in the model by setting $n_1 = 1$ or $n_2 = 1$, resulting in $r_1 = 0$ or $r_2 = 0$.

$$S_t = 2\frac{t_{02}^2 t_{10}}{|F|^2}\,\mathrm{Re}\left[I_f - r_1 I_b\right] \tag{1.26}$$

$$S_r = 2\frac{E_i t_{01}}{|F|^2}\,\mathrm{Re}\left[\{r_1 - r_2\exp(-2ikL)\}\left\{I_b - r_2\exp(2ikL) I_f\right\}\right]. \tag{1.27}$$

The empty FP cell background vanishes for $L = m\lambda/2$ with $m \in \mathbb{N}$ if the two cell windows are identical. In that case, the reflected signal reduces to

$$S_r = \frac{\left|I_b - rI_f\right|^2}{(1+r)^2}. \tag{1.28}$$

Determination of the thickness

As a consequence of the proximity of the cell windows, an interferometric pattern may be observed due to the reflection of ambient on the inner interfaces of the cell, as shown in fig. 1.2d (the dark central halo corresponds to a point where optical contact is almost achieved). This pattern may be used to determine roughly the different cell thicknesses with the eye but will not yield a precise result. Theoretically speaking, the thickness can be calculated using the ratio of the intensity of the field reflected by the second window I_2 to the intensity reflected by the first window I_1. Using eqs. (1.23) to (1.25), this ratio can be written [105]

$$\frac{I_{R_2}}{I_{R_1}} = \frac{(1-R)^2}{R}\frac{F\sin^2(2\pi L/\lambda)}{1+F\sin^2(2\pi L/\lambda)}, \tag{1.29}$$

where we considered two identical windows of reflection coefficient r ($R = r^2$ is the reflection coefficient in intensity) and denoted $F = 4R/(1-R)^2$. This ratio is presented for several wavelengths in fig. 1.5 for L varying between 0 and 1600 nm.

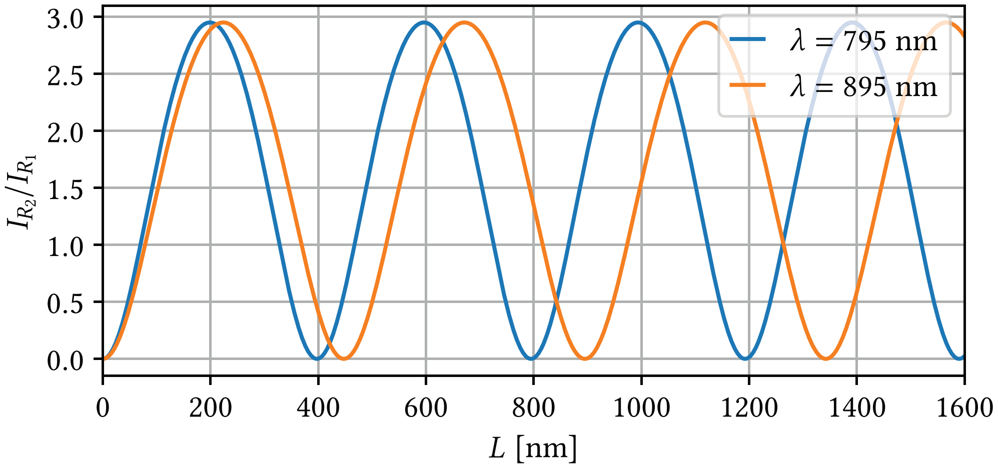

Figure 1.5 – Ratio of the reflected intensities as a function of the cell length for $\lambda = 795$ nm (Rb D_1 line) and $\lambda = 895$ nm (Cs D_1 line).

As expected from a FP cavity, we obtain constructive interferences for $L = (2m+1)\lambda/4$ and destructive interferences[8] for $L = m\lambda/2$ with $m \in \mathbb{N}$. The thickness therefore cannot be measured with a single evaluation of the ratio and either needs to be followed very carefully from a known position or to be measured using two perfectly aligned laser beams with different wavelengths [105, Section 2.4].

---

[8] In reality, one may not expect perfect extinction at $L = m\lambda/2$ due to possible losses caused, for example, by absorption, diffusion, or remaining birefringence, which are all neglected here.

1.3.3 Derivation of the macroscopic polarization

Let us consider a simple resonant two-level atomic medium of Rabi frequency Ω and decay rate Γ, as depicted in fig. 1.6. Now that we have derived the expressions of the transmitted and reflected fields, we need to determine the forward and backward responses I_f and I_b, ie. determine the macroscopic polarization of the atomic medium. In the density matrix formalism [details regarding this formalism are provided in appendix C], this macroscopic polarization $P_0(z,\omega)$ can be written as follows [23, 106]:

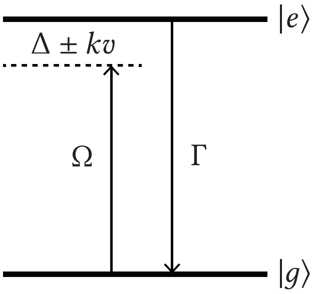

Figure 1.6 – Scheme of a two-level system of decay rate Γ driven by the Rabi frequency Ω.

$$P_o(z,\omega) = Nd\left\langle \rho_{eg}(z,v)\right\rangle = Nd_{eg}\int M(v)\rho_{eg}(z,v)\mathrm{d}v, \tag{1.30}$$

where N is the number density, d_{eg} the transition dipole moment, $M(v)$ is the atomic velocity distribution (assumed to be Maxwellian[9], as shown in fig. 1.7) and ρ_{eg} are the off-diagonal elements of the density matrix, whose dynamical behavior is given by the Liouville - von Neumann equation:

$$\frac{\mathrm{d}\rho}{\mathrm{d}t} = -\frac{i}{\hbar}\left[\mathcal{H},\rho\right] + \mathcal{L}(\rho), \tag{1.31}$$

where $[\mathcal{H},\rho]$ is the commutator of the total Hamiltonian (bare states + laser interaction) and the density matrix ρ, and $\mathcal{L}(\rho)$ is the Lindblad operator describing dissipative processes occurring in the system (for example spontaneous decay and dephasing). In the general case, the density matrix of a thermal vapor is a function of the atomic position $\mathbf{r}$ and can be written

$$\frac{\mathrm{d}\rho(\mathbf{r},t)}{\mathrm{d}t} = \left(\frac{\partial\rho(\mathbf{r},t)}{\partial x}v_x + \frac{\partial\rho(\mathbf{r},t)}{\partial y}v_y + \frac{\partial\rho(\mathbf{r},t)}{\partial z}v_z\right) + \frac{\partial\rho(\mathbf{r},t)}{\partial t} \tag{1.32}$$

$$= \boldsymbol{\nabla}\rho(\mathbf{r},t)\cdot\mathbf{v} + \frac{\partial\rho(\mathbf{r},t)}{\partial t} \tag{1.33}$$

We can introduce the so-called *reduced* density matrix by performing a transformation to a rotating frame:

$$\rho(z,v,t) = \sigma(z,v)\exp\left[i(kz-\omega t)\right] + \text{c.c.} \tag{1.34}$$

Due to the geometry of our problem, we can limit ourselves to the one-dimensional case. Keeping only the z-component and assuming $v \equiv v_z$, one can rewrite eq. (1.31) as

$$\frac{\partial}{\partial t}\rho(z,v,t) + v\frac{\partial}{\partial z}\rho(z,v,t) = -\frac{i}{\hbar}\left[\mathcal{H},\rho\right] + \mathcal{L}(\rho). \tag{1.35}$$

Injecting eq. (1.34) into eq. (1.35) allows us to find the evolution of the reduced density matrix in the steady state regime

$$v\frac{\partial\sigma(z,v)}{\partial z} = -\frac{i}{\hbar}\left[\mathcal{H},\sigma\right] + \mathcal{L}(\sigma) + i(\omega - kv)\sigma, \tag{1.36}$$

---

[9] The most probable thermal velocity [the peak of the probability density function $v^2M(v)$] is given by $u = \sqrt{2k_BT/m}$ and the mean thermal velocity is $\langle v\rangle = \sqrt{8k_BT/\pi m} = 2v_p/\sqrt{\pi}$, where m is the atomic mass (in kg).

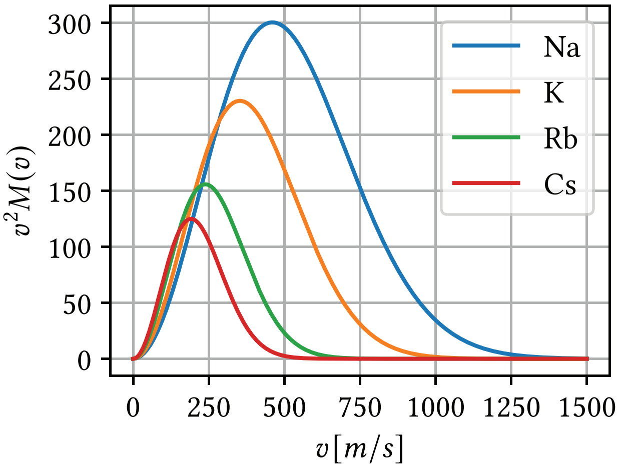

Figure 1.7 – Probability density function of the Maxwell-Boltzmann velocity distribution $M(v)$ calculated for Na, K, Rb, and Cs at room temperature ($T = 293.15$ K).

which gives for the coherences

$$v\frac{\partial \sigma_{eg}}{\partial z} = i\Omega(\sigma_{gg} - \sigma_{ee}) - \Lambda_{\pm}\sigma_{eg}, \tag{1.37}$$

where $\Lambda_{\pm} = \Gamma/2 - i(\Delta \mp kv)$ if we only take into account the natural decay rate (homogeneous linewidth) of the system. The term $\Gamma/2$ can be replaced by γ such that $\gamma = \Gamma/2 + \gamma_{dec}$ to account for a potential additional broadening arising from decoherence effects.
Using the reduced density matrix, the induced polarization [eq. (1.30)] finally becomes

$$P_0(z) = Nd_{eg}\int_{-\infty}^{+\infty} M(v)\sigma_{eg}(z,v)\mathrm{d}v \tag{1.38}$$

$$= Nd_{eg}\int_{0}^{+\infty} M(v)\left[\sigma_{eg}^{+}(z,v) + \sigma_{eg}^{-}(z,-v)\right]\mathrm{d}v. \tag{1.39}$$

Equation (1.39) is valid if the cell windows are not antireflection-coated. In that case, we can safely assume that the atoms lose coherence when colliding with the windows [$\sigma_{eg}(0,v) = \sigma_{eg}(L,v) = 0$]. This allows to decompose the coherences into two parts: $\sigma_{eg}^{+}(z,v)$ corresponding to atoms moving from $z = 0$ to $z = L$ at velocity $+v$ and $\sigma_{eg}^{-}(z,-v)$ corresponding the atoms moving from $z = L$ to $z = 0$ at velocity $-v$. One can thus split the integral in eq. (1.38) assuming $M(v)$ is symmetrical, which yields a more convenient expression for numerical simulations.

1.3.4 Linear regime of interaction approximation

Working with closed atomic systems imposes the condition $\sigma_{gg} + \sigma_{ee} = 1$. Upon excitation by a weak, non-saturating laser field ($\Omega \ll \Gamma$), we may neglect the population of the upper state $|e\rangle$ so that

$$\sigma_{gg} + \sigma_{ee} \simeq \sigma_{gg} \simeq 1. \tag{1.40}$$

This implies, for atoms moving from $z = 0$ to $z = L$ (positive velocities), that eq. (1.37) becomes:

$$\frac{\partial \sigma_{eg}^{+}}{\partial z} = i\frac{\Omega}{v} - \frac{\Lambda_{+}}{v}\sigma_{eg}^{+}. \tag{1.41}$$

This can be easily solved by taking into account the boundary conditions on the coherences mentioned earlier, yielding the solution

$$\sigma_{eg}^{+}(z,+v,\Delta) = \frac{i\Omega}{\Lambda_+}\left[1-\exp\left(\frac{-\Lambda_+}{v}z\right)\right] \tag{1.42}$$

$$\sigma_{eg}^{-}(z,-v,\Delta) = \frac{i\Omega}{\Lambda_-}\left\{1-\exp\left[\frac{-\Lambda_-}{v}(L-z)\right]\right\}. \tag{1.43}$$

Let us now come back to the expressions of the fields [eqs. (1.17) and (1.18)] and the continuity relations [eq. (1.8)] derived earlier. Assuming the atomic medium is dilute, ie. $E_t^{\mathrm{FP}} \gg E_t^{\mathrm{R}}$ and $E_r^{\mathrm{FP}} \gg E_r^{\mathrm{R}}$, the field $E_0(z)$ inside the vapor driving the polarization $P_0(z)$ mainly consists in the field $E_0^{\mathrm{FP}}(z)$ inside an empty FP:

$$E_0(z) = E_0^{\mathrm{FP}}(z) + E_0^{\mathrm{R}}(z) \simeq E_0^{\mathrm{FP}}(z), \tag{1.44}$$

where the components $E_0^{\mathrm{FP}}(z)$ and $E_0^{\mathrm{R}}(z)$ are defined in a similar manner as in section 1.3.1. We may assume that the atomic medium responds linearly to the weak incident field. In that frame, one may show that we have

$$E_0(z) = E_i t_{10}\left(1 - r_2\exp[-2ik(z-L)]\right). \tag{1.45}$$

We can decompose $E_0(z)$ and $P_0(z)$ into forward and backward contributions:

$$E_0(z) = \frac{1}{2}\left\{E_0^{+}\exp\left[-i(\omega t - kz)\right] + E_0^{-}\exp\left[-i(\omega t + kz)\right]\right\} + \text{c.c.} \tag{1.46}$$

$$P_0(z) = \frac{1}{2}\left\{P_0^{+}\exp\left[-i(\omega t - kz)\right] + P_0^{-}\exp\left[-i(\omega t + kz)\right]\right\} + \text{c.c.}, \tag{1.47}$$

where the forward and backward polarization amplitude $P_0^+(z)$ and $P_0^-(z)$ are driven only by the constant forward and backward field amplitudes E_0^+ and E_0^- respectively. After injecting eq. (1.45) in eq. (1.46), by identification one easily obtains

$$E_0^{+} = E_i t_{10}/F \quad \text{and} \quad E_0^{-} = -r_2\exp(2ikL)E_0^{+}, \tag{1.48}$$

with $F = 1 - r_1 r_2 \exp(2ikL)$. Since eq. (1.47) has to be consistent with eq. (1.7), we have

$$P_0(z) = P_0^{+}(z) + \exp(-2ikz)P_0^{-}(z). \tag{1.49}$$

Making some assumptions regarding the symmetry of the problem[10], we can write

$$P_0^{-}(L-z) = -r_2\exp(2ikL)P_0^{+}(z) \tag{1.50}$$

This allows us get rid of the backward contribution P_0^- in eq. (1.49) by reformulating it as follows:

$$P_0(z) = P_0^{+}(z) - r_2 P_0^{+}(L-z)\exp\left[2ik(L-z)\right]. \tag{1.51}$$

The field $E_0(z)$ driving the polarization $P_0(z)$ is therefore seen by the atoms as a traveling wave of constant amplitude E_0^+, corresponding to a single constant Rabi frequency $\Omega = d_{eg}E_0^+/\hbar$. In that case, the induced polarization given by eq. (1.39) can be reduced to

$$P_0^{+}(z) = N d_{eg}\int_0^{+\infty} M(v)\left[\sigma_{eg}^{+}(z,v) + \sigma_{eg}^{-}(z,-v)\right]\mathrm{d}v. \tag{1.52}$$

---

[10] Namely considering symmetrical atom-surface interactions and symmetrical velocity distribution.

One can thus express the resonant contribution to the transmitted and reflected fields as a combination of the common transmission and reflection signals calculating with only one traveling-wave excitation:

$$
\begin{aligned}
I_T^l &= \frac{ik}{2\epsilon_0}\int_0^L P_0^+(z)\mathrm{d}z && (1.53)\\
&= \frac{ik}{2\epsilon_0}Nd_{eg}\int_0^{+\infty} M(v)\left(\int_0^L\left[\sigma_{eg}^+(z,v)+\sigma_{eg}^-(z,-v)\right]\mathrm{d}z\right)\mathrm{d}v && (1.54)\\
I_R^l &= \frac{ik}{2\epsilon_0}P_0^+(z)\exp\left(2ikz\right)\mathrm{d}z. && (1.55)\\
&= \frac{ik}{2\epsilon_0}Nd_{eg}\int_0^{+\infty} M(v)\left(\int_0^L\left[\sigma_{eg}^+(z,v)+\sigma_{eg}^-(z,-v)\right]\exp\left(2ikz\right)\mathrm{d}z\right)\mathrm{d}v. && (1.56)
\end{aligned}
$$

Combining the latter with eqs. (1.15) and (1.16) we eventually obtain

$$
\begin{aligned}
I_f &= I_T^l - r_2 I_R^l && (1.57)\\
I_b &= I_R^l - r_2\exp\left(2ikL\right)I_T^l. && (1.58)
\end{aligned}
$$

The last step is now to perform the integration over z in eqs. (1.54) and (1.56). Doing so, the final expressions of the transmitted and reflected intensities read

$$
\begin{aligned}
I_T^l &= \frac{N|d_{eg}|^2}{2\hbar\epsilon_0}\frac{t_{10}E_i}{F}\int_{-\infty}^{+\infty} M(v)g(v,\Delta)\mathrm{d}v && (1.59)\\
I_R^l &= \frac{N|d_{eg}|^2}{2\hbar\epsilon_0}\frac{t_{10}E_i}{F}\int_{-\infty}^{+\infty} M(v)h_\pm(v,\Delta)\mathrm{d}v && (1.60)
\end{aligned}
$$

with the functions g and h given by

$$
\begin{aligned}
g(v,\Delta,L) &= -\frac{-k}{\Lambda_+}\left\{L-\frac{|v|}{\Lambda_+}\left[1-\exp\left(-\frac{\Lambda_+L}{|v|}\right)\right]\right\} && (1.61)\\
h_\pm(v,\Delta,L) &= \frac{1}{2i}\left(\frac{1}{\Lambda_\mp}-\frac{\exp\left(2ikL\right)}{\Lambda_\pm}\right)-\frac{k|v|}{\Lambda_+\Lambda_-}\exp\left(\frac{-\Lambda_\mp L}{|v|}\right). && (1.62)
\end{aligned}
$$

The general procedure used to compute spectra we use throughout this thesis is therefore the following:

1. Compute the functions g and h [eqs. (1.61) and (1.62)],
2. Inject the result into eqs. (1.59) and (1.60) and averaging over the velocity distribution $M(v)$ to obtain I_T^l and I_R^l,
3. Calculate the forward and backward responses I_f and I_b [eqs. (1.57) and (1.58)] using the previous results,
4. Inject I_f and I_b into eqs. (1.26) and (1.27) to obtain the reflected and transmitted signals.

Alternatively, one can expand eq. (1.31) and solve the system of ODEs to obtain the induced polarization. In most cases, it will not be possible to extract analytical solutions apart from the approximations derived in this section.

1.3.5 Lineshape analysis

Before simulating real spectra, we will try to reproduce the theoretical lineshapes presented in [79] to check whether our simulations are correct. In fig. 1.8a, we present theoretical transmission line shapes computed for a realistic NC made of two identical sapphire windows of refractive indices $n_1 = n_2 = 1.76$, corresponding to $r_1 = r_2 \simeq 0.275$. The cell thickness L varies between $\lambda/4$ and $9\lambda/8$ with a step of $\lambda/8$.

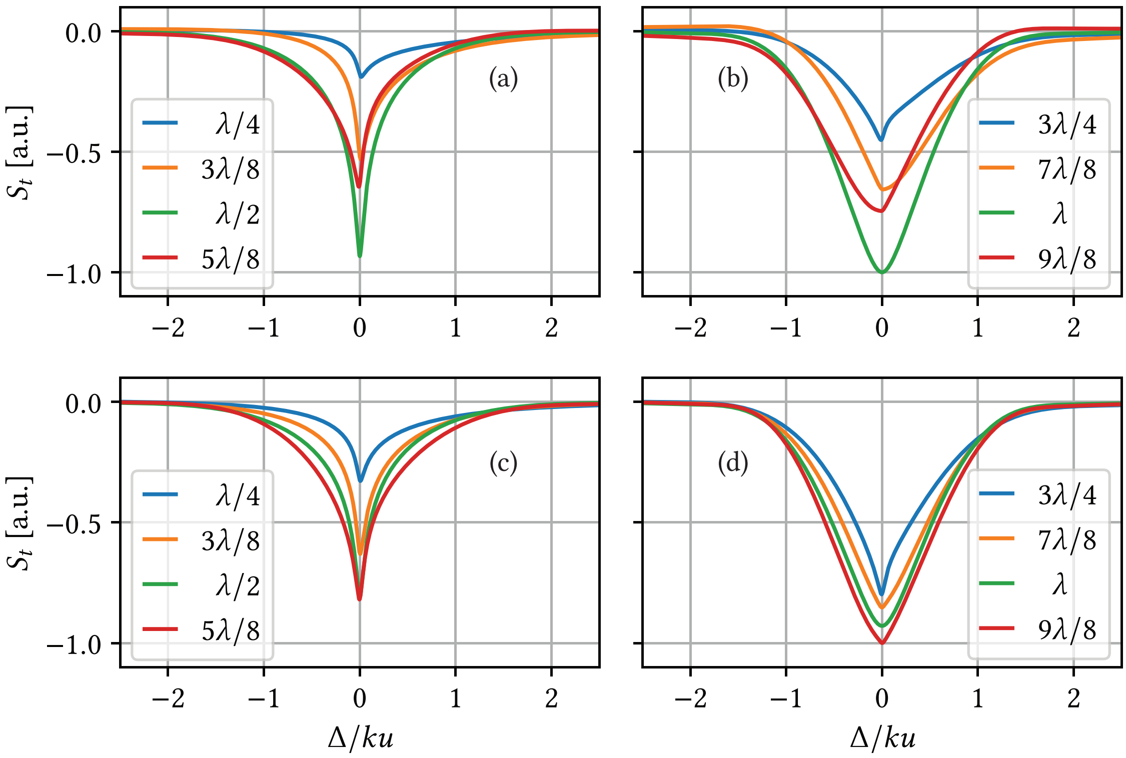

Figure 1.8 – Normalized transmitted signal S_t for various cell thicknesses in a cell made of two identical sapphire windows without (a-b) and with (c-d) antireflection coating on the second window. The lines were calculated with $\gamma/ku = 0.025$.

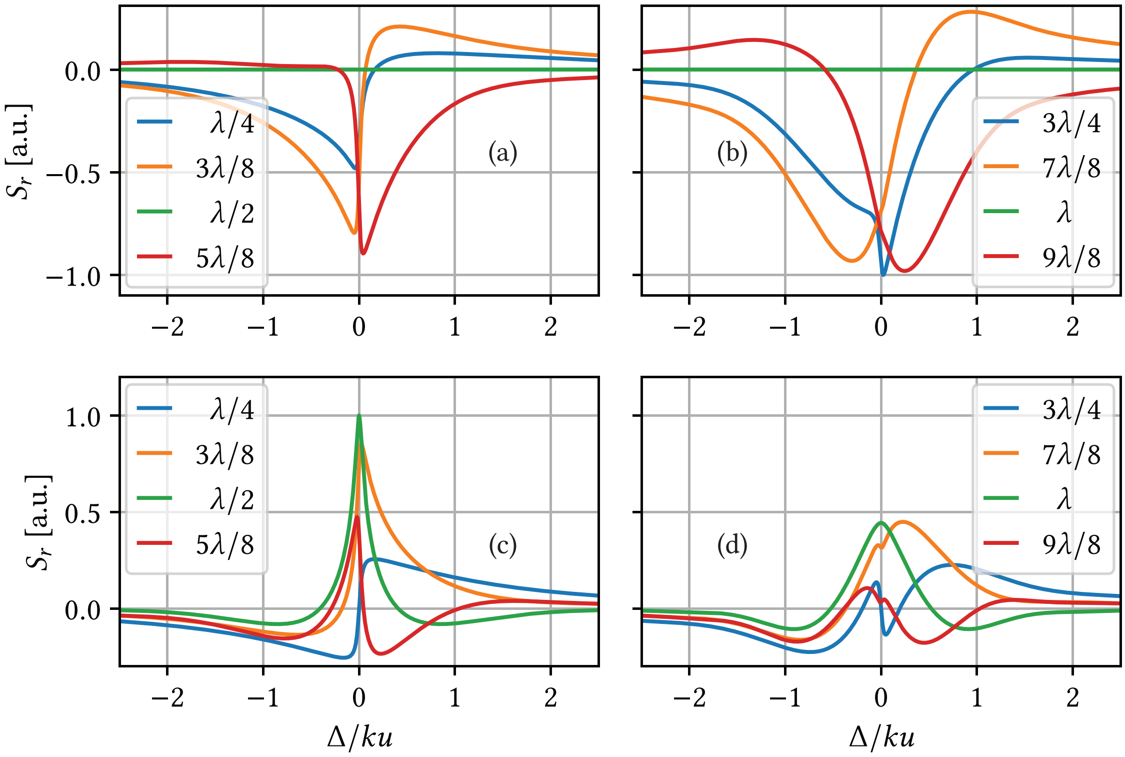

Figure 1.9 – Normalized reflected signal S_r for various cell thicknesses in a cell made of two identical sapphire windows without (a-b) and with (c-d) antireflection coating on the second window. The lines were calculated with $\gamma/ku = 0.025$.

Following the derivation performed earlier, one can clearly see that the signal transmitted through a thin cell is an interferometric combination of the common transmitted and reflected signals I_T^l and I_R^l:

$$I_T = [1 + r_1 r_2 \exp(2ikL)] I_T^l - (r_1 + r_2) I_R^l. \tag{1.63}$$

The transmitted signal includes a dispersive contribution and results in a strongly asymmetric line profile. Even if the spectra exhibit sub-Doppler features [arising from the contribution of atoms undergoing a long interaction time, ie. flying perpendicularly to the incident laser, see eqs. (1.59) and (1.60)], one can observe additional narrowing of the transmission lineshape for $L = (2p+1)\lambda/2$, $p \in \mathbb{N}$. This phenomenon was first observed in the microwave domain [95] and is called coherent Dicke narrowing. An additional shift of the line profile was unveiled by Ermolaev and Vartanyan in [107] arising from quenching of the atomic polarization upon collisions of atoms with the cell windows, this is not taken into account here. Figure 1.8b presents the case of a second window being antireflection-coated ($r_2 = 0$). In that case, we recover some symmetry, the cell does not behave like a FP cavity anymore and the results are in agreement with what was predicted in [78]. The reflected signal (presented in fig. 1.9) can be expressed as

$$I_R = [1 + r_2^2 \exp(2ikL)] I_R^l - 2r_2 \exp(2ikL) I_T^l \tag{1.64}$$

and involves a transmission contribution. The reflection profile is also asymmetric and, as a manifestation of the FP nature of the cavity, vanishes for $L = p\lambda/2$ [as predicted by eq. (1.27)]. Let us note that in this model, the linewidth of the system is a free parameter that can be fitted to the experimental measurements. Moreover, the impact of the temperature is not properly reflected on the lineshapes obtained with this model. One only observes an increase in the signal amplitude with the number density N. One would expect to observe broadening due to the increase in the number of atom-atom and atom-surface collisions with the temperature.

1.3.6 Ensemble of two-level systems

Until now, we have considered a toy vapor consisting of an ensemble of identical two-level systems. In practice, we can approximate real alkali vapors by an ensemble of two-level systems with different transition frequencies and transition dipole moments. In that case, each two-level system having a transition dipole moment d_k will see the incident laser with a detuning $\Delta_k = \omega - \omega_k$, where ω_k is the transition frequency of the system. The transmitted and reflected contributions I_T^l and I_R^l [eqs. (1.59) and (1.60)] become

$$I_T^l = \sum_k C_k \int_{-\infty}^{+\infty} M(v)\, g(v, \Delta_k)\, \mathrm{d}v \tag{1.65}$$

$$I_R^l = \sum_k C_k \int_{-\infty}^{+\infty} M(v)\, h_\pm(v, \Delta_k)\, \mathrm{d}v, \tag{1.66}$$

where C_k is, rigorously, a strength factor given by

$$C_k = \frac{N|d_k|^2 t_{10} E_i}{2\hbar\epsilon_0 F}. \tag{1.67}$$

We can then sum the contribution of each system to the induced atomic polarization to obtain

$$P_0^+(z) = N \sum_k d_k \int_0^{+\infty} M(v) \left[\sigma_{eg}^+(z, v, \Delta_k) + \sigma_{eg}^-(z, -v, \Delta_k)\right] \mathrm{d}v. \tag{1.68}$$

The computing procedure for a full spectrum with several transitions (each modeled by an independent two-level system) is the same as before, but looped over the different systems, summing all the contributions. One can for example compute spectra of the D_1 and D_2 lines of alkali atoms, as presented

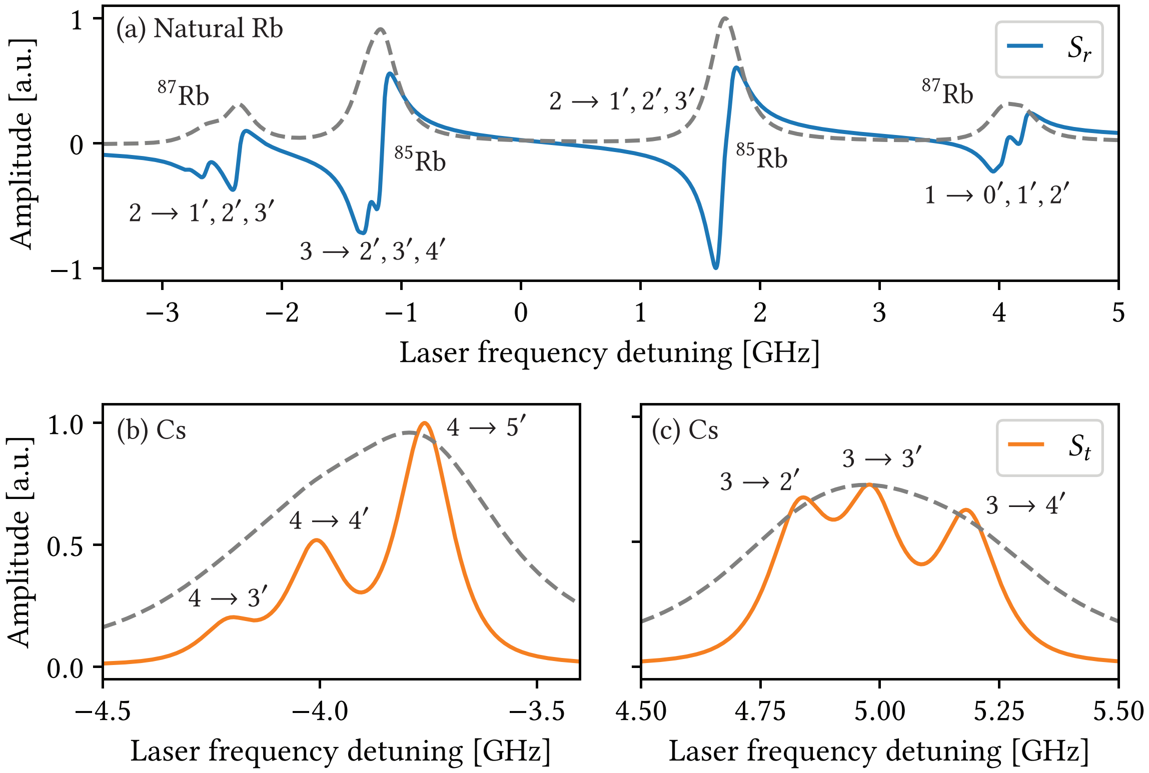

Figure 1.10 – (a) Typical theoretical SR spectrum of Cs D_2 line obtained for $L = 350$ nm. (b-c) Theoretical transmission spectrum of Cs D_2 line obtained for $L = \lambda/2$. The dashed lines are usual Doppler-broadened transmission profiles that would be obtained in regular cells.

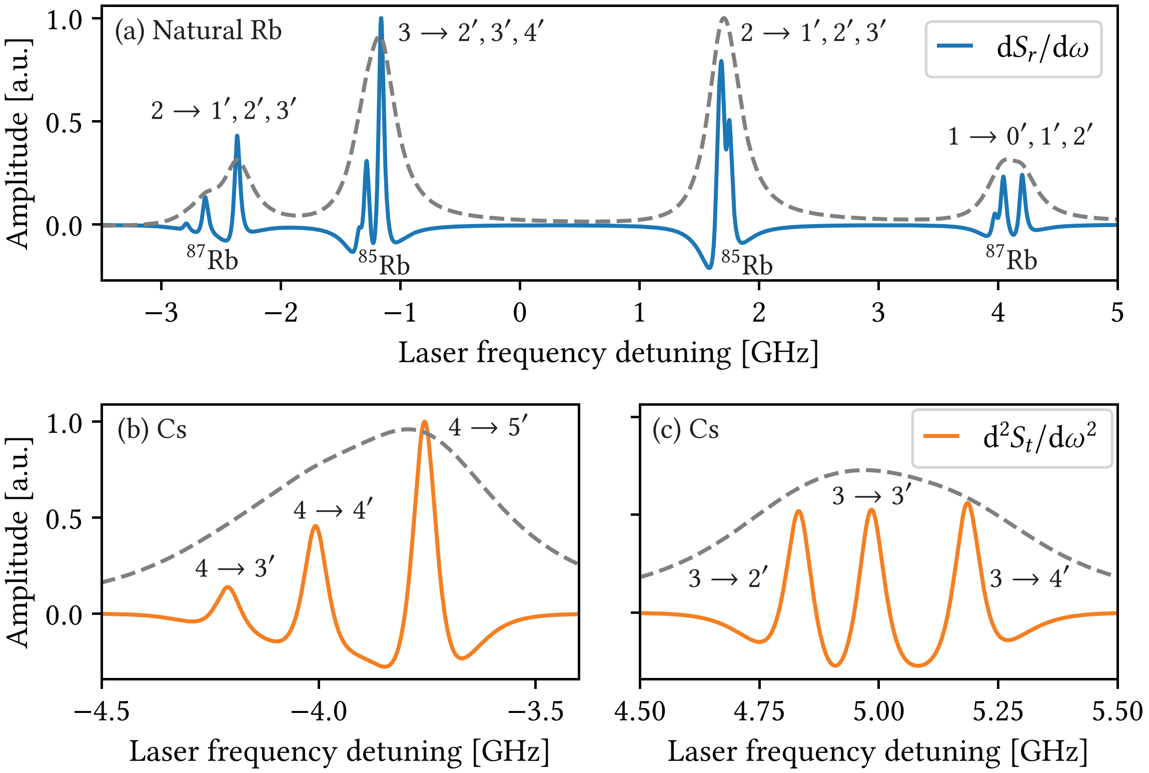

Figure 1.11 – (a) Typical theoretical dSR spectrum of natural Rb D_2 line obtained for $L = 350$ nm. (b-c) Theoretical SD spectrum of Cs D_2 line obtained for $L = \lambda/2$.

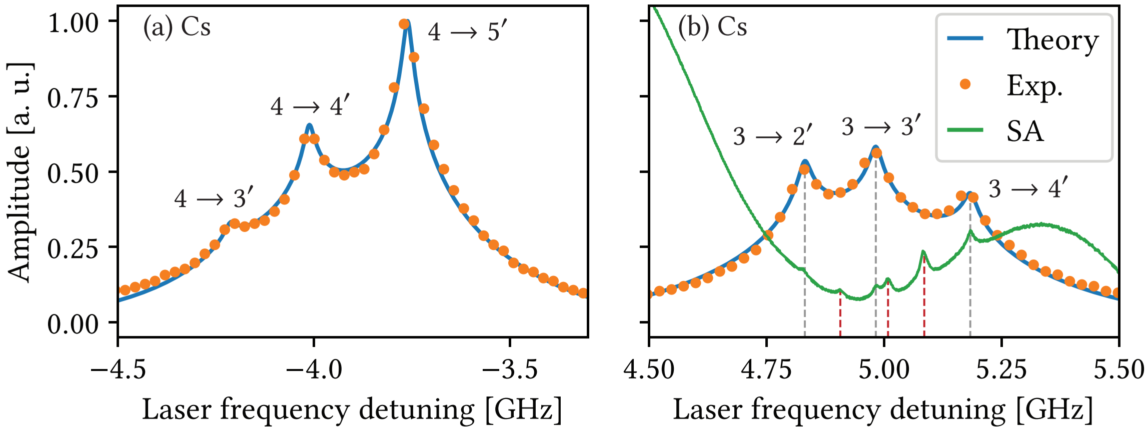

Figure 1.12 – Theoretical (blue) and experimental (orange dots) spectra of Cs D_2 line $4 \longrightarrow 3', 4', 5'$ transitions (a) and $3 \longrightarrow 2', 3', 4'$ transitions (b) recorded with a NC ($L = \lambda/2$, $T = 110$ °C). Green: SA spectrum recorded with a usual cm-long cell. The grey dashed lines indicate the position of the transitions and the red dashed lines indicate cross-over resonances.

in fig. 1.10. As NCs allow to obtain sub-Doppler resolution, one can safely consider for example each hyperfine transition of Rb D_2 line as an independent two-level system and apply the procedure given above. In fig. 1.10a, we present a theoretical SR spectrum of natural Rb D_2 line obtained for $L = 350$ nm where the hyperfine structure is mostly resolved. In fig. 1.10b and fig. 1.10c, we present a transmission (S_t) spectrum of Cs D_2 line. For clarity, we present the red (b) and blue (c) wings of the spectrum separately. Here, we see that the hyperfine structure is resolved (compared with the Doppler-broadened profiles plotted in dashed lines). All spectra were obtained for an arbitrary $\gamma \simeq 60$ MHz (HWHM). We may now come back to fig. 1.3 and compare our experimental results with the theoretical model. In fig. 1.12, we present the two wings ($F_g = 4$ and $F_g = 3$) of Cs D_2 line. The model is in very good agreement with the theoretical measurements. To improve the resolution and obtain clearer spectra, one can study either the derivative of selective reflection (dSR) ($\mathrm{d}S_r/\mathrm{d}\omega$) or the second derivative (SD)[11] of the transmitted signal ($\mathrm{d}^2S_t/\mathrm{d}\omega^2$), as presented in fig. 1.11. This combined with the use of NCs allows to completely resolve the hyperfine structure in most cases and is one of the main experimental techniques used throughout this thesis.

1.4 Atom-surface interactions

In this section, we will present some results recently obtained on atom-surface interaction in Rb and Cs NCs. We experimentally observe the so-called "retardation" of the vdW effect predicted by de Aquino Carvalho *et al.* [80, 81], using the techniques described above. The work presented in this section gave rise to the following journal article:

- A. Sargsyan, R. Momier, C. Leroy, and D. Sarkisyan. *Competing van der Waals and dipole-dipole interactions in optical nanocells at thicknesses below 100 nm.* Phys. Lett. A **483** (2023), p. 129069

1.4.1 Van der Waals effect

In the theoretical treatment we performed in section 1.3, we considered that atom-surface interactions are negligible. However, as the cell size decreases, the distance between the atoms and the surface of the cell is reduced and, consequently, the influence of the cell windows on the spectroscopic characteristics of the atom cannot be ignored anymore. Numerous studies of the influence of the cell windows on

---

[11] This technique may lead to a slight loss of accuracy in the transition intensities, as can be seen when comparing fig. 1.10c with fig. 1.11c. This is not a problem if we are only interested in studying frequency positions.

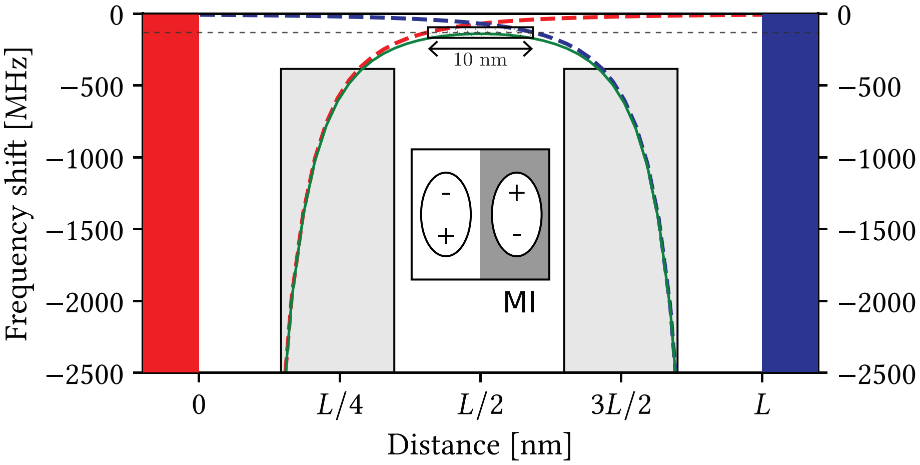

Figure 1.13 – Transition frequency shift versus atom-windows distance for the interwindow distance $L = 50$ nm. The red and blue rectangles labeled represent the sapphire windows of the NC, respectively located at $z = 0$ and $z = L = 50$ nm. The red dashed line shows the red frequency shift caused by the left window, while the blue dashed line shows the frequency shift caused by the right window. The green curve shows the total frequency shift $\Delta\nu_{\text{vdW}}$ caused by both windows simultaneously.

the atoms are based on the analysis of the shape of SR lines, see eg. [107–110] and references therein, where the determining contribution to the shape comes from atoms located $L \sim \lambda/2\pi \sim 100$ nm away from the cell window. However, due to the smallness of the vdW interaction of atoms with the surface of the window, such values of L lead to small redshifts of the transition frequencies of several MHz, which are difficult to accurately determine in noisy SR spectra. The NCs developed by our group are a convenient tool for such studies as they allow to reach $L < 100$ nm and proved useful to measure the vdW coefficient C_3 of Cs, Rb and ^{39}K atoms $D_{1,2}$ lines through either absorption [100, 102, 111, 112], SR [56, 113] or fluorescence [44, 101] measurements.

In what follows, we show that vdW and dipole-dipole (Lorentz-Lorenz Rb-Rb or Cs-Cs) interactions cause a redshift of the transition frequencies and that dipole-dipole interactions (neglected in [110]) induce an additional frequency shift and results in an overestimation of previous measurements of the C_3 coefficient. We also observe experimentally the recently predicted so-called "retardation" of the vdW effect. To do so, we have studied the D_1 lines of Cs (by absorption) and Rb (by SR), due to the large hyperfine splitting of their excited states (1168 and 814 MHz, respectively), which makes it possible to study individual transitions. In the inset of fig. 1.13 we schematically show an atom (as a dipole) and its mirror image by one of the cell windows. The atom is influenced by the electric field induced by its mirror image on the dielectric window. This electric field affects the atomic transitions, inducing a shift and a spectral broadening of the transitions. The frequency shift $\Delta\nu_{\text{vdW}}$ induced by the interaction of the vapor with a dielectric window can be estimated with [114]:

$$\Delta\nu_{\text{vdW}} = -\frac{C_3}{z_3} - \frac{C_3}{(L-z)^3}. \tag{1.69}$$

The contributions of each window, as well as the total shift $\Delta\nu_{\text{vdW}}$, are plotted in fig. 1.13 for Cs D_1 line, with $C_3 = 1.0$ kHz μm^3 and $L = 50$ nm. From eq. (1.69), we see that in the center of the cell ($z = L/2$), the total frequency shift is

$$\Delta\nu_{\text{vdW}} = -\frac{16C_3}{z_3}. \tag{1.70}$$

Atoms located at $L/2 \pm 5$ nm from the windows experience a relatively small frequency shift, around 30 MHz (shown by the small shaded box in fig. 1.13), compared to those situated at $L/4 \pm 5$ nm from either window, which encounter a much larger frequency shift of approximately 2500 MHz (shown by the gray rectangles). Assuming an even distribution of atoms across the windows, it is thus apparent from the plotted curve that the spectral density in the absorption spectrum is maximum for atoms positioned at the center of the NC ($z = L/2$), where the frequency shift is minimal. Measuring the frequency shift of the absorption or SR spectra at specific cell thicknesses combined with eq. (1.70), allows us to determine the C_3 coefficient governing the van der Waals interactions between the atoms and the cell windows.

1.4.2 Experimental setup

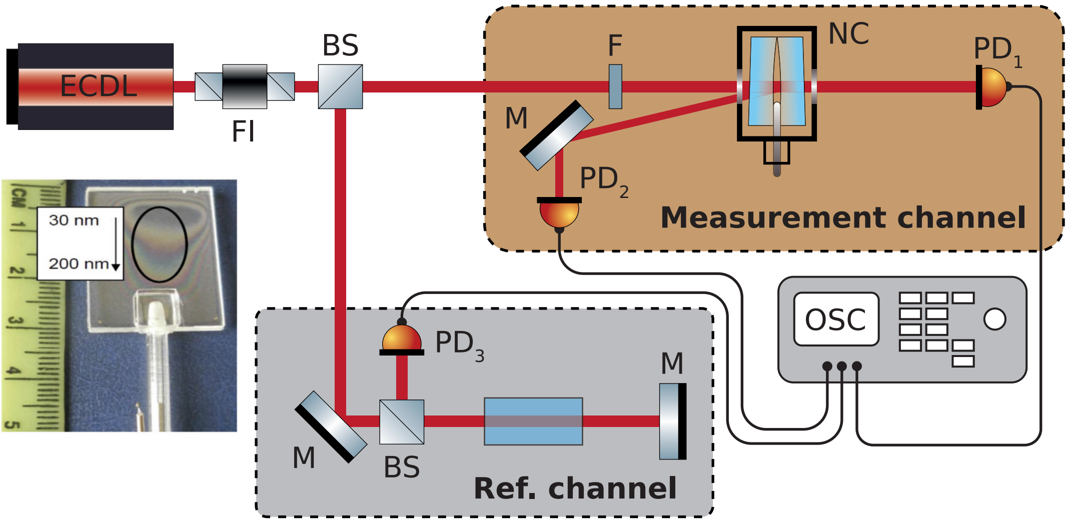

Figure 1.14 – Scheme of the experimental setup. FI: Faraday insulator, NC: nanocell (in its oven) containing either Rb or Cs atoms, F: filter, M: mirror, BS: beam splitter, PD: photodetector, OSC: oscilloscope. The NC height can be adjusted to modify the thickness L with the help of the interference rings visible in the inset picture.

In fig. 1.14, we illustrate the experimental setup used to investigate atom surface interactions. For Cs absorption measurements, we used an extended cavity diode laser (ECDL) [115] with a wavelength $\lambda = 895$ nm and a linewidth of 1 MHz. Another laser with $\lambda = 795$ nm resonant with Rb D_1 line was used for SR measurements with the Rb cell. In both cases, the laser beam (diameter 0.6 mm, 100 μW) was directed perpendicularly through a cell mounted on a micrometric state so that its height could be adjusted. Due to the wedged inner shape of the cell, this allows us to perform measurements at various cell thicknesses (see section 1.2). Absorption or SR was measured while scanning the laser frequency near Rb and Cs D_1 lines. Signals were recorded by photodiodes, amplified, and sent to a Tektronix TDS2014B oscilloscope. Additionally, part of the laser radiation was directed to a separate cell (Ref. channel) to create a SA frequency reference using a 1 cm-long cell.

1.4.3 Van der Waals effect on Cs and Rb D_1 lines

As discussed before (in sections 1.2 and 1.3), it was shown that using a NC with thickness $L = \lambda/2$ yields nearly four times spectral narrowing of the atomic transitions in the absorption spectrum compared to Doppler broadened spectra recorded in cm-long cells (where the typical width is $\simeq 400 - 600$ MHz). This narrowing is even more important when taking the second derivative of the spectrum. In that case, as expected, correct frequency intervals between transitions and correct relative transition probabilities are observed [61]. In fig. 1.15, SD spectra of Cs D_1 line $4 \longrightarrow 3', 4'$ transitions for various cell thicknesses (200 ± 5, 90 ± 5, 70 ± 5, 55 ± 5 and 45 ± 5 nm) are presented. The solid vertical lines are to guide the eye, showing the unshifted position of the transitions. It can be seen that a redshift of the transitions occurs from $L \leq 90$ nm onwards. For $L = 200 \pm 5$ nm, the temperature of the cell reservoir was set to $T = 120$ °C. As long as the absorption is small, it follows $\sigma N L$, where σ is the cross section of Cs D_1 line

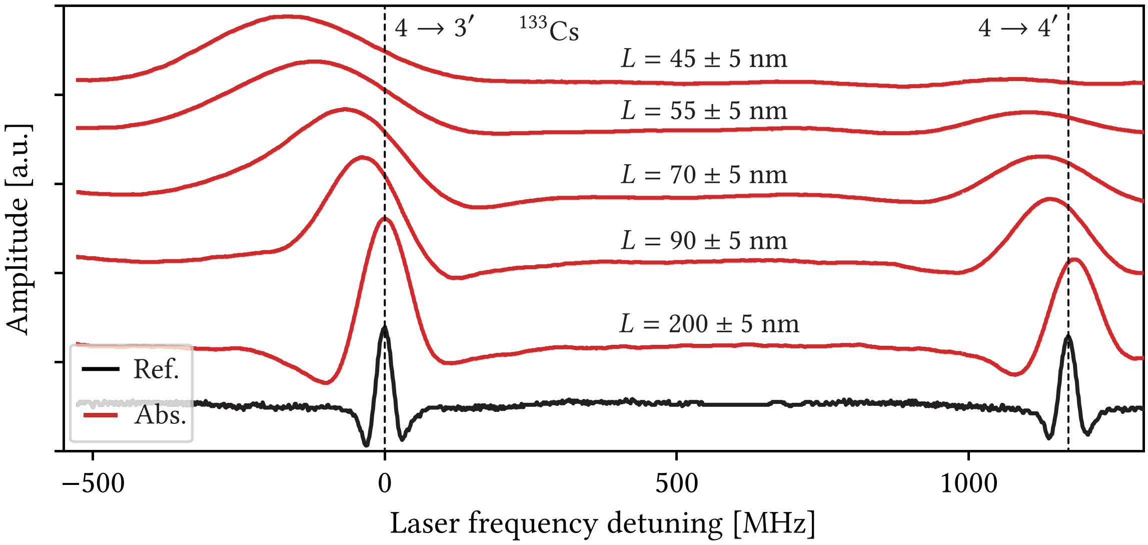

Figure 1.15 – Spectra of the $4 \longrightarrow 3', 4'$ transitions of Cs D_1 line for various cell thicknesses. The dashed vertical lines are the positions of unshifted atomic transitions from which the total $\Delta\nu = \Delta\nu_{\text{vdW}} + \Delta\nu_{\text{LL}}$ frequency shift is measured. The lower curve is a reference spectrum (SD of SA).

($\sigma \simeq 10^{-11}$ cm^2), resulting in around 1% absorption at $L \simeq 400$ nm and $T = 120$ °C ($N \simeq 5 \times 10^{13}$ cm^{-3}). The absorption decreases with the cell thickness, making increasing the vapor density necessary for reliable registration of the signal. Below $L < 70$ nm the reservoir temperature is increased to $T = 170$ °C ($N \simeq 5.5 \times 10^{14}$ cm^{-3}). In this regime, the relation $N/k^3 \gg 1$ is fulfilled and Cs-Cs dipole-dipole interactions are observed. The dipole-dipole (Lorentz-Lorenz) induced frequency shift can be estimated by

$$\Delta\nu_{\text{LL}} = -\frac{\pi N \Gamma}{k^3}, \tag{1.71}$$

and is clearly visible as long as $L/\lambda \ll 1$ [100]. Therefore, the total red transition frequency shift consists of two terms:

$$\Delta\nu = \Delta\nu_{\text{vdW}} + \Delta\nu_{\text{LL}}. \tag{1.72}$$

For thicknesses $L < 60$ nm the “Lorentz-Lorenz” shift $\Delta\nu_{\text{LL}}$ is ~ -44 MHz while for $L = 90$ and 200 nm (because the temperature T of the NC reservoir was lower), this shift was −7 MHz and −4 MHz, respectively. In fig. 1.16a, we show the shift of the $4 \longrightarrow 3'$ transition of ^{87}Rb D_1 line while the temperature (and thus the vapor density) is varied from 170 to 325 °C and the cell thickness is fixed to $L = 60 \pm 5$ nm. Both dipole-dipole and vdW (atom-wall) frequency shifts are indicated with respect to the original transition frequency, shown on the reference SA spectrum. In fig. 1.16b, the dipole-dipole frequency shift is plotted against the vapor density. Since in this regime, the shift is linear with respect to the density, it is possible to extrapolate the measurements on the small density side and extract a “purely” atom-wall related vdW shift, in that case around $\simeq -60$ MHz. Therefore, to determine correctly $\Delta\nu_{\text{vdW}}$ from the total frequency shifts presented in fig. 1.15 (−4, −37, −60, −117 and −180 MHz), we subtract $\Delta\nu_{\text{LL}}$, yielding $\Delta\nu_{\text{vdW}} = 0, -30, -38, -70$ and −136 MHz respectively. Using the quantities of $\Delta\nu_{\text{vdW}}$ and the corresponding cell thicknesses, the coefficient C_3 of vdW interaction for Cs D_1 line with the sapphire windows of the NC is measured according to eq. (1.70), as presented in fig. 1.18a. The relatively large inaccuracy on the C_3 coefficients measurements is due to the inaccuracy ±5 nm in the determination of the cell thickness. It was shown in [56, 113] that the SR of laser radiation for thicknesses $L \ll \lambda/2$ is also a convenient tool for the study of the vdW interaction of an atom with the NC window. In the bottom panel of fig. 1.17 we present an experimental and a theoretical SR spectrum of the $1 \longrightarrow 1', 2'$ transitions of ^{87}Rb D_1 line recorded at $L = 130 \pm 5$ nm. As expected from SR, the line shapes are dispersive. In the top panel, dSR spectra for various cell thicknesses ($L = 80 \pm 5$ nm, 50 ± 5 nm, and 35 ± 5 nm, respectively) are presented. The dotted curves are to guide the eye and show the original transition frequencies.

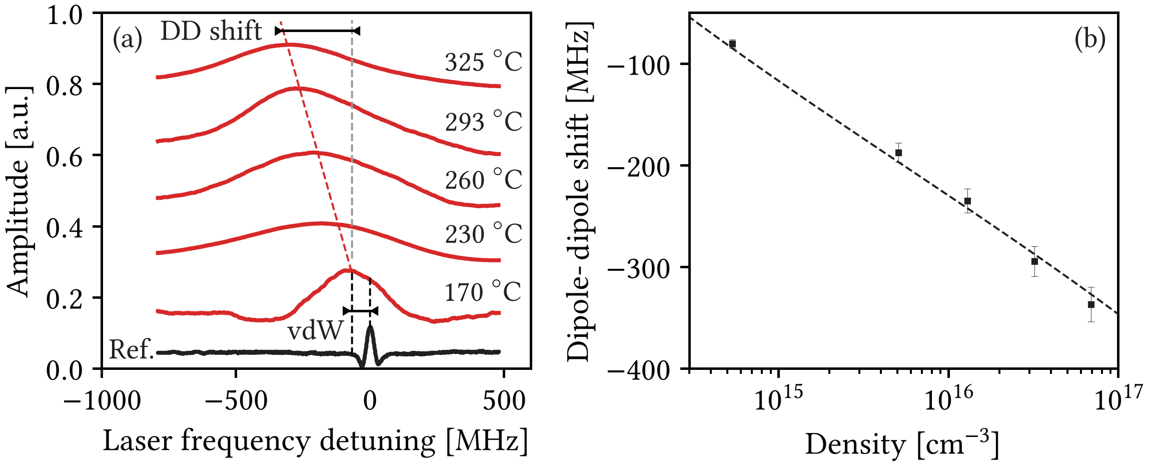

Figure 1.16 – a) SD of absorption spectra of the 4 ⟶ 3′ transition of Cs D_1 line as a function of the cell temperature for a fixed thickness $L = 60 \pm 5$ nm. The lower curve (Ref.) is a reference spectrum showing the initial transition frequency. The dipole-dipole and vdW shifts are indicated. b) Dipole-dipole frequency shift as a function of the atomic vapor density.

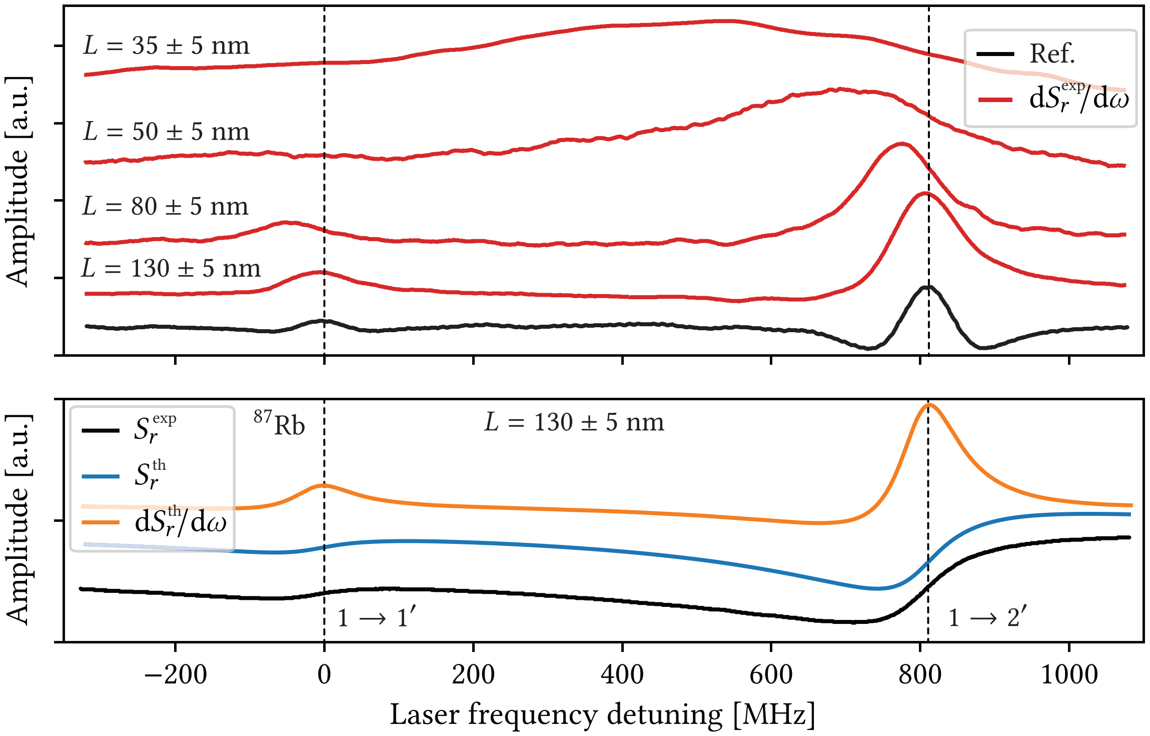

Figure 1.17 – Spectra of the 1 ⟶ 1′, 2′ transitions of ^{87}Rb D_1 line. Bottom: experimental SR spectrum (black), theoretical SR spectrum (blue), and theoretical dSR spectrum (orange), all obtained for $L = 130 \pm 5$ nm. Top: reference spectrum (derivative of SA, black) and experimental dSR spectra obtained for different cell thicknesses. The dashed lines indicate the frequencies of the 1 ⟶ 1′, 2′ transitions.

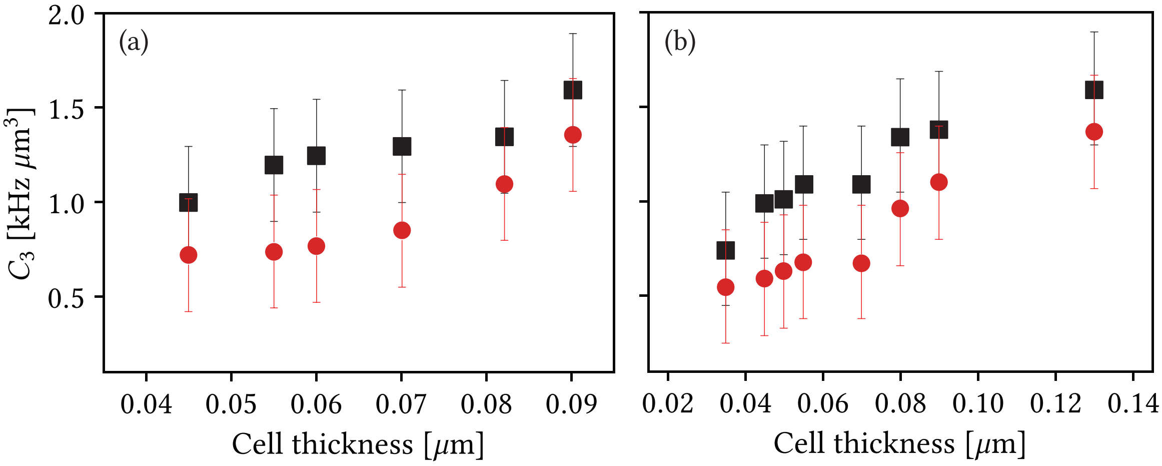

Figure 1.18 – Values of the C_3 coefficient of Cs D_1 line (a) and Rb D_1 line (b) as a function of the thickness L, calculated with eq. (1.70). Black squares: total red frequency shift $\Delta\nu_{\mathrm{vdW}} + \Delta\nu_{\mathrm{LL}}$ was used, red circles: only $\Delta\nu_{\mathrm{vdW}}$. Since it is commonly accepted to give the value C_3 in kHz μm^3, the cell thickness is given in μm on the x-axis.

The total $\Delta = \Delta\nu_{\mathrm{vdW}} + \Delta\nu_{\mathrm{LL}}$ frequency shift of the dSR peaks as the thickness L decreases is clearly visible. As before with the absorption, the dSR amplitude decreases with the cell thickness. Thus, for reliable registration of the spectra, the temperature T of the NC reservoir was increased from 145 °C (at L = 130 nm) to 220 °C (at L = 35 nm), corresponding to $N \simeq 5.5 \times 10^{14}$ cm^{-3}. From these spectra, the values of $\Delta\nu_{\mathrm{vdW}}$ for different thicknesses (subtracting $\Delta\nu_{\mathrm{LL}}$) are $\Delta\nu_{\mathrm{vdW}}$ (130 nm) = −10 MHz, $\Delta\nu_{\mathrm{vdW}}$ (80 nm) = −30MHz, $\Delta\nu_{\mathrm{vdW}}$ (50 nm) = −81 MHz and $\Delta\nu_{\mathrm{vdW}}$ (35 nm)= −205 MHz. The values of C_3 for ^{87}Rb D_1 line obtained with eq. (1.70) are presented in fig. 1.18b. It is relevant to note that $\Delta\nu_{\mathrm{vdW}}$ for a given atom will be the same if it is measured by absorption or SR for a given thickness L, i.e., unlike SR in a centimeter cell, where only the input window is involved, both cell windows are involved in the formation of SR when using a NC. From fig. 1.18 it follows that neglecting dipole-dipole interaction in previous works led to an erroneous, overestimated value of the coefficient C_3. Thus, in [110], the ≃ 100 MHz redshift of Cs D_1 line for the thickness L = 80 nm measured by SR is attributed exclusively to the vdW interaction, but there is no information regarding the temperature T for which the shift was obtained[12]. The aim there was to demonstrate a large redshift. However, if we assume that the cell temperature was 180 °C, then the value of $\Delta\nu_{\mathrm{LL}}$ reaches ~ 65 MHz, which reduces the real vdW shift to −35 MHz.

1.4.4 Retardation of the vdW effect

In fig. 1.18, at $L < 100$ nm a slight decrease of the C_3 coefficient is visible. This decrease was also experimentally observed in [111, 113] for K atoms, however no explanation was given. In these articles, due to the big Doppler broadening of K atoms (around 0.9 GHz), the spectra of vdW interaction consist of several overlapped transitions, and full resolution of the hyperfine structure was not achieved. This behavior of the vdW process was theoretically predicted in recent papers [80, 81] and was named "retardation" of the vdW effect. Therefore, due to the smaller Doppler broadening of Rb and Cs, here pure experimental "retardation" was measured. The calculated curves for the C_3 coefficient taking into account the "retardation" effect presented in fig. 1a (inset) of [80] for the Cs D_1 line transition fit well with our experimental results. Particularly, for $L \simeq 100$ nm, 70 and 50 nm, the theoretical C_3 coefficient is ~ 1.5, ~ 1.4 and ~ 1.3 kHz μm^3, meanwhile in our experiment we obtain 1.36 ± 0.3, 0.85 ± 0.3 and 0.8 ± 0.3 kHz μm^3, respectively. The signal (SR/absorption) measures the difference between the potential of the excited state and the ground state. The excited state potential does not feel so much retardation effects ($-C^3/z^3$ is a good approximation) but the ground state "feels" retardation effects. In fact, for the ground state the $-C^3/z^3$ dependence quickly (after ~ 50 nm) turns to a $-C^4/z^4$ faster decay. The difference between the two potentials thus actually appears larger than when predicted simply by applying the $-C^3/z^3$ approximation, as shown in [80, Fig. 1a]. Observation of this delicate effect therefore requires a NC with thickness below 100 nm.

---

[12] In this work, one of the NCs produced at our laboratory was used.

1.5 Conclusion

In summary, we have shown that NCs are extremely useful spectroscopic tools. We have provided an overview of their manufacture and theoretical modeling, as well as their advantages. By modeling the cell as a FP cavity, it is possible to compute accurate transmission and SR spectra in excellent agreement with the experimental measurements. We have then investigated experimentally atom-surface interactions. By examining the spectral characteristics of Cs and Rb D_1 lines using absorption and SR techniques, we uncovered redshifts in transition frequencies attributable to vdW and dipole-dipole interactions. Accounting for the latter led to more accurate measurements of the vdW coefficient C_3. Moreover, we observed a slight decrease in C_3 at smaller NC thicknesses, consistent with theoretical predictions of retardation effects in vdW interactions. The development of NC techniques offers a powerful platform for exploring such interactions and opens avenues for further exploration in the field of quantum optics and atomic physics. Aside from atom-surface interaction studies, NCs are very promising candidates for sensing applications due to their small size. In the next chapters, we will consider the influence of an external magnetic field on the atomic vapor, both theoretically and experimentally, and dig deeper into this perspective.

Chapter 2

Alkali vapors in a magnetic field

In this chapter, we describe the interaction between an alkali atom and an external static homogeneous magnetic field starting from the fundamental Dirac equation for a single electron. We perform a thorough theoretical description of the behavior of sodium D lines with respect to the magnetic field. We then study in details both experimentally and theoretically the so-called "forbidden" transitions of Rb D_2 line, as they exhibit quite surprising magneto-optical properties. The results are applicable to all alkali isotopes with nuclear spin $3/2$.

Contents

2.1 Introduction . . . **29**
2.2 The Dirac equation, hyperfine structure and Zeeman effect . . . **30**
  2.2.1 General overview . . . 30
  2.2.2 Fine structure . . . 31
  2.2.3 Zeeman effect . . . 32
2.3 Spectra of alkali D lines in a magnetic field . . . **35**
  2.3.1 Energy shifts and transition frequencies . . . 35
  2.3.2 Transition dipole moments . . . 36
  2.3.3 Sodium D_1 line . . . 38
  2.3.4 Sodium D_2 line . . . 44
2.4 Magnetically-Induced Circular Dichroism in alkali metal isotopes with nuclear spin $3/2$ . . . **49**
  2.4.1 Experimental setup . . . 50
  2.4.2 Experimental results . . . 51
2.5 Conclusion . . . **54**

2.1 Introduction

The Zeeman effect, named after physicist Pieter Zeeman who discovered it in 1896, is a fundamental phenomenon in atomic physics. It describes how the spectral lines emitted or absorbed by atoms are split into multiple components when a magnetic field is applied. Notable applications of the Zeeman effect includes laser cooling experiments [116], laser frequency stabilization [117], electron spin and nuclear magnetic resonance spectroscopy [118, 119] or single photon sources [120]. Tremblay et al. [57] proposed a theoretical model to describe the behavior of alkali D lines under the influence of an external magnetic field. Their model focused on magnetic fields up to 2.5 kG, but they encountered limitations when dealing with weaker magnetic fields due to Doppler broadening. In chapter 2, we have demonstrated that the use of nanocells (NCs) allows to overcome this limitation.
This chapter is divided in three main parts:

- In section 2.2, we describe how alkali atoms behave in electromagnetic fields, starting with the fundamental Dirac equation. We study the different terms involved in the Dirac Hamiltonian, such as kinetic energy and spin-orbit coupling, to understand their significance. We consider the single valence electron of alkali atoms independent and use these results to derive the expression of the Hamiltonian describing the interaction of alkali atoms with a homogeneous static magnetic field. We discuss the interaction between nuclear spin and electronic angular momentum, giving rise to the hyperfine structure and the Zeeman effect induced by an external magnetic field. We present the main parts of the derivation of the model presented in [57], describing the evolution of alkali transition frequencies and intensities as a function of the magnetic field and write a computer program based on this model.

- In section 2.3 we apply the model to D lines of sodium coupled with the NC model derived in chapter 2 to explore the behavior of a sodium vapor in a NC under different magnetic fields and incident laser polarizations. We study in details all the possible Zeeman transitions of sodium D lines and their intensities. We highlight how magnetic-field induced state mixing influences the behavior of the transitions and discuss the selection rules. We analyze numerous spectra in different regimes. For sufficiently high magnetic fields, the strong-field limit of the Zeeman effect is reached. This effect is called hyperfine Paschen–Back (HPB) regime and corresponds here to the decoupling of the nuclear spin momentum **I** and the total electronic angular momentum **J**.
- In section 2.4, we explore magnetically induced circular dichroism (MCD) in alkali metal isotopes with a nuclear spin of $3/2$. We focus on forbidden transitions with $\Delta F = \pm 2$ which can have probabilities higher than ordinary atomic transitions under certain magnetic field conditions. We present a simple experimental setup used to study the absorption spectra of the D_2 line transitions of ^{87}Rb using circularly polarized laser radiation. We analyze the intensity ratios of magnetically induced (MI) transitions and found good agreement between theory and experiment. We highlight the potential of MI transitions for various applications, particularly in magneto-optical processes.

2.2 The Dirac equation, hyperfine structure and Zeeman effect

2.2.1 General overview

To describe an alkali atom in an electromagnetic field, we start from the Dirac equation. For a single electron[1] of mass m, charge $-e$ and spin momentum **S** the equation reads (to the order v^2/c^2)

$$\underbrace{\left[\frac{1}{2m}\left(\mathbf{p}+\frac{e}{c}\mathbf{A}\right)^2+\frac{e}{mc}\mathbf{S}\cdot(\boldsymbol{\nabla}\times\mathbf{A})-\frac{p^4}{8m^3c^2}-\frac{e\hbar}{8m^2c^2}\nabla^2V-\frac{e}{2m^2c^2}\mathbf{S}\cdot(\nabla V\times\mathbf{p})-eV\right]}_{\text{Dirac Hamiltonian}}\Psi=E\Psi, \tag{2.1}$$

where p is the magnitude of the electron generalized momentum **p**, and **S** its spin momentum[2]. The electromagnetic vector potential **A** and the scalar potential V are related to the electric and magnetic fields **E** and **B** such that

$$\mathbf{E}=\frac{\partial\mathbf{A}}{\partial t}-\boldsymbol{\nabla}V \quad \text{and} \quad \mathbf{B}=\boldsymbol{\nabla}\times\mathbf{A}. \tag{2.2}$$

Equation (2.1) includes many terms each describing something specific:

- $\frac{1}{2m}\left(\mathbf{p}+\frac{e}{c}\mathbf{A}\right)^2$ is the kinetic energy ($\mathcal{H}_k$) and interaction of the electron with the vector potential,
- $\frac{e}{mc}\mathbf{S}\cdot(\boldsymbol{\nabla}\times\mathbf{A})$ describes the interaction of the spin momentum with the magnetic field $\mathbf{B}=\boldsymbol{\nabla}\times\mathbf{A}$,
- $\frac{p^4}{8m^3c^2}$ is the first-order relativistic correction ($\mathcal{H}_r$) to the kinetic energy,
- $\frac{e\hbar}{8m^2c^2}\nabla^2V$ is called the Darwin term ($\mathcal{H}_D$) and induces a shift of the S-states,
- $\frac{e}{2m^2c^2}\mathbf{S}\cdot(\nabla V\times\mathbf{p})$ is the spin-orbit coupling term ($\mathcal{H}_{\mathrm{SO}}$) ,
- $-eV$ is a scalar potential energy (U).

---

[1] Alkali atoms have a single valence electron. This is the electron we consider here.

[2] $\mathbf{S}=\hbar/2\cdot\boldsymbol{\sigma}$ where $\boldsymbol{\sigma}=(\sigma_x,\sigma_y,\sigma_z)$ are the Pauli matrices.

2.2.2 Fine structure

Let us have a look at the non-field-dependent contributions to the Dirac Hamiltonian. For a non-relativistic[3] electron in the case $\{\mathbf{A} = 0, V\}$, eq. (2.1) reduces to the eigenvalue equation

$$[\mathcal{H}_k + U]\,\Psi = \left[\frac{\hbar^2}{2m}\nabla^2 + U\right]\Psi = \mathcal{H}_0\Psi = E\Psi, \tag{2.3}$$

where $\mathbf{p} = -i\hbar\nabla$. In spherical coordinates, eq. (2.3) reads

$$r^2\left[\frac{\partial^2}{\partial r^2} + \frac{2}{r}\frac{\partial}{\partial r}\right]\Psi + \frac{2mr^2}{\hbar^2}(E-U)\Psi = \frac{L^2}{\hbar^2}\Psi \tag{2.4}$$

where L is the orbital angular momentum. In a spherically symmetric Coulomb potential $U(r) = -Ze^2/r$ (the electron interacts with a nucleus of charge Ze), the eigenstates of eq. (2.4) are known to be

$$\Psi_{nlm}(r,\theta,\phi) = R_{nl}(r)Y_{lm}(\theta,\phi) \equiv |nlm\rangle\,, \tag{2.5}$$

where $-m < l < m$ and $0 < l < n-1$. These states are called bound[4] states and are functions of the spherical harmonics $Y_{lm}(\theta,\phi)$. Their energies are discrete and obey the famous relation

$$E_n = -R_\infty\frac{Z^2}{n^2}, \tag{2.6}$$

where $R_\infty = me^4/8\epsilon_0^2h^3c \simeq 109737\ \mathrm{cm}^{-1}$ is the Rydberg constant[5]. Let us now take a look at the spin-orbit interaction. The spin-orbit Hamiltonian $\mathcal{H}_{\mathrm{SO}}$ reads

$$\mathcal{H}_{\mathrm{SO}} = \frac{e}{2m^2c^2}\mathbf{S}\cdot(\nabla V \times \mathbf{p}). \tag{2.7}$$

This interaction is responsible for the atomic fine structure. Indeed, in the same spherical potential, the Hamiltonian can be rewritten as

$$\mathcal{H}_{\mathrm{SO}} = \frac{Ze^2}{2m^2c^2r^3}\mathbf{L}\cdot\mathbf{S}. \tag{2.8}$$

The Hamiltonian of an electron bound to a nucleus by a potential $V(r)$ taking into account spin-orbit interactions can be obtained by incorporating eq. (2.8) in eq. (2.3) which yields

$$\mathcal{H}_0 + \mathcal{H}_{\mathrm{SO}} = -\frac{\hbar^2}{2m}\nabla^2 - \frac{Ze^2}{r} + \frac{Ze^2}{2m^2c^2r^3}\mathbf{L}\cdot\mathbf{S}. \tag{2.9}$$

Using perturbation theory, one can show that the diagonal[6] elements of $\mathcal{H}_{\mathrm{SO}}$ in the coupled basis $|J,m\rangle$ are

$$\begin{aligned} E_{\mathrm{SO}} &= \langle J,m|\mathcal{H}_{\mathrm{SO}}|J,m\rangle \\ &= \frac{Ze^2}{4m^2c^2}\hbar^2\left[J(J+1) - L(L+1) - S(S+1)\right]\langle nL|r^{-3}|nL\rangle \\ &= \frac{Z^4e^2\hbar^2}{4a_0m^2c^2}\,\frac{J(J+1) - L(L+1) - S(S+1)}{n^2L(L+1)(L+1/2)}, \end{aligned} \tag{2.10}$$

where $\mathbf{J} = \mathbf{L} + \mathbf{S}$, ie. $|L-S| \le J \le L+S$ and $-J \le m \le J$. The matrix elements $\langle nL|r^{-k}|nL\rangle$ can be found in the literature [121] or can be calculated, see eg. [122, 123], and $a_0 = 4\pi\epsilon_0\hbar^2(me^2)^{-1} \simeq 0.53$ Å is the

---

[3] This implies that we can get rid of the terms proportional to c^{-2}.

[4] of Hydrogen if $Z = 1$, of Hydrogen-like atoms if $Z > 1$.

[5] The Rydberg constant R_∞ can be converted to the Rydberg unit of energy $R_y = hcR_\infty \simeq 13.6$ eV.

[6] L^2, S^2 and J^2 only have diagonal elements, see appendix A.

Bohr radius. Spin-orbit interaction raises the degeneracy of a given level $|n\rangle$: a given eigenvalue of $\mathcal{H}_0 + \mathcal{H}_{\mathrm{SO}}$ is degenerated $2J+1$ times. The first order relativistic correction term $\mathcal{H}_r$ can also be written

$$\mathcal{H}_R = -\frac{1}{2mc^2}\left(\mathcal{H}_0 + \frac{Ze^2}{r}\right)^2 \tag{2.11}$$

taking into account that $\mathcal{H}_0 = p^2/2m - Ze^2/r$. We may again use perturbation theory, considering the relativistic correction as a perturbation, to obtain its matrix elements. They read [124, Section 5.3]

$$\begin{aligned} E_R &= \langle J, m|\mathcal{H}_R|J, m\rangle \\ &= -E_n^2 \frac{Z^2\alpha^2}{n^2}\left(\frac{n}{L+1/2} - \frac{3}{4}\right). \end{aligned} \tag{2.12}$$

The Darwin term $\mathcal{H}_{\mathrm{D}}$ produces an energy shift affecting $L = 0$ states:

$$E_D = \frac{Z^4 e^2 \hbar^2}{2n^3 m^2 c^2 a_0^3}. \tag{2.13}$$

All the terms above form the atomic fine structure:

$$\mathcal{H}_{\mathrm{fs}} = \mathcal{H}_k + U + \mathcal{H}_{\mathrm{SO}} + \mathcal{H}_R + \mathcal{H}_D. \tag{2.14}$$

In the fine structure, it is predicted that the energies of the states $n^2S_{1/2}$ and $n^2P_{1/2}$ are identical. However, experiments using hydrogen atoms have shown small discrepancies. This difference, called the Lamb shift, can be corrected using higher-order radiative corrections [125].

2.2.3 Zeeman effect

Magnetic Hamiltonian, Landé factors

Let us consider a static uniform magnetic field[7] such that $\nabla \cdot \mathbf{A} = 0$, in other terms:

$$\mathbf{B} = \frac{1}{2}\boldsymbol{\nabla} \times (\mathbf{B} \times \mathbf{r}) \quad \text{and} \quad \mathbf{A} = \frac{1}{2}\mathbf{B} \times \mathbf{r}. \tag{2.15}$$

From eq. (2.1), the magnetic part $\mathcal{H}_m$ of the Dirac Hamiltonian reads

$$\mathcal{H}_m = \frac{1}{2m}\left(\mathbf{p} + \frac{e}{c}\mathbf{A}\right)^2 + \frac{e}{mc}\mathbf{S} \cdot (\boldsymbol{\nabla} \times \mathbf{A}). \tag{2.16}$$

As $\mathbf{p}$ and $\mathbf{A}$ do not necessarily commute[8] since $\mathbf{A}$ depends on $\mathbf{r}$ [see eq. (2.15)], the expansion of eq. (2.16) must be performed carefully. Dropping the kinetic term to focus only on the magnetic interaction part, $\mathcal{H}_m$ can be rewritten

$$\mathcal{H}_m = \frac{e}{2mc}\left[(\mathbf{B} \times \mathbf{r}) \cdot \mathbf{p} + 2(\mathbf{S} \cdot \mathbf{B})\right] \tag{2.17}$$

or equivalently, with $L = \mathbf{r} \times \mathbf{p}$,

$$\mathcal{H}_m = \frac{\mu_B}{\hbar}\mathbf{B}\left(\mathbf{L} + 2\mathbf{S}\right), \tag{2.18}$$

where $\mu_B = e\hbar/2mc$ is the Bohr magneton. Alternatively, eq. (2.18) can also be written

$$\mathcal{H}_m = -\boldsymbol{\mu}_L \cdot \mathbf{L} - \boldsymbol{\mu}_S \cdot \mathbf{S} \tag{2.19}$$

with $\boldsymbol{\mu}_L = -g_L \mu_B \hbar^{-1}\mathbf{B}$ and $\boldsymbol{\mu}_S = -g_S \mu_B \hbar^{-1}\mathbf{B}$ to be interpreted as magnetic moments associated to $\mathbf{L}$ and $\mathbf{S}$ respectively. These involve the electron orbital Landé factor g_L and spin Landé factor g_S. In this derivation, it comes that $g_L = 1$ and $g_S = 2$. In reality, g_L must account for the ratio between the mass of the electron m and the mass of the nucleus m_n such that

$$g_L = 1 - \frac{m}{m_n}. \tag{2.20}$$

The electron spin Landé factor g_S slightly deviates from 2 when quantum electrodynamics effects are considered, and its current up-to-date value is $g_S = 2.00231930436$ [126].

---

[7] This is a reasonable approximation due to the small size of the NCs.

[8] They do commute here since we chose $\nabla \cdot \mathbf{A} = 0$.

Matrix elements

We consider here a magnetic field directed along z ($\mathbf{B} = B_z \mathbf{e}_z$), chosen as the quantization axis of our problem. Using $\mathbf{J} = \mathbf{L} + \mathbf{S}$ and writing J_z and S_z as rank 1 Irreducible Tensor Operators (ITOs) [see appendix A], the magnetic Hamiltonian reads

$$\mathcal{H}_m = \frac{\mu_B}{\hbar}(g_L \mathbf{L} + g_S \mathbf{S}) \cdot \mathbf{B} = \frac{\mu_B}{\hbar} B_z \left[g_L J_0^{(1)} + (g_S - g_L) S_0^{(1)} \right]. \tag{2.21}$$

In the $|J, m\rangle$ basis, the matrix elements of $\mathcal{H}_m$ read

$$\begin{aligned} \langle J, m | \mathcal{H}_m | J', m' \rangle = \mu_B B_z \delta_{LL'} \delta_{SS'} \delta_{mm'} \Big[& g_L m_J \delta_{JJ'} - (-1)^{m+L+S} (g_S - g_L) \sqrt{2J+1} \sqrt{2J'+1} \\ & \times \sqrt{S(S+1)(2S+1)} \begin{pmatrix} J & 1 & J' \\ -m & 0 & m \end{pmatrix} \begin{Bmatrix} L & S & J \\ 1 & J' & S \end{Bmatrix} . \Big] \end{aligned} \tag{2.22}$$

By developing the Wigner $3j$- and $6j$-symbols [127, 128], this rather inconvenient formulation can be simplified. The diagonal elements ($J = J', m = m'$) become

$$\langle J, m | \mathcal{H}_m | J, m \rangle = E_0(J) - \mu_B g_J m B_z \tag{2.23}$$

where the Landé factor g_J is given by

$$g_J = g_L \frac{J(J+1) - S(S+1) + L(L+1)}{2J(J+1)} + g_S \frac{J(J+1) + S(S+1) - L(L+1)}{2J(J+1)}. \tag{2.24}$$

The off-diagonal terms read

$$\begin{aligned} \langle J, m | \mathcal{H}_m | J-1, m \rangle &= \langle J-1, m | \mathcal{H}_m | J, m \rangle \\ &= -\frac{\mu_B B_z}{2} (g_L - g_S) \sqrt{\frac{J^2 - m^2}{J(2J+1)(2J-1)}} \\ &\quad \times \sqrt{\frac{[(L+S+1)^2 - J^2][J^2 - (L-S)^2]}{J}} . \end{aligned} \tag{2.25}$$

As a consequence of the Wigner symbols, these terms are non-zero only if $\Delta L = L - L' = 0$, $\Delta J = J - J' = \pm 1$, and $\Delta m = m - m' = 0$.

Nuclear spin

It is important to note that the electron spin momentum appears naturally when constructing the Dirac equation and the atomic fine structure ($|J, m\rangle$ states) is a direct consequence of the latter. However, the interaction between the nuclear spin momentum $\mathbf{I}$ and the total electronic angular momentum $\mathbf{J}$ giving rise to the hyperfine structure ($\mathbf{F} = \mathbf{J} + \mathbf{I}$ thus $|I - J| \le F \le I + J$ and $-F \le m \le F$) is not taken into account. The zero-field Hamiltonian $\mathcal{H}_0$ can be rewritten as

$$\mathcal{H}_0 = \mathcal{H}_{\text{fs}} + \sum_k \mathbf{T}^{(k)} \cdot \mathbf{M}^{(k)} = \mathcal{H}_{\text{fs}} + \mathcal{H}_{\text{hfs}} \tag{2.26}$$

where $\mathcal{H}_{\text{fs}}$ is the fine structure Hamiltonian [eq. (2.14)] and the product of the spherical tensor operators $\mathbf{T}^{(k)}$ and $\mathbf{M}^{(k)}$ describes the electron-nucleus interaction. Expanding $\mathcal{H}_{\text{hfs}}$ to the 2nd order taking $\mathbf{T}^{(k)} = \mathbf{I}$ and $\mathbf{M}^{(k)} = \mathbf{J}$ yields

$$\mathcal{H}_{\text{hfs}} = A_{\text{hfs}} \mathbf{I} \cdot \mathbf{J} + B_{\text{hfs}} \frac{3(\mathbf{I} \cdot \mathbf{J})^2 + \frac{3}{2} \mathbf{I} \cdot \mathbf{J} - I(I+1)J(J+1)}{2I(2I-1)(2J-1)}, \tag{2.27}$$

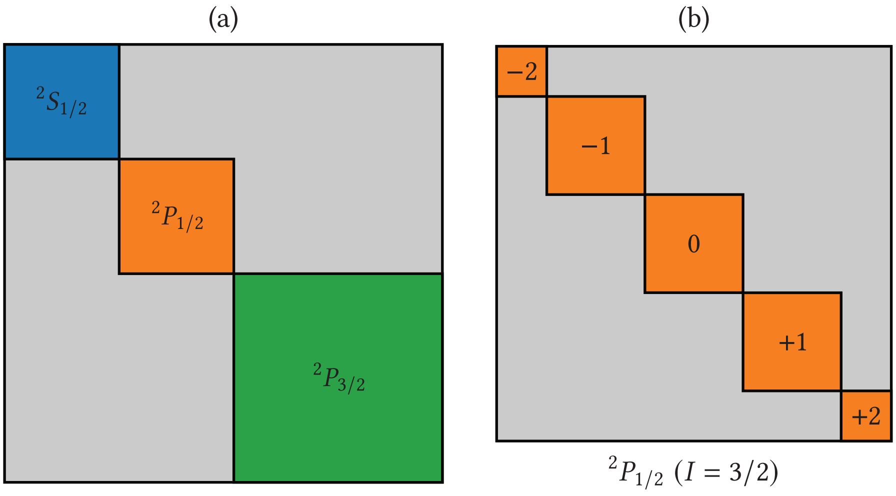

Figure 2.1 – Block structure of the magnetic Hamiltonian. a) Blocks representing the fine structure states. b) close-up on the $^2P_{1/2}$ state: the matrix is block diagonal in the $|F, m_F\rangle$ basis, each block corresponding to a different value of m_F, and F is equal to either 1 or 2.

where A_{hfs} and B_{hfs} are respectively the magnetic dipole and electric quadrupole interaction constants (odd k values in eq. (2.26) represent magnetic interactions while even k values represent electric interactions). The hyperfine energy shift is

$$\Delta E_{\text{hfs}} = \frac{A_{\text{hfs}}K}{2} + \frac{\frac{3}{2}K(K+1) - 2I(I+1)J(J+1)}{2I(2I-1)2J(2J-1)} \tag{2.28}$$

where $K = F(F+1) - I(I+1) - J(J+1)$. The higher-order terms (for example, magnetic octupole constant) can be neglected as they induce an energy shift of the order of the kHz [129]. As we did for the fine structure eq. (2.21), we can incorporate the hyperfine structure in the magnetic Hamiltonian:

$$\mathcal{H}_m = \frac{\mu_B}{\hbar} B_z (g_L L_z + g_S S_z + g_I I_z). \tag{2.29}$$

In the $|F, m_F\rangle$ basis, the diagonal matrix elements of $\mathcal{H}_m$ read

$$\langle F, m_F | \mathcal{H}_m | F, m_F \rangle = E_0(F) - \mu_B g_F m_F B_z \tag{2.30}$$

where the Landé factor g_J is given by

$$g_F = g_J \frac{F(F+1) - I(I+1) + J(J+1)}{2F(F+1)} + g_I \frac{F(F+1) + I(I+1) - J(J+1)}{2F(F+1)}. \tag{2.31}$$

The off-diagonal terms of $\mathcal{H}_m$ are non-zero only if $\Delta F = \pm 1$ and $\Delta m_F = 0$. They read

$$\begin{aligned} \langle F, m_F | \mathcal{H}_m | F-1, m_F \rangle &= \langle F-1, m_F | \mathcal{H}_m | F, m_F \rangle \\ &= -\frac{\mu_B B_z}{2}(g_J - g_I)\sqrt{\frac{F^2 - m_F^2}{F(2F+1)(2F-1)}} \\ &\times \sqrt{\frac{[(J+I+1)^2 - F^2][F^2 - (J-I)^2]}{F}}. \end{aligned} \tag{2.32}$$

The magnetic Hamiltonian $\mathcal{H}_m$, therefore, has a block diagonal structure. It can be represented by several blocks, one for each fine structure state ($^2S_{1/2}$, $^2P_{1/2}$, $^2P_{3/2}$) [fig. 2.1a]. Each of these blocks is itself block diagonal, each block corresponding to a different value of m_F (fig. 2.1b).

2.3 Spectra of alkali *D* lines in a magnetic field

Our goal is to study the evolution of alkali D lines in a magnetic field. Starting from the expression of the magnetic Hamiltonian $\mathcal{H}_m$ [eqs. (2.30) and (2.32)], we first observe how the energy levels $|F, m\rangle$ will shift according to the magnetic field and show the evolution of the transition frequencies. We will then recall the procedure used to calculate transition dipole moment which, coupled to the theoretical model developed in chapter 2, will allow us to generate spectra of alkali D lines in a magnetic field taking into account the geometry of the cell. The work presented in this section gave rise to the following publication:

- R. Momier, A. V. Papoyan, and C. Leroy. *Sub-Doppler spectra of sodium D lines in a wide range of magnetic field: Theoretical study.* J. Quant. Spectrosc. Radiat. Transf. **272** (2021), p. 107780

The discussion presented hereafter is valid for all alkali atoms, the only difference being the nuclear spin value (up to 7/2 for ^{133}Cs, which will give rise to a different number of Zeeman sublevels) and the magnetic dipole and electric quadrupole interaction constants. The calculation procedure does not change.

2.3.1 Energy shifts and transition frequencies

Weak magnetic field regime

In a weak magnetic field $B_z \ll B_0 = A_{\text{hfs}}/\mu_B$, the magnetic Hamiltonian $\mathcal{H}_m$ simply acts as a small perturbation of the eigenstates of $\mathcal{H}_{\text{hfs}}$ and, to the lowest order, the energy levels split according linearly according to eq. (2.30):

$$\Delta E_{|F,m_F\rangle} = -\mu_B g_F m_F B_z. \tag{2.33}$$

This regime is called the *anomalous* Zeeman effect and $|F, m_F\rangle$ is a good basis, as represented in fig. 2.2.

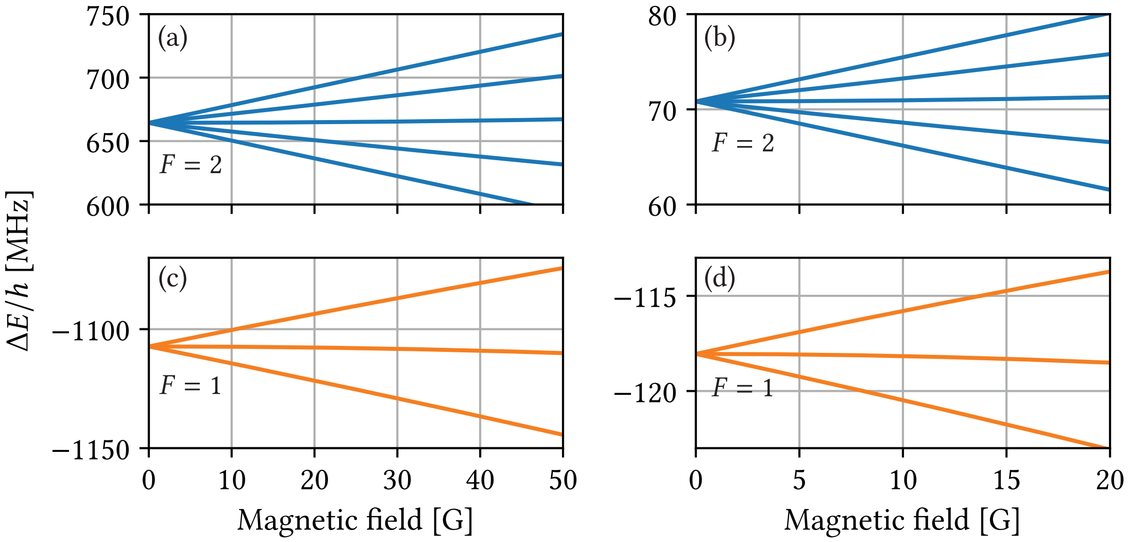

Figure 2.2 – Hyperfine structure of the (a-c) ground state $3^2S_{1/2}$ and (b-d) excited state $3^2P_{1/2}$ of sodium D_1 line in a weak magnetic field ($|F, m_F\rangle$ basis).

Strong magnetic field regime

In a strong magnetic field $B_z \gg B_0$, only J is a good quantum number. The magnetic Hamiltonian can be written as

$$\mathcal{H}_m = \frac{\mu_B}{\hbar} B_z (g_J J_z + g_I I_z). \tag{2.34}$$

and dominates the hyperfine energies. In the $|J, m_J, I, m_I\rangle$ basis, the energy levels shift according to

$$\Delta E_{|J,m_J,I,m_I\rangle} = A_{\text{hfs}} m_I m_J + B_{\text{hfs}} \frac{3(m_I m_J)^2 + \frac{3}{2} m_I m_J - I(I+1)J(J+1)}{2J(J-1)I(2I-1)} + \mu_B (g_J m_J + g_I m_I) B_z. \tag{2.35}$$

Intermediate magnetic field regime

For intermediate magnetic fields, the energy shifts are usually obtained by numerically diagonalizing $\mathcal{H}_m$ except in special cases. The *Breit-Rabi* [130] formula can be used to compute analytically the shifts of the ground states of D lines ($^2S_{1/2}$):

$$E_{|1/2,m_J,I,m_I\rangle} = -\frac{A_{\text{hfs}}(I+1/2)}{2(2I+1)} + g_I \mu_B (m_I \pm m_J) B_z \pm \frac{A_{\text{hfs}}(I+1/2)}{2} \sqrt{1 + \frac{4(m_I \pm m_J)x}{2I+1} + x^2}, \tag{2.36}$$

with

$$x = \frac{(g_J - g_I)\mu_B B_z}{A_{\text{hfs}}(I+1/2)}. \tag{2.37}$$

The transition frequencies can then simply be obtained as follows:

$$\omega_{eg}(B_z) = \frac{E_e(B_z) - E_g(B_z)}{\hbar}. \tag{2.38}$$

In fig. 2.3, we present the eigenvalues of sodium D_1 line obtained by diagonalizing $\mathcal{H}_m$, where the three different regimes are clearly visible. For convenience, throughout this thesis we will always refer to the Zeeman states in the $|F, m_F\rangle$ basis even when F is not a good quantum number.

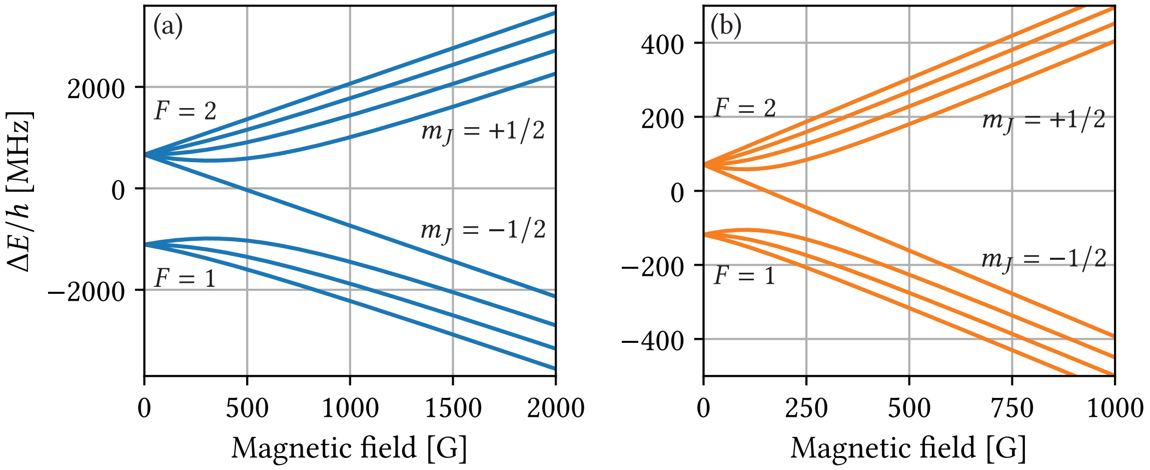

Figure 2.3 – Hyperfine structure of the (a) ground $3^2S_{1/2}$ and (b) excited $3^2P_{1/2}$ states of sodium D_1 line as a function of the magnetic field obtained by numerical diagonalization of $\mathcal{H}_m$.

2.3.2 Transition dipole moments

We now want to compute the evolution of the transition intensities between Zeeman sublevels as a function of the magnetic field. Let us consider an atomic electric dipole **D** interacting with a laser field **E**. The interaction term is $-\mathbf{D} \cdot \mathbf{E}$, where **D** and **E** are, in terms of standard components, given by

$$\mathbf{D} \cdot \mathbf{e} = \sum_q (-1)^q D_{-q} e_q \quad \text{and} \quad \mathbf{E} \cdot \mathbf{e} = \sum_q (-1)^q E_{-q} e_q. \tag{2.39}$$

where $\mathbf{e}_q$ are unit vectors of the spherical basis linked to the usual cartesian coordinates by

$$\mathbf{e}_{\pm 1} = \mp \frac{\mathbf{e}_x \pm i\mathbf{e}_y}{\sqrt{2}} \quad \text{and} \quad \mathbf{e}_0 = \mathbf{e}_z. \tag{2.40}$$

Since the z-axis was chosen as the quantization axis of our problem eq. (2.21), $E_{q=0}$ corresponds to a linearly polarized electric field and $E_{q=+1}$ (resp. $E_{q=-1}$) corresponds to a left-circularly (resp. right-circularly) polarized electric field. In our case, the magnetic field induces a mixing of the Zeeman states having the same m. Transitions will therefore occur, rigorously, between mixed states $|\Psi(F,m)\rangle$ called *perturbed* states. These states[9] read

$$|\Psi(F,m)\rangle = \sum_{F'} \alpha_{FF'}\,|F',m\rangle\,, \tag{2.41}$$

where the mixing coefficients $\alpha_{FF'}$ are obtained by diagonalizing $\mathcal{H}_m$. It was shown in [131] that the spontaneous emission probability A between two states $|\Psi(F_g,m_g)\rangle$ and $|\Psi(F_e,m_e)\rangle$ can be written

$$A_{|\Psi(F_e,m_e)\rangle\to|\Psi(F_g,m_g)\rangle} = \frac{\omega^3}{3\pi\epsilon_0\hbar c^3}|\,\langle\Psi(F_e,m_e)|D_q|\Psi(F_g,m_g)\rangle\,|^2 \tag{2.42}$$

Injecting eq. (2.41) in eq. (2.42) allows us to write the mixed states in terms of the original unperturbed Zeeman states:

$$\begin{aligned} A_{|\Psi(F_e,m_e)\rangle\to|\Psi(F_g,m_g)\rangle} &= \frac{\omega^3}{3\pi\epsilon_0\hbar c^3}\left(\sum_{F'_g}\sum_{F'_e}\alpha_{F_eF'_e}\,\langle F'_e,m_e|D_q|F'_g,m_g\rangle\,\alpha_{F_gF'_g}\right)^2 \\ &= \frac{\omega^3}{3\pi\epsilon_0\hbar c^3}a^2[\Psi(F_e,m_e),\Psi(F_g,m_g),q], \end{aligned} \tag{2.43}$$

where $a^2[\Psi(F_e,m_e),\Psi(F_g,m_g),q]$ are *modified* transfer coefficients due to the influence of the magnetic field. The standard component of D_q of the electric dipole moment $\mathbf{D}$ [eq. (2.39)] may be written as

$$\langle F_e,m_e|D_q|F_g,m_g\rangle = (-1)^{1+I+J_e+F_e+F_g-m_e}\sqrt{2F_e+1}\sqrt{2F_g+1}\begin{pmatrix} F_e & 1 & F_g \\ -m_e & q & -m_g\end{pmatrix}\begin{Bmatrix} F_e & 1 & F_g \\ J_g & I & J_e\end{Bmatrix}\langle J_e\|D\|J_g\rangle\,. \tag{2.44}$$

Using the properties derived in appendix A and the relation [131]:

$$\Gamma = |\,\langle J_e\|D\|J_g\rangle\,|^2\frac{\omega^3}{3\pi\epsilon_0\hbar c^3}\frac{1}{2J_e+1} \tag{2.45}$$

we can define the following *unperturbed* transfer coefficients:

$$a(F_e,m_e,F_g,m_g,q) = (-1)^{1+I+J_e+F_e+F_g-m_e}\sqrt{2F_e+1}\sqrt{2F_g+1}\sqrt{2J_e+1}\begin{pmatrix} F_g & 1 & F_e \\ m_g & q & -m_e\end{pmatrix}\begin{Bmatrix} F_e & 1 & F_g \\ J_g & I & J_e\end{Bmatrix}. \tag{2.46}$$

These coefficients are such that

$$\begin{aligned} A_{|\Psi(F_e,m_e)\rangle\to|\Psi(F_g,m_g)\rangle} &= \Gamma a^2[\Psi(F_e,m_e),\Psi(F_e,m_e),q] \\ &= \Gamma\left(\sum_{F'_g}\sum_{F'_e}\alpha_{F_eF'_e}a(F_e,m_e,F_g,m_g,q)\alpha_{F_gF'_g}\right)^2, \end{aligned} \tag{2.47}$$

where $q = \Delta m$ is the same standard component as in eq. (2.39) which thus corresponds to the following selection rule (where F denotes a ground state and F' an excited state):

- a linearly polarized electric field E_0 (along z) will excite transitions between a ground $|F,m\rangle$ and an excited $|F',m\rangle$ state having the same m, ie. $q = \Delta m = 0$. These transitions are called π transitions.

---

[9] Energy level crossings may cause degeneracy of the eigenvector components. This needs to be taken into account when performing the diagonalization to ensure proper assignment of each transition.

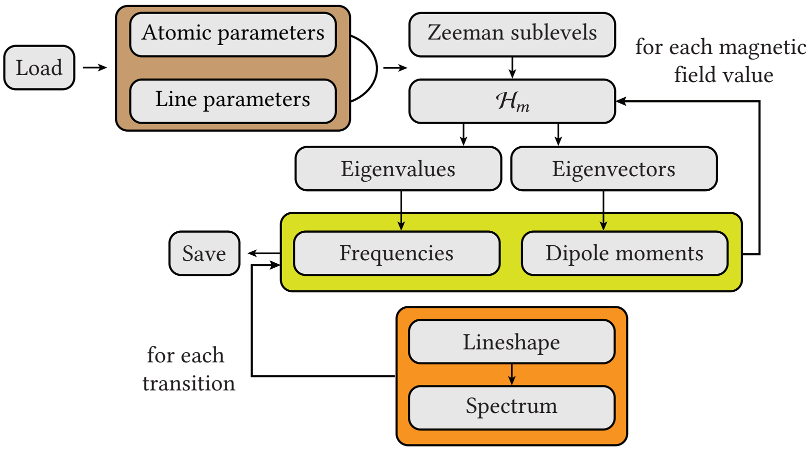
Load
Atomic parameters
Line parameters
Zeeman sublevels
for each magnetic field value
$\mathcal{H}_m$
Eigenvalues
Eigenvectors
Save
Frequencies
Dipole moments
for each transition
Lineshape
Spectrum

Figure 2.4 – Block scheme of the program used to compute transition dipole moments, frequencies, and spectra.

- a left-circularly polarized electric field E_{+1} will excite transitions between a ground $|F, m\rangle$ and an excited $|F', m+1\rangle$ ie. $q = \Delta m = +1$. These transitions are called σ^+ transitions.
- a right-circularly polarized electric field E_{-1} will excite transitions between a ground $|F, m\rangle$ and an excited $|F', m-1\rangle$ ie. $q = \Delta m = -1$. These transitions are called σ^- transitions.

Following the derivation performed in the previous chapter, we may consider the vapor confined in the NC as an ensemble of independent two-level systems. Each transition between two $|F, m\rangle$ states has a transition frequency given by eq. (2.38) and a dipole moment proportional to the spontaneous emission probability given by eq. (2.42) and ultimately eq. (2.47). Looping the computation of the lineshape (described in section 1.3.6) over all the possible Zeeman transitions allows us to generate spectra with enough resolution to distinctively observe them. A schematic diagram of the computational procedure is presented in fig. 2.4.

2.3.3 Sodium D_1 line

Sodium only has one stable isotope ^{23}Na with a natural abundance of nearly 100%. Its D_1 line corresponds to transitions occuring between the states $F = 1, 2$ of $3^2S_{1/2}$ and $F' = 1, 2$ of $3^2P_{1/2}$. The Zeeman manifold is thus analogous to that of ^{87}Rb or ^{39}K D_1 line. A π-polarized incident laser will excite 14 transitions, whereas left (or right) circularly polarized light will excite only 12 transitions. In total for sodium D_1 line, 38 $|F, m\rangle \longrightarrow |F', m'\rangle$ Zeeman transitions are possible. A scheme depicting all of them is presented in fig. 2.5.

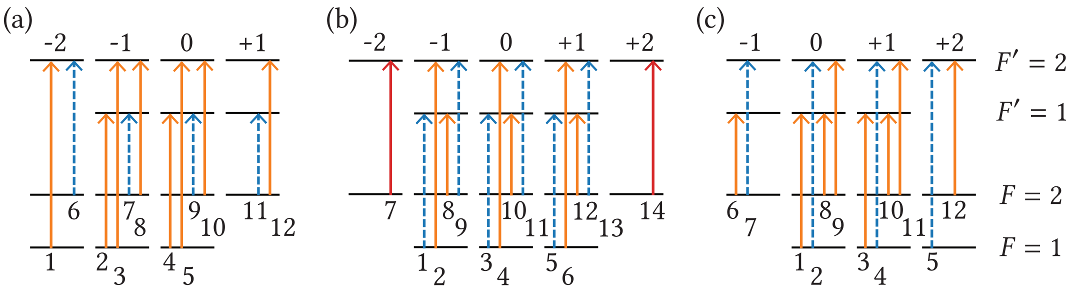
(a)
-2
-1
0
+1
6
7
8
9
10
11
12
1
2
3
4
5
(b)
-2
-1
0
+1
+2
7
8
9
10
11
12
13
14
1
2
3
4
5
6
(c)
-1
0
+1
+2
6
7
8
9
10
11
12
1
2
3
4
5
$F' = 2$
$F' = 1$
$F = 2$
$F = 1$

Figure 2.5 – All Zeeman transitions of the D_1 line of sodium in the basis $|F, m_F\rangle$. a) σ^--transitions, b) π-transitions, c) σ^+-transitions.

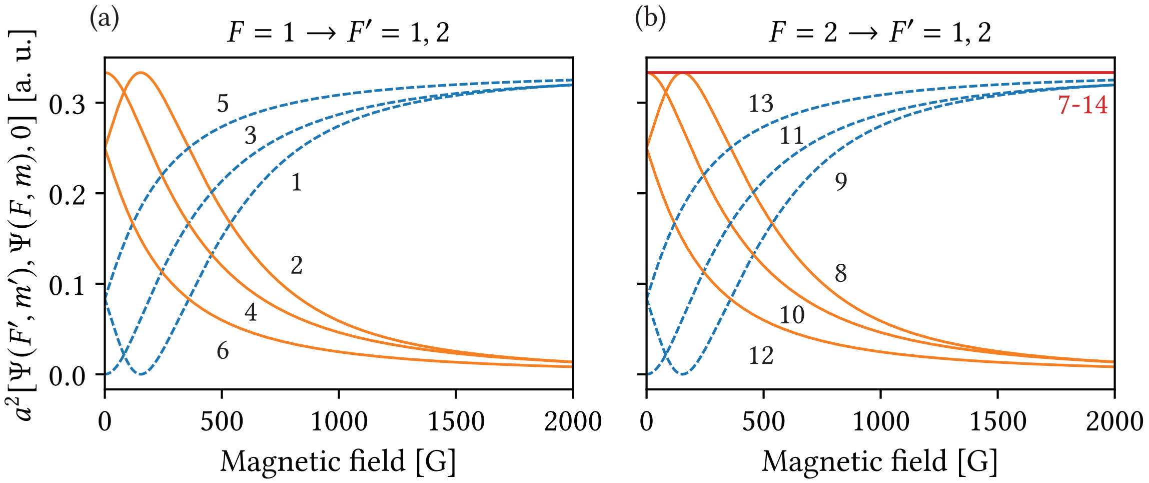

Figure 2.6 – Sodium D_1 line Zeeman transition intensities for linear (π) polarization in arbitrary units. a) transitions from $F = 1$, b) transitions from $F = 2$. Transitions occuring between extreme angular momentum states ($|2, -2\rangle \longrightarrow |2, -2\rangle$ and $|2, +2\rangle \longrightarrow |2, +2\rangle$ are represented by a red line. In blue (dashed lines), we represent the transitions whose intensities remain considerable past $B_0 \simeq 633$ G, as opposed to the orange curves (solid lines). The magnetic field varies up to 2000 G here for clarity. Numbering and color coding are consistent with fig. 2.5b.

Linearly polarized incident radiation

Let us first focus on π-transitions. As mentioned before, 14 transitions are possible in this case. All these transitions are so-called “allowed” since they respect the selection rule $\Delta F = 0, \pm 1$. The results obtained for $a^2 [|\Psi(F', m')\rangle, |\Psi(F, m)\rangle, 0]$ are presented in fig. 2.6.
Several observations can be made from fig. 2.6. The amplitudes of transitions 1, 3 and 5 (fig. 2.6a), 7, 9, 11, 13 and 14 (fig. 2.6b) remain considerable for $B_z \gg B_0$, implying that 8 transitions will remain present in the spectrum when the magnetic field is high enough. These transitions will be denoted as r-transitions, where r stands for *remaining*. Here, they obey the selection rule $\Delta F = 0$ at low magnetic fields, and $\Delta m_I = \Delta m_J = 0$ for high magnetic fields where F is not a good quantum number anymore. The r-transitions 1, 3, 5 occur between $F = F' = 1$ and the others between $F = F' = 2$. Analogously, transitions 2, 4, 6, 8, 10 and 12 will be called v-transitions, where v stands for *vanishing*, since their amplitude becomes negligible for $B_z \gg B_0$. One can notice that some of the r-transitions show $a^2 \approx 0$ for a low magnetic field and experience a huge amplitude growth as the magnetic field increases. For this reason, we call them MI (MI1 in [86]), although they are theoretically allowed by the selection rule $\Delta F = 0, \pm 1$. Another peculiarity that appears is the presence of two r-transitions (7 and 14) having a constant amplitude throughout the whole magnetic field range. These transitions occur between extreme angular momentum states [following the definition of relation eq. (2.41)]: such states do not experience any mixing with their neighbors (with the same m value), thus leading to magnetic-field-independent transition amplitudes. These transitions are usually called guiding transitions (GTs) [132]. For further analysis, we present in fig. 2.7 the transition frequencies computed from eq. (2.38). From fig. 2.7, one can notice the following: the two guiding transitions (represented by red lines) have a perfectly linear frequency shift with respect to B_z and only differ by sign. Going back to the model of section 2.2.3, the uncoupled states give rise to “1×1” blocks in $\mathcal{H}_m$, and thus their Zeeman splitting is described by relation eq. (2.33). It is straightforward to show that their slope is

$$s^{\pm} \approx \pm \frac{2\mu_B}{3}, \tag{2.48}$$

under the approximation $g_S \approx 2$, $g_L \approx 1$ and $g_I \ll g_J$. Numerically, using the values provided in appendix B [table B.2], we obtain a slope of ±0.935269 MHz/G. Each group of r-transitions is thus driven by one of the GTs, more precisely r-transitions 1, 3 and 5 are driven by the GT labeled 7 having a slope

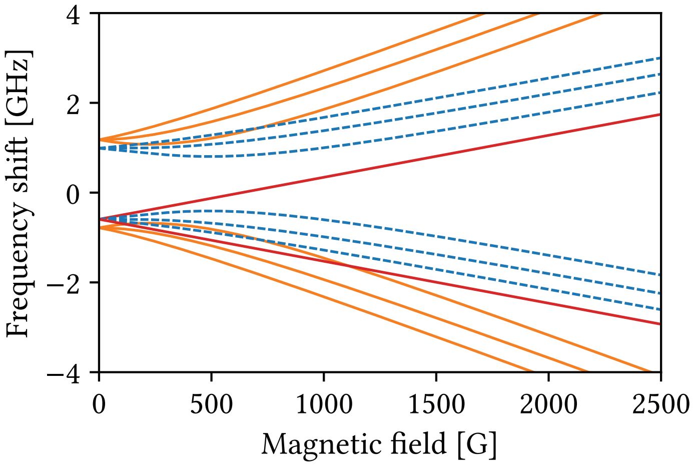

Figure 2.7 – Sodium D_1 line transition frequencies (π polarization) as a function of the magnetic field. The color code corresponds to the one used in figure fig. 2.6.

$s^- = -2\mu_B/3$, and r-transitions 9, 11 and 13 are driven by the GT labeled 14 having a slope $s^+ = 2\mu_B/3$. Here, driven means that each transition belonging to a given group is bounded in amplitude by either one of the GT and all the frequency shifts asymptotically tend to a linear behavior when $B_z \gg B_0$ is high enough, with the slope being $s_r^\pm = s^\pm$, as written in relation (2.48). Due to the absence of coupling between states, the *modified* transfer coefficient of a GT occurring between two uncoupled states is exactly equal to the *unperturbed* transfer coefficient $a^2(F_e, m_{F_e}, F_g, m_{F_g}, 0)$. For transitions 7 and 14, we obtain

$$a(2, \pm 2; 2, \pm 2; q = 0) = \pm\frac{1}{\sqrt{3}} \Rightarrow a^2 = \frac{1}{3}. \tag{2.49}$$

Past B_0, the 8 r-transitions remain in the spectrum, which is a manifestation of the HPB regime. This behavior has been observed experimentally for Cs, Rb, and K (for example in [133]). Experimental results are harder to provide due to the lack of diode lasers operating in the wavelength range of sodium in our laboratory. However, a sodium NC is available [62]. A set of theoretical absorption spectra for all π-transitions of sodium D_1 line is presented in fig. 2.8 for visualization. All the previous statements can be seen. As the magnetic field increases, the r-transitions can be separated into two groups, all tending to the same amplitude and a complete symmetry between the red and blue wings of the spectrum appears when B_z is high enough. Although becoming invisible, the v-transition frequency shifts also exhibit a linear behavior at high magnetic fields, tending to a slope twice bigger than that of the r-transitions. Precisely, $s_v^\pm \approx 2s_r^\pm \approx \pm 4\mu_B/3$ using the same approximations as before. It is usually estimated that the complete HPB regime is reached when a magnetic field $B_z > 10B_0$ is applied. This corresponds here to a magnetic field $B_z \approx 630$ G. As a comparison, for ^{87}Rb we would expect $B_z \approx 24000$ G [4] and for ^{133}Cs, $B_0 \approx 16000$ G [2]. Theoretically this makes sodium, as well as ^{39}K [134], more convenient than cesium or rubidium for the experimental study of magnetic-optical processes occurring in the complete HPB since it is reached for a much weaker magnetic field. However, since the natural linewidth of Na D_1 line $\Gamma/2\pi = 9.765$ MHz [5] is nearly twice bigger than that of the D_1 lines of Cs or Rb, one expects to obtain significantly broader lines. The linewidth is also affected by the inhomogeneous Doppler broadening Γ_D given by

$$\Gamma_D = \omega_0\sqrt{\frac{8k_BT\log 2}{mc^2}} \tag{2.50}$$

(see [53]), bigger for the D_1 line of sodium than in the case of rubidium or cesium. In eq. (2.50), ω_0 is the central angular frequency of the transition, m is the atomic mass, T is the temperature of vapor, c is the speed of light and k_B is the Boltzmann constant. In fig. 2.9, we present a theoretical absorption spectrum of sodium D_1 π-transitions, computed with the same numerical parameters as before, as long with the second derivative (SD) spectrum.

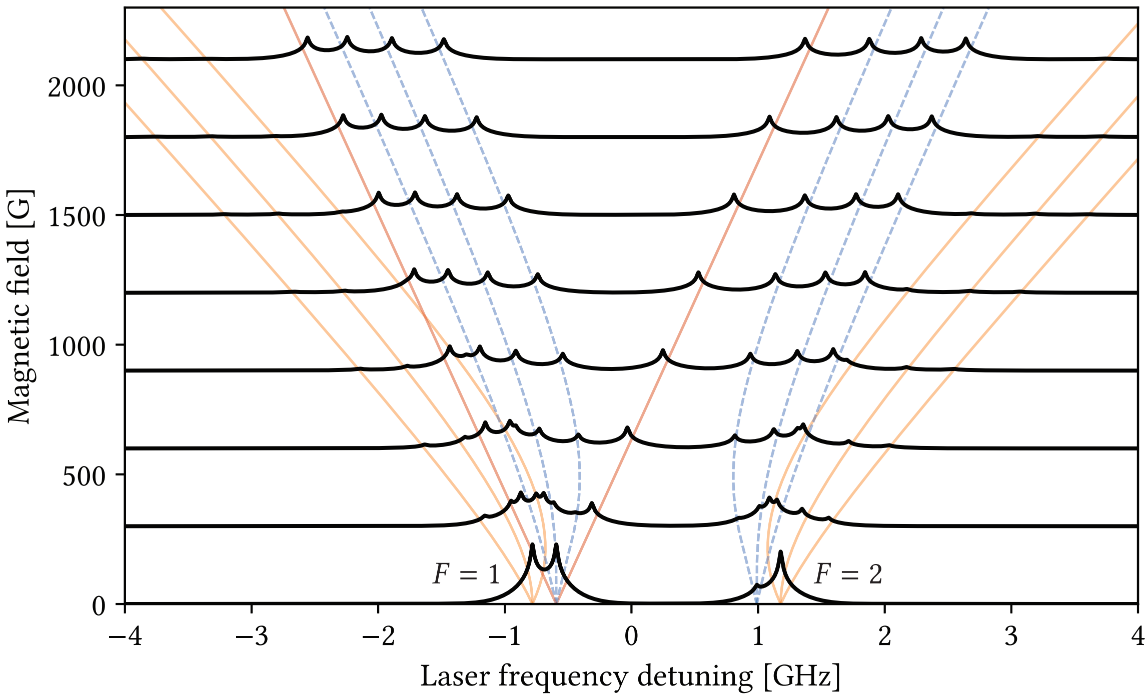

Figure 2.8 – Absorption spectra of sodium D_1 line for a magnetic field varying from 0 to 0.21 T with a step of 0.03 T in case of π excitation. Blue and orange shadow lines in the (x, y) plane represent the transition frequencies. As before, each peak has a FWHM of approximately 100 MHz.

Due to the linewidth $\omega_{\mathrm{FWHM}} \approx 100$ MHz, even for $B_z \gg 10B_0$ the peaks are not completely resolved, resulting in a variation of their amplitude. Experimentally, as hinted in fig. 2.9, SD would allow us to obtain completely resolved peaks, all having the same amplitude. derivative of selective reflection (dSR) would also be suitable here. One can also see that all the peaks are evenly spaced, which is a manifestation of the linear behavior of the frequency shifts mentioned earlier and a good sign HPB regime is reached. Moreover, the red and blue wings of the spectrum are completely symmetric. The frequency detuning $\Delta\omega_r$ between the two groups of 4 r-transitions (see the dashed blue lines in fig. 2.9) for $B_z \gg B_0$ can be estimated roughly by performing the difference between the two GTs, thus

$$\Delta\omega_r \approx \left|\frac{4\mu_B B_z}{3}\right| . \tag{2.51}$$

For a magnetic field $B_z = 9000$ G, we obtain $\Delta\omega_r \approx 16.8$ GHz which is in excellent agreement with the

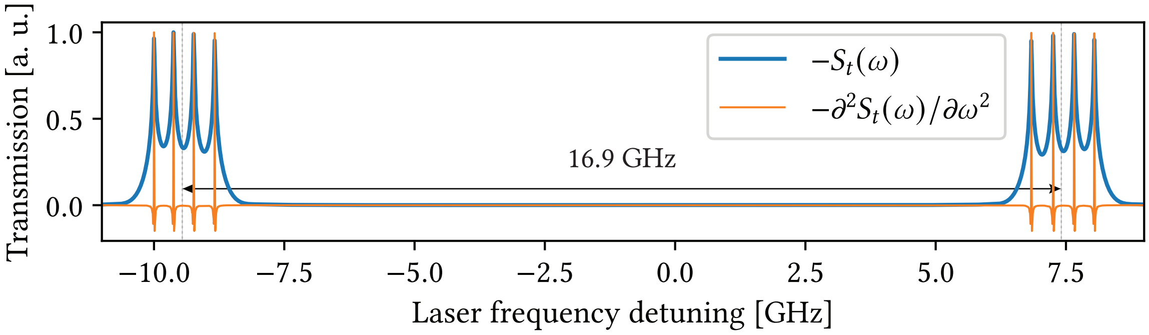

Figure 2.9 – Blue: Absorption spectrum of the D_1 line of sodium for π-polarized incident laser radiation in the HPB regime ($B_z = 9000$ G). Orange: SD spectrum. Both spectra have been normalized so that their maximum amplitude is 1.

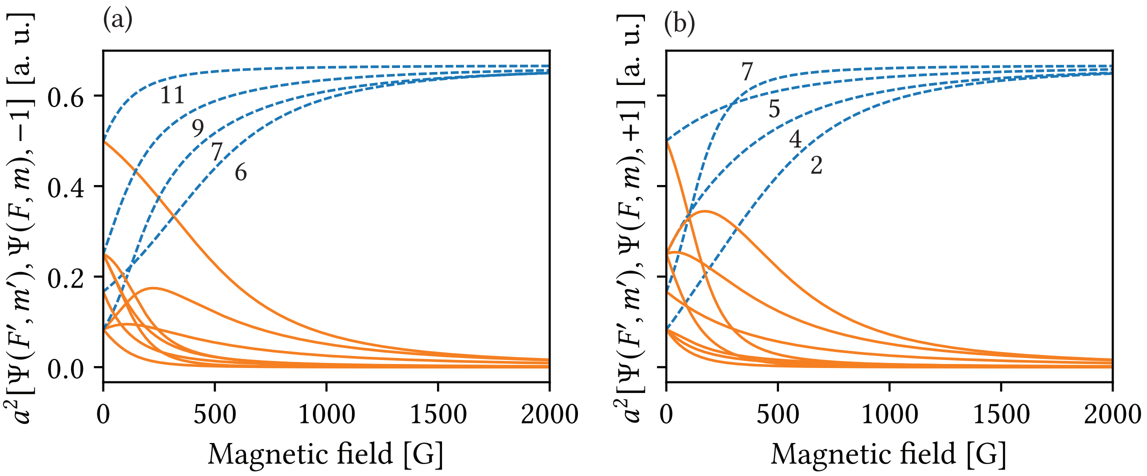

Figure 2.10 – Sodium D_1 line Zeeman transition intensities for circularly polarized laser radiation. a) σ^--transitions. b) σ^+-transitions. Labeling is provided only for the r-vanishing transitions (dashed blue lines) and is the same as in fig. 2.5a and fig. 2.5c.

value 16.9 GHz computed numerically and shown in fig. 2.9.

Circularly polarized incident radiation

All the possible σ^- (resp. σ^+) transitions of the D_1 line of sodium are schematized in fig. 2.5a (resp. fig. 2.5c) and their associated intensities are presented in fig. 2.10. As a first remark, no transition has a constant amplitude throughout the whole magnetic field range, which is because none occurs between uncoupled states. At best, only the excited state is uncoupled (transitions 1 and 6 for σ^-[fig. 2.5a], and their "symmetric" transitions 5 and 12 for σ^+ [fig. 2.5c]), but this is not enough to avoid the magnetic-field dependence of the transition intensities, implying there is no guiding behavior as for π-transitions. Each circular polarization gives rise to a group of four r-transitions, all tending to an amplitude ($\approx$ 0.66 a. u.) twice bigger than the amplitude of the π guiding transitions ($\approx$ 0.33 a. u.). The r-transitions obey the selection rules $\Delta m_I = 0$, $\Delta m_J = \pm 1$ depending on the sign of the incident polarization. A set of absorption spectra is presented in fig. 2.10. Due to the absence of GTs for circularly polarized incident radiation, fewer peculiarities occur in this case. As seen in fig. 2.11, the behavior of the r-transitions is somewhat different from before: for σ^+ polarization, the frequency shifts all tend to a linear behavior with a slope twice bigger than for the π r-transitions. For example, let us take a look at transition 11 (σ^-) occurring between the ground state $|2, 2\rangle$ and the excited state $|1', 1'\rangle$. Using eq. (2.30), we can easily determine that

$$E_g = \zeta - \mu_B B_z\,, \tag{2.52}$$

where ζ is the ground state hyperfine splitting [appendix B]. For the excited state, we only compute the block of $\mathcal{H}_m$ corresponding to $m' = 1$ using eq. (2.30). This leads to

$$\mathcal{H}_{m'=1} = \begin{pmatrix} X & -\sqrt{3}X \\ -\sqrt{3}X & \zeta' - X \end{pmatrix} \tag{2.53}$$

where we denoted $X = \mu_B B_z/6$. Diagonalizing $\mathcal{H}_{m'=1}$ and performing an asymptotic expansion allows to obtain the energy E' of state $|1, 1\rangle$ for $B_z \gg B_0$:

$$E_e = \frac{\zeta' + [\zeta'^2 - 4\zeta' X + 16X^2]^{1/2}}{2} \underset{X\to+\infty}{\sim} 2X + \frac{\zeta'}{4} + \frac{3\zeta'^2}{64X} + O\left(\frac{1}{X^2}\right). \tag{2.54}$$

Subtracting (2.52) to (2.54) gives $E_e - E_g = 8X + \zeta'/4 - \zeta + O(1/X)$, thus we obtain the asymptotic slope of the frequency shift of transition 11 (σ^-) and by extension of all $\sigma^\pm$ r-transitions:

$$s_r^\pm \approx \mp\frac{4\mu_B}{3}\,. \tag{2.55}$$

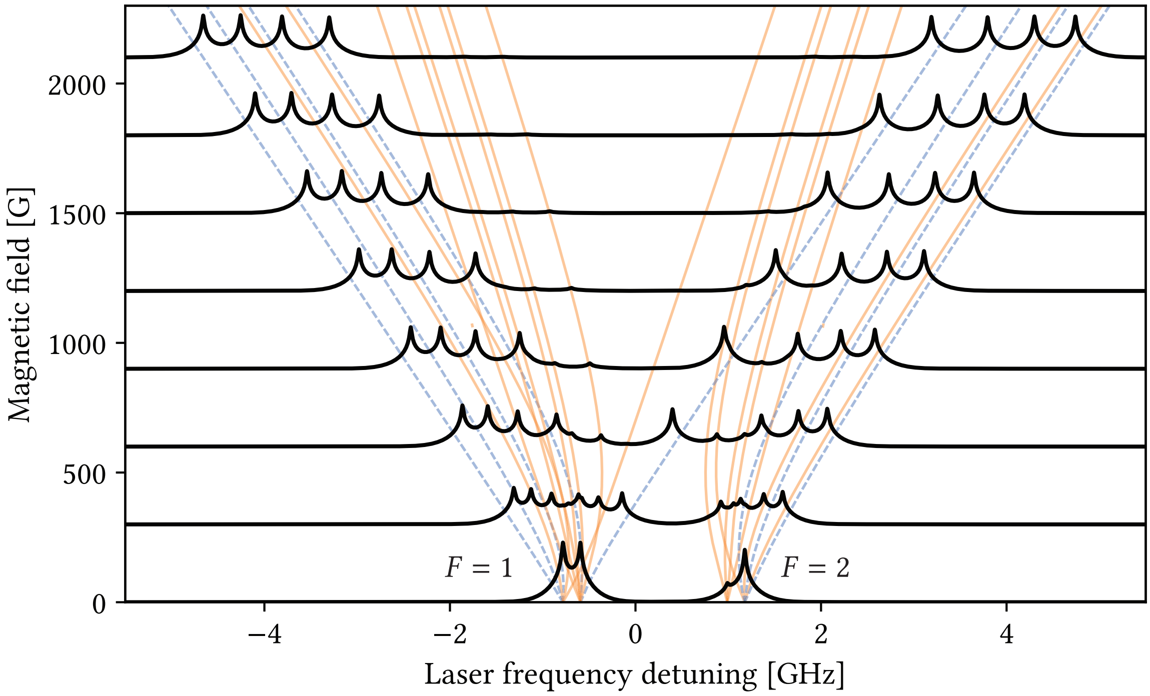

Figure 2.11 – Absorption spectra of sodium D_1 line for a magnetic field varying from 0 to 2100 G with a step of 300 G in case of simultaneous σ^+ and σ^- excitation. Blue and orange shadow lines in the (x, y) plane represent the transition frequencies. As before, each peak has a FWHM of approximately 100 MHz.

This method is the same that was used before for the π-transitions [eq. (2.48)]. As we can see in fig. 2.11, the v-transitions (orange solid lines) that are not overlapped with any r-transition (blue dashed lines) have a frequency shift slope twice smaller than the value given by relation eq. (2.55). We present two spectra for $B_z \gg B_0$ in fig. 2.12. The numerical parameters used for the computation of the spectra are the same as the ones used before in the case of π transitions. On the top panel, the peaks are overlapped due to the linewidth. However, a clear manifestation of the HPB regime is visible when looking at the derivative where all the peaks are evenly spaced and have the same amplitude. Because the slope of the frequency shifts corresponding to the two groups of r-transitions is twice bigger, the frequency detuning between them can also be roughly estimated by

$$\Delta\omega_r \approx \left|\frac{8\mu_B B_z}{3}\right| . \tag{2.56}$$

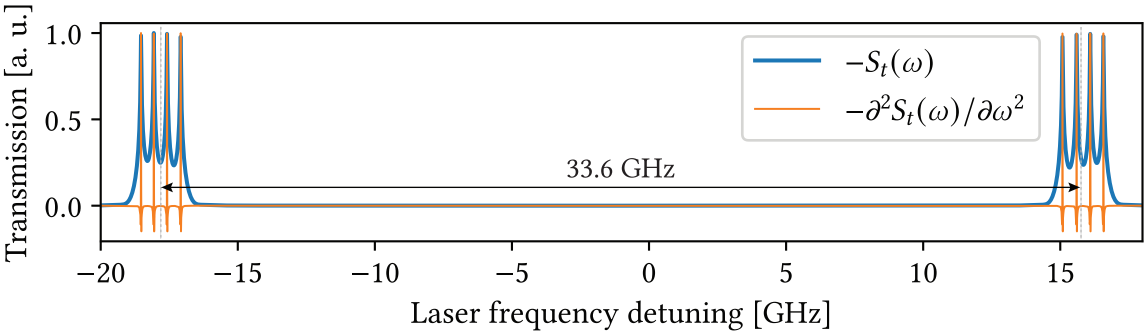

Figure 2.12 – Blue: absorption spectrum of the D_1 line of sodium for simultaneous $\sigma^{\pm}$-polarized incident laser radiation in the HPB regime ($B_z = 9000$ G). Orange: SD spectrum. Both spectra have been normalized so that their maximum amplitude is 1.

Here, we obtain $\Delta\omega_r \approx 33.59$ GHz which is in perfect agreement with the value 33.6 GHz measured in fig. 2.12. In this section, we have provided a complete description of the influence of the magnetic field on the behavior of the Zeeman transitions of sodium D_1 line for the three main types of incident laser radiation. We will now analyze deeply what happens for the D_2 line, with many more transitions, where different phenomena arise.

2.3.4 Sodium D_2 line

The D_2 line of sodium corresponds to the transitions occurring between the states $3^2S_{1/2}$ and $3^2P_{3/2}$. Due to the bigger value of J', many more transitions are possible than for the D_1 line (in total 68 for all three polarizations). Since natural sodium is only composed of one isotope of nuclear spin $I = 3/2$, the hyperfine manifold is simpler than the one of natural rubidium (two isotopes) or cesium (only one isotope but $I = 7/2$). For the numerical computations, we take the parameters given in appendix B and references therein.

Linearly polarized incident radiation

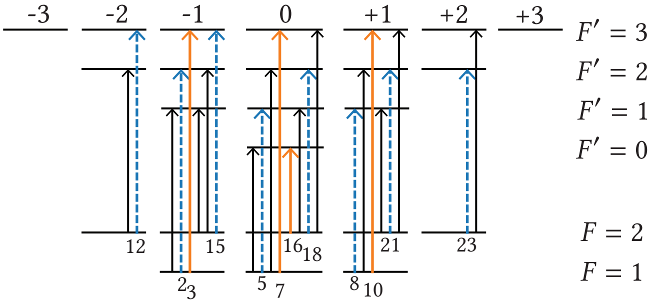

Figure 2.13 – Zeeman transitions of the D_2 line of sodium in the basis $|F, m_F\rangle$ for π excitation.

Twenty-four π transitions are possible for the D_2 line of sodium. A complete scheme as well as the transition intensities are presented in figs. 2.13 and 2.14. In this case, $F = 1, 2$ and $F' = 0, 1, 2, 3$ [5]. The behavior of the π transitions of sodium D_2 line is quite different from the D_1 line. Firstly, the absence of transitions between uncoupled states results in the absence of guiding transitions. Overall, the general shape is different, and this is because the states experience "more coupling" (for a given spectroscopic state in the case of D_1 line, the magnetic field can mix at most two F-levels, whereas for the D_2 line, the mixing goes up to four F levels. Many transition intensities are very small throughout the whole range of magnetic field, and most of them quickly vanish, as seen from the insets of fig. 2.14. Using the same denomination, we denote as r-transitions the transitions 2, 5, 8, 12, 15, 18, 21 and 23 since they obey the selection rules $\Delta m_I = \Delta m_J = 0$, and all the others will be denoted as v-transitions. It is worth noticing that for the D_1 line, we could emphasize the fact that all r-transitions obeyed $\Delta F = 0$. No such rule can be exhibited here in the uncoupled basis. In the previous section, we called MI the transitions whose intensity was 0 for a very small magnetic field. In fig. 2.14, this phenomenon is visible for r-transitions 5 and 18. For the sake of clarity, labeling is not presented here for the v-transitions although it is completely possible to assign each curve to a given transition. However, this notion of MI transitions needs to be completed. Here, we will also denote transitions 3, 7, 10, and 16 [fig. 2.13] as MI. All of them are v-transitions, and their amplitude tends to 0 for $B_z \to 0$, except for transition 3 ($|1, -1\rangle \to |3', -1\rangle$) which experiences a huge increase in amplitude. Here, MI refers to the fact that, due to the coupling of states by B_z, so-called "forbidden" transitions ($\Delta F = \pm 2$) become possible. These transitions are referred to as MI2 in [86]. Here, we have 3 r-transitions arising from $F = 1$ and 5 from $F = 2$ (transitions 12 and 23 are exactly overlapped in fig. 2.14). The total number of π r-transitions is the same as for the D_1 line but there are many more v-transitions here (16 compared to 6). In fig. 2.15, we present a set of absorption spectra along with the transition frequencies to observe their behavior

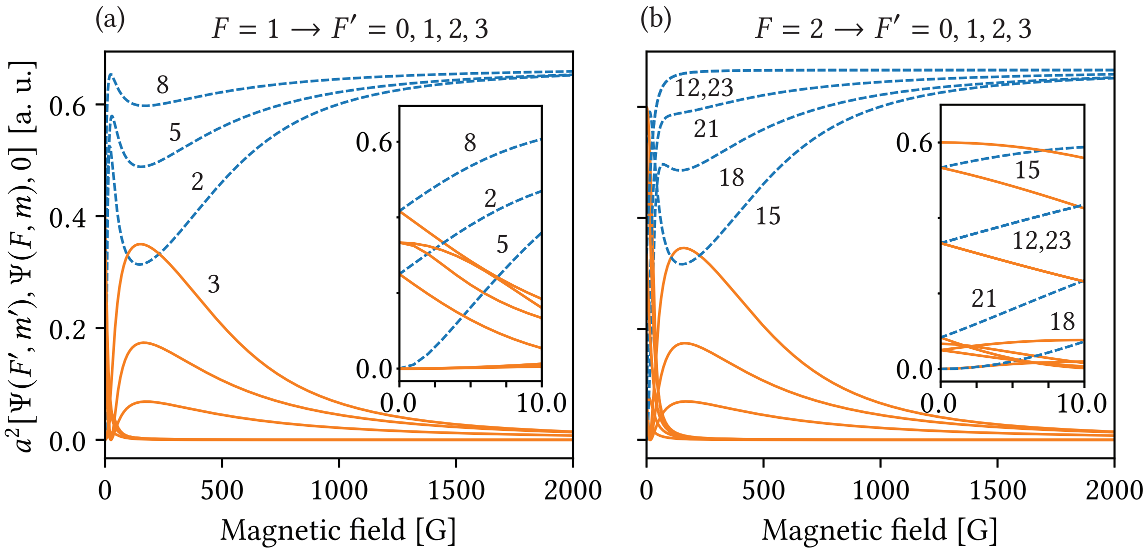

Figure 2.14 – Sodium D_2 line Zeeman transition intensities for linearly polarized laser radiation. a) transitions from $F = 1$. b) transitions from $F = 2$. Labeling is provided only for the transitions of interest and is the same as in fig. 2.13.

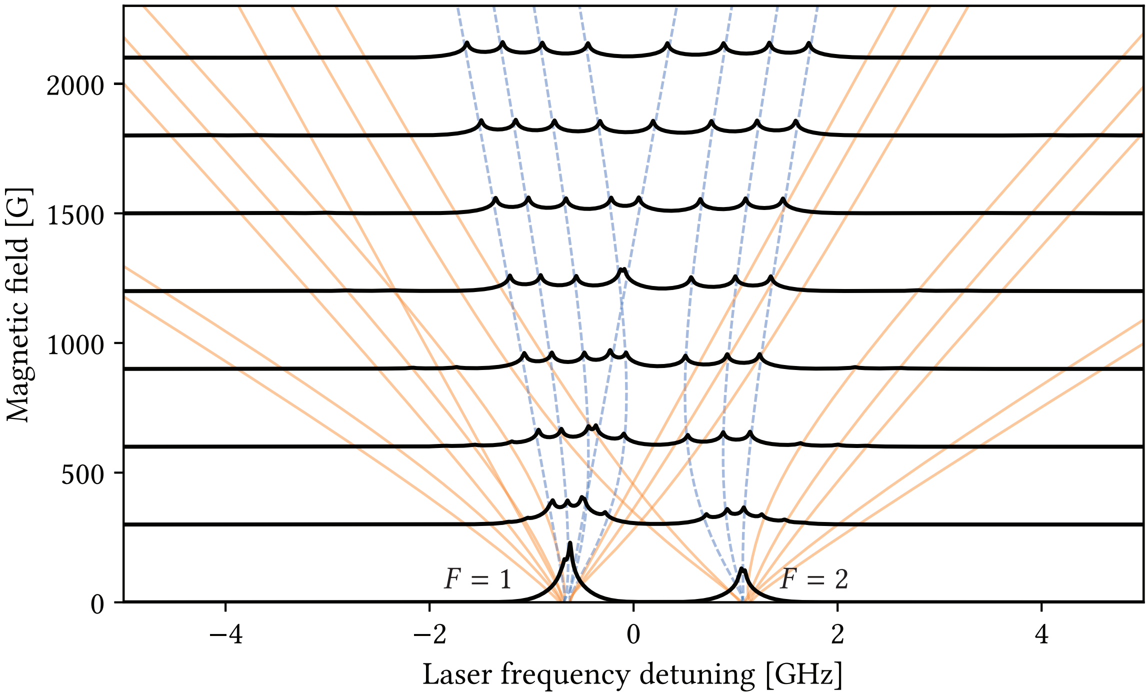

Figure 2.15 – Absorption spectra of the D_2 line of sodium for π-polarized incident laser radiation. The magnetic field intensity varies from 0 to 2100 G with a step of 300 G.

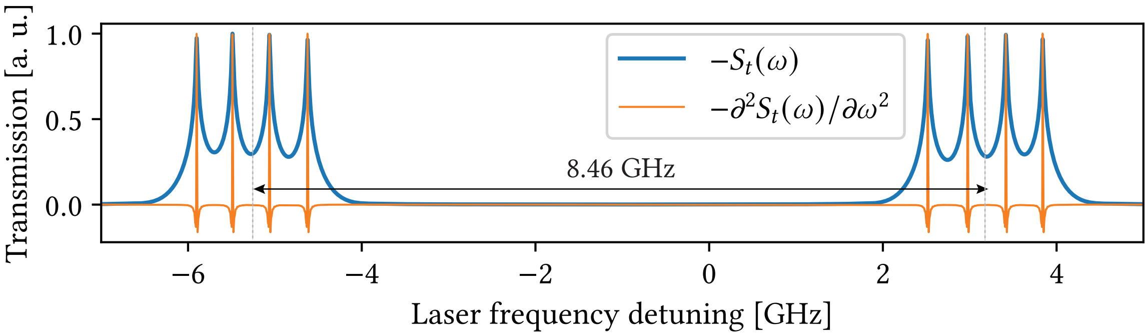

Figure 2.16 – Blue: absorption spectrum of the D_2 line of sodium for π-polarized excitation in the HPB regime ($B_z = 9000$ G). Orange: SD spectrum. Both spectra have been normalized so that their maximum amplitude is 1.

as the magnetic field increases. Since the hyperfine splittings of the state ${}^2P_{3/2}$ are much smaller for sodium than for rubidium or cesium (see appendix B) the peaks are in general much closer here. At zero-field, the 6 peaks remain completely overlapped. Using SD or dSR is a good way to recover the spectral information. At first, for the same values of the magnetic field as before, one notices that all the transitions experiencing the largest frequency shift with respect to the magnetic field are the 16 v-transitions. They can be divided into three groups of same frequency shift (in absolute value). The frequency shifts of the two groups of r-transitions tend asymptotically to a linear behavior with a slope

$$s_r^{\pm} \approx \pm\frac{\mu_B}{3}. \tag{2.57}$$

All the slopes are derived using similar procedures used in relations (2.52) to (2.55). The v-transitions undergo much bigger frequency shifts and can be divided into three groups having asymptotically the same slope in absolute value. Under the approximation $g_S \approx 2$, $g_L \approx 1$ and $g_I \ll g_J$, the first group of v-transitions (in terms of proximity with the r-transitions) experiences a frequency shift of asymptotic slope $\pm\mu_B$. The frequency shifts of the second group of v-transitions have an asymptotic slope $\pm 5\mu_B/3$. The slope for the last group is $\pm 3\mu_B$. This is consistent with fig. 2.15 where we can see the last group of v-transitions experiencing the biggest shifts (more than 4 MHz/G, 9 times more than the r-transitions). Numerically, we obtain respectively ±1.40061, ±2.29035 and ±4.15417 MHz/G. A spectrum for $B_z \gg B_0$ is presented in fig. 2.16. HPB regime is reached since all the peaks are evenly spaced and tend to have the same amplitude. It is again possible to estimate the frequency detuning between the two groups of r-transitions as

$$\Delta\omega_r \approx \left|\frac{2\mu_B B_z}{3}\right|. \tag{2.58}$$

Here, we obtain $\Delta\omega_r \approx 8.40$ GHz (by numerical computation, we obtain 8.46 GHz). The small variation is because when calculating the slopes, the hyperfine splittings are neglected.

Circularly polarized incident laser radiation

Fourty-four Zeeman transitions are possible in the case of circularly polarized radiation for the D_2 line of sodium. All these possible $\sigma^{\pm}$-transitions are schematized in fig. 2.17.

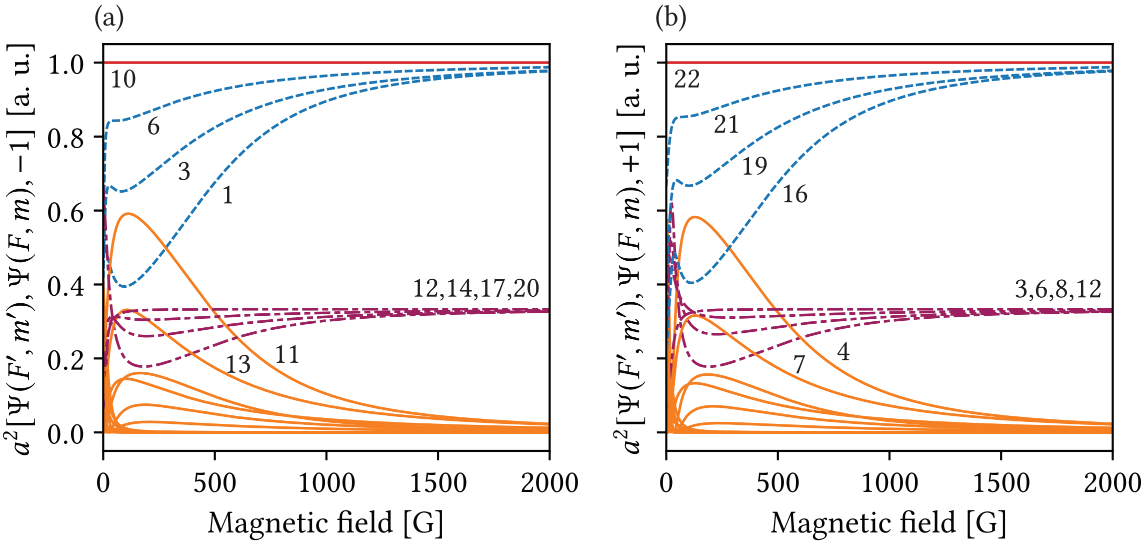

Figure 2.18 – Sodium D_2 line Zeeman transition intensities for circularly polarized laser radiation. a) σ^- transitions. b) σ^+ transitions. Labeling is provided only for the transitions of interest and is the same as in fig. 2.17.

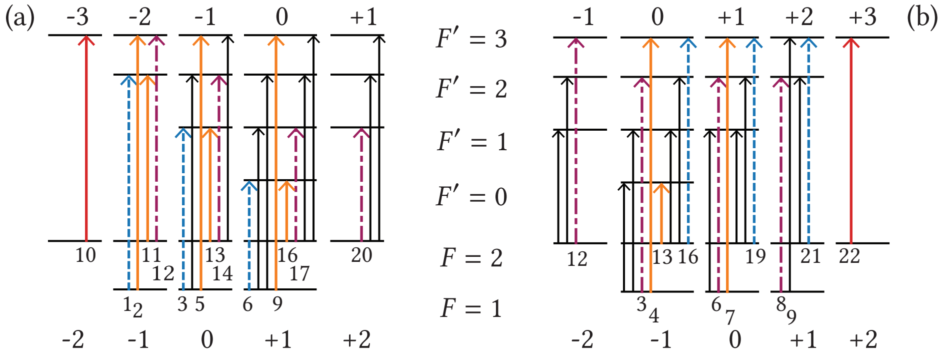

Figure 2.17 – All possible $\sigma^\pm$ Zeeman transitions for the D_2 line of sodium in the basis $|F, m_F\rangle$. a) σ^--transitions. b) σ^+-transitions.

One directly sees on the manifold presented in fig. 2.17 that, due to the selection rule $\Delta m_F = \pm 1$, transitions between uncoupled states are again possible. These transitions are labelled 10 (σ^-) and 22 (σ^+). They occur between states $|2, \pm 2\rangle$ and $|3, \pm 3\rangle$ depending on the polarization, and obey $\Delta F = 1$. They are again called GTs and their constant amplitude for any magnetic field is visible in fig. 2.18. For each polarization appears a group of r-transitions (1, 3, 6 and 10 for σ^- and 16, 19, 21, 22 for σ^+) denoted $r1$-transitions. Transition 10 (σ^-) is a GT for transitions 1, 3 and 6, and transition 22 (σ^+) is a GT for transitions 16, 19 and 21. As we did in relation (2.49), we can prove that for both of these transitions, the squared *modified* transfer coefficients a^2 (relation (2.46)) are always equal to 1. Two other groups of r-transitions, denoted as $r2$-transitions, represented in purple (dash-dotted lines), appear and all tend to an amplitude equal to a third of the amplitude of the $r1$-transitions. For both polarizations, $r2$-transitions tend to reach their maximum amplitude much faster than $r1$-transitions. In orange are represented the vanishing transitions (v-transitions) for each polarization. Apart from transitions 11 and 13 (σ^-) and transitions 4 and 7 (σ^+), all the v-transitions have overall smaller amplitudes than all $r1$ and $r2$-transitions.

The 22 possible σ^--transitions are shown in fig. 2.19. The GT (labeled 10 in fig. 2.17a) has a constant amplitude, and the three other $r1$-transitions are also driven by the GT in terms of frequency shift. The

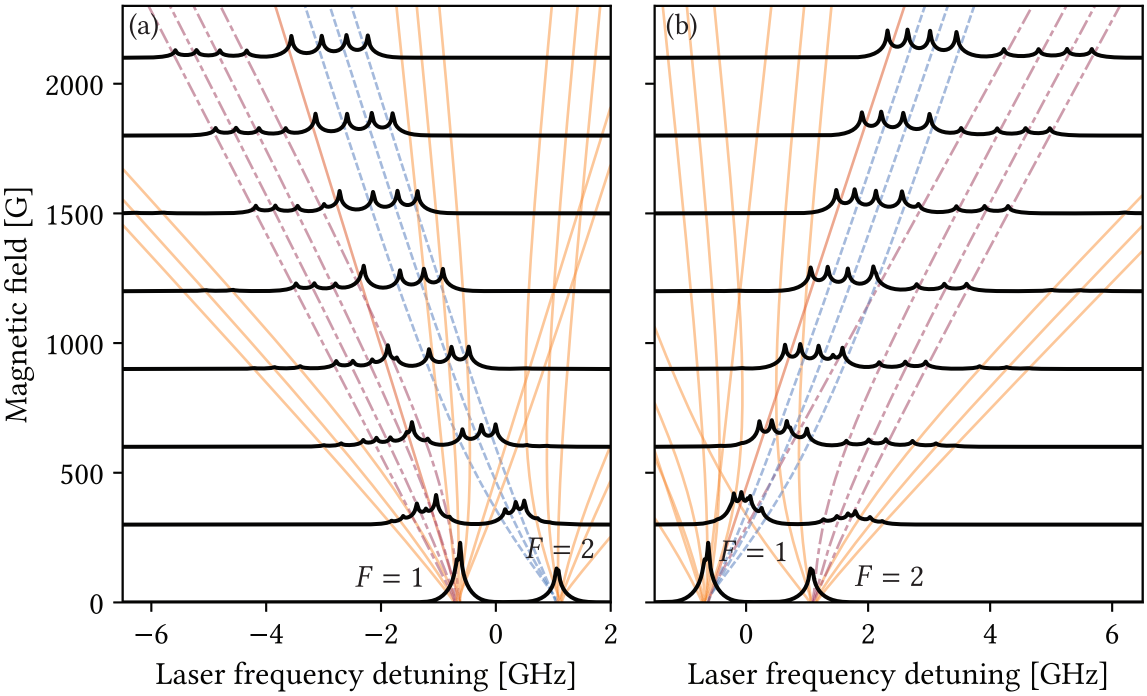

Figure 2.19 – Absorption spectra of the D_2 line of sodium for σ^--polarized incident laser radiation (a) and σ^+-polarized incident laser radiation (b). The magnetic field varies from 0 to 2100 G with a step of 300 G.

GT has a perfectly linear frequency shift of slope

$$s_{GT} \approx \mu_B, \tag{2.59}$$

under the usual approximations, the numerical value being ≈ −1.39958 MHz/G. The $r2$-transitions, having an amplitude three times smaller, experience a frequency shift of approximately $5\mu_B/3$ for high B_z. Numerically, we obtain approximately −2.331 MHz/G. As for the previous cases, the v-transitions experience much bigger frequency shifts, reaching again as much as approximately $3\mu_B = -4.199$ MHz/G (numerically, −4.202 MHz/G). The behavior of the σ^+ is symmetrical compared to that of σ^- transitions, as we can see in fig. 2.19. The guiding transition (in this case 22) experiences a frequency shift $-s_{GT}$ and so do all the $r1$-transitions when B_z is high enough so that the frequency shift becomes linear. The $r2$-transitions will also similarly experience a linear frequency shift $-5\mu_B/3$ (numerically, ≈ 2.331 MHz/G). When the HPB regime is reached ($B_z > 10B_0$), only the $r1$ and $r2$-transitions of each polarization remain visible in the spectrum (16 peaks in total). This is demonstrated in figure 2.20 where the spectrum is presented in case of simultaneous $\sigma^\pm$ excitation for $B_z = 9000$ G. From the obtained slopes, we can estimate that the frequency detuning between the two groups of $r1$-transitions is approximately

$$\Delta\omega_{r1} \approx |2\mu_B B_z| \, , \tag{2.60}$$

leading to $\Delta\omega_{r1} \approx 25.19$ GHz, perfectly consistent with the value 25.15 GHz on the top panel of fig. 2.20, again with the difference coming from the fact that hyperfine splittings are neglected. Similarly, we can estimate $\Delta\omega_{r2}$ to be

$$\Delta\omega_{r2} \approx \left|\frac{10\mu_B B_z}{3}\right| \tag{2.61}$$

that is to say approximately 41.98 GHz, to compare with the value 42.07 GHz of fig. 2.20. Reaching the HPB regime combined with sub-Doppler spectroscopic techniques allows for the formation of narrow resonances far-detuned from the resonant frequency of the transitions. Choosing the right alkali atom

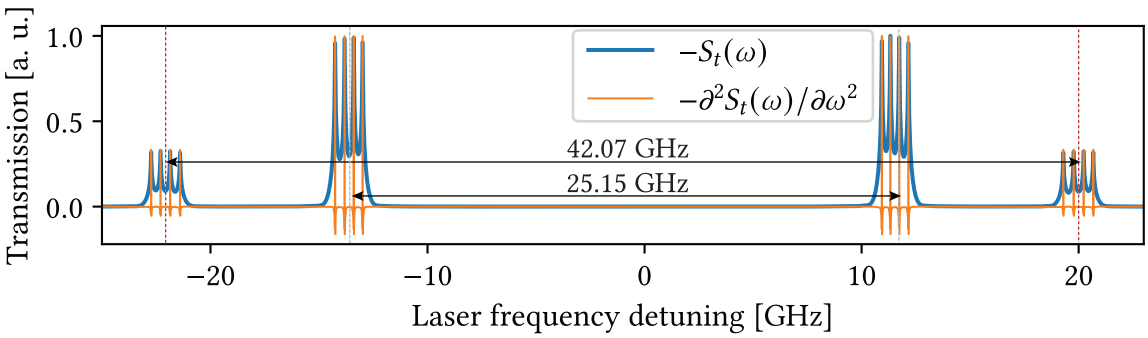

Figure 2.20 – Blue: Absorption spectrum of the D_2 line of sodium for simultaneous $\sigma^{\pm}$ polarized excitation in the HPB regime ($B_z = 9000$ G). Orange: SD spectrum. Both spectra have been normalized so that their maximum amplitude is 1.

for such studies is a key point since B_0 varies a lot. Hyperfine splittings and natural linewidths are also to be taken into account depending on the desired resolution.

In this section, we have performed a complete theoretical description of the behavior of a sodium vapor confined in a NC cell for a wide range of magnetic fields (varying up to 10 kG) and for three incident laser polarizations (linear, left- and right-circular). While the Zeeman structure of sodium is identical to the one of ^{87}Rb or ^{39}K, several changes can be reported such as B_0 and the hyperfine splittings, leading to slight changes in the behavior of transition intensities and transition frequencies. As mentioned before, the natural linewidth Γ of sodium is twice bigger than for other alkalis and leads to much broader absorption lines. However, for the same temperature, the vapor pressure of sodium is much smaller than for heavier alkali atoms ($\simeq 10^{-7}$ torr, whereas for cesium it is $\simeq 6 \times 10^{-4}$ torr and $\simeq 2.5 \times 10^{-4}$ torr for ^{85}Rb). This leads to smaller collisional broadening, but also makes the transmitted and reflected signal smaller so that either a higher temperature or more sensitive detectors would be required to record the signal when performing experiments. In addition, we provided rough estimates of the frequency detuning between the various groups of transitions that remain present in the spectra when the hyperfine Paschen-Back regime is reached.

2.4 Magnetically-Induced Circular Dichroism in alkali metal isotopes with nuclear spin 3/2

We will now focus on the so-called forbidden transitions, obeying $\Delta F = \pm 2$. MI transitions are interesting objects of study because, in certain ranges of magnetic fields, their probabilities can significantly exceed the probabilities of ordinary atomic transitions allowed at $B_z = 0$. The work presented in this section gave rise to the following publication:

- A. Sargsyan, A. Tonoyan, R. Momier, C. Leroy, and D. Sarkisyan. *Dominant magnetically induced transitions in alkali metal atoms with nuclear spin 3/2.* J. Opt. Soc. Am. B **39** (4) (2022), p. 973

As mentioned before, the frequency shifts of MI transitions can reach 20 − 30 GHz, which is of practical interest for example to stabilize lasers on strongly shifted resonances [18]. The first type of MI transitions MI1 includes $|F, 0\rangle \longrightarrow |F' = F, 0\rangle$ exhibiting a zero-probability at $B_z = 0$ (see section 2.3.3). The second type MI2 (see section 2.3.4) transitions $|F, m\rangle \longrightarrow |F', m'\rangle$,where $F' = F \pm 2$ and $m' - m = 0, \pm 1$. In this case, there is a steep rise in the probability of these transitions as B_z increases. However, with a further increase of the magnetic field $B \gg B_0$, the probabilities of these transitions tend back to zero. Nevertheless, the $1 \longrightarrow 3'$ MI2 transitions of the D_2 line ^{87}Rb can be detected up to 8 kG magnetic fields. In this case, a strong frequency shift of 30 GHz occurs relative to the initial (zero-field) transition frequency. In [58], the following rule was established for the probabilities (intensities) of MI2 transitions: MI2 transitions obeying $\Delta F = +2$ are maximum when excited with σ^+-polarized laser radiation, while the probabilities of the MI2 transitions obeying $\Delta F = -2$ are maximum when excited with σ^--polarized laser radiation. For some MI2 transitions, the difference between the intensities obtained when using σ^+ or σ^- radiation can reach several orders of magnitude. This difference has been termed Type 1 Magnetically Induced Circular Dichroism (MCD1). Revealing the strongest MI2 transitions which, in certain intervals of magnetic fields have probabilities that can exceed the ones of many ordinary (so-called allowed) atomic transitions, is a key point for their application in magneto-optical processes. It was demonstrated in [135] that the strongest transition of the MI2 group $2 \longrightarrow 4'$ of ^{85}Rb (nuclear spin $I = 5/2$) is the transition $|2,-2\rangle \longrightarrow |4',-1'\rangle$ (σ^+-transition). Its intensity is approximately 2 times higher (in the range of magnetic fields 0.2 kG - 2.5 kG) than the intensity of the strongest σ^- MI2 transition. It was demonstrated in [59] that the strongest transition of the MI2 group (transition $3' \longrightarrow 5'$ of Cs, nuclear spin $I = 7/2$) when using σ^+ radiation is the σ^+ transition $|3,-3\rangle \longrightarrow |5',-2'\rangle$. Its intensity is approximately twice higher (in the range of magnetic fields 0.2 kG - 5 kG) than the intensity of the strongest σ^- MI2 transition. This difference has been termed Type 2 Magnetically Induced Circular Dichroism (MCD2). Here, we will present experimental evidence that for atoms with a nuclear spin $I = 3/2$ (^{87}Rb, ^{39}K, ^{23}Na, ^{7}Li) the probability of the strongest σ^+ MI2 transition of the group $1 \longrightarrow 3'$ (transition $|1,-1\rangle \longrightarrow |3',0'\rangle$ is about four times higher than the probabilities of the strongest σ^- MI2 transitions $|1,-1\rangle \longrightarrow |3',-2'\rangle$ and $|2,+1\rangle \longrightarrow |0',0'\rangle$ for $B_z > 100$ G. We will consider ^{87}Rb but the results will be similar for all other alkali isotopes with $I = 3/2$.

2.4.1 Experimental setup

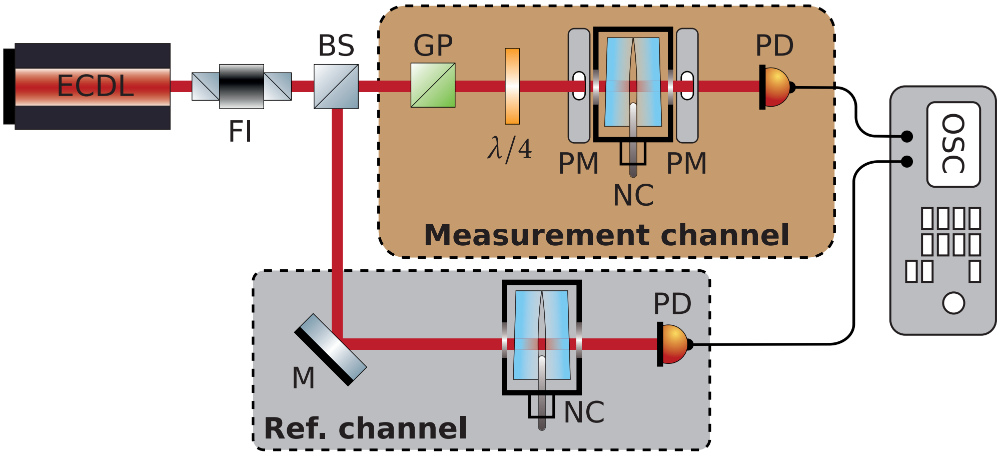

Figure 2.21 – Layout of the experiment. ECDL: continuous wave (CW) diode laser with the wavelength $\lambda = 780$ nm, FI: Faraday insulator, BS: beam splitter, GP: Glan polarizer, $\lambda/4$: quarter waveplate, NC: nanocell (in its oven), PM: permanent magnets, PD: photodiodes, OSC: oscilloscope. A second NC (ref. channel) was used to create a frequency reference.

Figure 2.21 shows the layout of the experimental setup. A MOGLabs Cateye extended cavity diode laser (ECDL) with a wavelength of 780 nm and a spectral width of around 100 kHz was used. The laser beam diameter is 1 mm. To detect the transmission (absorption) spectrum, we used a NC filled with Rb atomic vapor of thickness $\lambda/2$ ($\simeq$ 390 nm) along the direction of the laser radiation, λ being the resonant wavelength of Rb D_2 line. A NC with thickness $L = \lambda/2$ method was used to ensure the narrowing of atomic lines in the absorption spectrum. To further narrow the atomic lines, we study the SD of the absorption spectra. This is particularly important to separate transitions in case some of them overlap. The NC was placed in a furnace with a hole allowing for the laser radiation passage and was heated to 120 $°C$ to ensure an atomic density $N \approx 2 \times 10^{13}$ cm^{-3} (details of the design of the NC are presented in chapter 2). The main NC was placed between strong permanent magnets which produce a strong longitudinal magnetic field, and the wave vector of laser radiation $\mathbf{k}$ was directed along the magnetic field B [136] to be consistent with the theoretical model derived in chapter 2. To form a frequency reference, we used the SD of the absorption spectrum of an additional 390 nm-thick cell containing Rb, towards which part of the laser radiation was directed [61]. The absorption signals were recorded by FD-24K photodiodes, the signals from which were fed to a Tektronix TDS2014B oscilloscope.

2.4.2 Experimental results

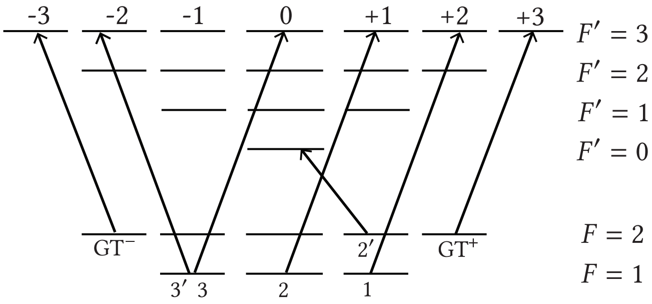

Figure 2.22 – Scheme of ^{87}Rb D_2 line transitions. The $1 \longrightarrow 3'$ σ^+ MI transitions are numbered 1-3, the strongest of them is denoted 3, transitions $|2,2\rangle \longrightarrow |3',3'\rangle$ and $|2,-2\rangle \longrightarrow |3',-3'\rangle$ are respectively labelled GT$^+$ and GT$^-$. The strongest σ^- MI transitions are numbered $2'$ and $3'$.

Figure 2.22 shows a diagram of the atomic transitions of the D_2 line of ^{87}Rb. The group of MI transitions $1 \longrightarrow 3'$ (hereafter, we consider only MI2 transitions, so we omit the number "2") excited by σ^+ radiation are numbered 1-3. The strongest of them, the transition $|1,-1\rangle \longrightarrow |3',0'\rangle$ is denoted 3. The σ^+ transition $|2,+2\rangle \longrightarrow |3',+3'\rangle$ is labeled as GT$^+$ and the σ^--transition $|2,-2\rangle \longrightarrow |3',-3'\rangle$ is labeled as GT$^-$. GT$^+$ and GT$^-$ transitions are called "guiding transitions" [sections 2.3.3 and 2.3.4]: their intensities are constantly equal to each other and do not depend on the B-field since they occur between states that are not mixed by the magnetic field [68]. These features of the GT transitions are used in the experiment described below to compare the amplitudes of MI transitions upon excitation by circularly polarized laser radiation (σ^+ or σ^-). Registering the spectra upon excitation by σ^- (which contains MI transitions on the low-frequency wing of the spectrum) and by σ^+ radiation (which contains MI transitions on the high-frequency wing of the spectrum) and direct comparison of their amplitudes can lead to errors (the parameters of the used diode laser can change when scanning the frequency in a wide frequency range). Therefore, we compare the amplitude of the MI transition to the GT transition located close to it in frequency. Since the intensities of GT transitions for σ^+ or σ^- radiations are equal to each other $A(\mathrm{GT}^+) = A(\mathrm{GT}^-)$, this allows us to determine the intensities of the MI transitions of ^{87}Rb of interest. This technique with the involvement of GT transitions was successfully used to study MI transitions of ^{85}Rb and Cs in [59, 135].

The upper red curves in fig. 2.23a-c (Abs.) are the experimental absorption spectra of transition $1,2 \longrightarrow 0',1',2',3'$ of the D_2 line of Rb (both isotopes are present in the spectra) for the following magnetic field values: $B_z = 850$ G (a), $B_z = 950$ G (b), and $B = 1450$ G (c) obtained by the $L = \lambda/2 = 390$ nm method when σ^- polarized radiation is applied (transitions frequencies are shifted towards low frequencies as the magnetic field increases). The laser power was 30 μW. As can be seen, some transitions in the absorption spectra are partially overlapped. Orange lines (SD exp.) are SD of absorption spectra (here and below, the SD is inverted for convenience). The transition $|2,+1\rangle \longrightarrow |0',0'\rangle$ numbered $2'$ is among the strongest MI transitions (along with transition numbered $3'$ shown in fig. 2.22). The spectra also include the guiding transition GT$^-$ (^{87}Rb) whose application is discussed above. We need to determine the ratio of the amplitude of the GT$^-$ transition to the amplitude of the transition numbered $2'$, in the cases indicated in fig. 2.23b and c, the GT$^-$ transition is overlapped with other atomic transitions; therefore, the insets show the fitted spectra. The ratios of the amplitude of the GT$^-$ transition to the amplitude of the transition numbered $2'$ for 850, 950, and 1450 G (experimental results are also given for other values of B_z) are presented in fig. 2.24a. Blue lines (Theor.) are the SD of theoretical absorption

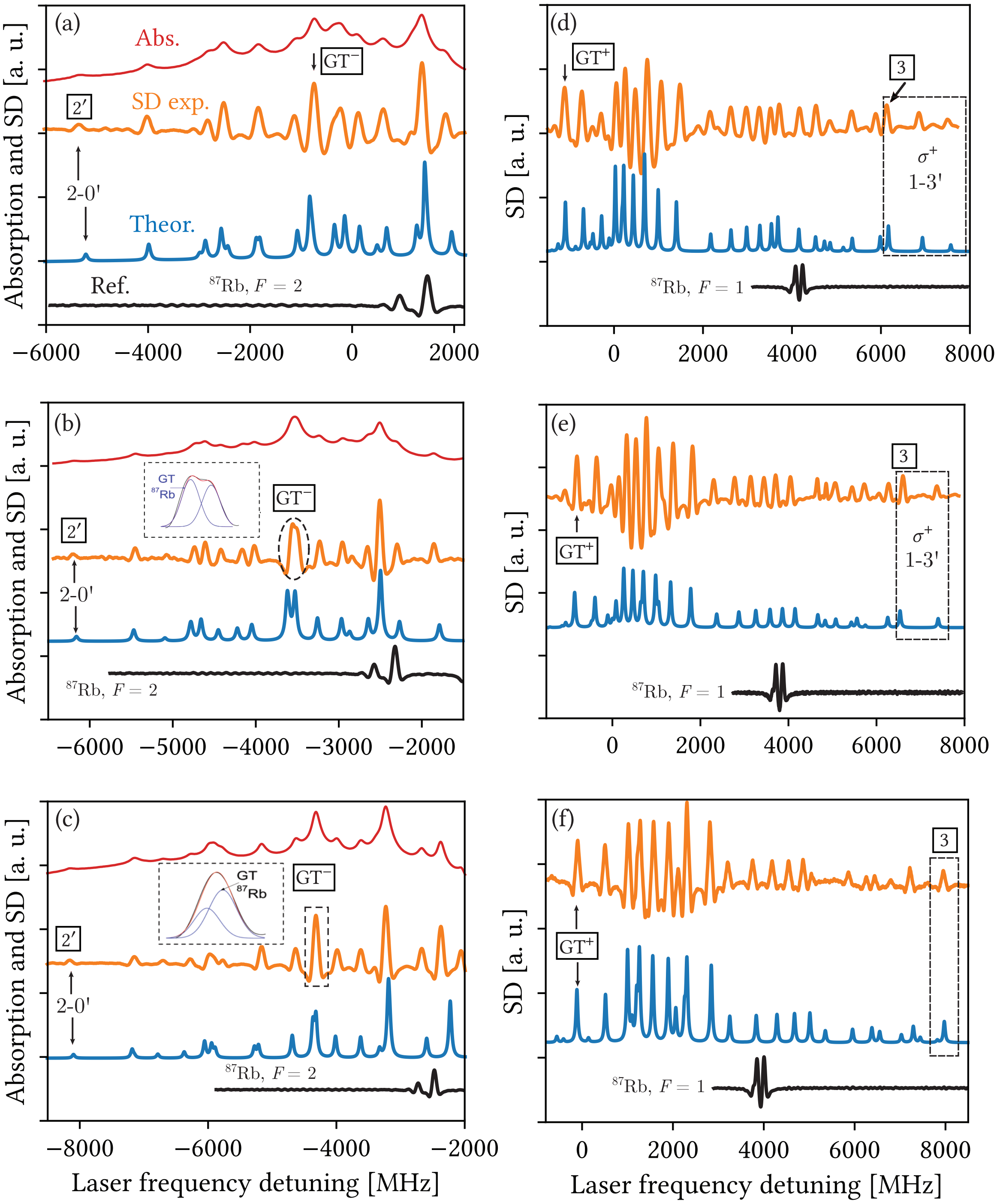

Figure 2.23 – (a-c) Absorption spectra of transitions $1, 2 \longrightarrow 0', 1', 2', 3'$ of the D_2 line of ^{87}Rb for σ^- polarized incident laser radiation. (d-f) SD of absorption spectra of transitions $1, 2 \longrightarrow 0', 1', 2', 3'$ of the D_2 line of ^{87}Rb for σ^+ polarized incident laser radiation. (a,d) $B_z = 850$ G, (b,e) $B_z = 950$ G, (c,f) $B_z = 1450$ G. The spectra were all obtained with a cell of thickness $L = 390$ nm. For each figure, the orange curve is the SD of the experimental absorption spectrum (SD exp.), and the blue curve (Theor.) is theoretical. When provided, absorption spectra (Abs.) are represented in red. The lower black curves (Ref.) are the SD of the peaks corresponding to $F = 1$ transitions. Occasional non-linearity of the laser frequency scanning is caused by the imperfect grating control of the laser.

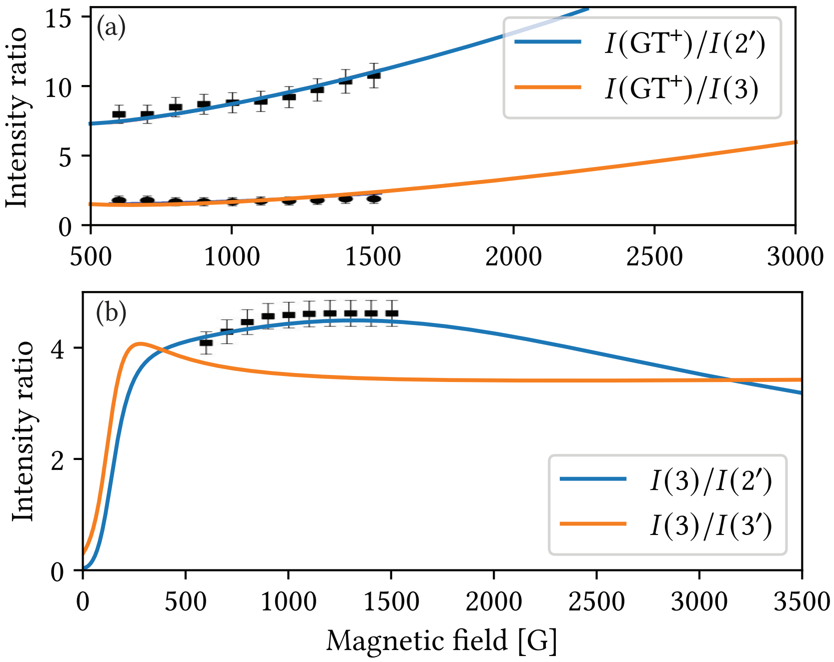

Figure 2.24 – Calculated transition intensity ratios with respect to the magnetic field B_z. a) Blue curve: $I(\mathrm{GT}^+)/I(2')$ ($|2,1\rangle \longrightarrow |0',0'\rangle$). Orange curve: $I(\mathrm{GT}^+)/I(3)$ ($|1,-1\rangle \longrightarrow |3',0'\rangle$) b) Blue curve: $I(3)/I(2')$. Orange curve: $I(3)/I(3')$. Experimental measurements are depicted by the black squares with error bars. Experimental measurements are depicted by the black squares with error bars.

spectra for atomic transitions with a FWHM (full width at half maximum) of 40 MHz. As is seen, there is a good agreement between experiment and theory regarding the amplitude and the (frequency) position of the peaks. The orange lines in fig. 2.23d-f are SD of the experimental absorption spectra (not shown) for the σ^+ transitions $1, 2 \longrightarrow 0', 1', 2', 3'$, at $B_z = 850$ G (d), $B_z = 950$ G (e) and 1450 G (f). Transitions frequencies are shifted from the zero field frequencies towards the high-frequency wing of the spectrum. The transition $|1,-1\rangle \longrightarrow |3',0'\rangle$ labelled 3 is the strongest σ^+ MI transition. The spectra also include the guiding transition GT^+. We need to determine its amplitude but there is no need to fit the absorption peak corresponding to this transition as it is not overlapped with any other transition. The ratio of the amplitude of the GT^+ transition to the amplitude of the transition labeled 3 for 850, 950, and 1450 G are presented in curve 2 of Fig. 2.24a (experimental points for other values of B are also provided). Blue lines (Theor.) in Fig. 2.23d-f are the SD of the calculated absorption spectra with a FWHM of 40 MHz. It can be seen here again that good agreement between the theory and experiments is obtained. Lower lines (Ref.) in fig. 2.23d-f are the SD of the absorption spectra of transitions $1 \longrightarrow 0', 1', 2'$ at zero magnetic field. The inset in Fig. 2.23d shows the SD spectrum of the MI transition numbered 3 for σ^+ polarized radiation and MI transition numbered $3'$ for σ^- polarized radiation (which are normalized to the amplitudes of GT^- and GT^+), the ratio of the amplitudes is equal to 4. The frequency distance between them is around 3 GHz for $B \approx 1000$ G. Nevertheless, for comparison, we brought them together. As it is seen from the inset, the ratio of the amplitudes of MI transitions $A(3)/A(3')$ is equal to 4, which coincides with the value predicted theoretically and measured experimentally [58]. In Fig. 2.24a curve 1 is the ratio of amplitudes of the GT^+ transition to the MI transition numbered $2'$ with respect to the magnetic field B, the theory and the experimental are in perfect agreement. The ratio of the amplitude of the GT^+ transition to the amplitude of the MI transition numbered 3 for $B = 850$, 1000, and 1500 G is presented by the curve 2 in Fig. 2.24a (experimental results are also given for other values of B). The ratio of the amplitude of the MI transition numbered 3 to the amplitude of the transition numbered $2'$ with respect to the magnetic field B is presented by curve 1 in Fig. 2.24 (both the theory and the experiment). The calculated ratio of the amplitude of the transition numbered 3 to the amplitude of the transition numbered $3'$ as a function of the magnetic field is presented by curve 2 in Fig. 2.24. As seen from curve 1 in Fig. 2.24 for $B > 500$ G, the probability of the strongest σ^+ MI transition ($F = 1 \longrightarrow F = 3$) is 4.5 times higher than the probability of the strongest σ^- MI transition. Let us note that the short range of experimental data is due to the overlapping of the transitions of ^{87}Rb and ^{85}Rb occurring for stronger magnetic fields (the cell is filled with natural Rb).

2.5 Conclusion

Starting from the Dirac equation, we have derived the theoretical model used to describe the behavior of an alkali vapor under the influence of an external magnetic field. This model, coupled with the Fabry–Pérot (FP) model presented in chapter 2, allows to simulate sub-Doppler spectra with complete resolution of each transition occuring between two Zeeman sublevels.

We have then performed a complete theoretical description of the behavior of a sodium vapor confined in a NC for a wide range of magnetic field (varying up to 10 000 G) and for three incident laser polarizations (linear, left- and right-circular). While the Zeeman structure of sodium is identical to the one of ^{87}Rb or ^{39}K, parameters such as the hyperfine splittings differ, leading to slight changes in the behavior of transition intensities and transition frequencies. As mentioned before, the natural linewidth Γ of sodium is twice bigger than for other alkalis, and leads to much broader absorption lines. However, for the same temperature the vapor pressure of sodium is much smaller than for heavier alkali atoms ($\simeq 10^{-7}$ torr, whereas for cesium it is $\simeq 6 \times 10^{-4}$ torr and $\simeq 2.5 \times 10^{-4}$ torr for ^{85}Rb). This leads to smaller collisional broadening, but also makes the transmitted and reflected signal smaller so that either a higher temperature or more sensitive detectors would be required to record the signal when performing experiments. In addition, we provided rough estimates of the frequency detuning between the various groups of transitions that remain present in the spectra when the HPB regime is reached.

Finally we have studied, both experimentally and theoretically, that for an atom with a nuclear spin $I = 3/2$ (here ^{87}Rb, but the results are similar for ^{39}K, ^{23}Na, and ^{7}Li) in magnetic fields larger than 100 G, the intensity of the strongest σ^+ MI transition $1 \longrightarrow 3'$ is 4.5 and 4 times higher than the probability of the strongest σ^- MI transitions $2 \longrightarrow 0'$ and $1 \longrightarrow 3'$, respectively. This difference, denoted MCD2, is more strongly expressed than that of the Cs and ^{85}Rb D_2 lines. Thus, it is important to note that the σ^+ MI transition $1 \longrightarrow 3'$ is very promising for applications of magneto-optical processes occuring in strong magnetic fields. This transition has for example been used experimentally for the creation of a dark resonance via electromagnetically induced transparency (EIT) in [137]. Formation of EIT on other MI transitions is presented in [138, 139] Complete description and understanding of all these magnetooptical processes are of utmost importance for further applications, for example in optical magnetometry. Upcoming experiments involving sodium NCs are planned at the Institute for Physical Research, NAS of Armenia, to provide an experimental verification of the results presented in this chapter. Complete agreement between experiments and theory is expected as it was proven for all other alkali (except lithium, for which it is very hard to fabricate a NC, see chapter 2). In the next chapter, we carry on the study of magneto-optical processes in alkali vapors by having a look at transition dipole moment cancellations.

Chapter 3

Transition cancellations in all stable alkali isotopes

In this chapter, we present a complete theoretical investigation of Zeeman transition cancellations of all stable and long-lived alkali isotopes. In the simplest cases, we are able to derive analytical formulas for the cancellation values. For more complicated manifolds, we perform a complete numerical analysis. These values, if measured extremely precisely, could become a standard for the calibration of magnetometers.

Contents

3.1 Introduction **55**
3.2 D_1 line: theoretical considerations **56**
  3.2.1 Zeeman Hamiltonian 57
  3.2.2 Transition intensities 58
3.3 Analytical treatment of D_1 and D_1 - like transitions **60**
  3.3.1 Sodium and potassium 62
  3.3.2 Rubidium 63
  3.3.3 Cesium 65
  3.3.4 Experimental feasibility 66
3.4 Numerical treatment of D_2 and D_2 like transitions of Rb **68**
  3.4.1 ^{87}Rb 68
  3.4.2 ^{85}Rb 71
3.5 Conclusion **71**

3.1 Introduction

In recent decades, there has been significant interest in investigating various magneto-optical processes in alkali metal vapors, primarily due to the development of new optical magnetometry techniques [14, 17]. These processes include modifications in the frequency and intensity of optical transitions between the magnetic sublevels of the hyperfine structure of atoms in a magnetic field. These modifications can be experimentally observed using sub-Doppler spectroscopic methods and specialized devices like a nanocell (NC) [140–142]. Notably, NC spectroscopy, such as the derivative of selective reflection (dSR) technique [60, 143], reduces inhomogeneous broadening of transitions while maintaining a linear response of the medium, where the atomic signal magnitude is directly proportional to the transition probability [79] (chapter 2). Among the observed phenomena are strong transitions forbidden by zero-field selection rules (magnetically induced transitions) and the significant suppression of initially allowed transitions, achieved by varying the polarization of the exciting laser radiation, as presented in chapter 2.

Here, we use a theoretical model to identify polarization configurations and magnetic field values that can completely cancel transitions between individual magnetic sublevels of alkali atoms, driving the transition probability to zero. The theory is valid for $n^2S_{1/2} \rightarrow k^2P_{1/2,3/2}$ transitions, where $k > n$ ($k \in \mathbb{N}$) is the principal quantum number of the excited $^2P_{1/2}$ or $^2P_{3/2}$ state. From the point of view of theoretical calculations, the only difference between these two types of transitions is the energy differences of the excited states. For the D_2 and $5^2S_{1/2} \rightarrow 6^2P_{3/2}$ transitions, the study is done mostly using numerical methods, but in several cases, we were able to extract analytical formulas depending on the size of the Hamiltonian submatrices. This information can enhance the precision of the fundamental physical constants used in the model. Additionally, we address the experimental feasibility of achieving

magnetic field cancellation of transitions and discuss potential applications, such as optical mapping of magnetic fields and magnetic field control of optical information.
This chapter is divided into three main parts:

- In section 3.2, we develop a theoretical model allowing us to determine the magnetic field values canceling D_1 and $5^2S_{1/2} \longrightarrow 6^2P_{1/2}$ transitions of all stable alkali isotopes. Starting from a general definition of the hyperfine structure, we build Hamiltonians corresponding to the ground and excited states of each Zeeman transition in the coupled basis $|F, m\rangle$. After simplifications and tedious calculations, we obtain a single analytical formula corresponding to the roots of specific transition intensities. We observe an intriguing symmetric "pair" behavior of some transitions.
- In section 3.3 we use this formula to determine all the possible cancellation values. After recalling the physical constants used in the computations, we give an exhaustive overview of which transitions are canceled or maximized and for which magnetic field magnitude. Relevant graphs and tables are presented, and the phenomenon is highlighted by the calculation of dSR spectra using the model described in chapter 2. We discuss the feasibility of an eventual experimental measurement of these magnetic field values.
- In section 3.4, we give an overview of all the possible cancellation values of the D_2 and $5^2S_{1/2} \longrightarrow 6^2P_{3/2}$ lines of ^{85}Rb and ^{87}Rb. Here, no analytical formula could be obtained, thus the magnetic field values are determined numerically. Due to the complexity of the hyperfine structure for the sake of readability, we only present tables.

The work presented in this section gave rise to the publication of the three following journal articles:

- R. Momier, A. Aleksanyan, E. Gazazyan, A. Papoyan, and C. Leroy. *New standard magnetic field values determined by cancellations of ^{85}Rb and ^{87}Rb atomic vapors $5^2S_{1/2} \longrightarrow 6^2P_{1/2,3/2}$ transitions.* J. Quant. Spectrosc. Radiat. Transf. **257** (2020), p. 107371
- A. Aleksanyan, R. Momier, E. Gazazyan, A. Papoyan, and C. Leroy. *Transition cancellations of ^{87}Rb and ^{85}Rb atoms in a magnetic field.* J. Opt. Soc. Am. B **37** (11) (2020), 3504–3514
- A. Aleksanyan, R. Momier, E. Gazazyan, A. Papoyan, and C. Leroy. *Cancellation of D_1 line transitions of alkali-metal atoms by magnetic-field values.* Phys. Rev. A **105** (4) (2022), p. 042810

3.2 D_1 line: theoretical considerations

As mentioned in the previous chapters, the atomic fine structure arises from the coupling between the orbital angular momentum **L** and the spin angular momentum **S** of the electron, yielding a total electron angular momentum **J**. Similarly, the hyperfine structure results from the coupling between the total electron angular momentum **J** and the nuclear angular momentum **I**, yielding a total atomic angular momentum **F**. Let us consider here the D_1 line of alkali atoms, corresponding in the general case to the following transition:

$$n^2S_{1/2} \longrightarrow n^2P_{1/2}\,. \tag{3.1}$$

where $n = 2$ for Li, $n = 3$ for Na, $n = 3$ for K, $n = 5$ for Rb and $n = 6$ for Cs. In that case, $J = 1/2$ for both ground and excited states. The total atomic angular momentum **F** thus obeys

$$I - 1/2 \leq F \leq I + 1/2. \tag{3.2}$$

Each fine state (ground $n^2S_{1/2}$ or excited $n^2P_{1/2}$) splits into two hyperfine states F_g^- and F_g^+ (resp. F_e^- and F_e^+) that take the following values:

$$F^{\pm}_{g,e} = I \pm 1/2. \tag{3.3}$$

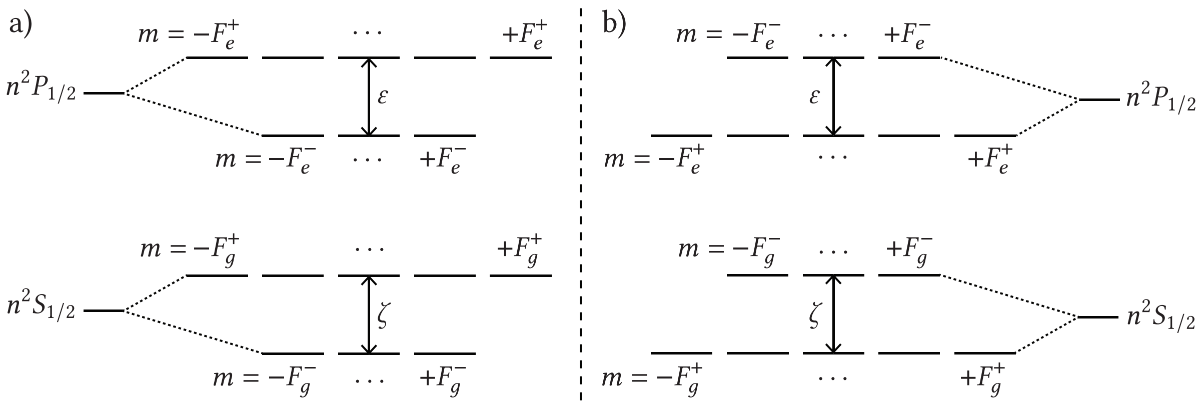

Figure 3.1 – Scheme of all the possible alkali D_1 lines in a magnetic field. a) I is an integer. b) I is a half-integer (the hyperfine structure is inverted).

3.2.1 Zeeman Hamiltonian

Within a magnetic field, the hyperfine states split into several magnetic (Zeeman) sublevels, as described in chapter 2. These levels are indexed by the magnetic quantum m that obeys

$$-F \leq m \leq F. \tag{3.4}$$

Schemes presenting the general cases are shown in fig. 3.1. In these schemes, n is the principal quantum number, ζ and ε are the ground and excited states hyperfine splittings $\zeta = E_0(F_g^+) - E_0(F_g^-)$ and $\varepsilon = E_0(F_e^+) - E_0(F_e^-)$. The hyperfine structure is inverted when the nuclear spin I is a half-integer quantity. With these new notations, the diagonal elements of the Zeeman Hamiltonian $\mathcal{H}_m$ given by eq. (2.30) [chapter 2, section 2.2.3] can be rewritten

$$\langle F_{g,e}^{\pm}, m | \mathcal{H} | F_{g,e}^{\pm}, m \rangle = E_0(F) - \mu_B g_F(F_{g,e}^{\pm}) m B_z. \tag{3.5}$$

The off-diagonal elements given by eq. (2.32) read

$$\begin{aligned} \langle F_{g,e}^{\pm}, m | \mathcal{H}_m | F_{g,e}^{\pm} - 1, m \rangle &= \langle F_{g,e}^{\pm} - 1, m | \mathcal{H}_m | F_{g,e}^{\pm}, m \rangle \\ &= -\frac{\mu_B B_z}{2}(g_J - g_I)\sqrt{1 - \left(\frac{2m}{1+2I}\right)^2}, \end{aligned} \tag{3.6}$$

where g_J and g_I are the total angular and nuclear Landé factors. We may denote as g_J^g the Landé g_J-factor of the ground state (resp. g_J^e for the excited state). From eq. (2.24) with $J = 1/2$ and $S = 1/2$, we have

$$g_J^g = g_S \quad \text{and} \quad g_J^e = \frac{4g_L - g_S}{3}. \tag{3.7}$$

Since F quantum numbers are the same for both ground and excited states, we obtain

$$g_F(F_{g,e}^-) = g_I + \frac{g_I - g_J^{g,e}}{2I+1} \quad \text{and} \quad g_F(F_{g,e}^+) = \frac{g_J^{g,e} + 2g_I I}{2I+1}. \tag{3.8}$$

Our goal being to obtain analytical magnetic field values for which specific Zeeman transitions get canceled, we are obviously not interested in transitions having a constant amplitude as the magnetic field varies. We thus forget about extreme angular momentum states that experience no mixing and write general 2×2 matrices for the ground and excited states. For the ground state, we can write the following Zeeman Hamiltonian $\mathcal{H}_g$ for any m_g except $m_g = \pm F_g^{\pm}$. The matrix reads

$$\mathcal{H}_g = \begin{array}{c} \\ \langle F_g^+, m_g| \\ \langle F_g^-, m_g| \end{array} \begin{array}{c} \begin{array}{cc} |F_g^+, m_g\rangle \hspace{10em} & |F_g^-, m_g\rangle \end{array} \\ \begin{pmatrix} \zeta - \mu_B \dfrac{f_g}{1+2I} m_g B & \mu_B \dfrac{g_g B}{2} \sqrt{1 - \left(\dfrac{2m_g}{1+2I}\right)^2} \\ \mu_B \dfrac{g_g B}{2} \sqrt{1 - \left(\dfrac{2m_g}{1+2I}\right)^2} & -\mu_B \left(g_I + \dfrac{g_g}{1+2I}\right) m_g B \end{pmatrix} \end{array}, \tag{3.9}$$

with $g_g = g_I - g_S$ and $f_g = g_S + 2g_I I$. The Hamiltonian of the excited state is very similar:

$$\mathcal{H}_e = \begin{array}{c} \\ \langle F_e^+, m_e| \\ \langle F_e^-, m_e| \end{array} \begin{array}{c} \begin{array}{cc} |F_e^+, m_e\rangle \hspace{10em} & |F_e^-, m_e\rangle \end{array} \\ \begin{pmatrix} \varepsilon - \mu_B \dfrac{f_e}{1+2I} m_e B & \mu_B \dfrac{g_e B}{2} \sqrt{1 - \left(\dfrac{2m_e}{1+2I}\right)^2} \\ \mu_B \dfrac{g_e B}{2} \sqrt{1 - \left(\dfrac{2m_e}{1+2I}\right)^2} & -\mu_B \left(g_I + \dfrac{g_e}{1+2I}\right) m_g B \end{pmatrix} \end{array}, \tag{3.10}$$

where we denoted $g_e = (3g_I - 4g_L + g_S)/3$ and $f_e = (4g_L - g_S + 6g_I I)/3$. These matrices can be diagonalized analytically. The eigenvalues, corresponding to the energy shift of the magnetic sublevels as a function of the magnetic field, read

$$\Lambda_g^{\pm} = \frac{\zeta - 2\mu_B g_I m_g B}{2} \pm \frac{1}{2} \sqrt{\zeta^2 + \mu_B^2 g_g^2 B^2 + \frac{4\zeta \mu_B g_g m_g B}{2I+1}} \tag{3.11}$$

$$\Lambda_e^{\pm} = \frac{\varepsilon - 2\mu_B g_I m_e B}{2} \pm \frac{1}{2} \sqrt{\varepsilon^2 + \mu_B^2 g_e^2 B^2 + \frac{4\varepsilon \mu_B g_e m_e B}{2I+1}}. \tag{3.12}$$

To calculate the transition intensities, we need to derive the eigenvectors of $\mathcal{H}_g$ and $\mathcal{H}_e$.

3.2.2 Transition intensities

Let us come back to the expression of the eigenvectors. The states experiencing mixing due to the external magnetic field can be expressed as a linear combination of the unperturbed states [chapter 2, eq. (2.41)]. In this case, they can be written as follows:

$$|\Psi(F_g^{\pm}, m_g)\rangle = \frac{1}{\sqrt{1+\kappa_{g\pm}^2}} |F_g^+, m_g\rangle + \frac{\kappa_{g\pm}}{\sqrt{1+\kappa_{g\pm}^2}} |F_g^-, m_g\rangle \tag{3.13}$$

$$|\Psi(F_e^{\pm}, m_e)\rangle = \frac{1}{\sqrt{1+\kappa_{e\pm}^2}} |F_e^+, m_e\rangle + \frac{\kappa_{e\pm}}{\sqrt{1+\kappa_{e\pm}^2}} |F_e^-, m_e\rangle, \tag{3.14}$$

with

$$\kappa_{g\pm} = \frac{2(2I+1)(\Lambda_g^{\pm} - \zeta) + 2\mu_B f_g m_g B}{\mu_B g_g B \sqrt{(2I+1)^2 - 4m_g^2}} \quad \text{and} \quad \kappa_{e\pm} = \frac{2(2I+1)(\Lambda_e^{\pm} - \zeta) + 2\mu_B f_e m_e B}{\mu_B g_e B \sqrt{(2I+1)^2 - 4m_g^2}}. \tag{3.15}$$

The *unperturbed* transfer coefficients [chapter 2, eq. (2.46)] can be simplified to

$$a(F_e, m_e, F_g, m_g, q) = (-1)^{3/2+I+F_e+F_g-m_e} \sqrt{2} \sqrt{2F_e+1} \sqrt{2F_g+1} \begin{pmatrix} F_g & 1 & F_e \\ m_g & q & -m_e \end{pmatrix} \begin{Bmatrix} F_e & 1 & F_g \\ 1/2 & I & 1/2 \end{Bmatrix}. \tag{3.16}$$

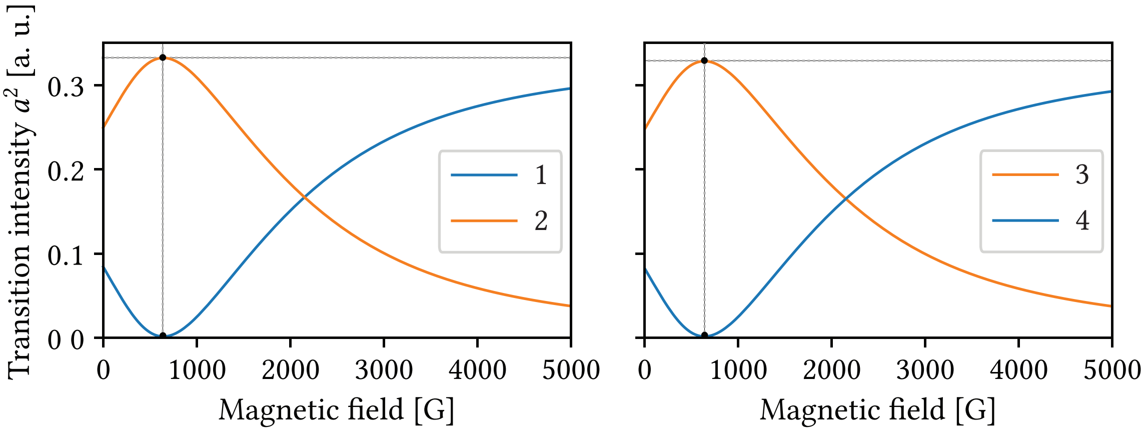

Figure 3.2 – Possible π transition intensities for a general system of two ground magnetic sublevels and two excited magnetic sublevels with $I = 3/2$ and $m = -1$. The numbering used here is consistent with eq. (3.17). The dashed lines are drawn to guide the eye.

We now focus on π transitions ($q = \Delta m = 0$). For a given m, four transitions are possible[1]. The four cases to consider are the following

$$\begin{aligned}
1 &: |F_g^-, m\rangle \longrightarrow |F_e^-, m\rangle \\
2 &: |F_g^+, m\rangle \longrightarrow |F_e^-, m\rangle \\
3 &: |F_g^-, m\rangle \longrightarrow |F_e^+, m\rangle \\
4 &: |F_g^+, m\rangle \longrightarrow |F_e^+, m\rangle
\end{aligned} \tag{3.17}$$

The four transition intensities are depicted in fig. 3.2 for $m = -1$. In that case, since $m_g = m_e = m$, we can obtain unperturbed transfer coefficients depending solely on m. We obtain for the first two cases

$$a(F_e^\pm, m; F_g^\pm, m; 0) = \pm\frac{2m}{\sqrt{3}\,(2I+1)}, \tag{3.18}$$

and for the last two cases

$$a(F_e^\pm, m; F_g^\mp, m; 0) = \frac{1}{\sqrt{3}}\sqrt{1-\left(\frac{2m}{2I+1}\right)^2}. \tag{3.19}$$

And the transfer coefficients [chapter 2, eq. (2.47)] corresponding to the transitions experiencing dipole moment cancellation (transitions 1 and 4) are finally

$$\begin{aligned}
a[|\Psi(F_e^\pm, m)\rangle, |\Psi(F_g^\pm, m)\rangle, 0] = {} & \frac{\kappa_{e\pm}}{\sqrt{1+\kappa_{e\pm}^2}} a(F_e^-, m, F_g^-, m, 0) \frac{\kappa_{g\pm}}{\sqrt{1+\kappa_{g\pm}^2}} \\
& + \frac{\kappa_{e\pm}}{\sqrt{1+\kappa_{e\pm}^2}} a(F_e^-, m, F_g^+, m, 0) \frac{1}{\sqrt{1+\kappa_{g\pm}^2}} \\
& + \frac{1}{\sqrt{1+\kappa_{e\pm}^2}} a(F_e^+, m, F_g^-, m, 0) \frac{\kappa_{g\pm}}{\sqrt{1+\kappa_{g\pm}^2}} \\
& + \frac{1}{\sqrt{1+\kappa_{e\pm}^2}} a(F_e^+, m, F_g^+, m, 0) \frac{1}{\sqrt{1+\kappa_{g\pm}^2}}.
\end{aligned} \tag{3.20}$$

---

[1] We still do not consider transitions between extreme angular momentum magnetic sublevels.

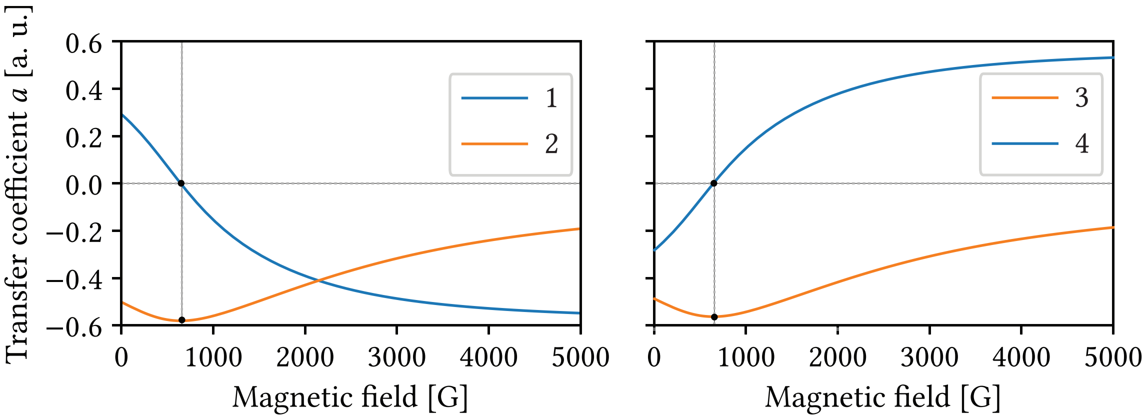

Figure 3.3 – Possible π transfer coefficients for a general system of two ground magnetic sublevels and two excited magnetic sublevels with $I = 3/2$ and $m = -1$. The numbering used here is consistent with eq. (3.17). The dashed lines are drawn to guide the eye.

As we look for transition cancellations, we want to solve $a[|\Psi(F_e^{\pm}, m)\rangle, |\Psi(F_g^{\pm}, m)\rangle, 0] = 0$ (fig. 3.3). Analytically, the solutions are given by

$$B_{\pm}^{\pm} = -\frac{4m\zeta\varepsilon}{\mu_B(2I+1)(g_g\varepsilon + g_e\zeta)}, \tag{3.21}$$

where m has to fulfill the condition

$$0 \leq (-1)^{2I} m \leq I - 1/2. \tag{3.22}$$

From eq. (3.21), we can notice that for isotopes having a half-integer nuclear spin, transition cancellations exist for π transitions between magnetic sublevels with $m = 0$. However, as the atomic states are degenerated, it is not possible to observe the cancellation of these transitions. The *modified* transfer coefficients $a[|\Psi(F_e^{\pm}, m)\rangle, |\Psi(F_g^{\mp}, m)\rangle, 0]$ (transitions 2 and 3) can not be equal to zero, but these quantities have a very interesting behavior. While for certain values of B, transition intensities corresponding to $a[|\Psi(F_e^{\pm}, m)\rangle, |\Psi(F_g^{\pm}, m)\rangle, 0]$ become zero (dipole moment cancellation), the transition intensities corresponding to $a[|\Psi(F_e^{\pm}, m)\rangle, |\Psi(F_g^{\mp}, m)\rangle, 0]$ reach a maximum value which corresponds to the intensity of a π transition occurring between pure states, ie the so-called guiding transitions (GTs) described in chapter 2. This is ensured by the calculation of the derivative of modified transfer coefficients squared with respect to the magnetic field

$$\frac{\mathrm{d}a^2[|\Psi(F_e^{\pm}, m)\rangle, |\Psi(F_g^{\mp}, m)\rangle, 0]}{\mathrm{d}B} = 0. \tag{3.23}$$

Equation (3.23) has the exact same solution as the one given in eq. (3.21). We will call quantities $a[|\Psi(F_e^{\pm}, m)\rangle, |\Psi(F_g^{\mp}, m)\rangle, 0]$ and $a[|\Psi(F_e^{\pm}, m)\rangle, |\Psi(F_g^{\pm}, m)\rangle, 0]$ pair-modified transfer coefficients, and the corresponding transitions will be called pair-transitions. As one can notice, cancellations occur only for transitions obeying $\Delta F = F_e - F_g = 0$ and maximum values take place when $\Delta F = F_e - F_g = \pm 1$. From now on, we use F to denote ground and F' to denote excited states, for clarity and to remain consistent with the rest of the thesis.

3.3 Analytical treatment of D_1 and D_1 - like transitions

In this section we will provide a complete analytical treatment of the D_1 line transition cancellations and maxima of all stable[2] and long-lived[3] alkali isotopes, as well as of the $5^2S_{1/2} \rightarrow 6^2P_{1/2}$ transition of both rubidium isotopes. Due to the lack of data, we do not study all alkali metal isotopes (e.g. Francium[4]). However, the theoretical considerations still hold.

---

[2] The following isotopes are stable: ^{23}Na, ^{39}K, ^{41}K, ^{85}Rb and ^{133}Cs.

[3] The half-life of ^{40}K is $1.248(3) \times 10^9$ years and that of ^{87}Rb is $49.23(22) \times 10^9$ years.

Isotope	I	Transition	Parameters	Reference
^{23}Na	$3/2$	D_1	$g_L = 0.99997613$	[5]
			$g_I = -0.00080461080(80)$	[6]
			$\zeta = 1771.6261288(10)$ MHz	[6]
			$\varepsilon = 188.697(14)$ MHz	[144, 145]
^{39}K			$g_L = 0.99997905339670(14)^*$	
			$g_I = -0.00014193489(12)$	[6]
			$\zeta = 461.73(14)$ MHz	[146]
			$\varepsilon = 57.696(10)$ MHz	[144]
^{40}K	4		$g_L = 0.99997974531640(14)^*$	
			$g_I = 0.000176490(34)$	[6]
			$\zeta = -1285.87(35)$ MHz	[146]
			$\varepsilon = -155.31(35)$ MHz	[146]
^{41}K	$3/2$		$g_L = 0.99998039390246(13)^*$	
			$g_I = -0.00007790600(8)$	[6]
			$\zeta = 253.99(12)$ MHz	[6, 134, 146]
			$\varepsilon = 30.50(16)$ MHz	[146]
^{85}Rb	$5/2$	D_1	$g_L = 0.999\ 99354$	[3]
			$g_I = -0.00029364000(60)$	[6]
			$\zeta = 3035.7324390(60)$ MHz	[6, 147]
			$\varepsilon = 361.58(17)$ MHz	[147–149]
		$5^2S_{1/2} \rightarrow 6^2P_{1/2}$	$g_L = 0.99999354$	[3]
			$g_I = -0.00029364000(60)$	[6]
			$\zeta = 3035.7324390(60)$ MHz	[6, 147]
			$\varepsilon = 117.33(66)$ MHz	[150]
^{87}Rb	$3/2$	D_1	$g_L = 0.99999369$	[4]
			$g_I = -0.0009951414(10)$	[6]
			$\zeta = 6834.682610904290(90)$ MHz	[151]
			$\varepsilon = 814.50(13)$ MHz	[6, 148, 149]
		$5^2S_{1/2} \rightarrow 6^2P_{1/2}$	$g_L = 0.99999369$	[4]
			$g_I = -0.0009951414(10)$	[6]
			$\zeta = 6834.682610904290(90)$ MHz	[151]
			$\varepsilon = 265.12(66)$ MHz	[150]
^{133}Cs	$7/2$	D_1	$g_L = 0.99999587$	[2]
			$g_I = -0.00039885395(52)$	[6]
			$\zeta = 9192.631770$ MHz (exact)	[2]
			$\varepsilon = 1167.680(30)$ MHz	[152, 153]

Table 3.1 – Table of hyperfine structure constants and Landé factors for various isotopes and transitions. The values marked with an asterisk (*) are theoretical, computed using the exact formula[5] of Phillips [154] and the values for the isotopes of Audi et al. [155]. The most imprecise values (ε) are given in red cells.

In table 3.1 we recall all the atomic parameters used in the calculations with their uncertainties. As one can see, the most imprecise values, in general, are ε (excited state hyperfine splitting, in red in the table). For ^{39}K, ^{40}K and ^{41}K even the ground state splittings are not precisely known. These quantities have the biggest influence on the uncertainties of the calculated B-values (all the other numerical parameters are known with at least 10-digit precision). It should be noted that when the value of I is an integer (only for ^{40}K in this work), the values of ζ and ε take a minus sign to be in agreement with our notation. Part of these numbers can be found in appendix B. For further calculations, for the Bohr magneton and g_S spin Landé factor we used the values $\mu_B/h = -1.3996245042(86)$ MHz/G and $g_S = 2.00231930436256(35)$, respectively. The magnetic field values are calculated directly using eq. (3.21).

---

[4] Francium's most stable isotope, ^{223}Fr, has a half-life of 22 minutes. Less than 30 grams of it exist on Earth.

[5] We noticed that $1/m$ is missing in the second term of the exact formula for g_L in [154]

3.3.1 Sodium and potassium

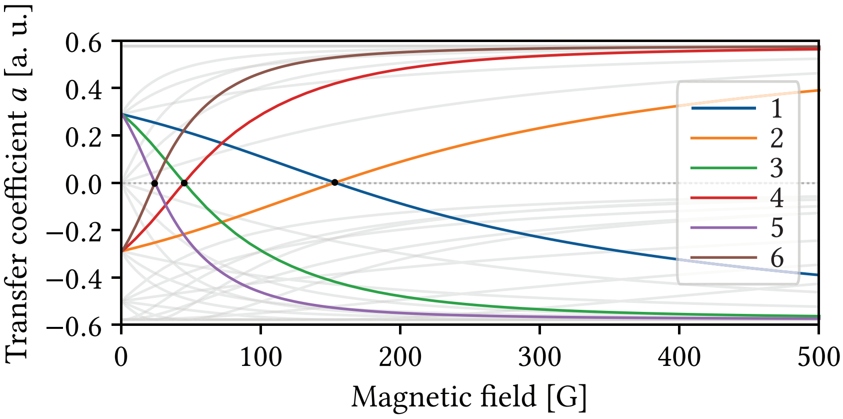

Figure 3.4 – π transitions ($m = -1$) of ^{23}Na, ^{39}K and ^{41}K exhibiting a cancellation. The labeling is given in table 3.2. All other transitions are represented in the background.

Isotope	Index	F	m	B [G]	B^* [G]
^{23}Na	1	1	-1	153.2007(86)	153.2007024(11)
	2	2			
^{39}K	3	1		44.991(10)	44.9915(37)
	4	2			
^{41}K	5	1		24.042(95)	24.0418(30)
	6	2			

Table 3.2 – Magnetic field values B and B^* cancelling $m = -1$ π transitions of ^{23}Na, ^{39}K and ^{41}K.

In fig. 3.4, we plot the ^{23}Na, ^{39}K and ^{41}K D_1 line π transitions showing a cancellation. As these three isotopes have the same nuclear spin $I = 3/2$, they share the same hyperfine manifold. Transitions will occur between $F = 1, 2$ and $F' = 1, 2$, and cancellations can be observed only for $m = -1$. In table 3.2 we present all the magnetic field values cancelling the D_1 transitions of ^{23}Na, ^{39}K and ^{41}K plotted earlier. The index (column 2) is consistent with fig. 3.4. The third column gives the angular momentum F of both ground and excited states, as cancellations appear only for $\Delta F = 0$. In the fourth column, we give the value of the magnetic quantum number of both ground and excited states (π transitions are such that $\Delta m = 0$). In the last columns, we present the values for which the transitions are canceled. These values are calculated using eq. (3.21), where B is obtained by taking into account all uncertainties, and B^* is obtained by ignoring the uncertainty on the excited state hyperfine splitting ε. The goal of these calculations is to show how precisely the magnetic field values could be determined if ε was more precisely known. The most crucial part is thus to improve the precision of ε. If this was done, these B^* values could become a new standard for the calibration of magnetometers as they depend only on fundamental physical constants. Potassium 40 (^{40}K) has a slightly weirder hyperfine structure since its nuclear spin is an integer. Transitions occur between $F = 9/2, 7/2$ and $F' = 9/2, 7/2$. Cancellations are observed for $m = 7/2, 5/2, 3/2$ and $m = 1/2$. The magnetic field values corresponding to these cancellations are presented in table 3.3, with the same formatting as before.

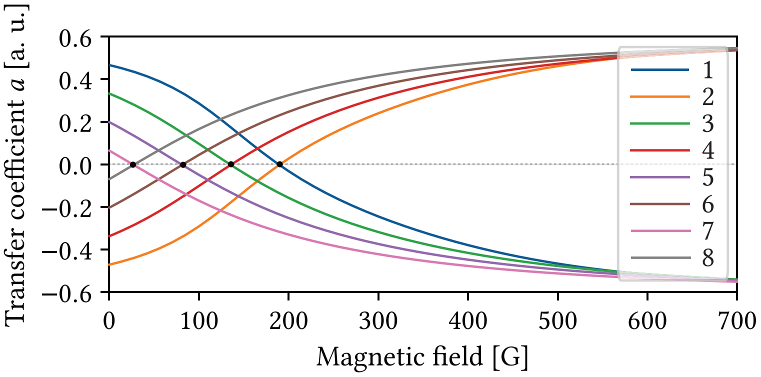

Figure 3.5 – ^{40}K D_1 line π transitions exhibiting a cancellation. Labeling is given in table 3.3. The dashed line is drawn to guide the eye.

Isotope	Index	F	m	B [G]	B^* [G]
^{40}K	1	9/2	7/2	190.20(33)	190.204(13)
	2	7/2			
	3	9/2	5/2	135.85(24)	135.8602(98)
	4	7/2			
	5	9/2	3/2	81.5(15)	81.5161(59)
	6	7/2			
	7	9/2	1/2	27.171(48)	27.1720(19)
	8	7/2			

Table 3.3 – Magnetic field values B and B^* cancelling π transitions of ^{40}K.

3.3.2 Rubidium

Let us now look at ^{85}Rb D_1 line π transitions. For this isotope, transitions will occur between $F = 2, 3$ and $F' = 2, 3$. The transfer coefficients a and transition intensities a^2 [eq. (3.20)] are plotted in fig. 3.6a-c for $m = -3, -2$ and $m = -1$. Cancellations appear for $m = -2$ (transitions 1-2) and $m = -1$ (transitions 3-4) and again correspond to $\Delta F = 0$. The pair behavior described in section 3.2.2 is clearly visible here. The π transitions corresponding to $\Delta F = \pm 1$ (transitions 5-8) reach their maximum intensity while the others get canceled. In fig. 3.6a, the modified transfer coefficients $a[|\Psi(F', m)\rangle, |\Psi(F, m)\rangle, 0]$ quantities) are depicted for $m = -2$ and $m = -1$ for the D_1 line of ^{85}Rb. Transitions numbered 5, 6, 7, and 8 have no cancellation and are nothing more than transfer coefficients between ground and excited states with $\Delta F = \pm 1$. The dashed line shows that transitions 1 and 2 are equal to zero for the same value of B. In fig. 3.6b we show the squared transfer coefficients a^2 (i.e. the transition intensities). Comparing the two figures, it immediately appears that the maxima of transitions 1-2 and 3-4 respectively coincide with the minima of transitions 5-6 and 7-8. The maximum intensity is that of the guiding transition 9 ($|3, -3\rangle \longrightarrow |3', -3\rangle$) whose intensity is constant as neither its ground nor excited state experiences magnetic-field induced mixing. The situation is similar albeit simpler for ^{87}Rb. As it has a smaller nuclear spin, ^{87}Rb has less magnetic sublevels and transition cancellations occur only for $m = -1$. Transitions 1-2 ($|1, -1\rangle \longrightarrow |1', -1\rangle$ and $|2, -1\rangle \longrightarrow |2', -1\rangle$ reach their minimum while transitions 3-4 ($|1, -1\rangle \longrightarrow |2', -1\rangle$ and $|2, -1\rangle \longrightarrow |1', -1\rangle$) reach their maximum. The transfer coefficients and transition intensities are visible in fig. 3.6b-d. The calculated values of B and B^* corresponding to the minima and maxima are given in table 3.4. We also give the equivalent values for $5^2S_{1/2} \longrightarrow 6^2P_{1/2}$.

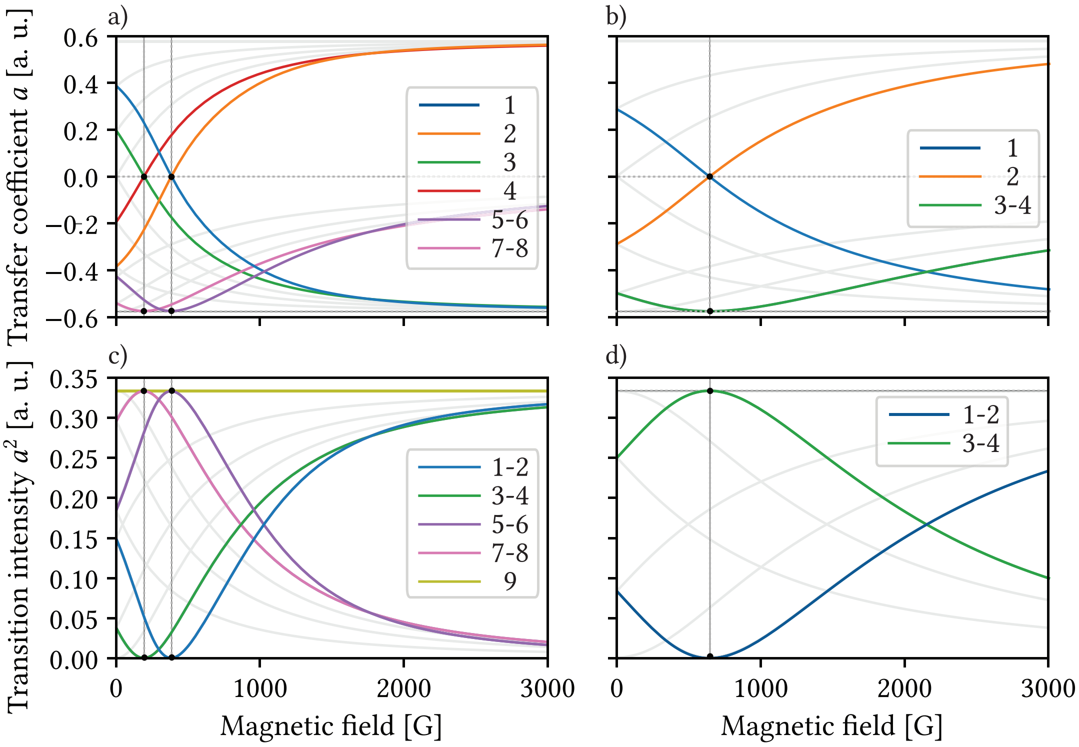

Figure 3.6 – Rubidium D_1 line π modified transfer coefficients (a-b) and transition intensities (c-d). a) ^{85}Rb, $m = -2$ and $m = -1$. b) ^{87}Rb, $m = -1$. c) ^{85}Rb, $m = -3, -2$ and -1. d) ^{87}Rb, $m = -1$. The dashed lines are drawn to guide the eye. All other transitions are represented in the background.

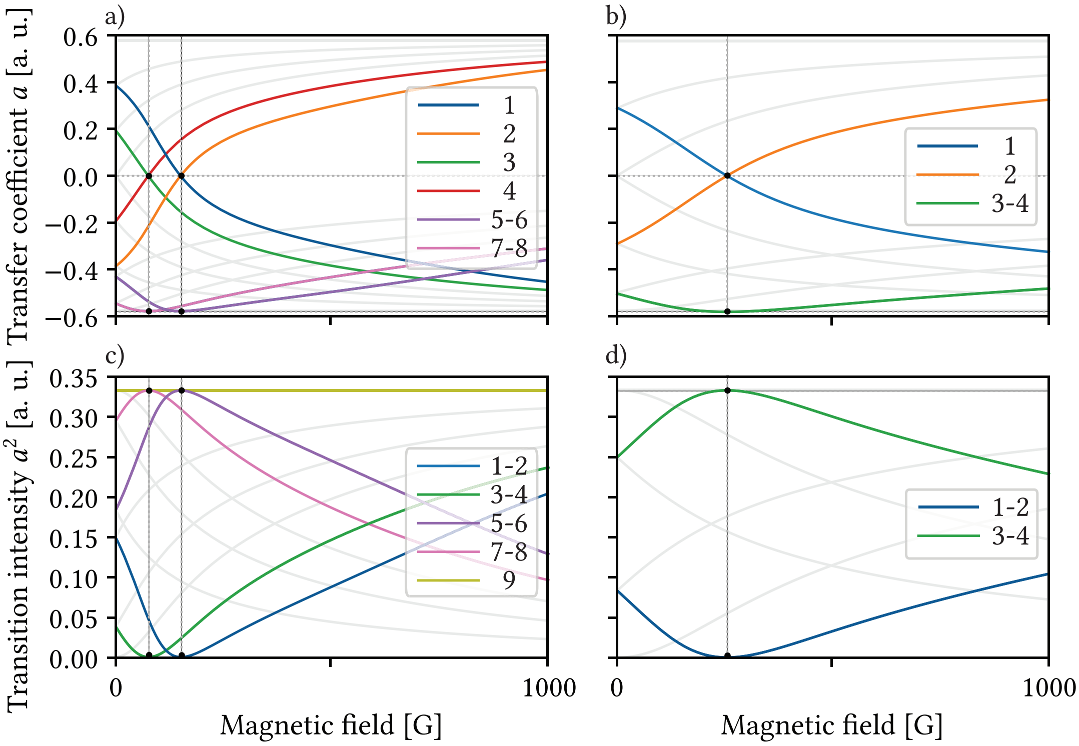

Figure 3.7 – Rubidium $5^2S_{1/2} \rightarrow 6^2P_{1/2}$ line π modified transfer coefficients (a-b) and transition intensities (c-d). a) ^{85}Rb, $m = -2$ and $m = -1$. b) ^{87}Rb, $m = -1$. c) ^{85}Rb, $m = -3, -2$ and -1. d) ^{87}Rb, $m = -1$. The dashed lines are drawn to guide the eye.

		Cancelled			Magnetic field		Maximised		
Isotope	Excited state	Index	F	m	B [G]	B^* [G]	Index	ΔF	m
^{85}Rb	$5^2P_{1/2}$	1	2	-2	380.73(13)	380.7362466(29)	5	-1	-2
		2	3				6	$+1$	
		3	2	-1	190.368(66)	190.3681233(15)	7	-1	-1
		4	3				8	$+1$	
	$6^2P_{1/2}$	1	2	-2	150.31(76)	150.31738954(20)	5	-1	-2
		2	3				6	$+1$	
		3	2	-1	75.15(38)	75.15869477(10)	7	-1	-1
		4	3				8	$+1$	
^{87}Rb	$5^2P_{1/2}$	1	1	-1	642.590(76)	642.5904743(48)	3	-1	-1
		2	2				4	$+1$	
	$6^2P_{1/2}$	1	1	-1	254.39(57)	254.398160387(80)	3	-1	-1
		2	2				4	$+1$	

Table 3.4 – Magnetic field values cancelling and maximizing several D_1 and $5^2S_{1/2} \rightarrow 6^2P_{1/2}$ π transitions of both Rb isotopes with their uncertainties.

3.3.3 Cesium

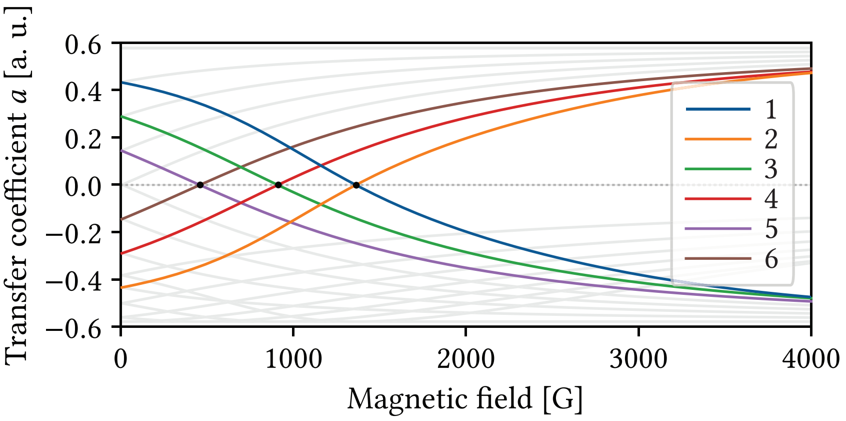

Figure 3.8 – ^{133}Cs D_1 line π transitions exhibiting a cancellation (for $m = -3$, $m = -2$ and $m = -1$. Labeling is consistent with table 3.5. All other transitions are represented in the background.

Isotope	Index	F	m	B [G]	B^* [G]
^{133}Cs	1	3	-3	1359.237(26)	1359.2372467(92)
	2	4			
	3	3	-2	906.158(17)	906.1581644(61)
	4	4			
	5	3	-1	453.0790(84)	453.0790822(31)
	6	4			

Table 3.5 – Magnetic field values cancelling D_1 transitions of ^{133}Cs with their uncertainties.

The isotope having the biggest Zeeman structure is ^{133}Cs with $F = 3, 4$ and $F' = 3, 4$. In that case, cancellations are observed for $m = -3$, $m = -2$, and $m = -1$. In fig. 3.8, modified transfer coefficients for all π transitions exhibiting a cancellation are plotted. The values corresponding to the transition cancellations are given in table 3.5. Since the ground state hyperfine splitting of ^{133}Cs is exactly known (table 3.1), the formula [eq. (3.21)] used to compute the magnetic field values yields more precision here.

3.3.4 Experimental feasibility

As an illustration of our calculations, we computed dSR spectra of ^{85}Rb (see chapter 2 for explanations and details regarding the simulations) for B = 300 G, B = 460 G and B = 380.73 G to highlight the cancellation of transition $|2,-2\rangle \longrightarrow |2,-2\rangle$ of ^{85}Rb D_1 line (table 3.4). In fig. 3.9, the peak labeled 1 is the one canceling for the mentioned value 380.73 G of B-field while, according to the theoretical model, the peak labeled 2 reaches its maximum for the same value. These spectra were obtained by simulating a dSR experiment performed with a nanocell of length $L = \lambda/2$ ($\lambda \simeq 794$ nm) at the typical temperature of 130 $^\circ C$ (corresponding to $N_{\mathrm{at}} \simeq 10^{13}$ cm^{-3}. These spectra clearly indicate the challenge of an eventual experimental determination of the magnetic field values discussed in this chapter. Since more transitions are considered here, we use a simpler labeling pattern described in fig. 3.10.

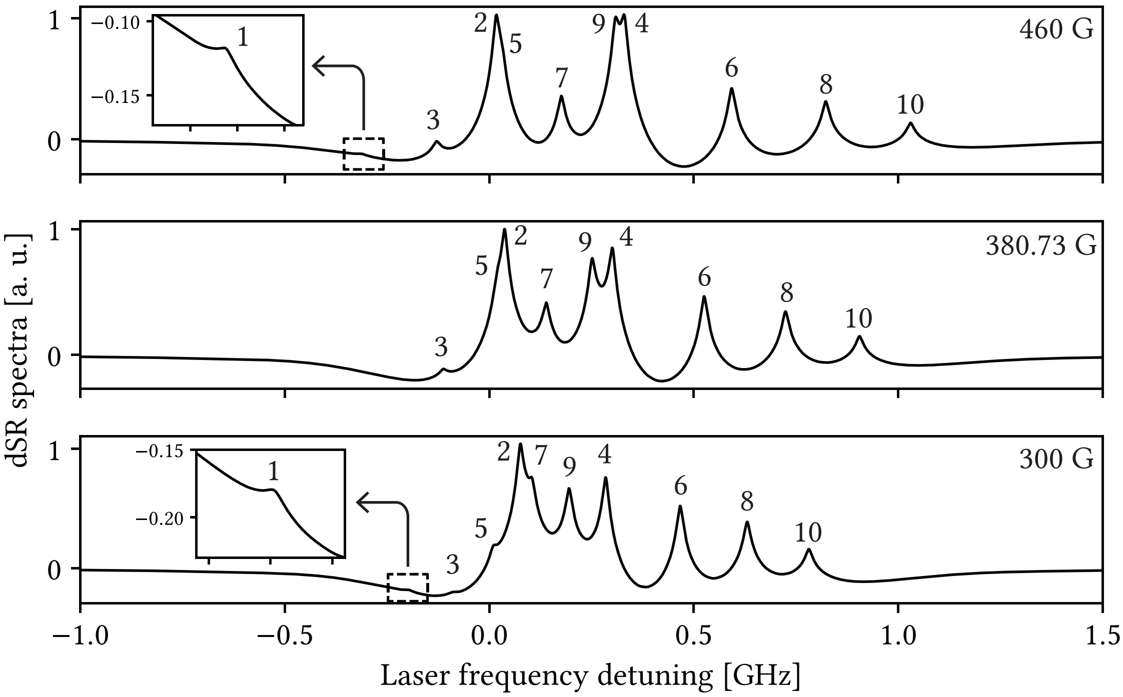

Figure 3.9 – dSR spectra of ^{85}Rb D_1 line $F = 2 \longrightarrow F' = 2, 3$ π transitions for different external magnetic field values. The parameters used for the simulation are $L = \lambda/2$, $P_L = 1$ μW, $T = 130$ °C. The dSR amplitudes are normalized to that of the second spectrum.

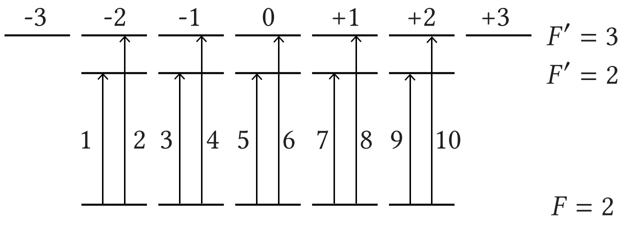

Figure 3.10 – Labelling of ^{85}Rb D_1 line $F = 2 \longrightarrow F = 2, 3$ π transitions.

The computation of transition cancellations in a magnetic field using the theoretical model described above is based on physical constants and fundamental parameters characterizing the atomic system, taken in the literature (see eg. table 3.1 and appendix B). Accurate measurement of the magnetic field at the point of optical transition cancellation can in principle help one to improve the precision on these parameters, notably of the frequency differences between the upper states (ϵ, α, β, γ) which currently have the biggest uncertainties. Achieving this would require a meticulously designed experimental

setup allowing to measure the applied magnetic field with an extremely high accuracy ($\simeq 10^{-10}$ G), making this a very challenging task.
Let us briefly analyze the requirements for the experimental setup and the characteristics needed to attain transition cancellation. This can be used, in particular, for precise calibration of magnetometers. In thermal atomic vapors, hyperfine transitions, especially those between magnetic sublevels of the hyperfine states, are Doppler-broadened and overlapped. To isolate a chosen individual transition, it must be frequency-separated from adjacent ones. High-resolution spectroscopic techniques providing sub-Doppler or Doppler-free frequency resolution, such as NC spectroscopy, can achieve this, as described in chapter 2. Additionally, the tuning range of a single-frequency continuous wave (CW) laser should be sufficiently large to track the frequency shift of the chosen transition in a B field. Inexpensive diode lasers and Rb vapor nanocells with a thickness of approximately $\lambda/2$ in a selective reflection (SR) configuration, providing a $\simeq 40$ MHz linewidth, or in a fluorescence configuration providing a $\simeq 60$ MHz linewidth, fulfill these requirements. These widths are adequate for the complete separation of individual transitions in magnetic fields above $\simeq 100$ G. Both techniques assure a linear response of the atomic medium [140, 156], unlike saturated absorption (SA) spectroscopy. Nanocells are also advantageous due to the extremely small size of the interaction region inside which the magnetic field can be considered uniform. The measurement of the maximum of a pair-transition [which is easier than directly measuring the cancellation value due to bigger signal to noise ratio (SNR) ratio] then yields the cancellation value.
Detection sensitivity is another crucial factor. The precision of transition cancellation is physically limited by the noise level, with the SNR being the figure of merit. The level of a typical SR signal varies within $\simeq 5\%$ of the incident light signal, whereas the fluorescence signal has a zero off-resonance background. Conventional signal acquisition and processing techniques enable reliable detection with an SNR up to 10 000. For selective reflection and fluorescence measurements, the magnitude of a canceled transition is estimated to be about 0.1% of the initial value. The signal magnitude can also be affected by the accuracy of setting and maintaining the NC thickness in the interaction region, which is manageable by controlling the radiation beam diameter and precise positioning of the beam using a micro-controlled translation stage.
The main limitations are expected to come from the precision of applying and measuring the B field. Two aspects need to be distinguished:

1. the accuracy of the magnitude and direction of the applied B field needed to cancel the transition
2. the precision of measuring this field.

A promising solution combining magnetic field control and measurement is optical compensation magnetometry [157]. Here, the interaction region, i.e., the vapor nanocell, is placed within a system of calibrated Helmholtz coils (three mutually perpendicular pairs). Coil currents are scanned according to a special algorithm controlled by the studied transition signal. Through successive approximations, a magnetic field value corresponding to the minimum atomic signal is achieved, and from the corresponding coil currents, the canceling field value is determined. This method allows for control and measurement of a B field with $\simeq 1$ mG accuracy.
Furthermore, during the measurements, the laser radiation frequency should be stabilized on the transition under study. This can be achieved by implementing feedback-based tunable locking of the radiation frequency to an atomic resonance with approximately 2 MHz accuracy [143], using an auxiliary setup with a second nanocell.
The realistic accuracy of applying and measuring the B field in the experiment remains less precise than the calculated values provided in sections 3.3 and 3.4. However, uncertainties in excited state frequency differences can be reduced by measuring the cancellation B field values for different transitions, where the uncertainties depend on a single frequency difference (for example, the last line of table 3.8). Besides more accurate determination of physical quantities, the results have practical applications in magnetometry and optical information processing. Continuous detection of an atomic signal while moving the NC across a highly nonuniform magnetic field enables high-contrast optical mapping of a B

field. Modulating the magnetic field around the transition cancellation point allows modulation of the amplitude of the optical atomic signal carrying optical information.

Finally, not all B field values canceling transitions are relevant for specific practical tasks. Another critical factor is the rate of variation of the transition probability with the B field around the cancellation value. The higher this rate, the more accurately one can determine the canceling B field value.

3.4 Numerical treatment of D_2 and D_2 like transitions of rubidium

We will now present a thorough investigation of the D_2 line and $5^2S_{1/2} \longrightarrow 6^2P_{3/2}$ transitions of ^{85}Rb and ^{87}Rb. In this general case, we were not able to derive formulas describing the magnetic field values. We will provide numerical values obtained by using Newton's method[6], carefully observing the change of sign in $a[|\Psi(F', m')\rangle\,; |\Psi(F, m)\rangle\,; q]$ to ensure the nullity of the transition intensities. To ensure this procedure is reliable, we performed the same analysis on the transitions presented in the previous section and compared the results with the analytical results obtained for 2×2 matrices. Both methods are in excellent agreement, with 10^{-12} adequacy. It is therefore reasonable to use the same procedures to compute cancellations of the $5^2S_{1/2} \longrightarrow 6^2P_{3/2}$ transitions, involving 3×3 and 4×4 Hamiltonian blocks[7]. We have studied all the possible hyperfine transitions (π , σ^+ and σ^-) of the D_2 line and $5^2S_{1/2} \longrightarrow 6^2P_{3/2}$ transition of ^{87}Rb and ^{85}Rb. We will provide a complete set of precise magnetic field values for both lines. Graphs are provided only for ^{87}Rb $5^2S_{1/2} \longrightarrow 6^2P_{3/2}$ line for the sake of readibility. The procedure is fully reliable and may be used for any alkali atom. An atlas summarizing all possible transition cancellations of D_1, D_2 and $6^2P_{3/2}$ lines of all alkali atoms would be a convenient tool for magnetometer calibration and is envisaged.

3.4.1 ^{87}Rb

π transitions

Isotope	Line	Splitting	Value	Ref	Isotope	Value	Ref
^{87}Rb	D_2	α	72.2180(40)	[158]	^{85}Rb	29.372(90)	[6, 148]
		β	156.9470(70)			63.401(61)	
		γ	266.6500(90)			120.640(68)	
	$6^2P_{3/2}$	α	23.744 (28)	[150]		9.802(25)	[150]
		β	51.445(25)			20.850(24)	
		γ	87.050(23)			39.265(23)	

Table 3.6 – Hyperfine splittings of the D_2 and $6^2P_{3/2}$ lines of both Rb isotopes

All the modified transfer coefficients exhibiting a cancellation are represented in fig. 3.11. In this case, transitions 3, 7, 10, and 16 are forbidden in the general case but none of them cross the x-axis. In this figure, all the curves vary according to the magnetic field since none of them correspond to transitions between two pure states. Among the 24 possible transitions, the transitions labeled 6, 9, 14, 17, and 20 have a cancellation. These transitions have a magnetic quantum number of either −1, 0 or +1, unlike for D_1 and $5^2S_{1/2} \longrightarrow 6^2P_{1/2}$ transitions where we only had $m = -1$ for ^{87}Rb. Here, each transition is canceled for a different value of B. However, experimental measurements could be more difficult in this case due to the proximity of certain values.

---

[6] An iterative root-finding algorithm providing approximations of the roots of real-valued functions. This method is implemented in Mathematica as the `FindRoot` function.

[7] In this cases, the eigenvalues of 3×3 and 4×4 matrices can be calculated with Cardano and Ferrari's formulas [135], which we were not able to simplify. Analytical formulas analogous to eq. (3.21) exist, but it is yet unclear whether they can be written in a compact, convenient form.

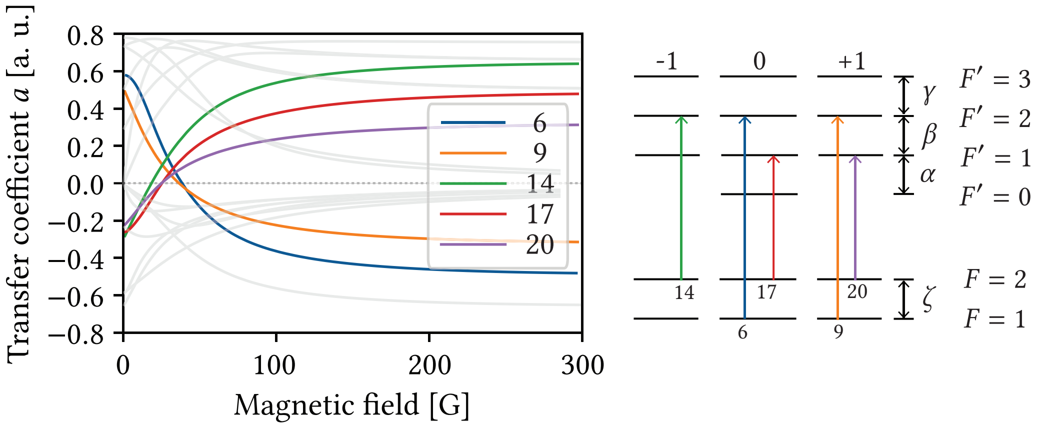

Figure 3.11 – $5^2S_{1/2} \longrightarrow 6^2P_{3/2}$ π transition modified transfer coefficients and scheme. For the sake of clarity, only the ones with a cancellation are labeled. As an indication, all other remaining transitions are plotted in the background.

Isotope	Line	Index	F	F'	m	B [G]	B^* [G]	ΔE_e
^{87}Rb	$6^2P_{3/2}$	6	1	2	0	38.21(19)	38.211312878(40)	α, β, γ
		9			+1	36.31(16)	36.318455634(38)	β, γ
		14	2		-1	17.895(66)	17.895382415(19)	
		17		1	0	24.77(13)	24.771185393(26)	α, β, γ
		20			+1	24.36(11)	24.361280734(26)	β, γ
	D_2	6	1	2	0	118.7058(51)	118.70586363(82)	α, β, γ
		9			+1	114.2418(50)	114.24183482(79)	β, γ
		14	2		-1	55.6964(22)	55.69646550(39)	
		17		1	0	77.5048(35)	77.50487199(54)	α, β, γ
		20			+1	77.2414(35)	77.24147013(54)	β, γ

Table 3.7 – B-values cancelling ^{87}Rb D_2 and $5^2S_{1/2} \longrightarrow 6^2P_{3/2}$ π transitions.

Table 3.7 shows the B-values for each cancellation, determined numerically with (third column) and without (fourth column) taking into account the uncertainty on the energies of the excited states. The last column, ΔE_e, shows which hyperfine splitting is involved in the calculation of the transition intensity. The numerical values are given in table 3.6.

σ transitions

All the modified σ^+ transfer coefficients are plotted and schematized in fig. 3.12a.
Eight σ^+ transitions (respectively labelled 1, 10, 13, 14, 15, 17, 18 and 20) are cancelled for a certain value of B. Transition 13 is a forbidden transition. The B-values are presented in table 3.8. Note the important number of cancellations compared to the case of $5^2S_{1/2} \longrightarrow 6^2P_{1/2}$ where no cancellation could be observed for $\sigma^\pm$. We notice that the three B-values of transitions 1, 10, and 13 have much bigger uncertainties than the others. For transition 20, we were able to exhibit the following analytical formula (among all these transitions it is the only one where Hamiltonians are of maximum 2×2 dimension):

$$B = -\frac{1}{\mu_B} \frac{4\gamma\zeta[3g_I(\gamma - \zeta) + 2\zeta g_L + g_S(\zeta - 3\gamma)]}{c_1 c_2} \tag{3.24}$$

where we denoted $c_1 = 6\gamma g_I - 3\zeta g_I + 2\zeta g_L - 6\gamma g_S + \zeta g_S$ and $c_2 = 2\gamma g_I - 3\zeta g_I + 2\zeta g_L - 2\gamma g_S + \zeta g_S$. This formula provides a B-value for the cancellation $B = 64.133588295$ G (all uncertainties ignored) showing the theory to be in perfect agreement with the simulation.

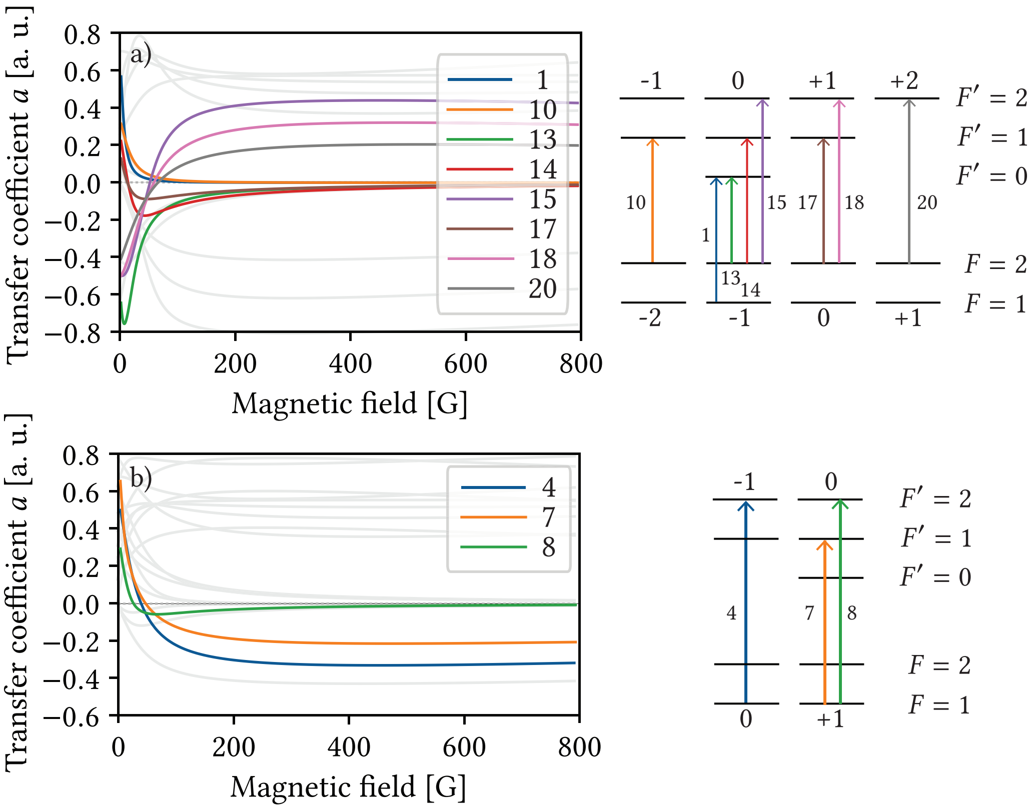

Figure 3.12 – $5^2S_{1/2} \longrightarrow 6^2P_{3/2}$ $\sigma^{\pm}$ modified transfer coefficients and scheme. a) σ^+, b) σ^-. For the sake of clarity, only the ones with a cancellation are labeled.

Isotope	Line	Index	F	F'	m	B [G]	B^* [G]	ΔE_e
^{87}Rb	$6^2P_{3/2}$	1	1	0	-1	524(68)	517.98168965(55)	α, β, γ
		10	2	1	-2	633(45)	630.07368077(67)	β, γ
		13		0	-1	606(45)	603.37498565(64)	α, β, γ
		14		1		12.219(77)	12.219830989(13)	
		15		2		50.30(20)	50.306012284(52)	
		17		1	0	11.259(66)	11.259065240(12)	β, γ
		18		2		57.11(20)	57.111350606(60)	
		20		2	+1	64.13(20)	64.133588295(68)	γ
	D_2	1	1	0	-1	1595.84(93)	1595.846039(12)	α, β, γ
		10	2	1	-2	1792.8(1.2)	1792.854752(13)	β, γ
		13		0	-1	1762.3(1.7)	1762.305097(13)	α, β, γ
		14		1		37.7187(20)	37.71876912(27)	
		15		2		157.6244(63)	157.6244550(11)	
		17		1	0	35.0323(19)	35.03235682(25)	β, γ
		18		2		183.1469(71)	183.1469403(13)	
		20		2	+1	211.1182(80)	211.1182479(15)	γ

Table 3.8 – Magnetic field values cancelling ^{87}Rb D_2 and $5^2S_{1/2} \longrightarrow 6^2P_{3/2}$ σ^+ transitions. The most imprecise values are given in red cells.

Isotope	Line	Index	F	F'	m	B [G]	B^* [G]	ΔE_e
^{87}Rb	$6^2P_{3/2}$	4	1	2	0	36.32(16)	36.320508551(38)	β, γ
		7		1	+1	44.13(31)	44.137763913(46)	α, β, γ
		8	1	2		23.01(18)	23.016986486(24)	
	D_2	4	1	2	0	114.3072(50)	114.30723113(80)	β, γ
		7		1	+1	140.8256(71)	140.82560775(98)	α, β, γ
		8	1	2		71.9264(47)	71.92641933(50))	

Table 3.9 – Magnetic field values cancelling ^{87}Rb $5^2S_{1/2} \longrightarrow 6^2P_{3/2}$ σ^- transitions.

The modified transfer coefficients corresponding to σ^- transitions are represented in fig. 3.12b. Since canceled transitions involve 3×3 or 4×4 blocks, we do not derive any analytical formula although it should be possible based on Ferrari and Cardano's formulas.

Among all transitions, three get cancelled (transitions 4, 7 and 8, corresponding to respectively $m_{F_g} = 0, +1, +1$) for precise values of B. Unlike before, no transition starting from $F_g = 2$ is canceled. The magnetic field values canceling the transitions are given in table 3.9. We will now present numerical data obtained for all $5^2S_{1/2} \longrightarrow 6^2P_{3/2}$ transitions of ^{85}Rb.

3.4.2 ^{85}Rb

Hereafter we present all the $5^2S_{1/2} \longrightarrow 6^2P_{3/2}$ and D_2 transitions of rubidium 85 which show a cancellation and their associated B-values. The ^{85}Rb D_2 and $6^2P_{3/2}$ lines are much more complicated systems than the ^{87}Rb D_2 and $6^2P_{3/2}$ lines, with large total atomic angular momentum (F) numbers. For the sake of clarity, we will not show any scheme or transfer coefficients concerning transitions since 116 transitions are possible in total. We present only tables where magnetic field values that cancel certain transitions are indicated. As one can notice, for the ^{85}Rb D_2 line, the frequency differences between the excited states are smaller than in the case of the ^{87}Rb D_2 line. Because of that, the values of the B field that cancel certain transitions are generally smaller than the B field values obtained in the case of ^{87}Rb. One may notice that some of the magnetic field values are quite big. Accordingly, the uncertainties of these values are big too. There are no such results for ^{87}Rb. In some cases, transitions can exhibit two cancellations. In this table, red cells indicate values for which the uncertainty is relatively big. These values correspond to asymptotic cancellations where the transition intensity variation is almost flat.

3.5 Conclusion

In the first two parts of this work (sections 3.2 and 3.3), we have studied the D_1 and $5^2S_{1/2} \longrightarrow 6^2P_{1/2}$ lines of all stable alkali isotopes. For specific values of the applied external magnetic field, some π transitions (this behavior does not occur for σ transitions in this case) exhibit a cancellation, ie. their intensity reduces to zero, while others reach their maximum intensity. We have determined an analytical formula allowing us to calculate these "roots". We have calculated all the transition-canceling B-values using two different methods. In the first method, all the physical parameters involved in the calculation are kept with their uncertainties. The precision is strongly affected by the uncertainty of the excited state frequency differences. In the second method, the excited state frequency differences uncertainties were not taken into account.

In the second part [section 3.4], we dressed an overview of transitions cancellations in the D_2 and $5^2S_{1/2} \longrightarrow 6^2P_{3/2}$ lines of Rb. In this case, transitions occur between strongly mixed states (the Hamiltonian blocks of the excited state are 3×3 or even 4×4) thus we were not able to determine a single formula like before. Only some hints of a formula were obtained in very specific cases. We have determined the magnetic field values using numerical methods tested against the analytical results. Excellent agreement (10^{-10}) was obtained, ensuring the reliability of the determination even when no formula can be found. There are several important reasons for determining these values with high precision. Firstly, highly

q	F	F'	m	Line	B [G]	B^* [G]	Line	B [G]	B^* [G]
σ^-	2	3	-1	$6^2P_{3/2}$	14.972(15)	14.972413447(12)	D_2	46.630(40)	46.63046914(32)
		4			5158(27)	5158.554086(13)		4718(20)	4718.168407(41)
		2	0		16.224(22)	16.224059190(13)		50.440(68)	50.44005212(34)
		3			10.393(14)	10.3937170637(80)		32.361(41)	32.36112827(22)
		3			4807(24)	4807.443620(13)		4354(19)	4354.588882(38)
		2	+1		16.708(28)	16.708656930(13)		51.930(93)	51.93093445(35)
		3			9.456(17)	9.4569409901(74)		29.726(51)	29.72652541(20)
		3			4467(22)	4467.802090(12)		4005(19)	4004.977769(35)
		2	-2		16.853(33)	16.853016860(14)		52.27(12)	52.27464320(36)
		3			8.759(18)	8.7592563674(69)		27.764(58)	27.76483242(19)
		3			4139(22)	4139.600083(11)		3669(21)	3669.632908(32)
q	F	F'	m	Line	B [G]	B^* [G]	Line	B [G]	B^* [G]
π	3	3	−2	$6^2P_{3/2}$	10.3043(87)	10.3043976319(79)	D_2	31.977(23)	31.97774839(22)
	2	2	-1		2.2199(46)	2.2199898843(17)		6.565(17)	6.565192522(44)
	2	3			14.860(17)	14.860250029(12)		48.463(58)	48.46368819(33)
	2	4			6271(30)	6271.265407(16)		5686(29)	5686.364269(49)
	3	2			11.416(14)	11.4168589034(88)		35.228(43)	35.22828802(24)
	3	3			4.1621(39)	4.1621397468(32)		12.811(11)	12.811030753(85)
	2	3	0		15.369(18)	15.369857179(12)		47.491(54)	47.49141288(32)
	2	4			6603(33)	6603.849559(17)		6013(29)	6012.951766(52)
	3	2			11.334(14)	11.3343927931(88)		35.218(43)	35.21852774(24)
	2	3	+1		15.812(19)	15.812955622(12)		46.336(49)	46.33622671(31)
	2	4			6942(36)	6942.545196(18)		6345(29)	6345.448972(54)
	3	2			11.147(14)	11.1479877220(88)		34.945(40)	34.94502121(24)
	2	3	+2		14.322(16)	14.322575163(11)		45.099(42)	45.09972813(31)
	2	4			7285(40)	7285.070415(19)		6681(30)	6681.226747(57)
	3	2			10.953(13)	10.9539851230(87)		34.689(33)	34.68962622(24)
q	F	F'	m	Line	B [G]	B^* [G]	Line	B [G]	B^* [G]
σ^+	3	2	−3	$6^2P_{3/2}$	96.22(53)	96.220676416(72)	D_2	278.3(1.4)	278.3151250(19)
	2	1	-2		63.40(50)	63.398936275(50)		180.9(1.5)	180.9519212(13)
	3	1			87.42(52)	87.425519697(67)		254.1(1.3)	254.1070281(17)
	3	2			5.5486(85)	5.5486439413(42)		16.798(26)	16.79814373(12)
	3	3			20.228(20)	20.228037283(16)		62.626(59)	62.62663916(42)
	2	1	-1		56.18(53)	56.182412663(44)		156.9(1.6)	156.9842182(11)
	3	1			79.54(49)	79.538277943(62)		231.6(1.3)	231.6749004(16)
	3	2			5.2424(79)	5.2424910523(40)		15.983(23)	15.98380527(11)
	3	3			23.044(21)	23.044654730(18)		72.575(61)	72.57573219(49)
	2	1	0		50.02(54)	50.018924381(39)		137.2(1.6)	137.21112478(91)
	3	1			72.46(47)	72.459280144(56)		211.1(1.3)	211.1105805(15)
	3	2			4.9968(73)	4.9968609804(39)		15.337(20)	15.33734519(11)
	3	3			26.036(21)	26.036555825(21)		83.643(63)	83.64378929(57)
	3	2	+1		4.7932(69)	4.7932030491(38)		14.808(18)	14.80813301(10)
	3	3			29.242(21)	29.242109204(24)		96.085(66)	96.08519850(66)
	3	3	+2		32.693(22)	32.693414753(27)		110.162(71)	110.16208826(76)

Table 3.10 – Magnetic field values cancelling ^{85}Rb D_2 and $5^2S_{1/2} \longrightarrow 6^2P_{3/2}$ σ^-, σ^+ and π transitions. The most imprecise values are given in red cells.

sensitive magnetometer calibration requires reliable standards, and these values would serve as excellent standards for atomic systems because they are independent of external conditions or parameters. Secondly, eq. (3.21) provides an exact theoretical expression for the B-values that cancel the transitions, based on fundamental quantities such as energy differences, Landé factors, Bohr magneton, nuclear spin value, and quantum numbers. Therefore, accurately determining these B-values experimentally can lead to improvements in the precision of these fundamental quantities.

Experimentally, it is more challenging to measure small signals precisely compared to larger ones due to the presence of noise. Consequently, direct measurement of transition cancellations is a challenging task. Since smaller peaks have a lower signal-to-noise ratio than larger peaks, it is more effective to measure peaks with higher intensity. Finding the magnetic field magnitude at which the transition intensity is at its peak will indicate a pair-transition cancellation value. To achieve this, we will calculate the derivative of the intensity with respect to the magnetic field around the maximum value. Although the change in transition intensity may be gradual, the point where the slope of the derivative changes sign will precisely indicate the B value at which the pair transitions reach their minimum. This problem requires the use of sub-Doppler spectroscopic methods such as NC spectroscopy, in which the applied magnetic field can be considered to be uniform.

However, in the experiments it is always more complicated to precisely measure small signals than big ones; thus the cancellation of transitions cannot be measured directly because of the existence of noise in any experiment. In other words, as for small peaks the SNR ratio is smaller than for higher peaks, so it is profitable to measure peaks with bigger intensity. Thus, as described in section 3.3.4 we may measure transitions (e.g., find maxima) that have a maximum value. If we can find a magnetic field magnitude for which the transition intensity is maximum, it will mean that we find a pair-transition cancellation value. The graph of the derivative of the intensity with respect to B should be calculated in the neighborhood of the maximum value, even though the change of transition intensity can be very smooth, as the change of sign of the slope of the derivative will give precisely the value for which it crosses the B-axis; thus will give the B-value for which the pair-transitions reach their minimum.

Chapter 4

Magnetometry with thin cells

In this chapter, we present two methods that allow to retrieve magnetic field values in various environments. Both methods rely on the analysis of spectra recorded using thin cells (either micrometric or nanometric) and may be used in challenging environments, for example, to measure fields with a strong gradient. The recorded spectra are in very good agreement with the theoretical predictions.

Contents

4.1 Introduction **75**
4.2 Experimental study: magnetometry with a ^{39}K nanocell **76**
  4.2.1 Spectroscopic nanocell filled with ^{39}K vapor 77
  4.2.2 Experimental setup 78
  4.2.3 Experimental results 78
4.3 Experiment: magnetometry with a ^{39}K microcell **82**
  4.3.1 Micrometric thin ^{39}K vapor cell 82
  4.3.2 Experimental setup 82
  4.3.3 Experimental results and discussion 83
4.4 Conclusion **85**

4.1 Introduction

Strong magnetic fields (0.1 – 10 kG) are necessary for the application of magneto-optical processes using alkali vapors [23, 67, 159–161]. In strong magnetic fields, which are determined from the conditions $B \gg B_0 = A_{\text{hfs}}/\mu_B$ where A_{hfs} is the magnetic dipole interaction constant of the state $^2S_{1/2}$ and μ_B is the Bohr magneton (the constants are given in [6, 162, 163]), the total electronic angular momentum J and nuclear spin I are decoupled [67]. This is called hyperfine Paschen–Back (HPB) regime [50, 67, 69]. In this regime the energy levels are best described by the magnetic numbers m_J and m_I. The B_0 values for ^{85}Rb, ^{87}Rb, and ^{133}Cs are approximately 700, 2400, and 1700 G, respectively. For $B \geq 2B_0$, the number of atomic transitions in the absorption spectrum decreases significantly. In the HPB regime, only 8 Zeeman transitions remain in the spectrum of the D_1 line of ^{39}K, while the probabilities of the 16 remaining Zeeman transitions tend to zero [68]. As shown for example in [61, 164, 165], taking the second derivative of the absorption spectrum of an atomic vapor allows us to obtain complete spectral resolution of the atomic transitions with correct reproduction of both frequency intervals and relative amplitudes. In this work, we will be using this procedure when recording absorption spectra.

In [166], an optical isolator based on a Rb vapor was described using $B \sim 6$ kG. In [167], interesting features were found in the saturated absorption (SA) spectrum of a Rb vapor in a strong magnetic field at the cross-over resonances. In [168], a four-wave mixing process was carried out in a 2 mm-size Rb cell at $B \sim 6$ kG. It was shown in [169] that at $B > 4$ kG, only 10 transitions are present in the transmission spectrum of the Rb D_1 line. In [170], a 40 μm-size Rb cell was used, in which the SA process was studied at $B \sim 6$ kG and the laser frequency was stabilized on low frequency-shifted atomic transitions.

Atomic potassium vapors are much less often used than Rb or Cs vapors since even at a moderate temperature of about 100 °C, the Doppler broadening reaches ~1 GHz. Moreover, the vapor density of K is very small at room temperature (around 5.8×10^8 cm^{-3}), therefore the hyperfine and Zeeman transition of ^{39}K transitions turn out to be fully hidden by the Doppler broadening when usual centimeter-long cells are used to study absorption or fluorescence processes. Laser spectroscopy of ^{39}K was investigated in a rather small number of works. Saturated absorption spectra of ^{39}K obtained with a 5 cm-long cell were experimentally and theoretically analyzed in [171, 172]. The magnetically induced dichroism of

^{39}K D_2 line in moderate magnetic fields was studied in [173]. Electromagnetically induced transparency (EIT) in a ^{39}K vapor was realized in [174], where an EIT-resonance with a linewidth significantly smaller than the natural width ($\sim$ 6 MHz) was formed. An efficient four-wave mixing process in potassium vapors was demonstrated in [175]. An optical resonance formed on N-type level configuration is described in [176]. SA spectroscopy of ^{39}K D_2 line was realized in [177].

For the formation of a strong magnetic field, permanent magnets made of a neodymium-iron-boron alloy are used, which create a magnetic field $B \sim 4$ kG near their surface, with a gradient of around 0.15 G/μm. In [56], selective reflection (SR) of laser radiation from a nanocell (NC) containing a Rb vapor was used to measure magnetic fields $>$ 1000 G. However, due to the large value of $B_0(^{87}\mathrm{Rb}) = 2400$ G the SR method was not convenient to use for the measurement of magnetic fields $<$ 1000 G, since the Zeeman components of ^{87}Rb and ^{85}Rb remain partially overlapped. Therefore, the development of methods for recording homogeneous and inhomogeneous magnetic fields in a wide range is of utmost importance.

It is promising to use ^{39}K for table-top vapor cell magnetometry setups as its characteristic magnetic field value $B_0 = 170$ G is substantially lower than the analogous value for Rb and Cs. Therefore, when ^{39}K atoms are placed in an external magnetic field, important specific features of the behavior of the Zeeman transitions, such as a strong change in their probability and a significant decrease of their number for $B \gg B_0$ (HPB regime) regime [6, 67–71]) can be easily observed by applying a magnetic field weaker by a factor of 10–15 than for Cs or Rb. (appendix B)

For a B_z-field $>$ 170 G, only 8 Zeeman transitions remain in the transmission spectrum of ^{39}K D_1 line (4 transitions for each circular polarization $\sigma^{\pm}$). Here, we will use these transitions to measure magnetic fields with a high spatial resolution. It is worth noting that transmission is more convenient than using SR since the resonances in the transmission spectrum have a symmetrical shape, whereas the SR technique gives rise to dispersion-like line shapes which are also sensitive to the NC thickness around $L = \lambda/2$ [77, 79, 140], as thoroughly described in chapter 1.

This chapter is divided into two main parts:

- In section 4.2, we present a method that allows to measure a magnetic field in the range of 0.1 - 10 kG with micrometer spatial resolution, which is relevant in particular for the determination of magnetic fields with large gradients (up to 3 G/μm). This method relies on the recording absorption spectra from a NC. We compare the experimental measurement with the theoretical results obtained using the models derived in chapters 1 and 2 and obtain very good agreement.
- In section 4.3, we present a similar method based on the recording of SA spectra from a microcell (MC) with a thickness of around 30 μm. The latter allows to form narrow atomic lines in the transmission spectrum without unwanted crossover (CO) resonances. This method is in principle easier to implement as manufacturing a MC is much easier than manufacturing the NCs used in our previous works. The downside of this method is a lower spatial resolution of 30 μm compared to the micrometer spatial resolution of the NC-based magnetometer.

The work presented in this chapter gave rise to the following publications:

- M. Auzinsh, A. Sargsyan, A. Tonoyan, C. Leroy, R. Momier, D. Sarkisyan, and A. Papoyan. *Wide range linear magnetometer based on a sub-microsized K vapor cell.* Appl. Opt. **61** (19) (2022), p. 5749
- A. Sargsyan, R. Momier, C. Leroy, and D. Sarkisyan. *Saturated absorption technique used in potassium microcells for magnetic field sensing.* Laser Phys. **32** (10) (2022), p. 105701

4.2 Experimental study: magnetometry with a ^{39}K nanocell

In fig. 4.1, we present the theoretical magnetic field dependence of the ^{39}K D_1 line Zeeman transitions intensities (probabilities) for σ^+- and σ^--polarized laser radiation. As ^{39}K and ^{23}Na share the same quantum numbers including nuclear spin, the behavior of ^{39}K is essentially the same as that of ^{23}Na

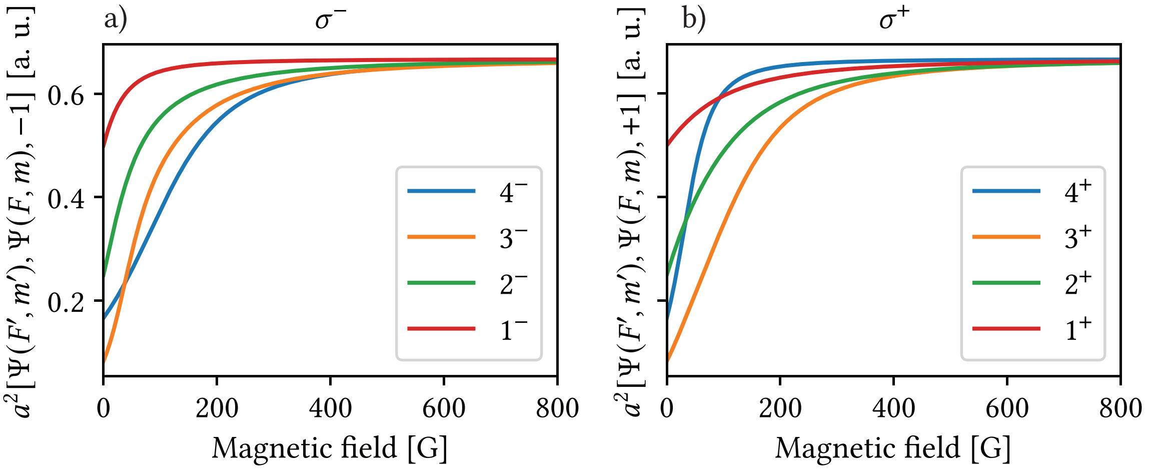

Figure 4.1 – Magnetic field dependence of the strongest (in the HPB regime) Zeeman transitions of the D_1 line of ^{39}K. a) σ^- transitions. b) σ^+ transitions. Transitions having a probability close to zero for $B > 100$ G are omitted for the sake of clarity as they are not used in this work.

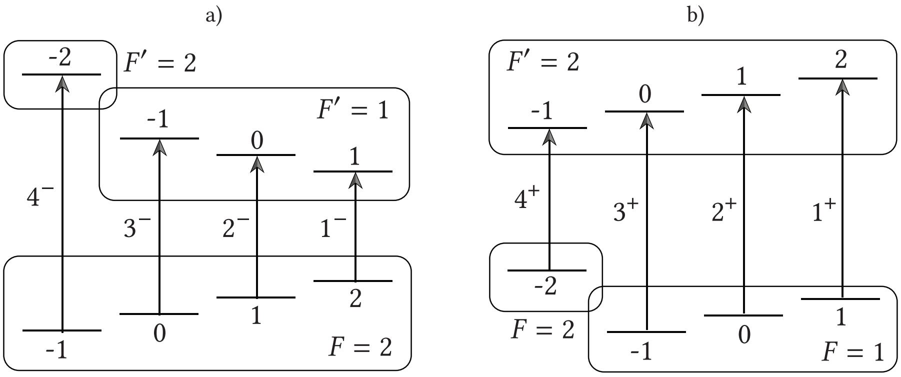

Figure 4.2 – Transition diagram corresponding to the labelling used in fig. 4.1. a) σ^- transitions. b) σ^+ transitions.

described in chapter 2. For relatively small magnetic fields[1], there are in total 24 atomic transitions for $\sigma^\pm$ radiation, meanwhile for $B > 2B_0$ only 8 transitions with approximately the same amplitudes and equidistant in frequency remain in the transmission/absorption spectra when interrogating the vapor with circularly polarized laser radiation (with respect to the magnetic field direction), meaning HPB regime is reached, as seen in fig. 4.1. The corresponding transitions are shown in fig. 4.2. The theory describing in detail the modifications of the Zeeman transitions probabilities in a static uniform magnetic field has been described in detail in several articles [57, 68], and a complete description was presented in chapter 2. The procedure used to compute absorption spectra of a NC was thoroughly described in chapter 1.

4.2.1 Spectroscopic nanocell filled with ^{39}K vapor

A specially fabricated NC with a relatively large area of thickness in the range of 50 – 400 nm was used. This type of cell is described in detail in chapter 1 and the same cell was used in [68]. The sapphire reservoir of the cell was filled with metallic (natural) K (93.26% ^{39}K, 0.01% ^{40}K and 6.7% ^{41}K) and heated to a temperature of 140 °C during the experiment, allowing to reach an atomic density $N \sim 7 \times 10^{12}$ cm^{-3}.

---

[1] Typically of the order of $B_0 = A_{\text{hfs}}/\mu_B \approx 170$ G, see appendix B for numerical data.

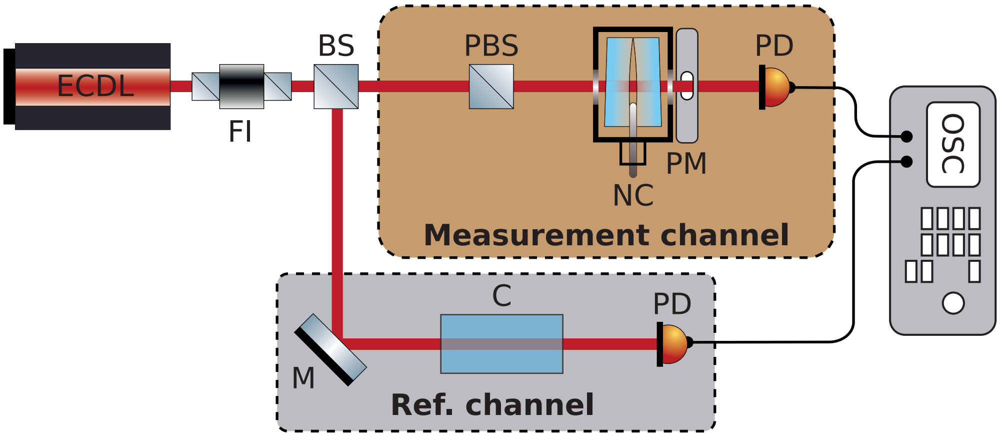

Figure 4.3 – Scheme of the experimental setup. ECDL: extended-cavity diode laser (λ = 770 nm), FI: Faraday isolator, NC: nanocell filled with K atoms. The thickness L of the vapor column can be adjusted in the range 120 – 390 nm. BS: beam splitter, PBS: polarizing beam splitter, C: auxiliary cm-long cell filled with K used to form a reference SA spectrum, PM: permanent magnet, M: mirror. **B** is oriented along the laser beam propagation direction ($\mathbf{B} = B_z\mathbf{e}_z$, $\mathbf{k} = k_z\mathbf{e}_z$), PD: photo-detectors, OSC: oscilloscope.

4.2.2 Experimental setup

The experimental layout is depicted in fig. 4.3. A VitaWave extended cavity diode laser (ECDL) with a wavelength of $\lambda = 770$ nm and a spectral linewidth of ~ 1 MHz [115] was used. As described earlier, the magnetic field was formed using a strong permanent magnet (PM) placed near the rear NC window and calibrated using a Hall effect magnetometer. The magnetic field can be varied by changing the distance between the PM and the window, as the cell is mounted on a micrometric stage. To form a frequency reference, part of the laser radiation was fed to a usual cm-size K cell to record zero-field SA spectra [171, 178, 179]. The signals were recorded by FD-24K photodiodes (PD), amplified and fed to a Tektronix digital oscilloscope (OSC).

4.2.3 Experimental results

As a first step, the NC thickness in the direction of laser beam propagation was chosen equal to half the resonant wavelength ($L = \lambda/2 = 385$ nm). The technique for measuring the thickness of an atomic vapor column in the NC is described in [180, 181] as well as in chapter 1. It has been demonstrated earlier that in this case (so-called $\lambda/2$ method), narrowing of atomic transitions (lines) in the absorption spectrum $A(\omega)$ of the NC occurs [61, 68, 79]. To obtain further narrowing of the atomic lines, we usually perform the second derivative (SD) of the absorption spectrum, $A''(\omega)$ [59, 61, 86, 165].

In fig. 4.4, the upper curve shows an experimental SD absorption spectrum of transitions $F = 1, 2 \longrightarrow F' = 1, 2$ of the D_1 line of ^{39}K for linearly polarized laser radiation (consisting of σ^+ and σ^- radiations) and a longitudinal B_z-field of 267 G. As mentioned earlier, the NC thickness is $L = 385$ nm, the reservoir temperature is 140 °C, and the laser power is 30 μW. There are four transitions that are excited by σ^- radiation located on the low-frequency wing of the spectrum, while the four transitions that are excited by σ^+ radiation are located on the high-frequency wing of the spectrum. The resonances are separated by nearly the same frequency interval ~ 150 MHz, which also remains the same for $B_z \gg B_0$. The middle curve shows a calculated SD absorption spectrum which is in very good agreement with the experimental spectrum. The lower curve shows the second derivative of a SA spectrum obtained with a usual cm-size K cell. In fig. 4.5a, experimental SD absorption spectra are shown for B_z increasing from 397 G to 794 G. As before, the two groups of σ transitions, highlighted by the brown and green boxes are clearly visible. Figure 4.5b shows calculated SD absorption spectra [the full width at half maximum (FWHM) is chosen to be 40 MHz] for the same conditions as in Figure 4.5a. The inaccuracy in the determination of strong B_z-fields is 5%, arising from the inhomogeneity of the magnetic field and the mm-dimensions of the measurement head of the Hall effect magnetometer. By measuring the frequency distance D between transitions labeled 4^+ and 4^- obtained by σ^+ and σ^- radiations and using the reference frequency interval of blue 461.7 MHz (obtained by SA, see fig. 4.4), it is possible to obtain a "calibration" curve which can be used to determine the magnitude of the B_z-field. The curve is presented in fig. 4.6a. Note that at $B = 10$ kG, we measure $D = 37$ GHz.

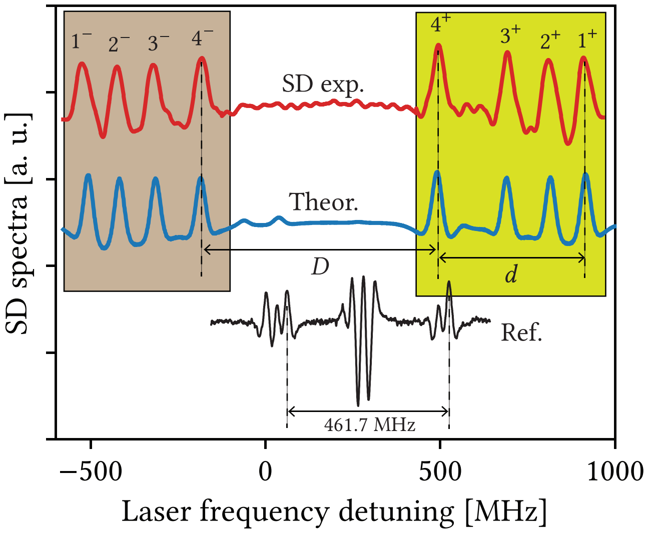

Figure 4.4 – ^{39}K D_1 line spectra recorded for $L = 385$ nm. Red curve (SD exp.): experimental SD absorption spectrum for σ^+ and σ^- radiation recorded for $B = 267$ G. Blue curve (Theor.): theoretical SD absorption spectrum. Lower curve: SD of a SA spectrum for reference. The transition labeling is consistent with fig. 2.22, σ^- and σ^+ transitions are shown in the brown and green regions respectively. D and d are defined in the text.

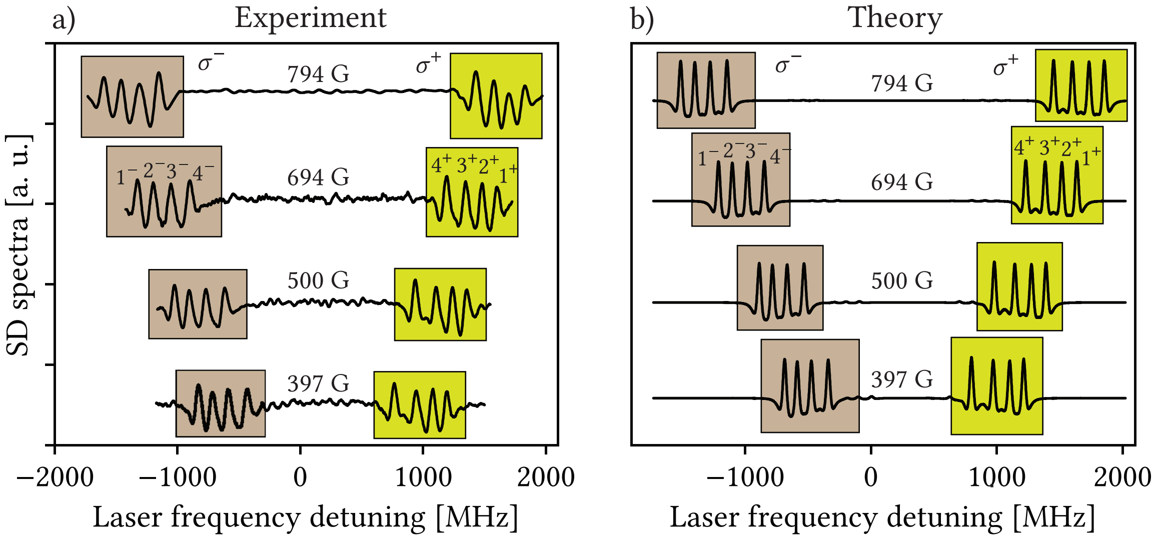

Figure 4.5 – ^{39}K D_1 line spectra recorded for $L = 385$ nm. a) Experimental SD spectra for σ polarized radiation recorded for $B = 397$, 500, 654 and 794 G. b) Theoretical SD spectra for the same values of B_z. The transition labeling is consistent with fig. 4.2, σ^- and σ^+ transitions are shown in the brown and green regions respectively.

A narrow-band distributed feedback (DFB) diode-laser such as the one described in [182] has a linear frequency scanning range of ~ 40 GHz. Such type of laser could thus be used for this method of B_z-field

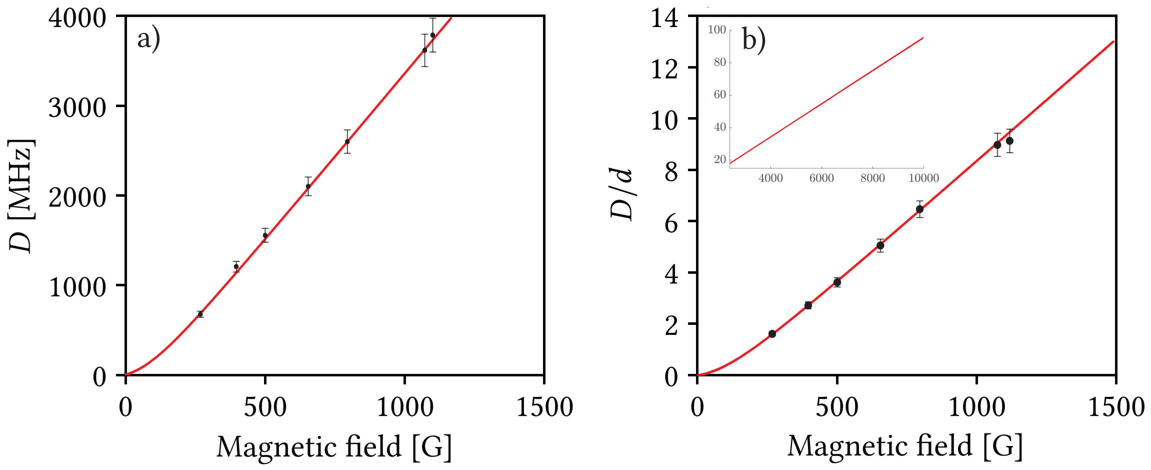

Figure 4.6 – a) Frequency difference D between transitions 4^+ and 4^- as a function of the magnetic field. Solid line: theory. Dots with error bars: experimental measurements. b) D/d as a function of the magnetic field. Solid line: theory. Dots with error bars: experimental measurements. In both cases, the inaccuracy is around 5%. The inset shows the theoretical ratio D/d with respect to the magnetic field up to $B = 10$ kG.

measurement in the range $0.1 - 10$ kG. The ECDL we used here has a small linear frequency scanning range of $\sim$ 4 GHz, making it only suitable for B_z-field measurements below 2.5 kG. This range of measurement for the determination of magnetic fields could be increased greatly with the use of a DFB laser. In [69, Fig. 2] we described a system that allows one to create a 10 kG magnetic field in a nanocell. Conveniently, the magnetic field measurements can also be carried out without using the frequency reference. This is made possible by measuring D and dividing it by the frequency distance d between atomic transitions 4^+ and 1^+ (shown in fig. 4.4a). The relationship D/d as a function of the magnetic field is shown in fig. 4.6b. The intervals D and d between atomic transitions are easily determined manually. A simple computer program substantially speeds up the data processing. It is intended for calculating B_z with the aid of a spectral analysis done on a computer (for this, the data displayed on the oscilloscope is quickly transferred to a computer). The program finds the significant maxima of the spectrum. The atomic transition with number 1^+, on the high-frequency wing, is singled out as the first one. Then each transition is assigned in descending order of coordinates. the fourth (4^+) and fifth (4^-) maxima, determines the distances (along the frequency axis) between the first and fourth maxima (d) and fourth and fifth maxima (D), and then calculates the ratio D/d. Further, to find B_z, the file of the dependence of the ratio D/d with respect to B_z is used (fig. 4.6b).

In [69], it is experimentally demonstrated that HPB regime is fulfilled for the D_1 lines of ^{85}Rb and ^{85}Rb up to $B = 7$ kG, and there is a good agreement with the theoretically calculated curves. In [183], it is experimentally demonstrated that HPB regime is fulfilled for the D_2 line of Cs atoms up to $B = 9$ kG, also showing a good agreement with the theory. For ^{39}K, the theoretically calculated ratio D/d with respect to B_z is presented in the inset of fig. 4.6b, which shows that the HPB regime is fulfilled up to 10 kG.

For some applications, it is important to record absorption spectra at smaller cell thicknesses. In fig. 4.7a, experimental SD absorption spectra are presented for B_z increasing from 440 G to 1110 G. The NC thickness is, in that case, $L = 120 \pm 5$ nm and the reservoir temperature is 155 °C. The laser power is 30 μW. The 8 transitions are still very well resolved. Note that for a fixed value of the atomic vapor density, there is a smooth decrease in absorption as L decreases from 385 nm to 120 nm without the appearance of any additional spectral feature that would pollute the measurements.

Apparently, $L = 120 \pm 5$ nm is the minimum acceptable NC thickness since, as shown in [56], for $L < 100$ nm a rapid broadening of the resonance lines occurs. This is due to atom-surface interaction between the vapor and the NC windows (so-called van der Waals interaction), which leads both to an asymmetric broadening of the resonance lines and to their frequency shift towards the low-frequency region of the spectrum [44, 110]. More details regarding atom-surface interactions at small NC thickness

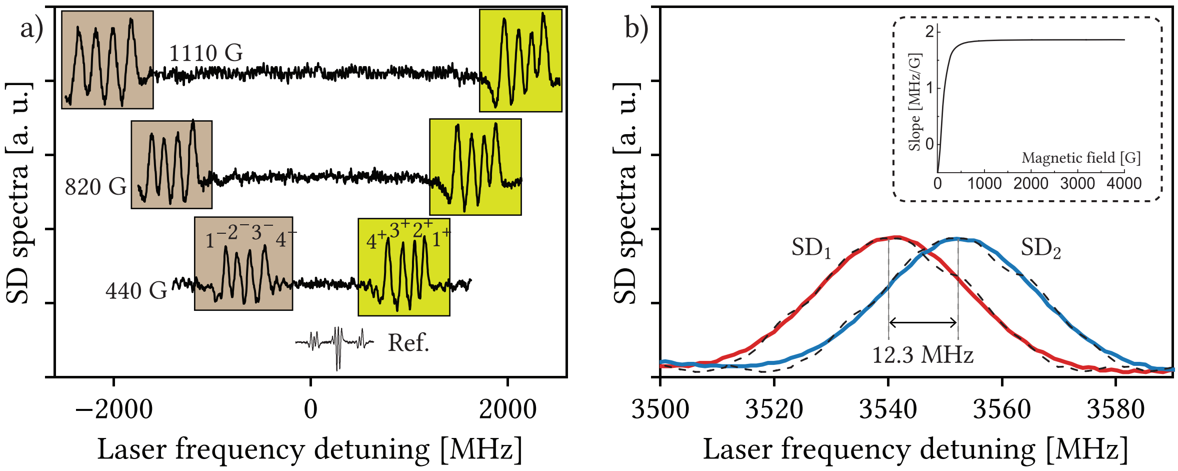

Figure 4.7 – ^{39}K D_1 line spectra recorded for $L = 120 \pm 5$ nm. a) SD absorption spectra for B_z increasing from 440 to 1110 G. Lower curve: SD of a saturated absorption spectrum for reference. Transition labeling is consistent with fig. 4.2, σ^- and σ^+ are shown in the brown and green regions respectively. b) The red curve has been calculated for $B_1 = 2000$ G and the blue curve for $B_2 = 2007$ G. Black curves depict experimental SD absorption spectra for B_1 and B_2, used to measure 3.3 G/μm gradient when the NC ($L = 120 \pm 5$ nm) is placed on a micrometer stage at $B_1 = 2000$ G and shifted by 2 μm relative to the initial position when B_2 becomes 2007 G. As can be seen, when moving the NC by 2 μm, the frequency shift is 12.3 MHz, which can be measured well. The inset shows the slope [MHz/G] of the $F = 1, 2 \rightarrow F' = 1, 2$ transitions.

can be found in chapter 1.

Reference [184] provides a description of a Stern-Gerlach type deflecting magnet, intended to deflect beams of paramagnetic nanoclusters, molecules, and atoms using a magnetic field with a gradient of 3.3 G/μm. Figure fig. 4.7b shows theoretical SD absorption spectra (red and blue solid lines with FWHM 80 MHz and fitted with a pseudo-Voigt profile) and experimental SD absorption spectra (presented by black dotted lines) that can be used to measure such a gradient if a NC with a thickness $L = 120 \pm 5$ nm is placed on a micrometer stage (magnetic field $B_1 = 2$ kG) and shifted by 2 μm with respect to the initial position (the magnetic field becomes $B_2 = 2006.6$ G). The red curve has been calculated for $B_1 = 2000$ G, and the blue curve has been calculated for $B_2 = 2006.6$ G. The black curves depict experimental SD absorption spectra for B_1 and B_2. Transition 4^+ was chosen for measurements. As can be seen from fig. 4.7b, when moving the NC by 2 microns (fields B_1 and B_2), the frequency shift is 12.3 MHz which can be measured well. Note that if the gradient is 2 times larger, then by moving the NC by 1 μm the frequency shift will also be 12.3 MHz. It is crucial to note that the use of the above-mentioned Hall effect magnetometer, of which the sensor part has an area of a few mm^2, will lead to large inaccuracies in the determination of magnetic fields with a large gradient. The advantage of our experimental setup compared to a regular Hall gauge magnetometer is the small size of the gauge, which is simply delimited by the interaction region and therefore the dimensions of the vapor column. The inset in fig. 4.7b shows the slope [MHz/G] of $F = 1, 2 \rightarrow F' = 1, 2$ transitions, which is ~ 1.9 MHz/G for $B > 1000$ G and remains nearly constant in strong magnetic fields.

Different types of magnetometers are described in the reviews [72, 73]. Particularly, magnetic sensors based on superconducting quantum interference devices (SQUIDs) are able to detect the human heart and brain magnetic fields on the order of 100 pT and 1 pT respectively, but they require cryogenics which prevents their miniaturization. Optical magnetometers based on nitrogen-vacancy centers in diamond are also sensitive to magnetic fields but require heavy temperature stabilization and microwave fields. Moreover, their operational range is limited by the ground state level anticrossing occurring at $B \sim 1024$ G [185]. Meanwhile, our experimental setup based on a ^{39}K nanocell is pretty simple and compact, and has the advantage of being immune to electric perturbations and thermal drift. This work shows the advantage of a magnetometer based on a ^{39}K NC in comparison with a commercial magnetometer based on the Hall effect for the measurement of inhomogeneous magnetic fields. Such type of NC-based magnetometer with high spatial resolution could be useful for example for high-gradient magnetic field mapping in nuclear tomography or magnetic field measurement in challenging environments.

4.3 Experiment: magnetometry with a ^{39}K microcell

The manufacturing of the NC used above and described in chapter 1 is technically a more complicated problem than the manufacture of a MC due to the necessity to provide wide regions where the gap thickness is of the order of the wavelength and/or half-wavelength [61], meanwhile to form the gap in the case of the MC, it is sufficient to place thin platinum strips (spacers) with a thickness $\sim$ 30 μm between the windows. As manufacturing this type of MC can cause some technical difficulties, details on the construction are presented [183, Fig. 2]. Such cells can be easily manufactured in many laboratories. Other constructions of MCs were presented for example in [186, 187].

4.3.1 Micrometric thin ^{39}K vapor cell

Analogously to the manufacturing process described in chapter 1, the windows of the MC were made of well-polished crystalline sapphire. To minimize birefringence, the windows were cut so that the C-axis is perpendicular to their surface. To provide a gap of thickness $L \sim 30$ μm, thin platinum stripes were placed between the inner surfaces of the windows. In the lower part of the windows, a hole was drilled into which a thin sapphire tube with an outer diameter of $\sim$ 2 mm and an inner diameter of 0.8 mm was inserted before gluing. "Molybdenum" glass glued to the vacuum system was soldered to the sapphire tube. Then, filling the cell with natural potassium is carried out the same way as for glass cells.

4.3.2 Experimental setup

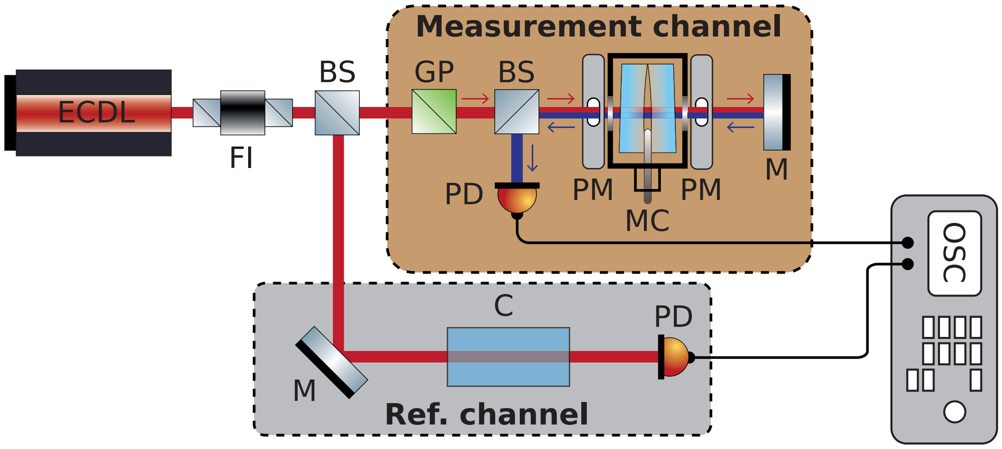

Figure 4.8 – Sketch of the SA experimental setup using a MC. ECDL: Extended Cavity Diode-Laser, $\lambda = 770$ nm. FI: Faraday Isolator, BS: beam splitter, GP: Glan polarizer, MC: Micrometric-Thin ^{39}K Cell. C: cm-long cell used to form a SA reference spectrum at $B = 0$. PM: permanent magnet, PD: photodetector, M: mirror, OSC: oscilloscope.

The experimental setup is depicted in fig. 4.8. SA spectrum are recorded using the MC filled with ^{39}K, whose thickness is 30 μm along the laser beam propagation direction. The MC was placed into an oven with two holes allowing passage of the laser radiation and was heated to $\sim$ 130 °C, providing an atomic density of $N \sim 2 \cdot 10^{11}$ cm^{-3}.
A VitaWave ECDL with a wavelength of $\lambda = 770$ nm and a spectral linewidth of 1 MHz [115] was used. The MC was placed between strong permanent magnets (PMs) with holes for the passage of

laser radiation. The PMs were fixed on nonmagnetic tables. The magnetic field in the MC was varied by changing the distance between the PMs. The magnetic field was calibrated using a Hall effect magnetometer. A fraction of radiation passing through the MC was directed precisely backward using a mirror (M) (in this case, the incident radiation serves as pumping, while the reflected radiation serves as probe radiation) to form a SA scheme. Neutral density filters (not shown in the scheme) were used to determine the optimum pumping and probe radiation powers required for the formation of narrow atomic velocity-selective optical pumping (VSOP) resonances and reaching their relatively large amplitude at a small spectral width. It has been shown in [170] that so-called CO resonances are almost absent in the saturated absorption spectrum of a Rb MC. This, together with the small spectral width of atomic transitions (~50 MHz), allows one to use the SA spectrum for the determination of frequencies and probabilities of individual transitions. As in the previous setup described in section 4.2, a fraction of the laser radiation was directed to a 1.5 cm-long ^{39}K cell in order to record a SA spectrum at $B_z = 0$.

4.3.3 Experimental results and discussion

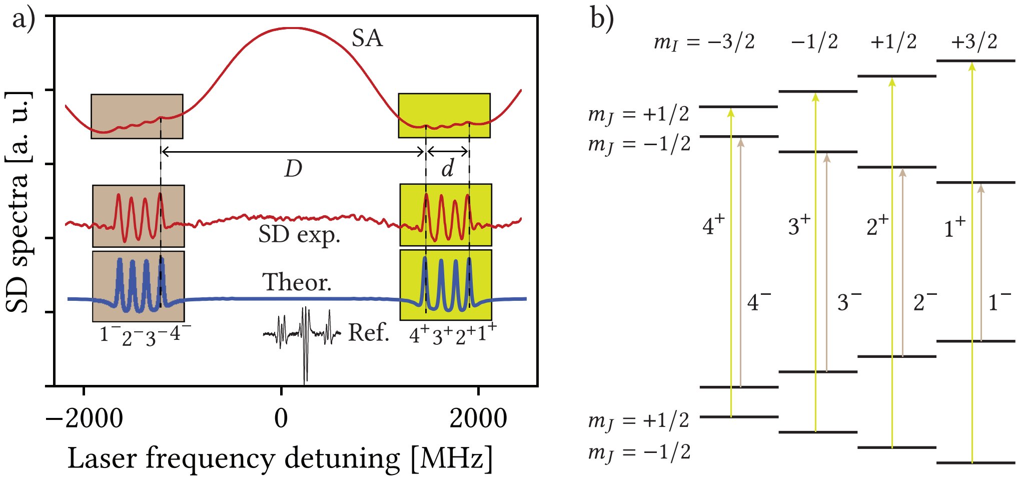

Figure 4.9 – a) Upper curve: experimental SA spectrum of the D_1 line of ^{39}K obtained using a MC and linearly polarized laser radiation when a longitudinal magnetic field $B = 822$ G is applied. Middle curve (SD exp.): SD of the SA spectrum (inverted for convenience). The σ^- and σ^+ transitions are represented in the brown and green boxes, respectively. Blue curve (Theor.): SD of a theoretical absorption spectrum. Bottom black curve: SD of a reference ($B = 0$) SA spectrum obtained with a 1.5 cm-long ^{39}K cell. b) Diagram depicting the 8 $\sigma^\pm$ transitions present in the HPB regime in the uncoupled basis $|m_I, m_J\rangle$. The transitions obey the selection rules $\Delta J = 0$, $\Delta m_I = 0$ and $\Delta m_J = \pm 1$ for $\sigma^\pm$ radiation. σ^+ and σ^- transitions are respectively shown in green and brown.

In the upper curve of fig. 4.9a, an experimental SA spectrum of ^{39}K D_1 line obtained using the MC for linearly polarized laser radiation and a longitudinal magnetic field $B = 822$ G is presented. The reservoir temperature is 130 °C and the laser power is ∼ 1mW. The middle curve is the SD of the SA spectrum. Since the condition $B \gg B_0$ required for HPB regime is nearly fulfilled, HPB regime is established. The curve labeled “Theory” is the SD of a theoretical absorption spectrum which correctly shows the frequency position of the 8 transitions and their amplitudes (the theoretical model is described in [57, 79] and chapters 1 and 2). Although the NC is filled with natural K (93.26% ^{39}K, 6.7% ^{41}K and 0.01% ^{40}K), we neglect the transitions of ^{40}K and ^{41}K in the theoretical calculations due do their very small influence on the spectra. This was reported for K D_2 line in [99, Sec. 3.3.3.]. The lower curve is the reference one (SD of SA spectrum) for $B = 0$ obtained with the 1.5 cm-long ^{39}K cell. All the possible σ^+ transitions labelled 1^+ to 4^+ (resp. σ^- transitions labelled 1^- to 4^-) in the uncoupled basis $|m_I, m_J\rangle$ are shown in green (resp. brown) in fig. 4.9b. All transitions obey the selection rules $\Delta J = 0$, $\Delta m_I = 0$, and $\Delta m_J = \pm 1$ for the $\sigma^\pm$ transitions. It is important to note that there are no unwanted CO resonances in the SA and

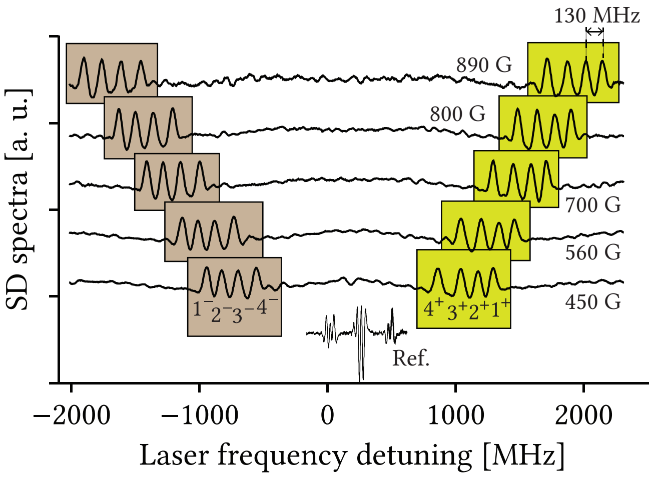

Figure 4.10 – SD of experimental SA spectra obtained using a MC filled with ^{39}K probed with linearly polarized laser radiation. The longitudinal magnetic field B_z is gradually increased from 450 to 890 G. Labelling of the transitions is consistent with fig. 4.9. The frequency distance between any two neighboring transitions is ~ 130 MHz, as calculated using eq. (4.1). Bottom black curve: SD of a reference ($B = 0$) SA spectrum obtained with a 1.5 cm-long ^{39}K cell.

SD spectra, while they are present in usual cm-long cells, as seen in the reference spectrum. These CO also split under the influence of a magnetic field, leading to undesirable overlapping with useful atomic resonances. They do not carry additional information relevant to our study and would only pollute the spectra [188]. Their absence is one of the key benefits of using a MC for magnetic field sensing.

The SD of experimental SA spectra obtained with the MC for linearly polarized laser radiation are presented in fig. 4.10, where the longitudinal magnetic field is gradually increased from 450 to 890 G. As before, the two groups of $\sigma^{\pm}$ transitions located on the low- and high-frequency wing of the spectra are visible. The lower curve is the reference spectrum for $B = 0$, and the spectra are shifted vertically for clarity.

In a strong magnetic field $B \gg B_0$, the energies of the lower and upper levels can be determined by the expression[2] [69]:

$$E_{|J,m_J,I,m_I\rangle} = A_{\text{hfs}} m_J m_I + \mu_B (g_J m_J + g_I m_I) B, \tag{4.1}$$

where A_{hfs} is the magnetic dipole interaction constant of the lower level $4^2S_{1/2}$ (~230.86 h·MHz) and upper level $4^2P_{1/2}$ (~27.77 h·MHz), and g_J and g_I are the total electronic momentum and nuclear momentum Landé factors, respectively. All the constants related to ^{39}K are presented in table B.2 (appendix B). The frequency spacing between any two neighboring transitions estimated with eq. (4.1) is

$$\Delta E = 0.5 A_{\text{hfs}}(4S_{1/2}) + 0.5 A_{\text{hfs}}(4P_{1/2}) = 129.3 \text{ MHz}. \tag{4.2}$$

The frequency distance ΔE ~130 MHz between two neighboring transitions agrees well with the experiment shown in fig. 4.10. The frequency slope of both groups of transitions is $s = \mp 4\mu_B/3 \approx \pm 1.86$MHz/G for $\sigma^{\pm}$ radiation respectively (chapter 2). The slope s is an asymptotic value to be reached at $B \gg B_0$. In a similar fashion as in section 4.2, measuring the frequency distance D between transitions labeled 4^+ and 4^- and dividing it by the frequency distance d between transitions 4^+ and 1^+ (as depicted in fig. 4.9) will allow to determine the magnitude of the B_z-field. The ratio D/d (experiment and theory) as a function of the magnetic field is presented in fig. 4.11. It should be noted that in this case the spatial resolution is bottlenecked by the dimension of the MC. A spatial resolution of 30 μm could be fulfilled. The ratio D/d was computed by averaging each time over five spectra to improve the accuracy. Further, D, d, and D/d are compared with theoretical calculations to estimate the value of B_z. The inaccuracy in

---

[2] This is a special case of eq. (2.35) derived in chapter 2 for $I = 3/2$ and $J = 1/2$.

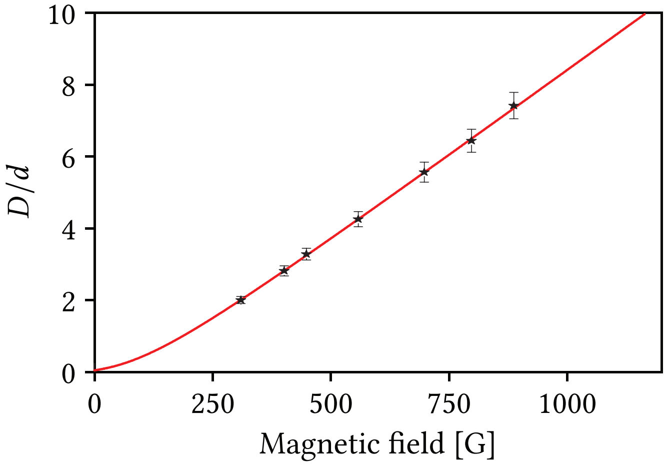

Figure 4.11 – Ratio D/d of the frequency intervals as a function of the magnetic field B_z. Stars with error bars: experimental measurements. Red line: theory. The inaccuracy is 5%.

the determination of D/d (and therefore B_z) is caused primarily by the nonlinear scanning of the ECDL lasers over a wide frequency range [115]. Here as well, the usage of a narrow-band DFB laser with a much bigger linear scanning range would allow one to use this method to determine magnetic fields in the range of 0.1 - 10 kG.

4.4 Conclusion

This chapter demonstrates the utility of using nanocells and microcells filled with ^{39}K for high spectral resolution table-top magnetometry. A notable advantage of ^{39}K is its small characteristic magnetic field value $B_0 \simeq 170$ G, the smallest among naturally abundant alkali metal isotopes. When HPB regime is reached, the absorption spectrum of linearly polarized radiation in a longitudinal magnetic field simplifies significantly: from 24 initial transitions to only 8, resulting in clean spectra that are easy to analyze. This greatly facilitates the measurement of magnetic fields using magnetometers based on these cells.

For the NC based magnetometer, two methods are presented for determining magnetic field magnitudes by recording the absorption spectra of atomic vapors within cells with thicknesses between 120 and 390 nm with and without calibration. This allows for the measurement of both uniform and strongly inhomogeneous magnetic fields across a wide range (0.1 - 10 kG). Unlike Cs and Rb atoms, which have numerous overlapping Zeeman transitions, ^{39}K atoms in a moderate magnetic field exhibit fewer transitions, enabling precise measurements of B_z below 1000 G. This precision makes the ^{39}K-based vapor cell magnetometers ideal for various applications including magnetic field mapping for free-electron lasers (which make use of strongly inhomogeneous magnetic fields), beam collimation in particle accelerators, metal detection, NMR or nuclear medicine. Most importantly, the small thickness (120 ± 5 nm) of the ^{39}K NC would enable the determination of large magnetic field gradients (of the order of 3 G/μm), useful for example in Stern-Gerlach-type experiments.

We also demonstrate the prospects of using ^{39}K MCs to study the peculiarities of the behavior of atomic levels in magnetic fields that are lower by a factor of 10-15 than what is needed to observe the same peculiarities for the Cs or Rb atoms. This is due to the high spectral resolution provided by the Saturation Absorption technique and particularly the absence of unwanted CO resonances in MCs (which are present in cm-long cells). These cells are much easier to manufacture than NCs and can be made following the recommendations given for example in [183]. The magnitude of the B_z-field in a wide range can also be retrieved with or without a frequency reference, albeit with a smaller spatial resolution of 30 μm is presented and can be carried out without using a frequency reference. In both cases, the experimental setups are relatively simple and require only one laser.

Several different types of magnetometers are described in the reviews [72, 73]. Modern state-of-the-art magnetometers now achieve excellent sensitivity but are focused on the measurement of extremely low magnetic fields in shielded environments. Optical magnetometers based on nitrogen-vacancy (NV) centers in diamond are extremely sensitive but require heavy temperature stabilization and a microwave coupling field, making them unusable in highly perturbed environments. Moreover, their operational range is affected by the ground-state level anti-crossing occurring at $B \sim 1024$ G [185]. Meanwhile, our atomic magnetometer scheme based on a ^{39}K microcell is simple and has the advantage of being immune to external perturbations and thermal drift. The advantage of our experimental setup compared to a regular Hall gauge magnetometer is the small size of the gauge which is given by the size of the vapor cell. Such a type of magnetometer with high spatial resolution could be useful in various fields such as nuclear medicine, NMR, and nuclear tomography.

Chapter 5

Coherent processes

In this chapter, we analyze two different coherent processes in short and long cells: EIT and N-resonances. Both resonances are all-optical and are great candidates for atomic frequency standards and laser frequency stabilization systems. We first study EIT resonances formed on three-level systems consisting of forbidden transitions of Cs, strongly shifted from the D_2 line transition frequency. We then perform a comprehensive analysis of the influence of buffer gas pressure on the contrast and linewidth of N-resonances in 0.8 cm long cells. Both resonances are also studied in an external magnetic field, and the results are compared with theoretical predictions.

Contents

5.1 Introduction 87
5.2 Formation of EIT resonances using "forbidden" transitions in the HPB regime 88
  5.2.1 Probabilities and frequency shifts of the MI transitions of Cs D_2 line 88
  5.2.2 Theoretical description of the EIT process 90
  5.2.3 Experimental setup 91
  5.2.4 Experimental results 92
5.3 Buffer gas influence on the formation of N-resonances 95
  5.3.1 Experiment 96
  5.3.2 N-resonances in a magnetic field 100
  5.3.3 Discussion 102
5.4 Conclusion 103

5.1 Introduction

As it was shown in chapter 2 as well as in several papers [55, 57–59, 167, 189, 190], the application of a strong magnetic field can significantly change the intensities of the Zeeman transitions. High interest has recently been focused on atomic transitions between ground and excited levels that satisfy the condition $F' - F = \Delta F = \pm 2$, so-called forbidden magnetically induced (MI) transitions [58, 59, 189].

MI transitions are of great interest because, over a wide range of magnetic fields, their probabilities can be much higher than the probabilities of usual ("allowed", satisfying the selection rule on F) transitions. It is important to note that the slope of the frequency shifts (obtained by diagonalizing the magnetic Hamiltonian chapter 2) as a function of the magnetic field B in strong magnetic fields can reach up to around 4 MHz/G, which is 3 times larger than in the case of ordinary transitions. Thus, the frequency shift of MI transitions in strong magnetic fields can reach several tens of GHz, which can be useful for working in higher frequency ranges, for example for the frequency stabilization of lasers on strongly shifted frequencies [18, 170].

It has been recently demonstrated that electromagnetically induced transparency (EIT) resonances (see appendix C and [75]) can be formed using a Λ-system made of $\Delta F = +2$ MI transitions only if both probe and coupling beams are σ^+-polarized. This statement was experimentally and theoretically verified for ^{87}Rb (MI transitions $F = 1 \longrightarrow F' = 3$) and ^{85}Rb (MI transitions $F = 2 \longrightarrow F' = 4$) [137, 191]. However, if the Λ-system is formed by MI transitions satisfying $\Delta F = -2$, then both probe and coupling radiation must be σ^--polarized in order to form EIT resonances. This statement was experimentally and theoretically verified for Cs $F = 4 \longrightarrow F' = 2$ MI transitions. This is a direct consequence of magnetically-induced circular dichroism [165].

Another type of resonances, so-called "N-resonances", share a majority of their characteristics with EIT resonances. They were first observed and studied by Zibrov et al. [192] and initially called *three-photon absorption resonances* or *three-photon EIT resonances* due to their resemblance with regular

EIT resonances. They result from a two-field (probe and coupling) three-photon absorption process involving a two-photon Raman transition combined with optical pumping (from the probe beam). N-resonances are promising candidates for small atomic frequency standards that can be realized with commercially available diode lasers [193–195], however, they cannot be observed in a nanocell (NC). This chapter is divided into two main parts:

- In section 5.2, we use for the first time the σ^+ $F = 3 \longrightarrow F = 5$ MI transitions of cesium as probe radiation to form EIT resonances in strong magnetic fields (1 - 3 kG) while the coupling radiation frequency is resonant with $F = 4 \longrightarrow F = 5$ σ^+ transitions. The experiment is performed using a NC ($L = \lambda$) filled with Cs vapor and a strong permanent magnet. The thickness of the vapor column is 852 nm, corresponding to the Cs D_2 line transition wavelength. Due to the large frequency shift slope of the MI transitions, it is possible to form high-contrast and strongly frequency-shifted EIT resonances. Preliminary calculations performed considering Doppler-broadened three-level systems in a NC are in reasonable agreement with the experimental measurements.
- In section 5.3, we study the formation of N-resonances in centimeter long cells. It was shown that N-resonances exhibit enhanced contrast and reduced linewidth when a buffer gas, typically Neon, is introduced in the alkali vapor cell. Despite extensive literature on the EIT process, research on N-resonances remains scarce. We use different centimetric vapor cells with varying buffer gas pressures, spanning from 0 to 400 Torr to investigate how these pressure conditions influence the contrast and linewidth of the N-resonance. Once the optimal pressure range is obtained, we examine the evolution of the resonance when an external magnetic field is applied and compare it with theoretical predictions.

The first part of this chapter gave rise to the publication of the following journal article:

- A. Sargsyan, A. Tonoyan, R. Momier, C. Leroy, and D. Sarkisyan. *Formation of strongly shifted EIT resonances using “forbidden” transitions of Cesium.* J. Quant. Spectrosc. Radiat. Transf. **303** (2023), p. 108582

The second part of this chapter has been submitted and is currently (as of June 2024) under review:

- A. Sargsyan, R. Momier, C. Leroy, and D. Sarkisyan. *Influence of buffer gas on the formation of N-resonances in rubidium vapors.* 2024. DOI: `10.48550/arXiv.2402.09184`. arXiv: `2402.09184 [physics]`. Pre-published

5.2 Formation of EIT resonances using “forbidden” transitions in the HPB regime

5.2.1 Probabilities and frequency shifts of the MI transitions of Cs D_2 line

In this work, we consider seven σ^+ MI transitions of Cs ($F_g = 3 \longrightarrow F_e = 5$, see fig. 5.1). The probabilities of these transitions increase highly in the range 0.3 - 3 kG and we used these transitions to form EIT resonances in strong B-fields. A NC filled with Cs vapor (thickness $L \approx 850$ nm, approximately the resonant wavelength of Cs D_2 line [2]) has been used. The advantages of using thin cells, including strong reduction of Doppler broadening, have been investigated in the previous chapters as well as in numerous papers [59, 61, 191].
The curves in fig. 5.2 were calculated using the theoretical model described in chapter 2. The block-diagonal (each block corresponding to a given value of the magnetic quantum number) magnetic Hamiltonian is built for each value of the magnetic field and then diagonalized in order to calculate the probability coefficients. This model was presented in several papers, e.g. [57, 58, 190]. The evolution of the probabilities of MI transitions (labeled 1 to 7, see fig. 5.1) with respect to the magnetic field B is shown in fig. 5.2a. Note that in the range 0.3 - 2 kG the probabilities of the MI transitions labeled 5, 6, and 7 are the strongest among all transitions occurring from $F = 3$ [59, 189].

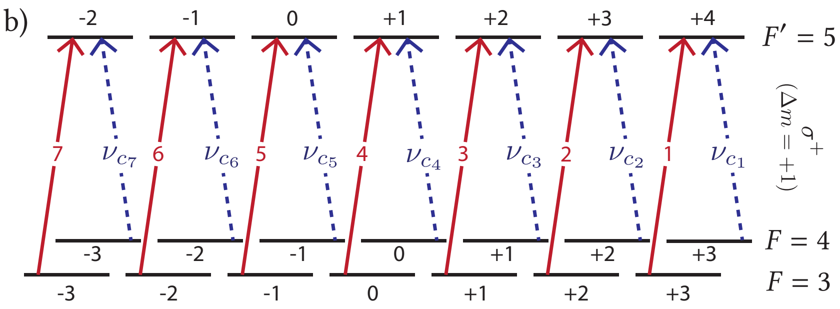

Figure 5.1 – Scheme of Cs D_2 line σ^+ transitions between $F = 3, 4$ and $F' = 5$. The probe frequency ν_p is scanned across the MI transitions labelled 1-7 ($F_g = 3 \longrightarrow F_e = 5$). The coupling frequencies ν_{c_n} ($n = 1, \dots, 7$) are resonant with $F = 4 \longrightarrow F' = 5$ transitions, forming seven Λ-systems. Only the states involved in the process under consideration are shown. Note that $|F, m_F\rangle$ is just a notation for visualization, as the atomic states are better described in the uncoupled basis $|J, m_J, I, m_I\rangle$ in high magnetic fields.

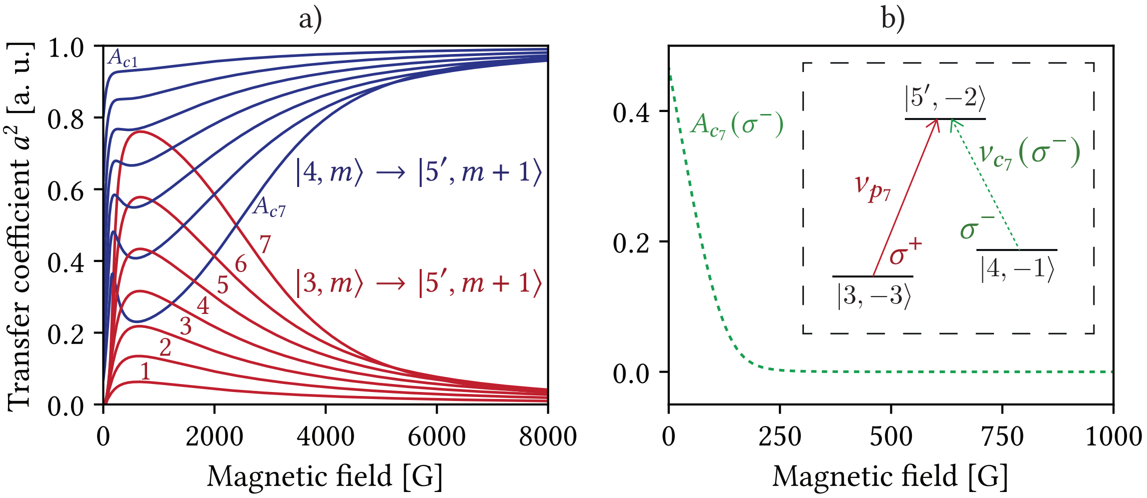

Figure 5.2 – Magnetic field dependence of the Zeeman transition intensities of the D_2 line of Cs. a) $F = 3 \longrightarrow F' = 5$ σ^+ MI transitions and $F = 4 \longrightarrow F' = 5$ σ^+ transitions. b) Transition $|4, -1\rangle \longrightarrow |5', -2\rangle$ (σ^-). This transition forms a Λ-system with transition 7 as shown in panel a) and in the right inset (see fig. 5.1). Its probability tends to 0 as the magnetic field increases, thus forming EIT resonances at high magnetic fields requires both probe and coupling beams to be σ^+-polarized. The inset in fig. 5.2b) depicts the decrease of the amplitude of transition 7 as the magnetic field increases.

The frequency shift slope of the MI transitions, obtained through the eigenvalues of the Hamiltonian, is quite large (~ 4 MHz/G) while for usual transitions the typical slope is 3 times smaller. Even though the probabilities of the MI transitions decrease as B increases, they can still be recorded easily at 8 kG. As noted below, this is because these transitions are formed far on the high-frequency wing where there are no intersections with other transitions (spectra are presented for Na in chapter 2, but Cs behaves almost identically).

The evolution of the probabilities of the corresponding seven coupling transitions $F = 4 \longrightarrow F' = 5$ (A_{c_1} to A_{c_7}) that are used to form seven Λ-systems (see fig. 5.1) with respect to the magnetic field are shown in fig. 5.2a. In the case of σ^- polarization, the probability of the strongest $F = 4 \longrightarrow F' = 5$ σ^- transition already tends to zero for $B > 300$ G, as shown in fig. 5.2b, implying that both probe and coupling beams must be σ^+-polarized in order to form EIT resonances.

5.2.2 Theoretical description of the EIT process

The general EIT phenomenon has been described in several papers, see for example the review [75]. To interpret our experimental results, we used the model outlined hereafter. The starting point of the calculations is the Liouville - von Neumann equation of motion, which gives the dynamical behavior of the density matrix ρ.

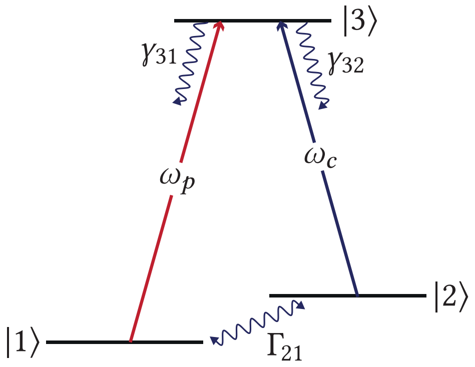

Figure 5.3 – Scheme of the three-level Λ-system used in the calculations. The total decay rate Γ_{33} of state $|3\rangle$ is $1/2(\gamma_{31}+\gamma_{32})$ [106]. The dephasing rate of coherence between the ground states is $\Gamma_{21}=(2\pi t)^{-1}$ where t is the time of flight of the atoms through the cell (at the most probable velocity $u=\sqrt{2k_BT/M}$ where T is the vapor temperature and M the atomic mass).

For a 3-level Λ-system as described in fig. 5.3 [see appendix C], the evolution of the coherences [106] read as follows:

$$\begin{aligned}\dot{\rho_{32}} &= i\Omega_c(\rho_{22}-\rho_{33})+i\Omega_p\rho_{21}^*-(i\Delta_c+\gamma_{31}/2)\rho_{32}\\ \dot{\rho_{31}} &= i\Omega_p(\rho_{11}-\rho_{33})+i\Omega_c\rho_{21}-(i\Delta_p+\gamma_{32}/2)\rho_{31}\\ \dot{\rho_{21}} &= i\Omega_c^*\rho_{31}-i\Omega_p^*\rho_{32}+(i\Delta_R+\Gamma_{21})\rho_{21}\,,\end{aligned}$$

where Δ_p and Δ_c are respectively the detuning of the probe and of the coupling laser to the excited state $|3\rangle$, Δ_R is the two-photon Raman detuning, γ_{31} and γ_{32} are the population relaxation rates and Γ_{33} is the total decay of state out of the excited state $|3\rangle$. These parameters are all linked to each other following the relations that can be found for example in [106]. Γ_{21}, the coherence dephasing rate between the ground states, is influenced by the geometry of the cell through the relation $\Gamma_{21}=(2\pi t)^{-1}$, where t is the time of flight of atoms traveling along the laser beam at the most probable thermal velocity $u=\sqrt{2k_BT/M}$. It can be shown [196, 197] that the Doppler-broadened absorption profile of transition $|1\rangle\longrightarrow|3\rangle$ is then given by:

$$\begin{aligned}\langle A\rangle = &\frac{-4\pi\omega_pNt_2^2t_1}{cu\sqrt{u}}\frac{E_p}{|F|^2}\int_0^{+\infty}v_zM(v_z)\mathrm{d}v_z\int_0^{L/v}\mathrm{d}t\\ &\times\mathrm{Im}\left\{d_{31}\left[\rho_{31}^+\left(t,\Delta_p^+,E_{p0}(v_zt)\right)\left(1-r_1e^{2ik_pv_zt}\right)\right.\right.\\ &\left.\left.+\rho_{31}^-\left(t,\Delta_p^-,E_{p0}(L-v_zt)\right)\left(1-r_1e^{2ik_p(L-v_zt)}\right)\right]\right\},\end{aligned}\tag{5.1}$$

where $M(v_z)$ is the one-dimensional Maxwell velocity distribution and d is the transition dipole moment. Due to the geometry of the cell (chapter 1), we consider only a one-dimensional problem where the laser beam propagation direction z is chosen to be perpendicular to the cell of thickness L. The coherences ρ_{31}^+ and ρ_{31}^- therefore respectively relate to atoms flying with velocity v_z and $-v_z$ [$\rho_{31}^+\equiv\rho_{31}(z=v_zt)$ and $\rho_{31}^-\equiv\rho_{31}(z=L-v_zt)$], and $\Delta_{p,c}^{\pm}=\Delta_{p,c}\pm k_{p,c}v_z$. Due to its geometry, the cell exhibits a Fabry-Pérot cavity behavior, and E_{p0} represents the probe field inside the empty cell:

$$E_{p0}(z) = \frac{E_p t_1}{F}\left[1 - r_2 e^{2ik(L-z)}\right], \tag{5.2}$$

with E_p an external probe field, $F = 1 - r_1 r_2 e^{2ikL}$ the quality factor of the cavity, r_1, r_2, t_1 and t_2 being the reflection and transmission coefficients of the windows. More details regarding the derivation of the transmitted (and reflected) fields through a nanometric-thin vapor cell can be found in chapter 1 and a thorough description of EIT in such a cell including laser bandwidth-induced effects was performed in [196]. When both probe and coupling lasers are on, the absorption profile given by eq. (5.1) will exhibit an EIT resonance of spectral width [75]:

$$\gamma_{\text{EIT}} \approx 2\Gamma_{21} + \Omega_c^2/\gamma_N\,, \tag{5.3}$$

where γ_N is the natural linewidth of the transition. It is well known that an increase of Ω_c leads to an increase of EIT contrast. However, it follows from eq. (5.3) that it also leads to an increase in the spectral width of the EIT resonance. It is therefore necessary to find a compromise value. Estimates can be obtained from $\Omega_c/2\pi = \gamma_N(I/8)^{1/2}$ [198], where I is the laser intensity in mW/cm^2, and $\gamma_N \sim 5$ MHz, typical for alkali D lines transitions. This gives $I = 18$ mW/cm^2 for the Rabi frequency $\Omega_c/2\pi = 1.5\gamma_N$ used in the calculation. We will compare this profile with experimental measurements in section 5.2.4.

5.2.3 Experimental setup

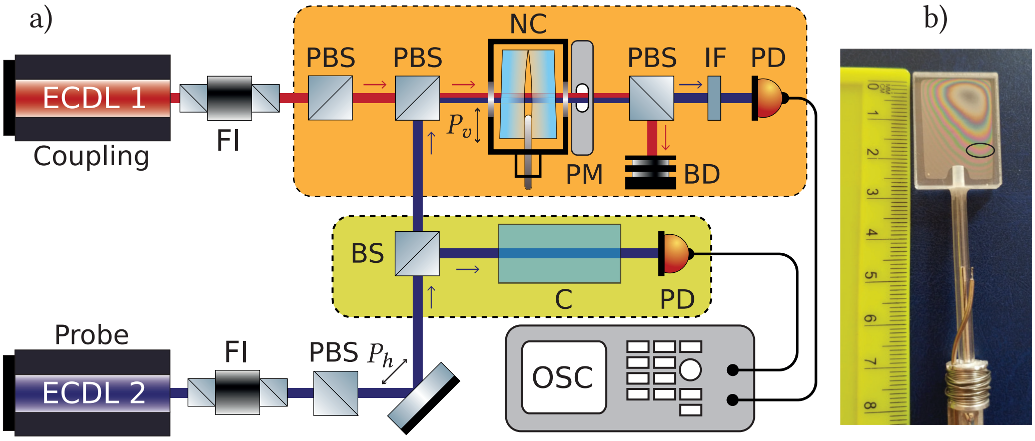

Figure 5.4 – a) Scheme of the EIT experimental setup. ECDL: CW narrow-band external-cavity diode lasers with $\lambda = 852$ nm (resonant with Cs D_2 line). FI: Faraday insulators. PBS: polarizing beam splitters. BS: beam splitter. IF: interference filter. C: saturated absorption spectroscopy unit for frequency reference. NC: nanocell placed in oven. PM: permanent magnet. PD: photodiodes. OSC: 4-channel digital oscilloscope. P_h and P_v stand for horizontal and vertical polarizations. b) Picture of the nanocell. The oval corresponds to the region where $L \approx \lambda$.

The layout of the experimental setup is shown on fig. 5.4. Two extended cavity diode laser (ECDL) are tuned in the vicinity of the Cs D_2 line, with a wavelength $\lambda \simeq 852$ nm. The Λ-systems shown in fig. 5.1 are formed by scanning the frequency ν_p of a VitaWave laser ($\delta\nu_p \sim 1$ MHz) [115] in the vicinity of the MI transitions $F = 3 \longrightarrow F' = 5$, while keeping the frequency ν_c from a MOGLabs “cateye” laser ($\delta\nu_p \simeq 0.1$ MHz) on resonance with one of the $F = 4 \longrightarrow F' = 5$ transitions. We use a 14 cm-long Fabry–Pérot (FP) etalon made with fused silica having nearly plane-parallel aluminum coated windows (90% reflectivity for $\lambda = 852$ nm). This etalon has a free spectral range of 780 MHz. The linearity of the laser scanning was tested by simultaneously recording the transmission spectrum of the etalon, and the nonlinearity has been evaluated to be around 1% throughout the spectral range. Since the saturated absorption (SA) technique shows quite accurately the frequency position of the transitions, the shift is then determined using the FP cavity. The presence of velocity-selective optical pumping (VSOP) peaks allows us to easily adjust the frequency of the coupling laser by slightly varying the input current of the laser. When the coupling laser is resonant with one of the $F = 4 \longrightarrow F' = 5$ transitions, an EIT resonance superimposed on the corresponding VSOP peak is formed. A fraction of about 10% of the coupling radiation power was sent to a frequency stabilization unit based on the dichroic atomic vapor laser locking method [199]. Probe radiation is vertically polarized, while the coupling radiation is horizontally polarized. In the case of a longitudinal B-field, linearly polarized laser radiation can be considered as consisting of σ^+ and σ^- radiations. Since we use mutually perpendicular polarizations, a polarizing beam splitter allows us to filter the signal so that only the probe radiation is directed towards the photo-receiver (orange part), while cutting off the coupling radiation. As noted above, in the case of MI transitions with $\Delta F = +2$ for the formation of the EIT resonance, both probe and coupling radiations must have σ^+ polarization. A photograph of the Cs NC is shown in fig. 5.4b. Interference fringes are formed by the reflection of light on the inner surfaces of windows. The region corresponding to a thickness $L \approx \lambda \sim 850$ nm is outlined by an oval. It was demonstrated in previous papers [137, 191, 200] that the use of a NC with thickness $L = \lambda$ is convenient to record high-contrast EIT resonances, which is due to its low absorption, even though frequent inelastic collisions of atoms with the windows of the NC induce a broadening of the EIT resonance. Studies of the EIT resonances were done using a strong neodymium–iron–boron alloy ring-shaped permanent magnet (PM). Due to the small thickness of the vapor column, the high-gradient field produced by the magnet can be considered uniform across the interaction region. The PM was placed after the rear window of the NC, with the axis aligned along the probe beam propagation direction. The magnetic field in the NC was simply varied by longitudinal displacement of the magnet, calibrated using a Hall effect magnetometer.

5.2.4 Experimental results

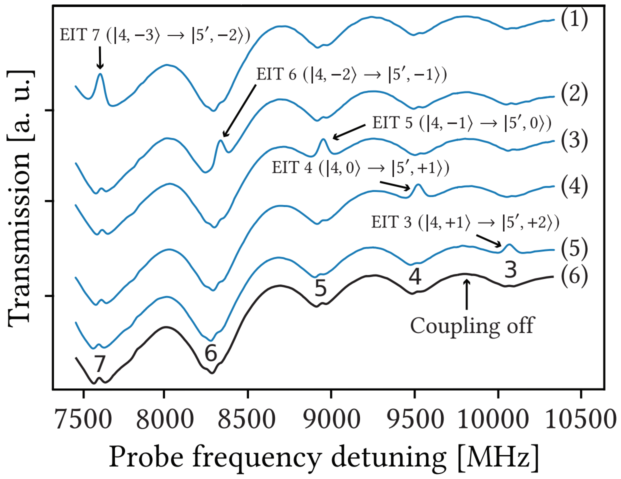

Figure 5.5 – Probe transmission spectra of the Cs nanocell ($L = \lambda = 852$ nm). The probe frequency is scanned so that it is successively resonant with transitions 3 to 7, following the labeling presented in fig. 5.1). Each spectrum (from 1 to 5) exhibits an EIT resonance. These EIT resonances are labeled EIT 3 to EIT 7, and the transition to which the coupling laser is tuned is specified. As an example, for EIT 3, the two lasers form a Λ-system with the probe laser resonant with transition 3 ($|3, -1\rangle \longrightarrow |5', -2\rangle$) and the coupling laser ν_{c_3} tuned to transition $|4, +1\rangle \longrightarrow |5', +2\rangle$. The bottom black line (spectrum 6) corresponds to the case where the probe is scanned but the coupling is turned off. The coupling powers are respectively 10 and 0.05 mW and the external magnetic field is $B = 1400$ G. Small VSOP peaks are visible on each atomic resonance. Zero frequency corresponds to the transition frequency of Cs D_2 line.

Curves 1 to 5 in fig. 5.5 show the experimental transmission spectra of the probe radiation which contain the resonances EIT 3 to EIT 7 in a longitudinal magnetic field $B = 1400$ G. The NC thickness is $L = \lambda = 852$ nm and the temperature of the reservoir is 100 °C (to prevent Cs vapor condensation on the windows[1]). The coupling and the probe powers are 20 mW and 0.1 mW, respectively. Note that since only σ^+ radiations participate in the formation of the EIT resonances (see fig. 5.1), only half of the power of these radiations must be considered, meaning 10 mW and 50 μW, respectively. Curve 6 is a probe spectrum when the coupling is blocked. Since the cell thickness is $L = \lambda$, small peaks formed by VSOP resonances are located exactly at the atomic transitions frequencies, as described in [55].

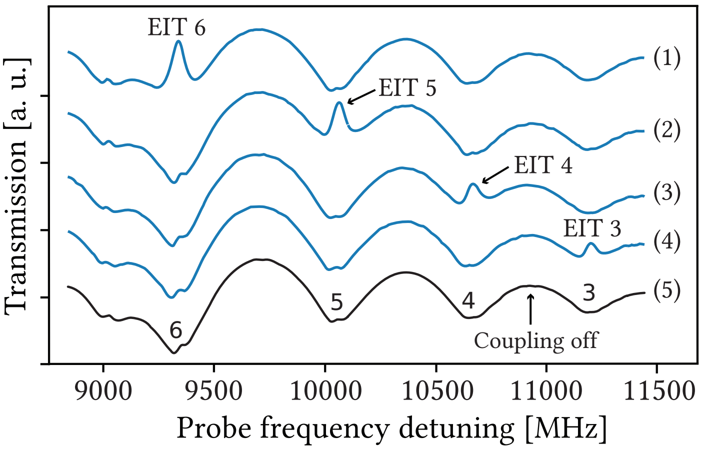

Figure 5.6 – Probe transmission spectra of the Cs nanocell ($L = \lambda \approx 850$ nm). Spectra 1 to 4 exhibit four EIT resonances, labeled EIT 3 to EIT 6, while the probe frequency is scanned across transitions 3 to 6. The external longitudinal magnetic field is $B = 1770$ G. Spectrum n° 5 is a probe transmission spectrum when the coupling is off. Small VSOP peaks are visible on each atomic transition. Zero frequency corresponds to the transition frequency of Cs D_2 line.

In fig. 5.6, curves 1 to 4 are probe transmission spectra containing EIT 6, EIT 5, EIT 4, and EIT 3 resonances for $B = 1770$ G. Curve 5 shows only the probe spectrum when the coupling is blocked. In fig. 5.7, lines 1 to 3 show the probe transmission spectra which contain EIT 6, EIT 4 and EIT 3 resonances for $B = 2880$ G. Curve 4 shows only the probe spectrum when the coupling is blocked. The inset shows the profile of EIT 6 fitted with a Gaussian profile with a full width at half maximum (FWHM) of ~ 35 MHz. There is also a small VSOP resonance which is formed when the coupling is blocked. The typical FWHM of VSOP resonances is 40 - 50 MHz. Preliminary theoretical calculations (shown in fig. 5.7b) were obtained following the procedure described in section 5.2.2. The Rabi frequencies of the coupling and probe lasers are respectively $\Omega_c = 1.5\gamma_N$ and $\Omega_p = 0.06\gamma_N$. Reasonable agreement between theory and experiment regarding the width and depth of the EIT resonance is obtained and the VSOP resonance is seen. Small discrepancies (asymmetry of the profile and amplitude of the VSOP resonance) can arise notably from the need to consider neighboring Zeeman sublevels (not shown in fig. 5.1), and therefore more than three levels, to obtain more accurate results. The amplitude of the EIT resonance is a factor ~10 larger than the amplitude of the VSOP resonance, whereas the spectral width of the EIT resonance is a factor of 1.5 smaller, which is characteristic of the EIT process [191, 201]. Note that the contrast of the EIT resonance, defined as the ratio of the EIT resonance amplitude to the peak absorption of the Cs vapor when the coupling is blocked, is at least 40-50%. This contrast level is typical when a NC is used [200]. The amplitude of EIT resonance 6 is ~ 50 times greater than that of the VSOP resonance and is spectrally narrower than the latter. In fig. 5.8 the solid lines indicate the calculated dependences of the frequency shifts for transitions 1 - 7 (figs. 5.1 and 5.2) and $F = 3 \longrightarrow F' = 4$ (marked with a dotted oval) to the magnetic field B. The black squares with error bars represent the experimental results. As mentioned earlier, due to the high value of the frequency shift slope for $B > 3$ kG, the group of MI transitions 1 - 7 is completely separated in frequency from $F = 3 \longrightarrow F' = 4$ transitions.

---

[1] To prevent condensation, the temperature of the windows is slightly higher.

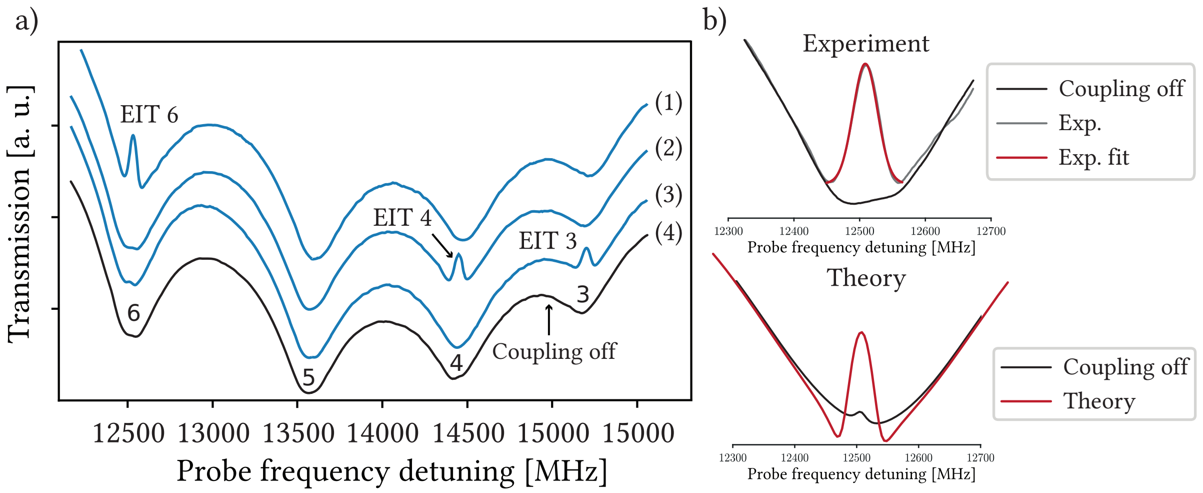

Figure 5.7 – a) Probe transmission spectra of the Cs nanocell ($L = \lambda = 852$ nm). Lines 1 to 3 show four EIT resonances, labeled EIT 4, EIT 5 and EIT 6. The external longitudinal magnetic field is $B = 2880$ G. Line 4 is a probe transmission spectrum when the coupling is off. b) Zoom on EIT 6 fitted with a Gaussian profile (FWHM 35 MHz) and comparison with theoretical calculations. The intensity of the coupling radiation was 18 mW/cm^2. Red: coupling on, black: coupling off. Small VSOP peaks are visible on each atomic transition formed by the probe radiation. Their typical linewidth is 40-50 MHz. Zero frequency corresponds to the transition frequency of Cs D_2 line.

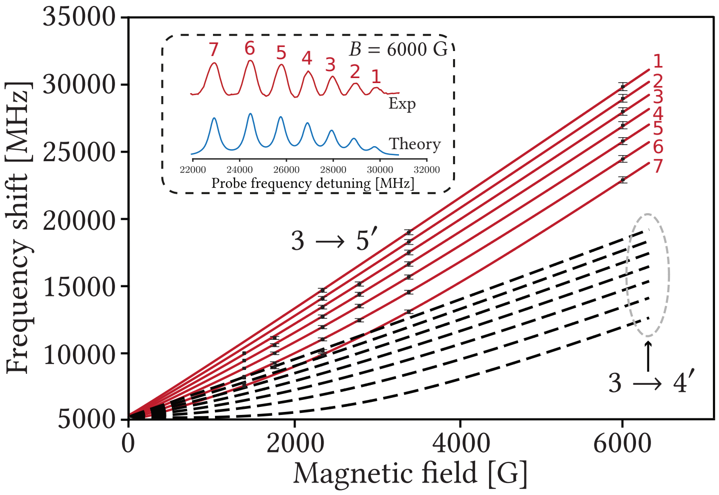

Figure 5.8 – Red solid lines: frequency shift of transitions 1 to 7 (see fig. 5.1) as a function of the magnetic field. The black squares with error bars represent experimental measurements performed using absorption spectra. The uncertainties for the measurements were derived from the non-linearity of the laser scanning which was evaluated to be around 1% throughout the spectral range. Black dashed lines: frequency shift of $F_g = 3 \longrightarrow F_e = 4$ transitions. For $B > 3$ kG, both groups are well separated in frequency. Inset: theoretical and experimental absorption spectra for $B = 6$ kG, the frequency shift reaches 30 GHz from the Cs D_2 line transition frequency.

The curves in the inset of fig. 5.8 show experimental and theoretical spectra (calculated by combining the models presented in chapters 1 and 2) of the seven MI transitions absorption for $B = 6$ kG when the frequency shift reaches ~ 30 GHz. Note that the amplitude of transition 6 is slightly bigger than that of transition 7 (while for $B < 5$ kG the amplitude of transition 7 is bigger, see fig. 5.2a) due to magnetic field mixing. One of the remarkable features of the σ^+ MI transitions $3 \longrightarrow 5'$ is that they are still well recorded for a magnetic field $B \approx 8$ kG. They are located in the high-frequency wing of the spectrum, as can be seen for example in [202, Fig. 18], where the frequency shift reaches 34 GHz.

In that paper, the $F = 3 \longrightarrow F' = 5$ are not denoted in the $|F, m_F\rangle$ basis as $|m_J, m_I\rangle$ is generally a more adequate basis in high magnetic fields. However, performing the calculations in the coupled $|F, m_F\rangle$ basis still adequately describes the behavior of the Zeeman transitions, as described throughout this thesis. The above-mentioned MI transitions can be exploited in such high B-fields as new frequency markers, for using new frequency ranges, as well as for the frequency stabilization of lasers at strongly shifted frequencies from the initial transition in unperturbed atoms [18, 170].

5.3 Buffer gas influence on the formation of N-resonances

N-resonances are narrow-band, all-optical Doppler-free absorptive resonances. They were first observed and studied by Zibrov et al. [192]. Initially referred to as *three-photon absorption resonances* or *three-photon EIT resonances* due to their resemblance with EIT resonances, they result from a two-field (probe and coupling) three-photon absorption process involving a two-photon Raman transition combined with optical pumping (from the probe beam). They are obtained in Λ-systems (as illustrated in fig. 5.9). In this paper, we study the D_1 optical transition of ^{85}Rb. The states involved in the process are thus $F = 2, 3$ and the (unresolved) excited electronic state $5^2P_{1/2}$. The coupling beam is detuned from the excited state by the ground state hyperfine frequency $\Delta_{\mathrm{HFS}} \simeq 3.036$ GHz [3]. When the Raman condition $\nu_p - \nu_c = \Delta_{\mathrm{HFS}}$ is fulfilled, a N-resonance appears in the absorption spectrum, in the form of an increase in absorption on top of the usual Doppler-broadened profile. Therefore, N-resonances differ from EIT resonances in that the latter result in a decrease in absorption [74–76, 203]. N-resonances are closely related to Electromagnetically Induced Absorption (EIA) resonances, which have been studied in vapors of other alkali atoms (Cs, Na and K) [176, 182, 192–194, 204–209]. As in EIT, the linewidth of a N-resonance strongly depends on ground-state hyperfine decoherence.

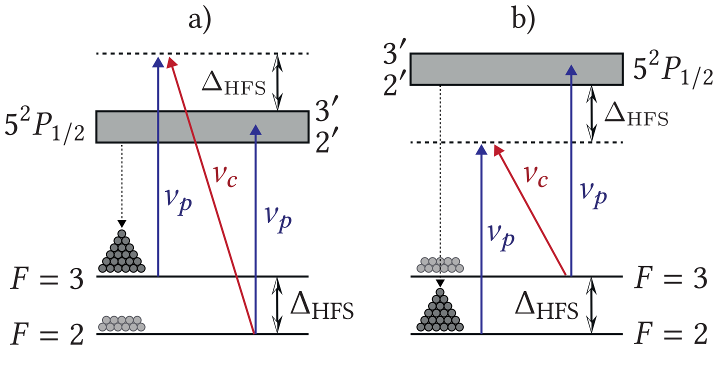

Figure 5.9 – Diagram of the Λ-system (^{85}Rb D_1 line) involved in the N-resonance process. The ground state level splitting is $\Delta_{\mathrm{HFS}} = 3036$ MHz. a) The probe laser is swept accross $2 \longrightarrow 2', 3'$ transitions while the coupling is fixed Δ_{HFS} higher than the $F = 2$ set of transitions. b) The probe laser is swept across $3 \longrightarrow 2', 3'$ transitions while the coupling is fixed Δ_{HFS} lower than the $F = 3$ set of transitions. In each case, the dotted arrow shows the population transfer due to optical pumping, which is reflected by the amount of grey beads on each of the ground states. The dotted line is a virtual level.

When an external magnetic field **B** is applied, EIT and N-resonances behave similarly: the number of components in which they split depends on the hyperfine structure of the system (namely the total angular momentum **F** of the lower ground states), the orientation of the magnetic field **B** with respect to the laser beam propagation direction **k** and the laser polarization. It was recently shown in [210] that EIT components formed in a magnetic field are useful tools that allow the retrieval of both the direction and magnitude of the magnetic field. In principle, this could also be true for N-resonances.

Previous studies [176, 182, 192–194, 206–208] have shown that N-resonances exhibit enhanced contrast and reduced linewidth when a buffer gas, typically Neon, is introduced in the alkali vapor cell. However, in-depth investigations to pinpoint the optical buffer gas pressure for the formation of N-resonances have been lacking. Despite the extensive literature on the EIT process (see for example [74–76, 203] and references therein), research on N-resonances remains limited. This highlights the importance of further investigation. Due to their weak light shift compared to CPT resonances, N-resonances are promising candidates for small atomic frequency standards that can be realized with commercially available diode lasers [193–195].

Here, we use five vapor cells with varying buffer gas pressures, spanning from 0 to 400 Torr. The objective is to investigate how these pressure conditions influence the contrast and linewidth of the N-resonance. By covering a broad spectrum of pressures, we aim to gain a comprehensive understanding of the behavior of the N-resonance under various experimental conditions. This allows us to observe how the spectral features behave and provides valuable insight into the optimal buffer gas pressure conditions required for the formation of a narrow and high-contrast N-resonance. Once the optimal pressure range is obtained, we examine the evolution of the resonance when an external magnetic field is applied and compare the frequency shift of its components with previous theoretical calculations.

5.3.1 Experiment

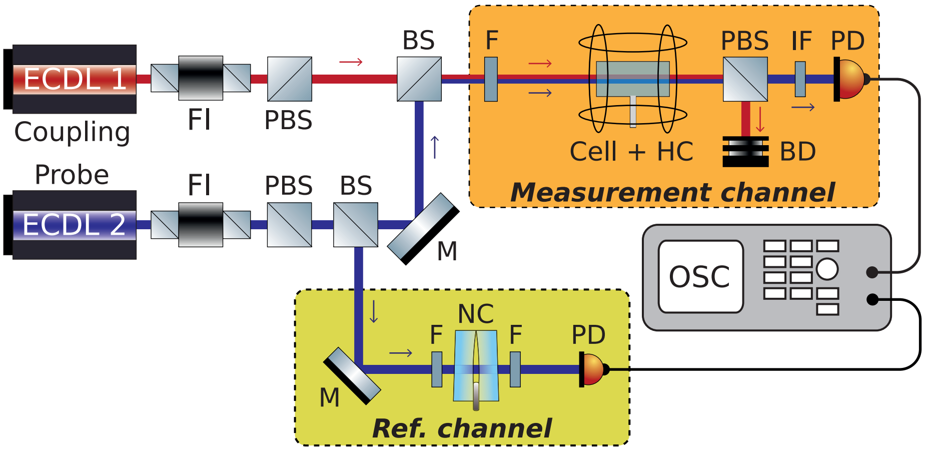

Figure 5.10 – Scheme of the N-resonance experimental setup. ECDL: extended-cavity diode laser, FI: Faraday isolator, PBS: polarizing beam splitter, BS: beam splitter, F: neutral density filter, Cell + HC: 0.8 cm vapor cell containing a mixture of Rb and Ne (buffer gas) placed between Helmholtz coils, IF: interference filter, BD: beam dump, PD: photodetector, M: mirror, NC: nanocell for the formation of reference spectra, OSC: oscilloscope.

The layout of the experimental setup is shown in fig. 5.10. Two VitaWave [115] ECDLs ($\delta\nu \sim 1$ MHz) diode lasers were used. Both lasers were tuned in the vicinity of the D_1 line of ^{85}Rb. Two beams with mutually perpendicular polarizations were formed, hereafter referred to as probe (ν_p) and coupling (ν_c) beams, using polarizing beam splitters. The probe laser frequency was tunable in order to scan the unresolved $5^2P_{1/2}$ excited state, while the frequency of the coupling laser was fixed. The probe power was kept in the range of 0.5 - 1 mW, while the coupling power could be increased up to 40 mW. Roughly 10% of the coupling laser was directed to a DAVLL frequency locking scheme [199], omitted in fig. 5.10 for the sake of clarity.

The probe and coupling beams were combined with a beam splitter and directed to a 0.8 cm-long vapor cell containing Rb and Ne buffer gas. Several rounds of measurements were performed with cells having a different Ne partial pressure. In all cases, the temperature of the cell was 50 °C, corresponding to a number density of the order of 10^{12} cm^{-3}. The photodetector was then used to record the probe radiation passing through the cell, the coupling radiation being cut out by an analyzer. The cell was placed in the middle of three pairs of Helmholtz coils, allowing the formation of a weak magnetic field. A fraction of the coupling radiation (Ref. channel) was directed to a NC with a thickness $L \sim \lambda = 795$ nm [208] to form a reference spectrum, as presented in fig. 5.11 (lower, blue curve).

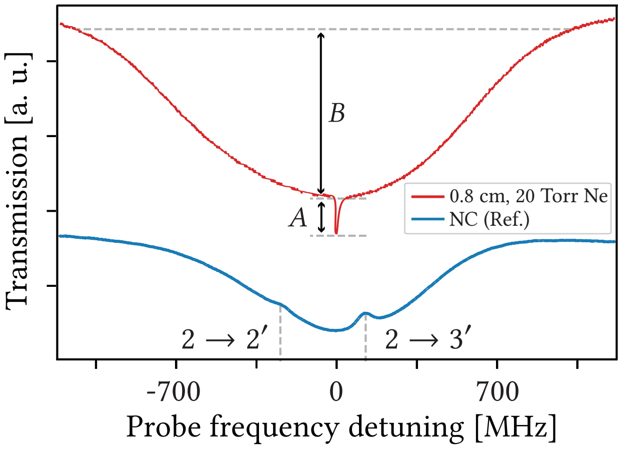

Figure 5.11 – Probe absorption spectrum (upper, red curve) scanning the $F = 2$ transitions of ^{85}Rb D_1 line, recorded with a 0.8 cm cell containing a mixture of Rb vapor and Ne buffer gas ($P_{\mathrm{Ne}} = 20$ Torr). The spectrum exhibits a N-resonance when the coupling laser is on, corresponding to the case depicted in fig. 5.9a. A is the N-resonance depth and B represents probe-only absorption. The lower (blue) curve is a reference spectrum obtained with a nanometric-thin cell, as depicted in fig. 5.10.

The red curve in fig. 5.11 is an absorption spectrum of the probe beam ν_p passing through a 0.8 cm cell ($P_{\mathrm{Ne}} = 20$ Torr) when the coupling beam ν_c is on. The spectrum contains a narrow N-resonance with a FWHM of 9 MHz and a contrast of around 20%. Throughout this section, the contrast is defined as the ratio of the depth of the N-resonance (A) to the probe-only absorption (B) [72]. The contrast increases with the power of the coupling laser, as can be seen in fig. 5.12, and can reach with this cell a maximum of 25% (approximately 2.5 greater than the contrast of a N-resonance formed in a cell without buffer gas). For a cell with 6 Torr Neon, the contrast can reach up to 40%.

In fig. 5.9, we present two diagrams of the energy levels of ^{85}Rb D_1 line involved in the N-resonance formation process. Two configurations are presented, depending on whether the probe laser is scanning the $F = 2$ or $F = 3$ set of transitions. In diagram a) the probe field ν_p, resonant with the transition between the lower-energy level of the ground state ($F_g = 2$) and the electronic excited state $5^2\mathrm{P}_{1/2}$, pumps the atoms into the upper ground state $F = 3$ [211], enhancing the probe transmission through the vapor, ultimately leading to population inversion. The coupling beam v_c is detuned from the $F = 2$ transition. If the two-photon absorption condition $\nu_c - \nu_p = \Delta_{\mathrm{HFS}}$ is fulfilled, atoms are driven coherently back to the lower energy level $F = 2$ via a two-photon absorption process [205], followed by a one-photon absorption from the probe bringing the atom to the excited state. The spectrum then shows a narrow, all-optical N-resonance induced by the three-photon non-linear process on top of a Doppler-broadened background caused by regular absorption, as it is shown in fig. 5.9. The frequency of the N-resonance can be easily changed by tuning the frequency of the coupling field. In diagram b), a similar behavior is depicted. The probe field, resonant with the transition between $F = 3$ and the excited state, pumps the atoms into the lower-energy level of the ground state. In this case, if the condition $\nu_p - \nu_c = \Delta_{\mathrm{HFS}}$ is fulfilled, atoms are driven coherently to $F = 3$, followed as before by a one-photon absorption from the probe bringing the atom to the excited state. More details about N-resonance formation are provided in section 5.3.3.

Figure 5.12 shows the dependence of the amplitude of the N-resonance ($P_{\mathrm{Ne}} = 6$ Torr) on the coupling power. Five different curves are provided, which were respectively obtained for $P_c = 1, 4, 9, 14$, and 36 mW (from top to bottom). The probe power was fixed at ~ 1 mW in all cases. Since the diameter d of both laser beams is ~ 2 mm, the intensity I for a laser of power P [mW/cm^2] is[2] $\sim 32\ P$. Note that reducing P_c and P_p to, say, 1 mW and 0.5 mW respectively allows to form a N-resonance with a smaller contrast (a few %) but with subnatural linewidth, as shown in the inset of fig. 5.12. The resonance was

---

[2] $I = P/S$ with $S = \pi d^2/4$.

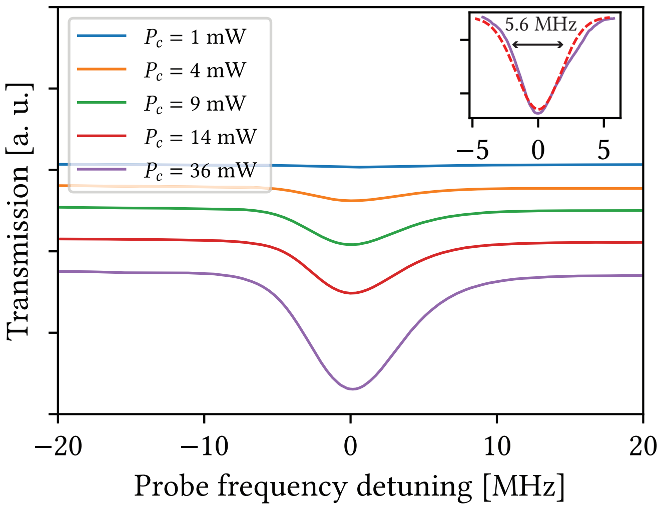

Figure 5.12 – Evolution of the N-resonance for different values of the coupling laser power P_c, recorded with a 0.8 cm cell filled with Rb and Ne (P_{Ne} = 6 Torr). The inset is a close-up on the N-resonance obtained with P_c = 1 mW, fitted with a Gaussian profile with a FWHM of 5.6 MHz.

fitted with a Gaussian profile (which is a good approximation for low coupling powers) and its FWHM is in that case around 5.6 MHz.

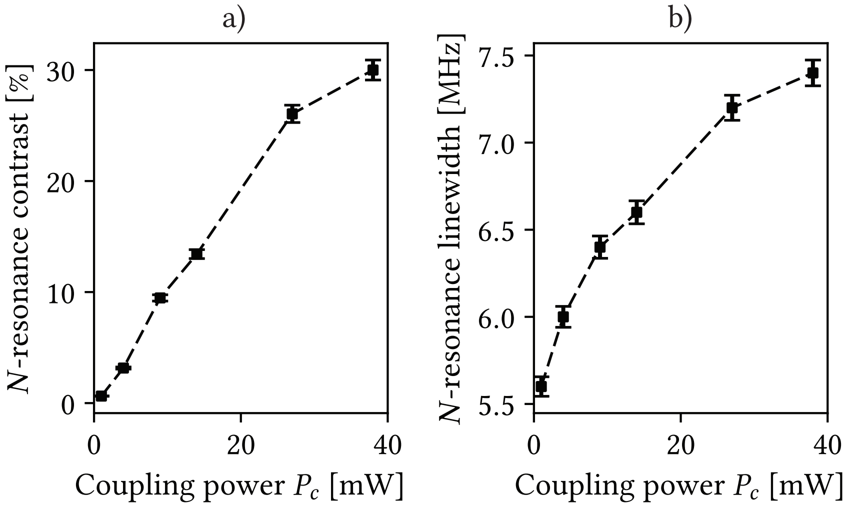

Figure 5.13 – Contrast (a) and Linewidth (b) of the N-resonance with respect to the coupling laser power P_c, each with 5% error bars. The experimental parameters are the same as in fig. 5.12. The dotted lines are drawn to guide the eye.

In fig. 5.13a, we show the dependence of the N-resonance amplitude on the coupling power P_c. We observe an increase in the amplitude with the coupling power following a somewhat linear dependency (the dashed lines are only to guide the eye). However, the increase in spectral width is much weaker with respect to the coupling power, as depicted in fig. 5.13b. This is important when studying the splitting of the N-resonance in an external magnetic field to avoid overlapping of the different components.

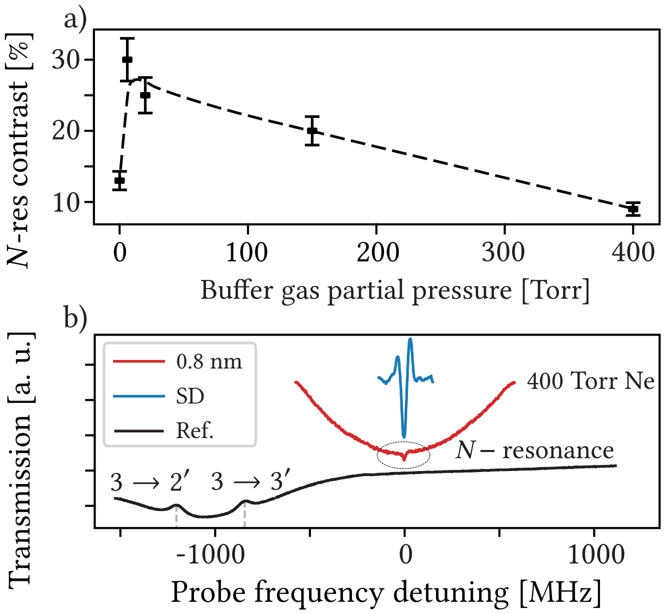

Figure 5.14 – a) Dependence of the contrast of the N-resonance on the buffer gas pressure measured in 0.8 cm long cells. Each black square (with an error bar) is an experimental measurement performed in a separate cell with fixed buffer gas pressure. The dotted line is drawn to guide the eye. b) Probe transmission spectra obtained with 400 Torr Ne. The N-resonance is clearly visible on the red curve, and the second derivative (SD, blue curve) is shown to depict the increase in transmission.

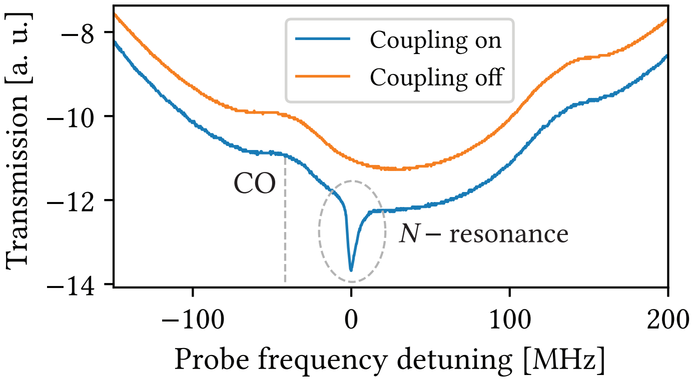

Figure 5.15 – Probe transmission spectra obtained with a 0.8 cm cell containing pure Rb without buffer gas when the coupling beam is off (upper, orange curve) and on (lower, blue curve). The N-resonance is visible only when the coupling beam is on. The sub-Doppler structure is caused by the reflection of the laser beam on the inner surfaces of the cell windows. A crossover (CO) resonance is visible, as in SA spectra [192].

Figure 5.14a shows the dependence of the contrast of the N-resonance on the Ne partial pressure, in the 0 to 400 Torr range. The coupling power is 1 mW and the probe power is 36 mW. It can be seen that the optimal Ne partial pressure is located between 6 and 30 Torr, where the contrast is maximum. It is interesting to note that this pressure is also optimal for the EIT process, see [74, Fig. 8].

In fig. 5.14b, we present a probe transmission spectrum recorded in a cell with 400 Torr Ne (red curve). The blue curve is the second derivative (SD) of the region highlighted by the dotted oval. In this case, the contrast is strongly reduced ($\simeq$ 10%), and the SD allows to see the resonance better. The lower curve in fig. 5.14b is a reference spectrum of the $3 \longrightarrow 2', 3'$ transitions of ^{85}Rb.

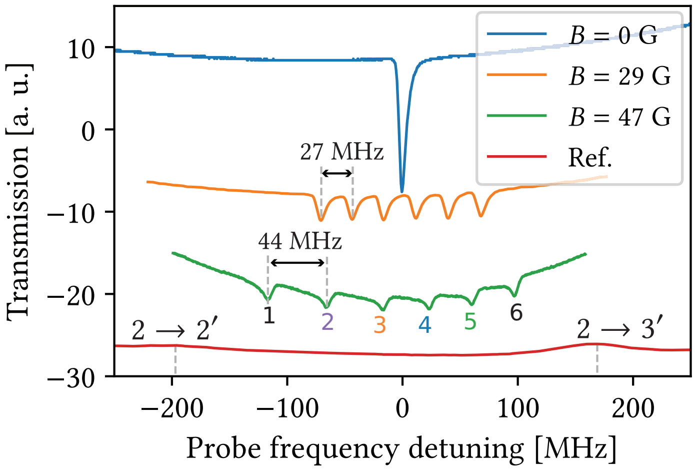

Figure 5.16 – Probe transmission spectra showing the behavior of the N-resonance when a transverse magnetic field ($\mathbf{B} \perp \mathbf{k}$) is applied. Due to the Zeeman effect, the single ($B = 0$) N-resonance is split into 6 components when $B = 29$ G is applied. As expected, the components move away from each other as the magnetic field increases ($B = 47$ G). The N-resonance spectra were obtained with a 0.8 cm cell filled with Rb and Ne (20 Torr Ne). The reference spectrum was obtained with a NC, as mentioned earlier.

.

It should be noted that despite the relatively low contrast of the N-resonance (~ 10 %) formed in a 400 Torr Ne vapor cell shown in fig. 5.14b, it is still easily recordable. The SA process, used in many experiments to form reference spectra, can not be performed in cells containing buffer gas (even as little as 0.1 Torr) [212].

In fig. 5.15, the upper orange curve shows the spectrum of only the probe radiation formed in a cell with pure Rb vapor, while the lower blue curve is a probe spectrum in the presence of the coupling radiation, which contains a N-resonance with a linewidth of 6 MHz. Since the one-photon Doppler width of Rb D_1 line is $\simeq 500$ MHz [212, 213], we observe strong narrowing of the N-resonance by ~ 83 times.

5.3.2 N-resonances in a magnetic field

To study the evolution of the N-resonance in an external magnetic field, we placed a vapor cell (Rb + 20 Torr Ne) in the middle of a system of three pairs of Helmholtz coils. This allows to create a magnetic field in the desired direction while zeroing the laboratory magnetic field. The spectra presented in fig. 5.16 correspond to the case where a transverse magnetic field ($\mathbf{B} \perp \mathbf{k}$) was applied to the cell. The zero field resonance ($B = 0$, upper curve) splits into 6 equidistant components, all having the same linewidth of around 6 MHz. The components move away from each other as the magnetic field increases, as we see with the spectra corresponding to $B \simeq 29$ G and $B \simeq 47$ G. Under the influence of B, the ground levels $F = 2$ and $F = 3$ respectively split into 5 and 7 Zeeman sublevels. Since the frequency shifts of these levels are respectively $\mp\mu_B/3 \simeq \mp 0.465$ MHz/G [3] (where μ_B is the Bohr magneton), the states are shifted in opposite directions and the distance between two adjacent components of the N-resonance can be easily estimated as

$$\Delta\nu = \frac{2\mu_B B}{3}, \tag{5.4}$$

yielding around 27 MHz for $B = 29$ G and 44 MHz for $B = 47$ G, which is consistent with what is seen in fig. 5.16. Equidistance of the components (as shown in fig. 5.17) is obtained in the small magnetic field regime ($B \ll B_0 = A_{\text{HFS}}/\mu_B$), where A_{HFS} is the magnetic dipole interaction constant [3, 67, 214, 215]. The value of B_0 for ^{85}Rb is ~ 0.7 kG. For higher magnetic fields, i.e. when $\mathbf{J}$ and $\mathbf{I}$ are decoupled and $|F, m_F\rangle$ are not good quantum numbers, the Breit-Rabi formula can be used (chapter 3) [3, 74, 214, 215]

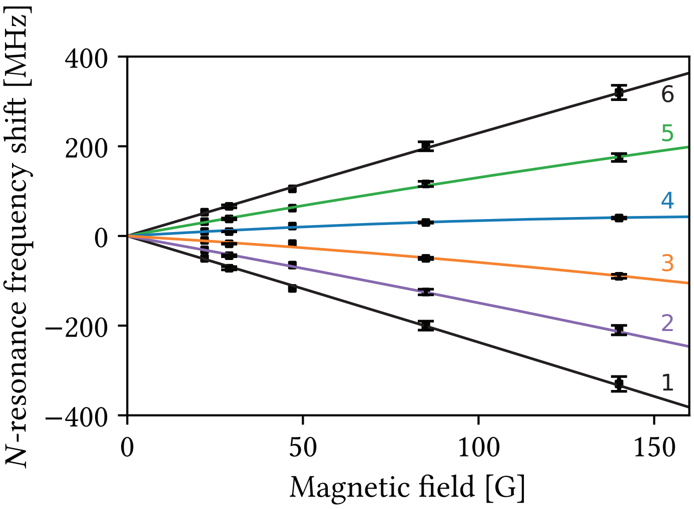

Figure 5.17 – Frequency shift of the 6 components of the *N*-resonance (shown in fig. 5.16) as a function of the magnetic field. The lines were computed theoretically, and the black squares are experimental measurements with 5% error bars. Labeling and line style are consistent with fig. 5.18.

to determine theoretically the frequency shifts of the states.

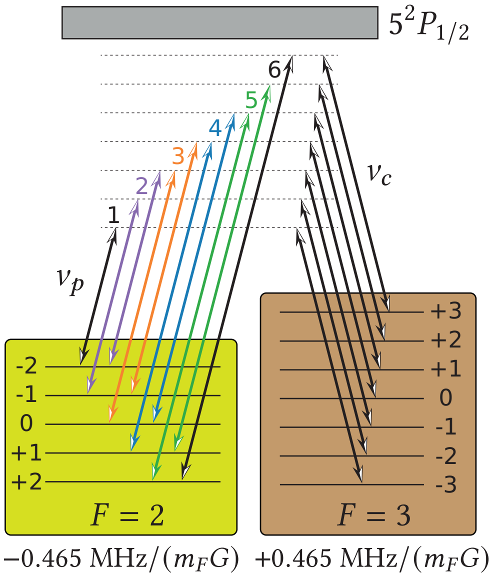

Figure 5.18 – Diagram of the $F = 2$ and $F = 3$ energy levels of ^{85}Rb, which respectively split into 5 and 7 Zeeman sublevels when a magnetic field is applied. To form a Λ-system, the coupling and probe lasers must have the same upper state $|F', m'\rangle$. Ten possible pairs of ν_c and ν_p frequencies are shown, the pairs for which the probe laser frequencies are the same are labeled 1 to 6. Components 1 and 6 only include a single probe transition.

Figure 5.18 is a diagram depicting the splitting of the $F = 2, 3$ states of ^{85}Rb in a magnetic field. For the sake of clarity, we did not show the splitting of the $F' = 2, 3$ levels of the excited state $5^2\mathrm{P}_{1/2}$. In the diagram, ten possible pairs of probe/coupling frequencies that can lead to two-photon absorption from $F = 2$ with transfer of atoms to $F = 3$ are shown. It can be observed that the probe laser frequencies are in some cases the same (such groups of two transitions with the same frequencies are depicted by two arrows of the same color in fig. 5.18). These 6 pairs lead to the splitting of the *N*-resonance into 6 different components, as seen in fig. 5.16 and 5.17. When $\mathbf{B} \parallel \mathbf{k}$, the σ^+ and σ^- polarizations form 5 Λ-systems with the $F = 2$ and $F = 3$ levels of the ground state, and the *N*-resonance splits into 5 equidistant narrow-band components [208]. This configuration is shown in fig. 5.19 for both EIT and N-resonances (a longitudinal magnetic field $B = 3$ G was applied). The linewidth of each component is about 1.5 MHz, 4 times narrower than the natural linewidth. However, it is clearly seen from the upper curve of fig. 5.19 that the EIT signal is "noisier" than that of the N-resonance, which is explained by a higher contrast of the latter i.e. higher signal to noise ratio (SNR).

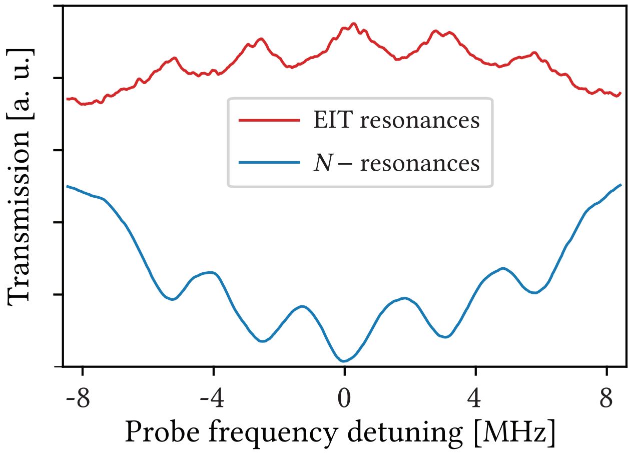

Figure 5.19 – Splitting of an EIT resonance (upper, red curve) and a N-resonance (lower, blue curve) into five components in a longitudinal magnetic field ($B = 3$ G) with the following experimental parameters: $P_{\mathrm{Ne}} = 6$ Torr, $P_c = 1$ mW, $P_p = 0.2$ mW. Each component has a width of around 1.5 MHz. The distance between the lower and higher frequency components is 4×0.93 MHz/G $\simeq 11$ MHz.

5.3.3 Discussion

Let us consider the diagram presented in fig. 5.9b (all the following conclusions, with small modifications, are also true for fig. 5.9a). As mentioned above, the purpose of adding a buffer gas (in this case, Ne) to a Rb cell is the following:

1. A strong Rb-Ne collisional broadening of the $5^2P_{1/2}$ state occurs [216], leading to greater absorption of the probe laser and, consequently, to an increase of the $N_2 - N_3$ value, where N_2 and N_3 are the populations of the ground states.
2. The speed of the atoms is greatly reduced, thereby increasing the time of flight of an atom through the laser beam, increasing the optical pumping process.

A theoretical consideration of the N-resonance formation process is given in [182]. Here, we present a qualitative consideration of the process according to [205].

The amplitude A of the N-resonance depends on the two-photon absorption resonance cross-section σ_{TPA} such that

$$A \propto \exp[\sigma_{\mathrm{TPA}}(N_2 - N_3)L], \tag{5.5}$$

where L is the length of the vapor cell. The two-photon absorption resonance cross-section is defined as:

$$\sigma_{\mathrm{TPA}} = \frac{\lambda^2}{16\pi^2}\frac{\Gamma_N}{\Gamma_{23}}\left(\frac{\Omega_c}{\Delta_c}\right)^2, \tag{5.6}$$

where Δ_c is the detuning of the coupling laser from the excited state $5^2P_{1/2}$, Γ_N is the natural linewidth of the excited state ($\Gamma_N/2\pi = 5.75$ MHz) and $\Gamma_{23}/2\pi = \gamma_{23}$ represents ground-state decoherence + other terms that may lead to line broadening [74, 75]. The coupling Rabi frequency, Ω_c, is defined as $dE_c/\hbar$, where E_c is the coupling electric field and d is the matrix element of the transition dipole moment of the $F = 3 \longrightarrow 5^2P_{1/2}$ transition. Estimates of the Rabi frequency can be obtained from [217]:

$$\frac{\Omega_C}{2\pi} \simeq \Gamma_N\sqrt{\frac{I}{8}}, \tag{5.7}$$

where I is the laser intensity [mW/cm^2]. For $P_c = 30$ mW, we obtain $I = 960$ mW/cm^2 which yields $\Omega_c \simeq 62$ MHz. Note that if the N-resonance is power-broadened, it is possible to estimate its linewidth with the formula given in [76]:

$$\gamma_{N_{\text{res}}} = \frac{\Omega_C^2}{\Gamma_{\text{Dopp}}} + \gamma_{23}, \tag{5.8}$$

where Γ_{Dopp} is the one-photon Doppler width [53]:

$$\Gamma_{\text{Dopp}} = \sqrt{\frac{8k_BT\log(2)}{mc^2}}, \tag{5.9}$$

with ω_0 the D_1 transition frequency (here $\omega_0 = 377.107385690$ THz) and m the atomic mass of ^{85}Rb (appendix B). In our case, $\gamma_{23} \simeq 1$ MHz, which gives $\gamma_{N_{\text{res}}} \simeq 8.2$ MHz. From equation (5.8), it is clear that by reducing the coupling intensity, one can obtain a N-resonance with subnatural linewidth. An important fact to note is that amplitude depends on $\exp(L)$, therefore, N-resonances cannot be formed at small thicknesses, i.e. in a microcell (MC). However, since the dependence on L is much weaker for EIT resonances, they can even be formed and detected in nanometric-thin cells [92, 218]. Another significant difference is that, when recording resonance fluorescence spectra during the EIT process, a narrow dip (decrease) can be observed on the fluorescence peak, while when a N-resonance is formed, we observe a narrow peak of increased fluorescence [205]. Moreover, the increase of absorption exhibited in N-resonance spectra can be changed into a decrease of absorption in the presence of an additional laser field [219].
It is important to note that the two-photon absorption resonance cross-section σ_{TPA} (eq. 5.6) is inversely proportional to Δ_c^2 (Δ_c is the detuning of coupling laser from the excited state $5^2\text{P}_{1/2}$). At high buffer gas partial pressures, a strong broadening of the excited state occurs [216], resulting in an increase in Δ_c. Since the buffer gas contributes to the population inversion required to form a N-resonance while simultaneously increasing the frequency detuning, there is an optimum for its partial pressure, as is clearly seen in fig. 5.14a.

5.4 Conclusion

In the first part of this chapter, we used forbidden transitions of Cs ($F = 3 \longrightarrow F' = 5$, more precisely $\sigma^+(\Delta m = +1)$ transitions) to create Λ-systems allowing the formation of EIT resonances. This was done in an external magnetic field, as such transitions have zero probability in the absence of a magnetic field. A NC filled with Cs vapor was used, with a thickness corresponding to the resonant wavelength of Cs D_2 line (≈ 850 nm), and the magnetic field was varied by longitudinal displacement of the permanent magnet along the propagation direction (fig. 5.4). As expected, when the coupling is blocked, small VSOP resonances are formed right at the different transition frequencies, while the coupling radiation allows for the formation of EIT resonances, spectrally narrower and with a bigger amplitude. We formed EIT resonances with 5 out of the 7 transitions depicted in fig. 5.1. This was possible up to 3 kG due to the big value of the frequency shift, reaching up to 4 MHz/G, therefore leading to EIT resonances shifted 12 GHz apart from the Cs D_2 line transition frequency [202]. This result is of great interest as the highly-shifted spectra can prove useful to be used as frequency references [18, 170], especially taking into account that these transitions are still easily recorded in strong magnetic fields. As for the theoretical description presented in section 5.2.2, further investigation is necessary, mainly in order to take into account the effect of neighboring states, and thus include more levels in the model. The complexity of the manifold and the number of coupled equations make it a challenging and computationally-intensive task. However, reasonable agreement was already achieved by simply considering an ensemble of three-level systems. To the best of our knowledge, there are no reports on obtaining EIT resonances in Λ-systems in such strong fields using the usual transitions of alkali atoms. We note that much narrower EIT resonances can be attained by using cm-long cells (to lower the effect of inelastic collisions of atoms with the windows), and by using coherently coupled probe and coupling radiations derived from a single narrow-band laser beam [75], but this implies losing the sub-Doppler structure.

In the second part, we have studied the formation of all-optical high-contrast narrow-band N-resonance in Λ-systems of ^{85}Rb D_1 line using two continuous-wave lasers. In the configurations studied in this chapter, the N-resonance consists in an increase of absorption on top of the usual Doppler-broadened (and additional broadening if the cell contains buffer gas) profile. We report for the first time the analysis of N-resonances in several Rb vapor cells containing different amounts of Ne buffer gas (from 0 to 400 Torr). It is demonstrated that the optimum of Ne partial pressure lies in the range of 6 - 30 Torr. The N-resonances can be in many ways compared to usual EIT resonances:

1. N-resonances show an increase of both absorption and resonance fluorescence, while EIT resonances show a decrease of absorption and fluorescence.
2. To obtain narrow and high-contrast N-resonances, the cell length must be quite large ($\geq \mu$m), while EIT resonances can be formed in cells as thin as 100 nm.
3. Under the same experimental parameters in the same Λ-systems, the contrast of the N-resonance is higher, meaning the SNR is bigger (see fig. 5.19).

In an external transverse magnetic field, six N-resonance components can be recorded (for ^{85}Rb D_1 line), the frequency positions of which are very well described by theoretical calculations. This statement is obviously also correct for EIT resonances. According to our expertise, forming a narrow and high-contrast N-resonance in a centimetric vapor cell is easier than forming EIT resonances while having a high SNR is crucial for applications. This is explained by the strong dependence of the N-resonance amplitude on the intensity of the coupling laser shown in fig. 5.12. Thanks to narrow linewidth and high contrast, N-resonances can have a number of important applications (as much as EIT resonances) in a variety of fields, such as information storage, quantum communication, optical magnetometry or metrology [74–76].

Conclusion and perspectives

In this thesis, we have explored the applications and benefits of using nanocells (NCs) and microcells (MCs) in atomic spectroscopy and magnetometry. Our work demonstrates how these tools can significantly improve our understanding of atom-surface interactions and the effects of magnetic fields on atomic vapors.

Initially, we modeled the cell as a Fabry–Pérot (FP) cavity, allowing us to calculate accurate transmission and selective reflection (SR) spectra that matched well with experimental data. This enabled us to investigate atom-surface interactions, identifying redshifts in transition frequencies caused by van der Waals (vdW) and dipole-dipole interactions. By considering these interactions, we refined measurements of the vdW coefficient C_3, noting a slight decrease in C_3 at smaller NC thicknesses, which is consistent with theoretical predictions of retardation effects [80, 81]. This demonstrates the utility of NC techniques for probing such interactions and suggests potential for further research in quantum optics and atomic physics.

We also examined the influence of external magnetic fields on alkali vapors, both theoretically and experimentally. Starting from the Dirac equation, we described the behavior of alkali vapors under magnetic fields, which, when combined with the FP model, enabled us to simulate sub-Doppler spectra with precise resolution of the transitions occurring between Zeeman sublevels. We studied a sodium vapor confined in a NC, highlighting its broader absorption lines due to a larger natural linewidth and lower vapor pressure. Experimentally, higher temperatures or more sensitive detectors will be necessary for accurate signal recording.

We also explored transition dipole moment cancellations in alkali isotopes, developing both analytical and numerical methods for calculating these magnetic field values. As several transitions exhibit a symmetrical behavior (one is canceled when another one is maximized), we suggested an experimental procedure relying on the measurement of higher intensity peaks to indirectly determine cancellation values, using sub-Doppler spectroscopic methods. High precision in these measurements is essential as they could be used as a standard for calibrating magnetometers or to improve fundamental physical constants.

In the context of high spatial resolution magnetometry, we showed the advantages of using NCs and MCs filled with ^{39}K. With fewer overlapping transitions and a small characteristic magnetic field value, ^{39}K-based magnetometers are well-suited for magnetic field measurements with a good spatial resolution, which could be useful in various applications such as free-electron lasers, particle accelerators, and nuclear medicine. MCs, being easier to manufacture than NCs, can also be used albeit with a smaller spatial resolution.

Additionally, we used "forbidden" transitions of cesium to create Λ-systems for electromagnetically induced transparency (EIT) resonances in strong magnetic fields, achieving highly-shifted spectra useful as frequency references [18, 170]. While further theoretical work is needed, our results already show reasonable agreement with experimental data. Finally, we studied N-resonances in ^{85}Rb, comparing them to EIT resonances, and observed that N-resonances offer higher contrast and a better signal-to-noise ratio with the use of an additional buffer gas, making them suitable for applications in quantum communication, information storage, and optical magnetometry.

In the near future, we envisage to clean up the codes and release a (Python) package allowing to generate spectra of alkali vapors taking into account the sub-Doppler geometry of the cell, similar to what has been done with `ElecSus` [162]. We are also willing to release an atlas summarizing all possible magnetic field values leading to transition cancellations of all D_1 - like and D_2 - like lines of all alkali isotopes. This would certainly help researchers willing to pursue this road to choose the most convenient isotope and transition to study. In this way, if precise measurements are performed, several values such as excited hyperfine splittings could be refined. One can also envisage the inverse process:

refining the excited state energies would be a good way to reduce the uncertainty of the cancellation values. Another thing would be to improve the precision of the magnetometer schemes presented in chapter 4. To do so, based on the work of Klinger [160], it could be a good idea to add a fully open-source computer interface to the setup and, why not, couple it to machine learning. Feeding it a database of experimental spectra measured in various conditions, it would technically be possible to make a measurement and retrieve immediately the magnetic field value. The question is to which extent would the precision be improved and whether it is worth implementing such a method. Finally, we will carry on with the theoretical calculations of EIT resonances in NCs. A Python package similar to the one released by Downes [220] for arbitrarily shaped systems with an arbitrary (but reasonable) number of levels and lasers is being written. Ideally, we would like to release such a program along with a graphical user interface.

Overall, this thesis highlights the significant potential of NCs and MCs in advancing atomic spectroscopy and atomic magnetometry. By refining theoretical models and conducting more and more precise experimental investigations, we provide research a good amount of useful data for future research. I am deeply convinced that there are still numerous opportunities for meaningful research and valuable discoveries in atomic spectroscopy.

Appendices

Appendix A

Properties of the angular momentum

In this appendix, we provide a summary of important properties related to the angular momentum that are used throughout this thesis. After recalling the commutation relations between the components of the angular momentum, we derive its eigenvalues. Then, we outline the procedure used to couple two and three angular momenta, cornerstones of the derivation of the fine and hyperfine structures. Most of the discussion is done with the total angular momentum **J***, but all the relations and conclusions also apply to other angular momentum operators, namely the electronic spin momentum operator* **S***, the orbital angular momentum* **L** *and the nuclear angular momentum* **I***.*

Contents

A.1 Quantification of the angular momentum 109
- A.1.1 Commutation relations 109
- A.1.2 Eigenvalues of the angular momentum operator 109

A.2 Coupling of angular momenta 112
- A.2.1 Coupling of two angular momenta 112
- A.2.2 Coupling of three angular momenta 114

A.3 Irreducible Tensor Operators, Wigner-Eckart theorem 115
- A.3.1 Irreducible Tensor Operators 115
- A.3.2 Wigner-Eckart theorem 116

A.1 Quantification of the angular momentum

A.1.1 Commutation relations

The total angular momentum **J** in quantum mechanics is a vector operator with components J_x, J_y and J_z obeying the following commutation relations:

$$[J_\alpha, J_\beta] = i\hbar \sum_\gamma \epsilon_{\alpha\beta\gamma} J_\gamma \,, \tag{A.1}$$

where $\epsilon_{\alpha\beta\gamma}$ is the Levi-Civita symbol, and the indices α, β, γ can take values x, y, z. With $\mathbf{J}^2 = J_x^2 + J_y^2 + J_z^2$ the square of the magnitude of the angular momentum operator, eq. (A.1) implies

$$\left[\mathbf{J}^2, J_z\right] = 0. \tag{A.2}$$

Equation (A.2) also applies to the other components J_x and J_y. The discussion is carried on with J_z as it is the most common use case, corresponding to quantization along the z-axis.

A.1.2 Eigenvalues of the angular momentum operator

From the definition of $\mathbf{J}^2$, it is obvious that

$$\left\langle \mathbf{J}^2 \right\rangle \geqslant \left\langle J_z^2 \right\rangle \,, \tag{A.3}$$

where $\langle . \rangle$ denotes the expectation value. From the mathematical definition of the variance of a discrete variable x, we have that

$$\begin{aligned} V(x) &= \frac{1}{n} \sum_{i=1}^{n} (x_i - \langle x \rangle)^2 \geqslant 0 \\ &= \left\langle x^2 \right\rangle - \langle x \rangle^2 \geqslant 0. \end{aligned} \tag{A.4}$$

Combining eq. (A.3) and eq. (A.4) yields the following very useful inequality:

$$\left\langle \mathbf{J}^2 \right\rangle \geqslant \left\langle J_z^2 \right\rangle \geqslant \left\langle J_z \right\rangle^2 \, . \tag{A.5}$$

As mentioned before, the z-axis is chosen as the quantization axis. We focus on J_z, although the relations are valid for any cartesian projection. From eq. (A.2), we can define a common eigenbasis of $\mathbf{J}^2$ and J_z such that

$$\begin{cases} \mathbf{J}^2 \left|(\kappa), \lambda, m\right\rangle = \lambda\hbar^2 \left|(\kappa), \lambda, m\right\rangle \\ J_z \left|(\kappa), \lambda, m\right\rangle = m\hbar \left|(\kappa), \lambda, m\right\rangle , \end{cases} \tag{A.6}$$

where $\lambda\hbar^2$ and $m\hbar$ are respectively the eigenvalues of $\mathbf{J}^2$ and J_z, and (κ) is a set of quantum numbers that fully describe the system[1]. The goal of this section is to determine the values of λ and m.
With the definition of the expectation value of an observable A in a normalized state $|\Psi\rangle$

$$A_\Psi = \langle \Psi | A | \Psi \rangle \, , \tag{A.7}$$

we get from eq. (A.6):

$$\begin{cases} \left\langle \mathbf{J}^2 \right\rangle = \langle (\kappa), \lambda, m | \, \mathbf{J}^2 \left|(\kappa), \lambda, m\right\rangle = \lambda\hbar^2 \\ \langle J_z \rangle = \langle (\kappa), \lambda, m | \, J_z \left|(\kappa), \lambda, m\right\rangle = m\hbar. \end{cases} \tag{A.8}$$

With eq. (A.5), we immediately deduce that $\lambda \geqslant m^2$.
For more convenience, we can combine J_x and J_y to form new (ladder) operators:

$$J_+ = J_x + iJ_y \qquad\qquad J_- = J_x - iJ_y \, . \tag{A.9}$$

These new operators exhibit useful commutation relations with J_z, namely

$$[J_z, J_\pm] = \pm\hbar J_\pm \, . \tag{A.10}$$

Applying J_z to $J_\pm \left|(\kappa), \lambda, m\right\rangle$ while keeping in mind the commutation relations eq. (A.10) gives

$$\begin{aligned} J_z J_\pm \left|(\kappa), \lambda, m\right\rangle &= (J_\pm J_z \pm \hbar J_\pm) \left|(\kappa), \lambda, m\right\rangle \\ &= J_\pm m\hbar \left|(\kappa), \lambda, m\right\rangle \pm \hbar J_\pm \left|(\kappa), \lambda, m\right\rangle \\ &= (m \pm 1)\hbar J_\pm \left|(\kappa), \lambda, m\right\rangle . \end{aligned} \tag{A.11}$$

We see that $J_\pm \left|(\kappa), \lambda, m\right\rangle$ are eigenvectors of J_z with associated eigenvalue $(m \pm 1)\hbar$. From eq. (A.6), we have

$$\begin{cases} J_z \left|(\kappa), \lambda, m \pm 1\right\rangle = (m \pm 1)\hbar \left|(\kappa), \lambda, m \pm 1\right\rangle \\ J_z(J_\pm \left|(\kappa), \lambda, m\right\rangle) = (m + 1)\hbar(J_\pm \left|(\kappa), \lambda, m\right\rangle). \end{cases} \tag{A.12}$$

Therefore, there exists a function $C_\pm(\lambda, m)$ of λ and m such that

$$J_\pm \left|(\kappa), \lambda, m\right\rangle = C_\pm(\lambda, m)\hbar \left|(\kappa), \lambda, m \pm 1\right\rangle . \tag{A.13}$$

Since $\lambda \geqslant m^2$, m necessarily has a maximum value. If we denote this maximum value $m_{\text{max}} = j$, we can write the corresponding eigenvector as $\left|(\kappa), \lambda, j\right\rangle$. However, applying the ladder operator to $\left|(\kappa), \lambda, j\right\rangle$ cannot yield a new eigenvector, thus

$$J_+ \left|(\kappa), \lambda, j\right\rangle = 0 \tag{A.14}$$

$$J_-(J_+ \left|(\kappa), \lambda, m\right\rangle = 0 \, . \tag{A.15}$$

Using the commutation relations

$$\begin{cases} [J_+, J_-] = 2\hbar J_z \\ [J_z, J_\pm] = \pm\hbar J_z \end{cases} \tag{A.16}$$

---

[1] As $\mathbf{J}^2$ is hermitian, λ is real, and same goes for m. The formulation adopted in eq. (A.6) is simply made to be consistent with the dimensions of $\mathbf{J}^2$ and J_z

allows us to write

$$\mathbf{J}^2 = J_z^2 + \frac{1}{2}(J_+J_- + J_-J_+) \tag{A.17}$$

$$J_\pm J_\mp = \mathbf{J}^2 - J_z^2 \pm \hbar J_z, \tag{A.18}$$

and, consequently, using eqs. (A.6) and (A.15), eq. (A.18) becomes

$$(\lambda - j^2 - j)\hbar^2 \left|(\kappa), \lambda, j\right\rangle = 0. \tag{A.19}$$

An analogous expression is obtained when applying the ladder operator to the minimum value j' that m can take:

$$(\lambda - j'^2 + j')\hbar^2 \left|(\kappa), \lambda, j'\right\rangle = 0\,. \tag{A.20}$$

However, both solutions are compatible only if either $j' = -j$ or $j' = j + 1$, the latter being impossible by definition. We thus finally obtain a proper expression for the eigenvalue λ of $\mathbf{J}^2$:

$$\lambda = j(j+1) \Rightarrow \left\langle \mathbf{J}^2 \right\rangle = \hbar^2 j(j+1) \text{ and } -j \leqslant m \leqslant j. \tag{A.21}$$

Applying the ladder operator J_- repeatedly to $\left|(\kappa), \lambda, j\right\rangle$ will eventually yield $\left|(\kappa), \lambda, -j\right\rangle$, or in other terms

$$(J_-)^{2j} \left|(\kappa), \lambda, j\right\rangle = C_-(\lambda, m)^{2j} \left|(\kappa), \lambda, -j\right\rangle, \tag{A.22}$$

implying that $2j \in \mathbb{N}^*$. We can now determine the expression of $C_\pm$ by calculating $\left|J_+ \left|(\kappa), \lambda, m\right\rangle\right|^2$ from eq. (A.13):

$$\begin{aligned}
&(J_+ \left|(\kappa), \lambda, m\right\rangle)^* (J_+ \left|(\kappa), \lambda, m\right\rangle) = (C_+(\lambda, m)\hbar \left|(\kappa), \lambda, m+1\right\rangle)^* C_+(\lambda, m)\hbar \left|(\kappa), \lambda, m+1\right\rangle \\
&\to \left\langle (\kappa), \lambda, m \right| J_-J_+ \left|(\kappa), \lambda, m\right\rangle = \hbar^2 \left|C_+(\lambda, m)\right| \\
&\to \left\langle (\kappa), \lambda, m \right| \mathbf{J}^2 - J_z^2 - \hbar J_z \left|(\kappa), \lambda, m\right\rangle = \hbar^2 \left|C_+(\lambda, m)\right|^2 .
\end{aligned} \tag{A.23}$$

We can rewrite eq. (A.23) as

$$\left\langle \mathbf{J}^2 \right\rangle - \left\langle J_z^2 \right\rangle - \hbar \left\langle J_z \right\rangle = \hbar^2 \left|C_+(\lambda, m)\right|^2 , \tag{A.24}$$

and we finally obtain

$$C_+(\lambda, m) = \sqrt{j(j+1) - m^2 - m} = \sqrt{j(j+1) - m(m+1)}\,. \tag{A.25}$$

Carrying the calculation with J_- gives an analogous expression for $C_-(\lambda, m)$:

$$C_-(\lambda, m) = \sqrt{j(j+1) - m^2 + m} = \sqrt{j(j+1) - m(m-1)}\,, \tag{A.26}$$

hence the final expression of $C_\pm(\lambda, m)$:

$$C_\pm(\lambda, m) = \sqrt{j(j+1) - m(m \pm 1)}\,. \tag{A.27}$$

In conclusion, we have derived the following useful relations:

$$\begin{cases}
\mathbf{J}^2 \left|(\kappa), j(j+1), m\right\rangle = \hbar^2 j(j+1) \left|(\kappa), j(j+1), m\right\rangle \\
J_z \left|(\kappa), j(j+1), m\right\rangle = m\hbar \left|(\kappa), j(j+1), m\right\rangle \\
J_\pm \left|(\kappa), j(j+1), m\right\rangle = \hbar\sqrt{j(j+1) - m(m \pm 1)} \left|(\kappa), j(j+1), m \pm 1\right\rangle .
\end{cases} \tag{A.28}$$

where $\left|(\kappa), j(j+1), m\right\rangle$ is usually written $\left|j, m\right\rangle$ since (κ) can be omitted and since there is a bijective relation between j and $j(j+1)$.

A.2 Coupling of angular momenta

Coupling of angular momenta is a very frequent phenomenon in atomic physics. Here, we look at the fundamental procedure used to couple two and three angular momenta. This is the key point of the derivation of the atomic fine (coupling of **L** and **S**) and hyperfine (coupling of **L**, **S** and **I**) structures. The coupling of more angular momenta, absolutely possible albeit quite tedious, is beyond the scope of this discussion.

A.2.1 Coupling of two angular momenta

Let us couple two quantum systems QS_1 (having a total angular momentum $\mathbf{J}_1$) and QS_2 (having a total angular momentum $\mathbf{J}_2$). If QS_1 (resp. QS_2) obeys the rules derived in section A.1, we can define according to eq. (A.28) a common eigenbasis $|j_1, m_1\rangle$ (resp. $|j_2, m_2\rangle$) of $\mathbf{J}_1^2$ and J_{1z} (resp. $\mathbf{J}_2^2$ and J_{2z}):

$$\begin{cases} \mathbf{J}_1^2 \, |j_1, m_1\rangle = \hbar^2 j_1(j_1+1) \, |j_1, m_1\rangle \\ J_{1z} \, |j_1, m_1\rangle = m_1\hbar \, |j_1, m_1\rangle \\ \mathbf{J}_2^2 \, |j_2, m_2\rangle = \hbar^2 j_2(j_2+1) \, |j_2, m_2\rangle \\ J_{2z} \, |j_2, m_2\rangle = m_2\hbar \, |j_2, m_2\rangle \, , \end{cases} \tag{A.29}$$

where $-j_i \leqslant m_i \leqslant j_i$ (with $i = 1, 2$). The tensor product of the $(2j_1+1)$ eigenvectors of QS_1 by the $(2j_2+1)$ eigenvectors of QS_2 is a possible basis of the total Hilbert space $\mathcal{H}_1 \otimes \mathcal{H}_2$. There are therefore $(2j_1+1)(2j_2+1)$ common eigenvectors of $\mathbf{J}_1^2, \mathbf{J}_2^2$, J_{1z} and J_{2z}. This basis can be indifferently denoted

$$|j_1, m_1\rangle \, |j_2, m_2\rangle \equiv |j_1 m_1, j_2 m_2\rangle \equiv |j_1 j_2, m_1 m_2\rangle \tag{A.30}$$

and is referred to as the uncoupled basis. If we consider the angular momentum of the "total" quantum system $\mathbf{J} = \mathbf{J}_1 + \mathbf{J}_2$, the Hilbert space $\mathcal{H}_1 \otimes \mathcal{H}_2$ can be also described by the following basis:

$$|j_1 j_2, jm\rangle \qquad \text{with} \qquad \begin{cases} |j_1 - j_2| \leqslant j \leqslant j_1 + j_2 \\ -j \leqslant m \leqslant j \end{cases} \tag{A.31}$$

referred to as the "coupled" basis.

Clebsch-Gordan coefficients

One can go from the uncoupled basis to the coupled via the completeness relation:

$$|j_1 j_2, jm\rangle = \sum_{m_1=-j_1}^{j_1} \sum_{m_2=-j_2}^{j_2} |j_1 m_1, j_2 m_2\rangle \, \langle j_1 m_1, j_2 m_2 | j_1 j_2, jm\rangle \, , \tag{A.32}$$

where $\langle j_1 m_1, j_2 m_2 | j_1 j_2, jm\rangle$ are Clebsch–Gordan (CG) coefficients. The opposite transformation is possible:

$$|j_1 m_1, j_2 m_2\rangle = \sum_{j=|j_1-j_2|}^{j_1+j_2} \sum_{m=-j}^{j} |j_1 j_2, jm\rangle \, \langle j_1 j_2, jm | j_1 m_1, j_2 m_2\rangle \, . \tag{A.33}$$

Since all CG coefficients are chosen to be real, we have

$$\begin{aligned} \langle j_1 m_1, j_2 m_2 | j_1 j_2, jm\rangle^* &= \langle j_1 j_2, jm | j_1 m_1, j_2 m_2\rangle \\ &= \langle j_1 m_1, j_2 m_2 | j_1 j_2, jm\rangle \, , \end{aligned} \tag{A.34}$$

which implies that CG coefficients allow to pass from one basis to the other and vice-versa. In some simple cases, CG coefficients are easy to calculate by hand. In general, for a given value of j_1 and j_2, one can show that we have the following recursive relation that allows for easier computation:

$$\begin{aligned} &\sqrt{(j \pm m)(j \mp m + 1)}\ \langle j_1 m_1, j_2 m_2 | j_1 j_2, j\ m \pm 1 \rangle \\ =&\sqrt{(j_1 \mp m_1)(j_1 \mp m_1 + 1)}\ \langle j_1\ m_1 \pm 1, j_2 m_2 | j_1 j_2, j\ m \rangle \\ +&\sqrt{(j_2 \mp m_2)(j_2 \mp m_2 + 1)}\ \langle j_1\ m_1 \pm 1, j_2\ m_2 \pm 1 | j_1 j_2, j\ m \rangle\,. \end{aligned} \tag{A.35}$$

3j-symbols

In the literature, it is common to encounter Wigner 3j-symbols. The 3j-symbols can be written in terms of CG coefficients as follows:

$$\begin{pmatrix} j_1 & j_2 & j_3 \\ m_1 & m_2 & -m_3 \end{pmatrix} = \frac{(-1)^{j_1 - j_2 + m_3}}{\sqrt{2j_3 + 1}} \langle j_1 m_1, j_2 m_2 | j_1 j_2, j_3 m_3 \rangle\,. \tag{A.36}$$

Wigner 3j-symbols are in most cases easier to handle than CG coefficients. Indeed, they exhibit interesting properties. For a 3j to be non-zero, all the following selection rules have to be satisfied:

- $-j_i < m_i < j_i$ for $i = 1, 2, 3$,
- $m_1 + m_2 + m_3 = 0$,
- $|j_1 - j_2| \leqslant j_3 \leqslant j_1 + j_2$,
- $j_1 + j_2 + j_3 \in \mathbb{N}$.

The "inverse" of eq. (A.36) reads

$$\langle j_1 m_1, j_2 m_2 | j_1 j_2, j_3 m_3 \rangle = (-1)^{-j_1 + j_2 - m_3} \sqrt{2j_3 + 1} \begin{pmatrix} j_1 & j_2 & j_3 \\ m_1 & m_2 & -m_3 \end{pmatrix}. \tag{A.37}$$

While describing the same physical phenomenon, 3j-symbols are often more convenient to work with because they exhibit a more symmetrical behavior than CG coefficients. For example:

- 3j-symbols are invariant under an even permutation of columns, while an odd permutation gives the phase factor $(-1)^{j_1 + j_2 + j_3}$:

$$\begin{pmatrix} j_1 & j_2 & j_3 \\ m_1 & m_2 & m_3 \end{pmatrix} = \begin{pmatrix} j_3 & j_1 & j_2 \\ m_3 & m_1 & m_2 \end{pmatrix} = (-1)^{j_1 + j_2 + j_3} \begin{pmatrix} j_2 & j_1 & j_3 \\ m_2 & m_1 & m_3 \end{pmatrix}, \tag{A.38}$$

- Changing the sign of all m_i gives the same phase factor:

$$\begin{pmatrix} j_1 & j_2 & j_3 \\ -m_1 & -m_2 & -m_3 \end{pmatrix} = (-1)^{j_1 + j_2 + j_3} \begin{pmatrix} j_1 & j_2 & j_3 \\ m_1 & m_2 & m_3 \end{pmatrix}. \tag{A.39}$$

Many other symmetries could be listed [128, pp. 244–248]. In our use cases, we encounter rather small quantum numbers. In the general case, 3j-symbols can be explicitly calculated with the Racah formula [221, 222]:

$$\begin{aligned} \begin{pmatrix} j_1 & j_2 & j_3 \\ m_1 & m_2 & m_3 \end{pmatrix} &= \delta_{m_1 + m_2 + m_3, 0} (-1)^{j_1 - j_2 - m_3} \sqrt{\Delta(j_1 j_2 j_3)} \\ \times\sqrt{(j_1 - m_1)!(j_1 + m_1)!(j_2 - m_2)!(j_2 + m_2)!(j_3 - m_3)!(j_3 + m_3)!} &\sum_{k=K}^{N} \frac{(-1)^k}{X}, \end{aligned} \tag{A.40}$$

where $N = \min\left(j_1 + j_2 - j_3, j_1 - m_1, j_2 + m_2\right)$, $K = \max\left(0, j_2 - j_3 - m_1, j_1 - j_3 + m_2\right)$,

$$\begin{aligned} X = k!(j_3 - j_2 + k + m_1)!(j_3 - j_1 + k - m_2)!(j_1 + j_2 - j_3 - k)! \\ \times(j_1 - k - m_1)!(j_2 - k + m_2)! \end{aligned} \tag{A.41}$$

and $\Delta(abc)$ is a triangle coefficient:

$$\Delta(abc) = \frac{(a+b-c)!(a-b+c)!(-a+b+c)!}{(a+b-c+1)!}. \tag{A.42}$$

This formulation is convenient for numerical calculations as long as the quantum numbers are small. In that case, a naive computer program can be written. For bigger quantum numbers, $3j$-symbols can be calculated using recursive formulas and making use of the symmetries.

A.2.2 Coupling of three angular momenta

Similarly, it is possible to couple three angular momenta such that $\mathbf{J} = \mathbf{J}_1 + \mathbf{J}_2 + \mathbf{J}_3$. This can be seen as the coupling of two angular momenta, one of them resulting from a prior coupling, ie. either $\mathbf{J} = \mathbf{J}_{12} + \mathbf{J}_3$, $\mathbf{J} = \mathbf{J}_1 + \mathbf{J}_{23}$ or $\mathbf{J} = \mathbf{J}_2 + \mathbf{J}_{13}$.

Recoupling coefficients

If we focus on the first coupling scheme $\mathbf{J} = \mathbf{J}_{12} + \mathbf{J}_3$, eq. (A.32) becomes

$$|j_{12} j_3, jm\rangle = \sum_{m_{12}} \sum_{m_3} |j_{12} m_{12}, j_3 m_3\rangle \langle j_{12} m_{12}, j_3 m_3 | j_{12} j_3, jm\rangle \,. \tag{A.43}$$

Keeping in mind that $\mathbf{J}_{12}$ is the result of a first coupling following the procedure described in section A.2.1, it can be shown that eq. (A.43) can be rewritten

$$\begin{aligned} |j_{12} j_3, jm\rangle = \sum_{m_{12}} \sum_{m_3} \sum_{m_1} \sum_{m_2} \sqrt{2j+1}\sqrt{2j_{12}+1} \frac{1}{(-1)^{j_{12}-j_3+m}} \frac{1}{(-1)^{j_1-j_2+m_{12}}} \\ \begin{pmatrix} j_{12} & j_3 & j \\ m_{12} & m_3 & -m \end{pmatrix} \begin{pmatrix} j_1 & j_2 & j_{12} \\ m_1 & m_2 & -m_{12} \end{pmatrix} |j_1, m_1\rangle \, |j_2, m_2\rangle \, |j_3, m_3\rangle \,, \end{aligned} \tag{A.44}$$

For the coupling scheme $\mathbf{J} = \mathbf{J}_1 + \mathbf{J}_{23}$,

$$\begin{aligned} |j_1 j_{23}, jm\rangle = \sum_{m_{23}} \sum_{m_3} \sum_{m_1} \sum_{m_2} \sqrt{2j+1}\sqrt{2j_{23}+1} \frac{1}{(-1)^{j_1-j_{23}+m}} \frac{1}{(-1)^{j_2-j_3+m_{23}}} \\ \begin{pmatrix} j_1 & j_{23} & j \\ m_1 & m_{23} & -m \end{pmatrix} \begin{pmatrix} j_2 & j_3 & j_{23} \\ m_2 & m_3 & -m_{23} \end{pmatrix} |j_1, m_1\rangle \, |j_2, m_2\rangle \, |j_3, m_3\rangle \,, \end{aligned} \tag{A.45}$$

Since the bases described by eqs. (A.44) and (A.45) describe the same physical phenomenon, there exists a unitary transformation allowing to pass from one basis to the other. One can show that this transformation reads

$$|j_1 j_{23}, jm\rangle = \sum_{j_{12}} \langle j_{12} j_3, jm | j_1 j_{23}, j'm'\rangle \, |j_{12} j_3, j'm'\rangle \, \delta_{jj'} \delta_{mm'}, \tag{A.46}$$

where $\langle j_{12} j_3, jm | j_1 j_{23}, j'm'\rangle$ are the so-called *recoupling* coefficients, the scalar product between the eigenfunctions of the two coupling schemes. These coefficients vanish unless $j = j'$ and $m = m'$. Using the properties of J_- from eq. (A.28) allows us to prove that the recoupling coefficients do not depend on m. The notation can therefore be simplified to

$$|j_1 j_{23}, jm\rangle = \sum_{j_{12}} \langle j_{12} j_3, j | j_1 j_{23}, j\rangle \, |j_{12} j_3, jm\rangle \,. \tag{A.47}$$

$6j$-symbols

The recoupling coefficients $\langle j_{12} j_3, j | j_1 j_{23}, j\rangle$ have different notations. The most used notation is the Wigner $6j$-symbol notation:

$$\begin{Bmatrix} j_1 & j_2 & j_{12} \\ j_3 & j & j_{23} \end{Bmatrix} = (-1)^{j_1+j_2+j_3+j} \frac{1}{\sqrt{(2j_{12}+1)(2j_{23}+1)}} \langle j_{12} j_3, j | j_1 j_{23}, j\rangle \,. \tag{A.48}$$

In the general case, they correspond to a sum of products of four $3j$-symbols:

$$\begin{aligned} \begin{Bmatrix} j_1 & j_2 & j_3 \\ j_4 & j_5 & j_6 \end{Bmatrix} = \sum_{m_1,\dots,m_6} (-1)^{\sum_{k=1}^{6}(j_k-m_k)} & \begin{pmatrix} j_1 & j_2 & j_3 \\ -m_1 & -m_2 & -m_3 \end{pmatrix} \begin{pmatrix} j_1 & j_5 & j_6 \\ m_1 & -m_5 & m_6 \end{pmatrix} \\ & \times \begin{pmatrix} j_4 & j_2 & j_6 \\ m_4 & m_2 & -m_6 \end{pmatrix} \begin{pmatrix} j_4 & j_5 & j_3 \\ -m_4 & m_5 & m_3 \end{pmatrix}, \end{aligned} \tag{A.49}$$

where the summation is performed over the six m_i values allows by the selection rules on $3j$-symbols mentioned in section A.2.1. They can also be computed using the Racah formula:

$$\begin{Bmatrix} j_1 & j_2 & j_3 \\ j_4 & j_5 & j_6 \end{Bmatrix} = \sqrt{\Delta(j_1 j_2 j_3)\Delta(j_1 j_5 j_6)\Delta(j_4 j_2 j_6)\Delta(j_4 j_5 j_3)} \sum_k \frac{(-1)^k (k+1)!}{X}, \tag{A.50}$$

where $\Delta(abc)$ is a triangle coefficient [eq. (A.42)] and

$$\begin{aligned} X = & (k-j_1-j_2-j_3)!(k-j_1-j_5-j_6)!(k-j_4-j_2-j_6)!(k-j_4-j_5-j_3)! \\ & \times (j_1+j_2+j_4+j_5-k)!(j_2+j_3+j_5+j_6-k)!(j_3+j_1+j_6+j_4-k)!. \end{aligned} \tag{A.51}$$

As the $3j$-symbols, $6j$-symbols have many symmetries. They are invariant

- under any column permutation:

$$\begin{Bmatrix} j_1 & j_2 & j_3 \\ j_4 & j_5 & j_6 \end{Bmatrix} = \begin{Bmatrix} j_2 & j_1 & j_3 \\ j_5 & j_4 & j_6 \end{Bmatrix} = \begin{Bmatrix} j_1 & j_3 & j_2 \\ j_4 & j_6 & j_5 \end{Bmatrix} = \begin{Bmatrix} j_3 & j_2 & j_1 \\ j_6 & j_5 & j_4 \end{Bmatrix}, \tag{A.52}$$

- if the lower and upper argument of two columns are interchanged:

$$\begin{Bmatrix} j_1 & j_2 & j_3 \\ j_4 & j_5 & j_6 \end{Bmatrix} = \begin{Bmatrix} j_4 & j_5 & j_3 \\ j_1 & j_2 & j_6 \end{Bmatrix} = \begin{Bmatrix} j_1 & j_5 & j_6 \\ j_4 & j_2 & j_3 \end{Bmatrix} = \begin{Bmatrix} j_4 & j_2 & j_6 \\ j_1 & j_5 & j_3 \end{Bmatrix}. \tag{A.53}$$

Computing CG coefficients, $3j$- and $6j$-symbols by hand can however be a tedious task. Many tables or online calculators are available. Throughout this thesis, all coefficients have been calculated using a self-made Python program[2].

A.3 Irreducible Tensor Operators, Wigner-Eckart theorem

A.3.1 Irreducible Tensor Operators

Let us consider a spherical vector operator **V**, sometimes also called a tensorial operator of rank 1, denoted $\mathbf{V}^{(1)}$. Its three components are

$$V_0^{(1)} = V_z \qquad V_{\pm 1}^{(1)} = \mp \frac{1}{\sqrt{2}} \left(V_x \pm i V_y\right). \tag{A.54}$$

---

[2] `https://github.com/momierr/wigner`

They obey the following relations:

$$\begin{cases} [J_\pm, V_q^{(1)}] = \hbar\sqrt{1(1+1) - q(q\pm 1)}\, V_{q\pm 1}^{(1)} \\ [J_z, V_q^{(1)}] = \hbar q V_q^{(1)} \end{cases} \quad \text{with } q = -1, 0, 1. \tag{A.55}$$

This can be generalized to the $(2k+1)$ components of an irreducible tensor operator (ITO)[3] $T_q^{(k)}$ of rank k:

$$\begin{cases} [J_\pm, T_q^{(k)}] = \hbar\sqrt{k(k+1) - q(q\pm 1)}\, T_{q\pm 1}^{(k)} \\ [J_z, T_q^{(k)}] = \hbar q T_q^{(k)}. \end{cases} \tag{A.56}$$

Such an operator can be built by taking the direct product of an ITO **V** of rank k_1 with an ITO **W** of rank k_2. This gives a relation analogous to eq. (A.32):

$$T_q^{(k)} = \left[V^{(k_1)} \times V^{(k_2)}\right]_q^{(k)} = \sum_{q_1=-k_1}^{k_1} \sum_{q_2=-k_2}^{k_2} \langle k_1 q_1, k_2 q_2 | k_1 k_2, kq\rangle\, V_{q_1}^{(k_1)} V_{q_2}^{(k_2)}. \tag{A.57}$$

A.3.2 Wigner-Eckart theorem

From eq. (A.56), we know that an ITO of rank k verifies

$$J_z T_q^{(k)} - T_q^{(k)} J_z = \hbar q T_q^{(k)}, \tag{A.58}$$

which yields

$$\langle(\alpha'), j'm'|J_z T_q^{(k)}|(\alpha), jm\rangle - \langle(\alpha'), j'm'|T_q^{(k)} J_z|(\alpha), jm\rangle = \hbar q \,\langle(\alpha'), j'm'|T_q^{(k)}|(\alpha), jm\rangle\,, \tag{A.59}$$

where (α) and (α') denote a set of quantum numbers completely characterizing the quantum system[4]. From the recursion relation given in eq. (A.35) by changing the notation ($j_1 = j$, $j_2 = k$, $j = j'$, $m_1 = m$, $m_2 = q$ and $m = m'$), it is possible to show that the matrix elements of the ITOs satisfy the same relations as CG coefficients. It is possible to “factor" the dependence on m, m', and q, ie. separate factors depending on the geometry of the system from those representing its physical characteristics. This is knows as the Wigner–Eckart (WE) theorem:

$$\langle(\alpha'), j'm'|T_q^{(k)}|(\alpha), jm\rangle\,, = \langle jm, kq|jk, j'm'\rangle\,\langle(\alpha'), j'\|T^{(k)}\|(\alpha), j\rangle\,. \tag{A.60}$$

One often finds the WE theorem formulated as follows:

$$\langle(\alpha), jm|T_q^{(k)}|(\alpha'), j'm'\rangle = (-1)^{j-m}\begin{pmatrix} j & k & j' \\ -m & q & m' \end{pmatrix}\langle(\alpha), j\|T^{(k)}\|(\alpha'), j'\rangle\,, \tag{A.61}$$

where $\langle(\alpha), j\|T^{(k)}\|(\alpha'), j'\rangle$ is the so-called reduced matrix element, independent of the quantization axis. The coefficient $\langle(\alpha), jm|T_q^{(k)}|(\alpha'), j'm'\rangle$ is 0 unless $\Delta m = q$, $j - k \leqslant j' \leqslant j + k$ and $j + j' \geqslant k$. This gives, for an ITO of rank $k = 1$ the selection rules:

- $\Delta j = 0, \pm 1$,
- $\Delta m = 0$,
- $j + j' \geqslant 1$.

---

[3] A tensor operator $T_q^{(k)}$ $(k \leqslant q \leqslant +k)$ is said to be irreducible if its $(2k+1)$ components are transformed into linear combinations of themselves under a rotation of the coordinate system. $T_q^{(k)} = 0$ unless $|q| \leqslant k$.

[4] For example $|nlm\rangle$ for the hydrogen atom.

Applying the WE theorem to the ITO $T_0^{(1)} = J_0^{(1)}$ gives

$$\langle J, m | J_0^{(1)} | J', m' \rangle = (-1)^{J-m} \begin{pmatrix} J & 1 & J' \\ -m & 0 & m' \end{pmatrix} \langle J \| J^{(1)} \| J' \rangle \,. \tag{A.62}$$

Keeping in mind that, as derived earlier, $\langle J, m | J_0^{(1)} | J', m' \rangle = \hbar m \delta_{JJ'} \delta_{mm'}$, and knowing that

$$\begin{pmatrix} J & 1 & J \\ -m & 0 & m' \end{pmatrix} = (-1)^{J-m} \frac{m}{\sqrt{J(J+1)(2J+1)}} \delta_{mm'}, \tag{A.63}$$

it directly comes that the reduced matrix element of $J^{(1)}$ reads

$$\langle J \| J^{(1)} \| J' \rangle = \hbar \sqrt{J(J+1)(2J+1)}\, \delta_{JJ'} \,. \tag{A.64}$$

Generalizing for every component of J, eq. (A.62) becomes

$$\langle Jm | \, J_q^{(1)} \, | J'm' \rangle = (-1)^{J-m} \begin{pmatrix} J & 1 & J' \\ -m & q & m' \end{pmatrix} \hbar \sqrt{J(J+1)(2J+1)}\, \delta_{JJ'} \,. \tag{A.65}$$

This relation is also valid for **L** and **S**. Another interesting property is that if we take an ITO $T^{(k)}$ that acts only on $|(\alpha_1), j_1 m_1\rangle$, one can show that the reduced elements in the coupled basis are related to those of the uncoupled basis by

$$\begin{aligned} \langle (\alpha_1) j_1, (\alpha_2) j_2, j \| T^{(k)} \| (\alpha_1') j_1', (\alpha_2') j_2', j' \rangle &= (-1)^{j_1 + j_2 + j' + k} \sqrt{2j+1}\sqrt{2j'+1}\, \delta_{\alpha_2 j_2, \alpha_2' j_2'} \\ &\times \begin{Bmatrix} j_1 & j_2 & j \\ j' & k & j_1' \end{Bmatrix} \langle (\alpha_1), j_1 \| T^{(k)} \| (\alpha_1'), j_1' \rangle \,, \end{aligned} \tag{A.66}$$

and analogously if $T^{(k)}$ only acts on $|(\alpha_2), j_2 m_2\rangle$:

$$\begin{aligned} \langle (\alpha_1) j_1, (\alpha_2) j_2, j \| T^{(k)} \| (\alpha_1') j_1', (\alpha_2') j_2', j' \rangle &= (-1)^{j_1 + j_2' + j + k} \sqrt{2j+1}\sqrt{2j'+1}\, \delta_{\alpha_1 j_1, \alpha_1' j_1'} \\ &\times \begin{Bmatrix} j_1 & j_2 & j \\ k & j' & j_2' \end{Bmatrix} \langle (\alpha_2), j_2 \| T^{(k)} \| (\alpha_2'), j_2' \rangle \,. \end{aligned} \tag{A.67}$$

The WE theorem is extremely useful when handling matrix elements of different angular momentum operators. It can also, for example, be used to calculate the matrix elements of $x = (R_{-1}^{(1)} - R_1^{(1)})/\sqrt{2}$, $y = i(R_{-1}^{(1)} + R_1^{(1)})/\sqrt{2}$ and $z = R_0^{(1)}$ in the wavefunctions of the hydrogen atom.

Appendix B

Properties of alkali atoms

In this appendix, we provide a number of numerical values used in the computations performed in this thesis. These values relate to the hyperfine structure of various alkali isotopes and are all either taken from the literature or recalculated. When possible, the bibliographic reference corresponding to the value is provided.

Contents

B.1 Hyperfine structure 119
B.2 Data tables 120

B.1 Hyperfine structure

In fig. B.1 we recall the hyperfine structure of Rb, Na, Cs, and ^{39}K D lines. The hyperfine splittings are taken from various articles, see tables B.1 to B.3.

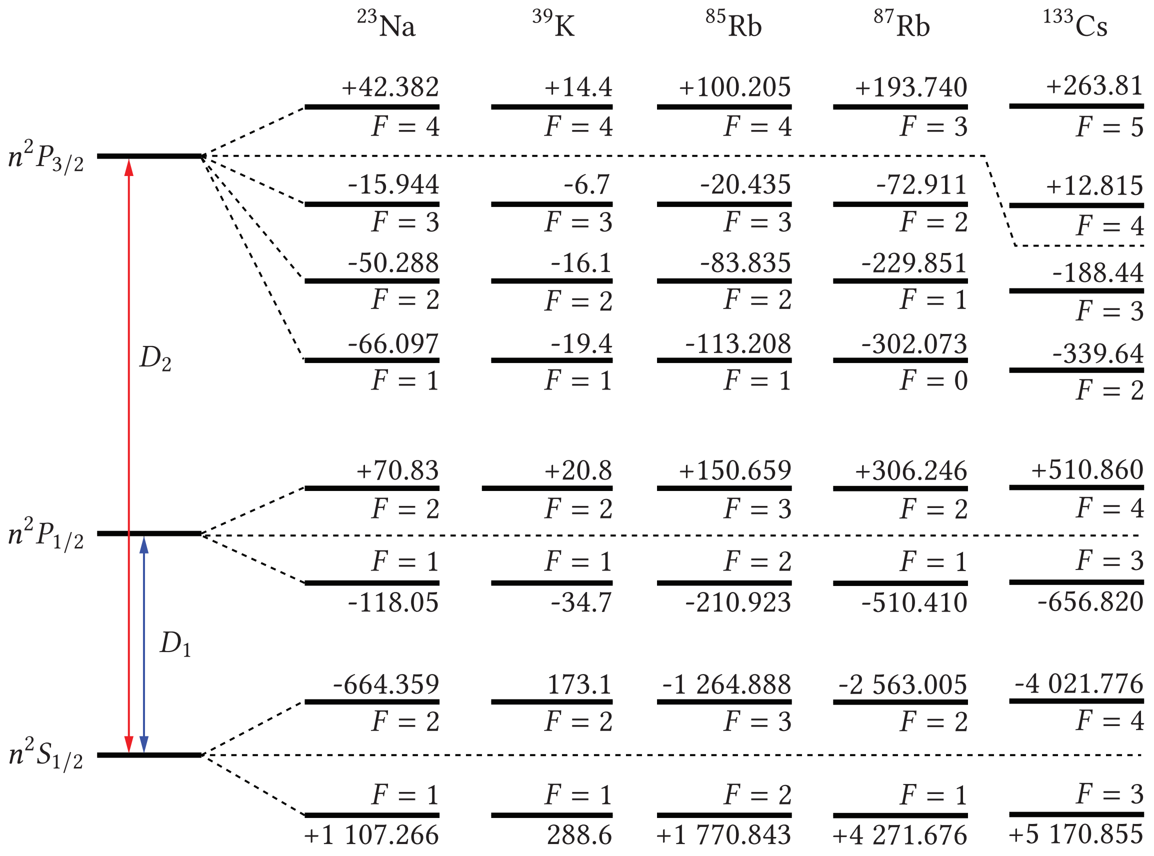
^{23}Na
^{39}K
^{85}Rb
^{87}Rb
^{133}Cs
$n^2P_{3/2}$
+42.382
F = 4
+14.4
F = 4
+100.205
F = 4
+193.740
F = 3
+263.81
F = 5
-15.944
F = 3
-6.7
F = 3
-20.435
F = 3
-72.911
F = 2
+12.815
F = 4
-50.288
F = 2
-16.1
F = 2
-83.835
F = 2
-229.851
F = 1
-188.44
F = 3
-66.097
F = 1
-19.4
F = 1
-113.208
F = 1
-302.073
F = 0
-339.64
F = 2
D_2
$n^2P_{1/2}$
+70.83
F = 2
+20.8
F = 2
+150.659
F = 3
+306.246
F = 2
+510.860
F = 4
F = 1
-118.05
F = 1
-34.7
F = 2
-210.923
F = 1
-510.410
F = 3
-656.820
D_1
$n^2S_{1/2}$
-664.359
F = 2
173.1
F = 2
-1 264.888
F = 3
-2 563.005
F = 2
-4 021.776
F = 4
F = 1
+1 107.266
F = 1
288.6
F = 2
+1 770.843
F = 1
+4 271.676
F = 3
+5 170.855

Figure B.1 – Hyperfine structure of Na, ^{39}K, Rb and Cs D line. The energies are rounded and given in MHz with respect to the fine states.

B.2 Data tables

In tables B.1 to B.3, we provide recent atomic and optical constants of the main alkali isotopes. These tables are not meant to be a comprehensive review of the literature, but only a support to help the interested reader find easily numerical data required in most application cases. Bibliographic references are provided when available. Most of the data comes from experimental measurements, some parameters are recalculated. For example, the transition strengths $S_{FF'}$ between two hyperfine states F and F' are computed as follows:

$$S_{FF'} = \sum_q (2F'+1)(2J+1) \begin{Bmatrix} J & J' & 1 \\ F' & F & 1 \end{Bmatrix}^2 . \tag{B.1}$$

As it can be verified in tables B.1 to B.3, the transition strengths verify

$$\sum_{F'} S_{FF'} = 1. \tag{B.2}$$

	Notation	^{133}Cs		Ref.
Atomic number	Z	37		
Abundance [%]	η	72.17(2)		[223]
Principal quantum number	n	55		
Atomic mass [u]	m_a	132.905 451 931(27)		[224]
Nuclear spin	I	7/2		
Magnetic dipole constant [h·MHz]	A_{hfs} ($n^2S_{1/2}$)	2 298.157 942 5		[6]
	A_{hfs} ($n^2P_{1/2}$)	291.920(19)		[152, 153]
	A_{hfs} ($n^2P_{3/2}$)	50.275(3)		[225]
Electric quadrupole constant [h·MHz]	B_{hfs} ($n^2P_{3/2}$)	-0.53(2)		[225]
Landé factors	g_S	2.002 319 304 362 56(35)		[163]
	g_L	0.999 995 87		
	g_I	-0.000 398 853 95(52)		[6]
	g_J ($n^2S_{1/2}$)	2.002 540 32(20)		
	g_J ($n^2P_{1/2}$)	0.665 90(9)		
	g_J ($n^2P_{3/2}$)	1.3340(3)		
Transition wavelength in vacuum [nm]	λ_{D_1}	894.592 959 86(11)		[152]
	λ_{D_2}	852.347 275 82(27)		[226]
Transition frequency [2π·THz]	$\omega_0^{D_1}$	335.116 048 807(41)		[152]
	$\omega_0^{D_2}$	351.725 718 50(11)		[226]
Natural linewidth [2π·MHz]	Γ_{D_1}	4.561 2(57)		[227–229]
	Γ_{D_2}	5.222 7(66)		
Relative $F \longrightarrow F'$ transition strength	$S_{FF'}$ (D_1)	$S_{33} = 1/4$	$S_{34} = 3/4$	Recalculated
		$S_{43} = 7/12$	$S_{44} = 5/12$	
	$S_{FF'}$ (D_2)	$S_{32} = 5/14$	$S_{43} = 7/12$	
		$S_{33} = 3/8$	$S_{44} = 7/24$	
		$S_{34} = 15/56$	$S_{45} = 11/18$	

Table B.1 – Summary of different physical and optical constants of ^{133}Cs, with their respective unit. When possible, the uncertainty on the value and the bibliographic reference are provided.

	Notation	^{23}Na		Ref.	^{39}K		Ref.
Atomic number	Z	11			19		
Abundance [%]	η	100		[223]	93.2581		[223]
Principal quantum number	n	3			4		
Atomic mass [u]	m_a	22.989 769 280 7(28)		[224]	38.963 706 68(20)		[155]
Nuclear spin	I	3/2			3/2		
Magnetic dipole constant [h·MHz]	A_{hfs} ($n^2S_{1/2}$)	885.813 064 4(5) MHz		[6]	230.859 860 1(3)		[6]
	A_{hfs} ($n^2P_{1/2}$)	94.44(13) MHz		[145]	27.775(42)		[146]
	A_{hfs} ($n^2P_{3/2}$)	18.534(15) MHz		[230]	6.093(25)		
Electric quadrupole constant [h·MHz]	B_{hfs} ($n^2P_{3/2}$)	2.724(30) MHz			2.786(71)		
Landé factors	g_S	2.002 319 304 362 56(35)		[163]	2.002 319 304 362 56(35)		[163]
	g_L	0.99997613			0.999 985 916 978 925		
	g_I	-0.000 804 610 8(8)		[6]	-0.000 141 934 89(12)		[6]
	g_J ($n^2S_{1/2}$)	2.002 296 0(7)			2.00229421		
	g_J ($n^2P_{1/2}$)	0.665 81(12)			2/3		
	g_J ($n^2P_{3/2}$)	1.334 2(2)			4/3		
Transition wavelength in air [nm]	λ_{D_1}	589.756 661 7(15)		[5]	770.108 385 049(123)		[146]
	λ_{D_2}	589.158 326 4(15)			766.700 921 822(24)		
Transition frequency [2π·THz]	$\omega_0^{D_1}$	508.3324657			389.286 058 716(62)		
	$\omega_0^{D_2}$	508.8487162			391.016 170 03(12)		
Natural linewidth [2π·MHz]	Γ_{D_1}	9.765(13)			5.956(11)		[231]
	Γ_{D_2}	9.795(11)			6.035(11)		
Relative $F \longrightarrow F'$ transition strength	$S_{FF'}$ (D_1)	$S_{11} = 1/6$	$S_{21} = 1/2$	Recalculated	$S_{11} = 1/6$	$S_{21} = 1/2$	Recalculated
		$S_{12} = 5/6$	$S_{22} = 1/2$		$S_{12} = 5/6$	$S_{22} = 1/2$	
	$S_{FF'}$ (D_2)	$S_{10} = 1/6$	$S_{21} = 1/20$		$S_{10} = 1/6$	$S_{21} = 1/20$	
		$S_{11} = 5/12$	$S_{22} = 1/4$		$S_{11} = 5/12$	$S_{22} = 1/4$	
		$S_{12} = 5/12$	$S_{23} = 7/10$		$S_{12} = 5/12$	$S_{23} = 7/10$	

Table B.2 – Summary of different physical and optical constants of ^{23}Na and ^{39}K, with their respective unit. When possible, the uncertainty on the value and the bibliographic reference are provided.

	Notation	^{85}Rb		Ref.	^{87}Rb		Ref.
Atomic number	Z	37			37		
Abundance [%]	η	72.17(2)		[223]	27.83(2)		[223]
Principal quantum number	n	5			5		
Atomic mass [u]	m_a	84.911 789 732(14)		[224]	86.909 180 520(15)		[224]
Nuclear spin	I	5/2			3/2		
Magnetic dipole constant [h·MHz]	A_{hfs} ($n^2S_{1/2}$)	1 011.910 813 0(20)		[6]	3 417.341 305 452 15(5)		[151]
	A_{hfs} ($n^2P_{1/2}$)	120.527(56)		[148, 149]	408.328(15)		[149]
	A_{hfs} ($n^2P_{3/2}$)	25.0020(99)		[6, 148]	84.7185(20)		[158]
Electric quadrupole constant [h·MHz]	B_{hfs} ($n^2P_{3/2}$)	25.790(93)			12.496 5(37)		
Landé factors	g_S	2.002 319 304 362 56(35)		[163]	2.002 319 304 362 56(35)		[163]
	g_L	0.999 993 54			0.999 993 69		
	g_I	-0.000 293 640 00(60)		[6]	-0.000 995 141 4(10)		[6]
	g_J ($n^2S_{1/2}$)	2.002 331 070(26)			2.002 331 13(20)		
	g_J ($n^2P_{1/2}$)	0.666			0.666		
	g_J ($n^2P_{3/2}$)	1.334 10(20)			1.336 2(13)		
Transition wavelength in vacuum [nm]	λ_{D_1}	794.979 014 933(96)		[149, 158]	794.978 850 9(8)		[149]
	λ_{D_2}	780.241 368 271(27)		[148, 149]	780.241 209 686(13)		[158]
Transition frequency [2π·THz]	$\omega_0^{D_1}$	377.107 385 690(46)		[149, 158]	377.107 463 5(4)		[149]
	$\omega_0^{D_2}$	384.230 406 373(14)		[148, 149]	384.230 484 468 5(62)		[158]
Natural linewidth [2π·MHz]	Γ_{D_1}	5.7500(56)		[232–235]	5.746(8)		[232]
	Γ_{D_2}	6.0666(18)			6.065(9)		
Relative $F \longrightarrow F'$ transition strength	$S_{FF'}$ (D_1)	$S_{22} = 2/9$	$S_{23} = 7/9$	Recalculated	$S_{11} = 1/6$	$S_{12} = 5/6$	Recalculated
		$S_{32} = 5/9$	$S_{33} = 4/9$		$S_{21} = 1/2$	$S_{22} = 1/2$	
	$S_{FF'}$ (D_2)	$S_{21} = 3/10$	$S_{32} = 5/63$		$S_{10} = 1/6$	$S_{21} = 1/20$	
		$S_{22} = 7/18$	$S_{33} = 5/18$		$S_{11} = 5/12$	$S_{22} = 1/4$	
		$S_{23} = 14/45$	$S_{34} = 9/14$		$S_{12} = 5/12$	$S_{23} = 7/10$	

Table B.3 – Summary of different physical and optical constants of ^{85}Rb and ^{87}Rb, with their respective unit. When possible, the uncertainty on the value and the bibliographic reference are provided.

Appendix C

Semi-classical atom-light interactions

In this appendix, we recall the main lines of the density matrix formalism for an ensemble of atoms interacting with a classical light field. We then build the interaction Hamiltonian of a three-level Λ-system using the dipole and rotating wave approximations and briefly explain the phenomenon of EIT in the dark state formalism.

Contents

C.1 Density matrix formalism **123**
  C.1.1 Definition 123
  C.1.2 Liouville equation of motion 124
  C.1.3 Building the system of equations 125
C.2 Interaction with a laser field **125**
  C.2.1 Electric Dipole Approximation 125
  C.2.2 Rotating wave approximation 126
C.3 Three-level Λ system **126**
  C.3.1 Building the interaction Hamiltonian 126
  C.3.2 Dark state, Electromagnetically-Induced Transparency 128

C.1 Density matrix formalism

Let us consider a quantum atom interacting with a classical electromagnetic field [236, 237]. The well-known time-dependent Schrödinger equation

$$i\hbar\frac{\partial}{\partial t}\left|\Psi\right\rangle = \mathcal{H}\left|\Psi\right\rangle \tag{C.1}$$

describes the evolution of the atomic wavefunction $\left|\Psi\right\rangle$, where $\mathcal{H}$ is the Hamiltonian of the system and

$$\left|\Psi\right\rangle = \sum_n c_n(t)\left|\psi_n\right\rangle . \tag{C.2}$$

The probability p_n of finding the system in the state $\left|\psi_n\right\rangle$ at any time t is given by

$$p_n = |c_n(t)|^2 = |\left\langle\psi_n|\,\Psi\right\rangle|. \tag{C.3}$$

This works very well for single atoms. However, for a large number of atoms, it is better to use a statistical method such as the density matrix formalism [23, 106].

C.1.1 Definition

For a pure state $\left|\Psi\right\rangle$, the density matrix ρ is defined as

$$\rho = \left|\Psi\right\rangle\left\langle\Psi\right| . \tag{C.4}$$

The diagonal elements $\rho_{nn} = \langle\Psi_n|\rho|\Psi_n\rangle$ thus represent the probabilities to find the system in a given state, they are called populations. The off-diagonal terms ρ_{nm}, called coherences, are expressed as

$$\rho_{nm} = \langle\Psi_n|\rho|\Psi_m\rangle = c_n(t)c_m^*(t). \tag{C.5}$$

For a mixed state (an ensemble of particles), the density matrix is defined as

$$\rho = \sum_i p_i\left|\Psi_i\right\rangle\left\langle\Psi_i\right| , \tag{C.6}$$

where p_i is the probability of finding the system in state $|\Psi_i\rangle$. The density matrix allows to calculate the statistical average of a given observable. In experiments, one measures the expectation value of the observable. The expectation value of an observable $\mathcal{A}$ reads

$$\langle \mathcal{A} \rangle = \sum_i p_i \, |\Psi_i\rangle \, \mathcal{A} \, \langle \Psi_i| \, . \tag{C.7}$$

Introducing the completeness relation[1] allows to rewrite eq. (C.7) as

$$\begin{aligned} \langle \mathcal{A} \rangle &= \sum_i p_i \, \langle \Psi_i| \, \mathcal{A} \sum_n |\psi_n\rangle \, \langle \psi_n| \, |\Psi_i\rangle \\ &= \sum_n \sum_i p_i \, \langle \Psi_i| \, \psi_n\rangle \, \langle \psi_n| \, \mathcal{A} |\Psi_i\rangle \\ &= \mathrm{Tr}(\rho \mathcal{A}), \end{aligned} \tag{C.8}$$

where $\mathrm{Tr}(\rho) = \sum_n \langle \psi_n | \rho | \psi_n \rangle$ is the trace.

C.1.2 Liouville equation of motion

Let us now take a look at the time evolution of the density matrix. The conjugate of eq. (C.1) is

$$-i\hbar \frac{\partial}{\partial t} \langle \Psi| = \langle \Psi| \, \mathcal{H}. \tag{C.9}$$

Differentiating eq. (C.4) and combining with eqs. (C.1) and (C.9) yields

$$\begin{aligned} \frac{\partial}{\partial t} \rho &= \frac{1}{i\hbar} \mathcal{H} \, |\Psi\rangle \, \langle \Psi| - \frac{1}{i\hbar} \, |\Psi\rangle \, \langle \Psi| \, \mathcal{H} \\ &= \frac{1}{i\hbar} [\mathcal{H}, \rho]. \end{aligned} \tag{C.10}$$

Equation (C.10) is called the Liouville - von Neumann equation of motion. This formalism is well suited for the inclusion of statistical effects. An ensemble of moving atoms will be described by the density matrix $\rho(v, t)$. Its time evolution is given by the Liouville - von Neumann equation, but the expectation values of the operators in this case become

$$\mathcal{A} = \int M(v) \mathrm{Tr}(\rho \mathcal{A}) \mathrm{d}v \tag{C.11}$$

where $M(v)$ is a velocity (typically Maxwell–Boltzmann) distribution. Phenomenological processes such as relaxation $\mathcal{R}$ (spontaneous decay, collisional decay, ...) or repopulation Λ (spontaneous transfer, ...) can also be easily included in this formalism by including the Lindblad operator $\mathcal{L}$. The Liouville - von Neumann equation then becomes

$$\begin{aligned} i\hbar \frac{\partial}{\partial t} \rho &= [\mathcal{H}, \rho] - i\hbar \, \{\mathcal{R}, \rho\} + i\hbar \Lambda \\ &= \frac{i}{\hbar} [\mathcal{H}, \rho] + \mathcal{L}(\rho), \end{aligned} \tag{C.12}$$

where $\{a, b\}$ is the anti-commutator.

---

[1] $\{\psi_n\}$ being an orthonormal basis of the Hilbert space, one has $\sum_n |\psi_n\rangle \, \langle \psi_n| = \mathrm{Id}$.

C.1.3 Building the system of equations

To build the density matrix, one may use the formulas from [106, Chap. 6]. The equations for the populations and coherences read

$$\frac{\partial}{\partial t}\rho_{mm} = -\frac{i}{\hbar}\sum_{n}\left[\mathcal{H}_{mn}\rho_{nm} - \rho_{mn}\mathcal{H}_{nm}\right] - \mathcal{R}_{mm}\rho_{mm} + \sum_{n\neq m}\Gamma_{nm}\rho_{nn} \tag{C.13}$$

$$\frac{\partial}{\partial t}\rho_{m'm} = -\frac{i}{\hbar}\sum_{n}\left(\mathcal{H}_{m'n}\rho_{nm} - \rho_{m'n}\mathcal{H}_{nm}\right) - \mathcal{R}_{m'm}\rho_{m'm}, \tag{C.14}$$

where $\mathcal{R}_{m'm}$ is given by

$$\mathcal{R}_{m'm} = \frac{1}{2}\left(\sum_{n\neq m'}\Gamma_{m'n} + \sum_{n\neq m}\Gamma_{mn}\right) + \left[1-\delta(m,m')\right]\gamma^{c}_{m'm}. \tag{C.15}$$

In this equation, Γ_{nm} parametrizes the flow of population from state $|n\rangle$ to state $|m\rangle$ at a rate $\tau_{nm} = 1/\Gamma_{nm}$, $\gamma^{c}_{m'm}$ represents an additional decoherence rate, due for example to collisions. Let us note that $\mathcal{R}_{nn} = \sum_{m\neq n}\Gamma_{nm}$ for a closed system (which is the case in our studies).

C.2 Interaction with a laser field

The Hamiltonian $\mathcal{H}$ is made up of two parts:

$$\mathcal{H} = \mathcal{H}_0 + \mathcal{H}_{\text{int}}(t), \tag{C.16}$$

where $\mathcal{H}_0$ is the atomic Hamiltonian in the absence of external radiation, and $\mathcal{H}_{\text{int}}(t)$ describes the interaction of the atom with a time-dependent electromagnetic field $\mathbf{E}$ [typically a continuous wave (CW) laser]. The latter interaction Hamiltonian takes the form

$$\mathcal{H}_{\text{int}}(t) = -\mathbf{d}\cdot\mathbf{E}, \tag{C.17}$$

where $\mathbf{d} = e\mathbf{r}$ is the dipole operator and $\mathbf{E}$ is assumed to be a plane wave

$$\mathbf{E}(\mathbf{r},t) = E_0\exp[-i(\omega t - \mathbf{k}\cdot\mathbf{r})]\mathbf{e} + \text{c.c.} \tag{C.18}$$

of complex amplitude E_0, wavevector $\mathbf{k}$ and polarized along $\mathbf{e}$.

C.2.1 Electric Dipole Approximation

The Electric Dipole Approximation consists in neglecting the spatial phase shift of the wave over the effective atomic space. We explain it hereafter in a simple way; a far more elaborated discussion can be found in [238, Sec. 24.5]. In eq. (C.18), $\mathbf{k}\cdot\mathbf{r} = 2\pi r/\lambda$. The atomic radius r_a of the “biggest” alkali atom studied in this thesis (cesium) is $r_a \sim 0.26$ nm. Thus, for wavelengths around 500 nm, $r/\lambda = 0.26/500 \simeq 5\times10^{-4} \ll 1$ and therefore

$$\exp(i\mathbf{k}\cdot\mathbf{r}) \sim 1 \quad \text{and} \quad \mathbf{E}(\mathbf{r},t) \simeq 2E_0\cos(\omega t)\mathbf{e}. \tag{C.19}$$

One would have arrived at the same conclusion with either the Bohr radius, the covalent radius, the van der Waals radius, or the atomic radius as they all range from 0.05 to 0.3 nm. The matrix elements $\mathcal{H}_{ij}$ of the interaction Hamiltonian thus reduce to

$$\mathcal{H}_{ij} = -d_{ij}\cdot E_0\left[\exp(-i\omega t) + \exp(i\omega t)\right]\mathbf{e}_d\cdot\mathbf{e}, \tag{C.20}$$

with $\mathbf{e}_d\cdot\mathbf{e} \sim 1$ if the dipole is aligned with the laser field. The matrix elements of the dipole moment d_{ij} are

$$d_{ij} = e\langle j|r|i\rangle = e\int \mathrm{d}\tau\Psi_j^{*}r\Psi_i = \exp[-i\omega_{ij}t]\left|d_{ij}\right|, \tag{C.21}$$

with $\omega_{ji} = (E_j - E_i)/\hbar$ the transition frequency between two bare states and

$$\left|d_{ij}\right| = \int d\tau\varphi_j^*(r)r\varphi_i(r). \tag{C.22}$$

Let us note that as the dipole operator is an odd function, the only possibility for the previous integral to be non-zero is to be evaluated between states of opposite parity.

C.2.2 Rotating wave approximation

Using eqs. (C.20) and (C.21) the matrix elements of the interaction Hamiltonian become

$$\mathcal{H}_{ij} = -|d_{ij}| \left(E_0 \exp[-i(\omega + \omega_{ij})t] + E_0^* \exp[i(\omega - \omega_{ij})t]\right). \tag{C.23}$$

For near-resonant light, one has $\omega - \omega_{ij} \ll 1$, while the term $\exp[-i(\omega + \omega_{ij})t]$ oscillates much faster than $\exp[i(\omega - \omega_{ij})t]$ because $\omega - \omega_{ij} \ll \omega + \omega_{ij}$. The rotating wave approximation (RWA), see e.g. [236, Sec. V. A. 3], then consists in neglecting the fast oscillating terms as they will average to zero on any physical time scale. Thus, eq. (C.23) may be simplified to

$$\mathcal{H}_{ij} = -\hbar\Omega_{ij} \exp(i\Delta t), \tag{C.24}$$

where $\Delta = \omega - \omega_{ij}$ is the detuning between the laser field and the transition frequency. The Rabi frequency Ω is defined as

$$\Omega_{ij} = \frac{|d_{ij}|E_0}{\hbar}. \tag{C.25}$$

In a closed non-lossy system, the Rabi frequency can be assumed real. However, applying the RWA one may lose some physical effects such as the Bloch-Siegert [239] shift of resonances.
To remove time dependence in the system Hamiltonian $\mathcal{H} = \mathcal{H}_0 + \mathcal{H}_{\text{int}}$, one can find a unitary transformation $\mathcal{U}$ transforming the eigenbasis into $|\tilde{\Psi}\rangle = \mathcal{U}|\Psi\rangle$, which verify the "new" Schrödinger equation

$$i\hbar\frac{\partial}{\partial t}|\tilde{\Psi}\rangle = \tilde{\mathcal{H}}|\tilde{\Psi}\rangle, \tag{C.26}$$

where the transformed Hamiltonian is

$$\tilde{\mathcal{H}} = \mathcal{U}\mathcal{H}\mathcal{U}^\dagger + i\hbar\frac{\partial}{\partial t}\mathcal{U}\mathcal{U}^\dagger. \tag{C.27}$$

C.3 Three-level Λ system

Here, we will briefly consider a three-level Λ system excited by two lasers as described in fig. C.1. This is the only case we consider here as it will naturally lead to the introduction of electromagnetically induced transparency (EIT). The reader may refer to the review of M. Fleischhauer et al. [75] and the excellent tutorial written by L. Downes [220] for a good overview of atom-light interaction in other systems (e.g. Ladder) and simple numerical methods that can be used to deal with them.

C.3.1 Building the interaction Hamiltonian

The system shown in fig. C.1 consists in three eigenstates $|1\rangle$, $|2\rangle$, and $|3\rangle$ with bare energies $\hbar\omega_n$. Following eq. (C.16), the atomic Hamiltonian $\mathcal{H}$ consists in the free-atom Hamiltonian $\mathcal{H}_0$ containing the eigenenergies and $\mathcal{H}_{\text{int}}$ is a perturbation describing the interaction of the atom with the laser. From completeness and orthonormality, we have

$$\mathcal{H}_0 = \left(\sum_n |n\rangle\langle n|\right)\mathcal{H}_0\left(\sum_n |n\rangle\langle n|\right) = \begin{pmatrix} \hbar\omega_1 & 0 & 0 \\ 0 & \hbar\omega_2 & 0 \\ 0 & 0 & \hbar\omega_3 \end{pmatrix}. \tag{C.28}$$

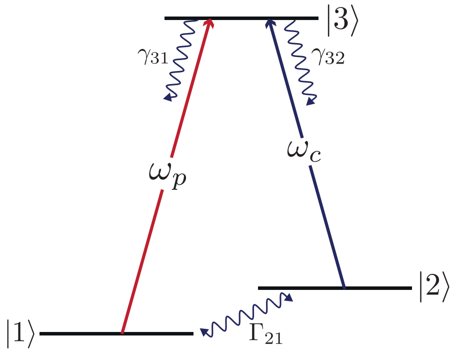

Figure C.1 – Three-level Λ system with two lasers.

If we drive transition $|2\rangle \longrightarrow |3\rangle$ with a control field of amplitude E_c and frequency ω_c (called coupling) and we drive transition $|1\rangle \longrightarrow |3\rangle$ with a weaker probe field of amplitude E_p and frequency ω_p, the electric field with which the atom interacts is given by

$$E = E_p \cos(\omega_p t - \mathbf{k}_p \cdot \mathbf{r}) + E_c \cos(\omega_c t - \mathbf{k}_c \cdot \mathbf{r}), \tag{C.29}$$

where $\mathbf{k}_p$ and $\mathbf{k}_c$ are the wavevectors of the probe and coupling lasers, respectively. Following the conclusion of section C.2.1, we may remove the terms $\mathbf{k}_c \cdot \mathbf{r}$ and $\mathbf{k}_p \cdot \mathbf{r}$ as $\lambda \gg r$ so that the electric field becomes simply

$$E = E_p \cos(\omega_p t) + E_c \cos(\omega_c t). \tag{C.30}$$

Assuming transition $|1\rangle \longrightarrow |2\rangle$ is forbidden and all other states are far enough not to interact with our system, the interaction Hamiltonian reads[2]

$$\mathcal{H}_{\text{int}} = -E \begin{pmatrix} 0 & 0 & d_{13} \\ 0 & 0 & d_{23} \\ d_{31} & d_{32} & 0 \end{pmatrix}. \tag{C.31}$$

We will now switch to the interaction picture using the time evolution operator $\mathcal{U}(t)$ which reads

$$\mathcal{U}(t) = \exp(i\mathcal{H}_0 t/\hbar) = \begin{pmatrix} \exp(i\omega_1 t) & 0 & 0 \\ 0 & \exp(i\omega_3 t) & 0 \\ 0 & 0 & \exp(i\omega_3 t) \end{pmatrix}. \tag{C.32}$$

The unitary transformation $\mathcal{U}\mathcal{H}_{\text{int}}\mathcal{U}^\dagger$ yields

$$\tilde{\mathcal{H}}_{\text{int}} = \mathcal{U}\mathcal{H}_{\text{int}}\mathcal{U}^\dagger = -E \begin{pmatrix} 0 & 0 & d_{13}\exp[i(\omega_1 - \omega_3)t] \\ 0 & 0 & d_{23}\exp[i(\omega_2 - \omega_3)t] \\ d_{31}\exp[i(\omega_3 - \omega_1)t] & d_{23}\exp[i(\omega_3 - \omega_2)t] & 0 \end{pmatrix}. \tag{C.33}$$

The laser field can be rewritten in complex notation

$$E = \frac{1}{2}\left(E_p\left[\exp(i\omega_p t) + \exp(-i\omega_p t)\right] + E_c\left[\exp(i\omega_c t) + \exp(-i\omega_c t)\right]\right). \tag{C.34}$$

We may easily inject the expression of the field and apply the RWA, ie. getting rid of all the quickly oscillating terms. Then, reverting to the Schrödinger picture gives for the interaction Hamiltonian

$$\mathcal{H}_{\text{int}} = \mathcal{U}^\dagger\tilde{\mathcal{H}}_{\text{int}}\mathcal{U} = -\frac{1}{2}\begin{pmatrix} 0 & 0 & d_{13}E_p\exp(i\omega_p t) \\ 0 & 0 & d_{23}E_c\exp(i\omega_c t) \\ d_{31}E_p\exp(i\omega_p t) & d_{32}E_c\exp(i\omega_c t) & 0 \end{pmatrix}. \tag{C.35}$$

---

[2] Atoms with spherically symmetric wavefunctions [106] have no permanent dipole moment, thus $d_{ii} = 0$. This assumption holds for the species studied in this thesis.

We can now separate the dipole moments into magnitude and phase such that

$$d_{13} = d_{31}^* = |d_{13}| \exp(i\varphi_p) \quad \text{and} \quad d_{23} = d_{32}^* = |d_{23}| \exp(i\varphi_c), \tag{C.36}$$

so that the final total atomic Hamiltonian $\mathcal{H} = \mathcal{H}_0 + \mathcal{H}_{\text{int}}$ reads

$$\mathcal{H} = \frac{\hbar}{2} \begin{pmatrix} 2\omega_1 & 0 & -\Omega_p \exp(i\varphi_p) \exp(i\omega_p t) \\ 0 & 2\omega_2 & -\Omega_c \exp(i\varphi_c) \exp(i\omega_c t) \\ -\Omega_p \exp(-i\varphi_p) \exp(-i\omega_p t) & -\Omega_c \exp(-i\varphi_c) \exp(i\omega_c t) & 2\omega 3 \end{pmatrix}, \tag{C.37}$$

where the Rabi frequencies are defined following eq. (C.25), ie

$$\Omega_{p,c} = \frac{E_{p,c} |d_{13,23}|}{\hbar}. \tag{C.38}$$

In the so-called rotating basis (see eg. [240, Chap. 1] for a full derivation), we may get rid of all time-dependence and phase factors. Rigorously, the rotating basis $|\tilde{n}\rangle$ is related to Schrödinger picture $|n\rangle$ by $|\tilde{n}\rangle = \tilde{U}(t) |n\rangle$ with

$$\tilde{U}(t) = \begin{pmatrix} \exp(-i\varphi_p) \exp(-i\omega_p)t & 0 & 0 \\ 0 & \exp(-i\varphi_c) \exp(-i\omega_c)t & 0 \\ 0 & 0 & 1 \end{pmatrix}. \tag{C.39}$$

After easy but tedious calculations, one can rewrite the total Hamiltonian in the rotating basis as follows:

$$\mathcal{H} = \frac{\hbar}{2} \begin{pmatrix} 0 & 0 & \Omega_p \\ 0 & -2\Delta_R & \Omega_c \\ \Omega_p & \Omega_c & -2\Delta_p \end{pmatrix}, \tag{C.40}$$

where $\Delta_p = \omega_{31} - \omega_p$ and $\Delta_c = \omega_{32} - \omega_c$ are the probe and coupling laser detuning to the upper state $|3\rangle$, and $\Delta_R = \Delta_p - \Delta_c$ is the two-photon Raman detuning.

C.3.2 Dark state, Electromagnetically-Induced Transparency

On two-photon resonance ($\Delta_R = 0$, $\Delta_p = \Delta_c = \Delta$), the eigenvalues of $\mathcal{H}$ in terms of the bare states are

$$\begin{aligned} |a^+\rangle &= \sin\theta \sin\Phi \,|1\rangle + \cos\theta \sin\Phi \,|2\rangle + \cos\Phi \,|3\rangle \\ |a^-\rangle &= \sin\theta \cos\Phi \,|1\rangle + \cos\theta \cos\Phi \,|2\rangle - \sin\Phi \,|3\rangle \\ |a^0\rangle &= \cos\theta \,|1\rangle - \sin\theta \,|2\rangle , \end{aligned} \tag{C.41}$$

with $\tan\theta = \Omega_p / \Omega_c$ and $\tan 2\Phi = \sqrt{\Omega_p^2 + \Omega_c^2} / \Delta$. The energies of these states are

$$\begin{aligned} \lambda_\pm &= \frac{\hbar}{2} \left(\Delta \mp \sqrt{\Omega^2 + \Delta^2} \right) \\ \lambda_0 &= 0. \end{aligned} \tag{C.42}$$

where $\Omega = \sqrt{\Omega_p^2 + \Omega_c^2}$ is the generalized Rabi frequency. Interestingly enough, the eigenstate $|a_0\rangle$ does not contain any contribution from the upper state $|3\rangle$ and does not interact with it. Since $|a_0\rangle$ is an eigenstate of the system, $\langle 3|\mathcal{H}|a_0\rangle = 0$ vanishes. Consequently, no interaction can drive the $|a_0\rangle \longrightarrow |3\rangle$ transition, and an atom prepared in the state $|a_0\rangle$ cannot absorb nor emit a photon. In that case, the medium becomes "transparent" to the probe beam, hence the name EIT. Population spontaneously decaying from the upper state $|3\rangle$ can be trapped in state $|a_0\rangle$ but cannot be re-excited back to $|3\rangle$. This is one of the methods used to perform coherent population trapping.

Bibliography

[1] T. H. Maiman. *Stimulated Optical Radiation in Ruby.* Nature **187** (4736) (1960), pp. 493–494. 1

[2] D. Steck. *Cesium D Line Data.* (2003). 1, 40, 61, 88

[3] D. Steck. *Rubidium 85 D Line Data.* (2019). 1, 61, 95, 100

[4] D. Steck. *Rubidium 87 D Line Data.* (2003). 1, 40, 61

[5] D. Steck. *Sodium D Line Data.* (2003). 1, 40, 44, 61, 121

[6] E. Arimondo, M. Inguscio, and P. Violino. *Experimental determinations of the hyperfine structure in the alkali atoms.* Rev. Mod. Phys. **49** (1) (1977), 31–75. 1, 2, 61, 68, 75, 76, 120, 121, 122

[7] M. E. Gehm. “Properties of ^{6}Li”. 2003. URL: `https://physics.ncsu.edu/jet/techdocs/pdf/PropertiesOfLi.pdf`. 1.

[8] S. Bhushan, V. S. Chauhan, M. Dixith, and R. K. Easwaran. *Effect of magnetic field on a multi window ladder type electromagnetically induced transparency with 87Rb atoms in vapour cell.* Phys. Lett. A **383** (125885) (2019). 1

[9] M. Bhattarai, V. Bharti, V. Natarajan, A. Sargsyan, and D. Sarkisyan. *Study of EIT resonances in an anti-relaxation coated Rb vapor cell.* Phys. Lett. A **383** (1) (2019), pp. 91–96. 1

[10] Z. Tao, M. Chen, Z. Zhou, B. Ye, J. Zeng, and H. Zheng. *Isotope ^{87}Rb Faraday filter with a single transmission peak resonant with atomic transition at 780 nm.* Opt. Express **27** (9) (2019), 13142–13149. 1

[11] J. Keaveney, S. A. Wrathmall, C. S. Adams, and I. G. Hughes. *Optimized ultra-narrow atomic bandpass filters via magneto-optic rotation in an unconstrained geometry.* Opt. Lett. **43** (17) (2018), 4272–4275. 1

[12] M. O. Scully and M. Fleischhauer. *High-sensitivity magnetometer based on index-enhanced media.* Phys. Rev. Lett. **69** (9) (1992), pp. 1360–1363. 1

[13] M. Fleischhauer and M. O. Scully. *Quantum sensitivity limits of an optical magnetometer based on atomic phase coherence.* Phys. Rev. A **49** (3) (1994), pp. 1973–1986. 1

[14] D. Budker and M. Romalis. *Optical magnetometry.* Nat. Phys. **3** (4) (2007), pp. 227–234. 1, 55

[15] R. Mhaskar, S. Knappe, and J. Kitching. *A low-power, high-sensitivity micromachined optical magnetometer.* Appl. Phys. Lett. **101** (24) (2012), p. 241105. 1

[16] B. Patton, E. Zhivun, D. Hovde, and D. Budker. *All-Optical Vector Atomic Magnetometer.* Phys. Rev. Lett. **113** (1) (2014), p. 013001. 1

[17] N. Wilson, P. Light, A. Luiten, and C. Perrella. *Ultrastable Optical Magnetometry.* Phys. Rev. Appl. **11** (4) (2019), p. 044034. 1, 55

[18] R. S. Mathew, F. Ponciano-Ojeda, J. Keaveney, D. J. Whiting, and I. G. Hughes. *Simultaneous two-photon resonant optical laser locking (STROLLing) in the hyperfine Paschen–Back regime.* Opt. Lett. **43** (17) (2018), 4204–4207. 1, 3, 49, 87, 95, 103, 105

[19] M. Faraday, M. Faraday, W. Collin, R. S. G. Britain), and d. D. Burndy Library. *On the magnetization of light and the illumination of magnetic lines of force* (1846). 1

[20] R. Drampyan, A. D. Greentree, and A. V. Durrant. *Two field nonlinear Faraday rotation in rubidium vapor in a Doppler-free geometry.* Opt. Commun. **276** (2) (2007), pp. 251–260. 1

[21] D. A. Van Baak. *Resonant Faraday rotation as a probe of atomic dispersion.* Am. J. Phys. **64** (6) (1996), pp. 724–735. 1

[22] W. Hanle. *über magnetische Beeinflussung der Polarisation der Resonanzfluoreszenz.* Zeitschrift für Physik **30** (1) (1924), pp. 93–105. 1

[23] M. Auzinsh, D. Budker, and S. M. Rochester. *Optically Polarized Atoms : Understanding Light-Atom Interactions* (2010). 1, 15, 75, 123

[24] J. Alnis, K. Blushs, M. Auzinsh, S. Kennedy, N. Shafer-Ray, and E. R. I. Abraham. *The Hanle effect and level crossing spectroscopy in Rb vapour under strong laser excitation*. J. Phys. B: At. Mol. Opt. Phys. **36** (6) (2003), p. 1161. 1

[25] E. Breschi and A. Weis. *Ground-state Hanle effect based on atomic alignment*. Phys. Rev. A **86** (5) (2012), p. 053427. 1

[26] R. H. Dicke. *The Effect of Collisions upon the Doppler Width of Spectral Lines*. Phys. Rev. **89** (2) (1953), pp. 472–473. 1

[27] O. Firstenberg, M. Shuker, A. Ben-Kish, D. R. Fredkin, N. Davidson, and A. Ron. *Theory of Dicke narrowing in coherent population trapping*. Phys. Rev. A **76** (1) (2007), p. 013818. 1

[28] S. Brandt, A. Nagel, R. Wynands, and D. Meschede. *Buffer-gas-induced linewidth reduction of coherent dark resonances to below* 50 *Hz*. Phys. Rev. A **56** (2) (1997), R1063–R1066. 1

[29] E. E. Mikhailov, V. A. Sautenkov, Y. V. Rostovtsev, and G. R. Welch. *Absorption resonance and large negative delay in rubidium vapor with a buffer gas*. JOSA B **21** (2) (2004), pp. 425–428. 1

[30] K. Dieckmann, R. J. C. Spreeuw, M. Weidemüller, and J. T. M. Walraven. *Two-dimensional magneto-optical trap as a source of slow atoms*. Phys. Rev. A **58** (5) (1998), pp. 3891–3895. 1

[31] D. Budker, L. Hollberg, D. F. Kimball, J. Kitching, S. Pustelny, and V. V. Yashchuk. *Microwave transitions and nonlinear magneto-optical rotation in anti-relaxation-coated cells*. Phys. Rev. A **71** (1) (2005), p. 012903. 1

[32] A. Papoyan, S. Shmavonyan, A. Khanbekyan, K. Khanbekyan, C. Marinelli, and E. Mariotti. *Magnetic-field-compensation optical vector magnetometer*. Appl. Opt. **55** (4) (2016), pp. 892–895. 1

[33] A. I. Parkhomenko and A. M. Shalagin. *Transversely diode-pumped alkali metal vapour laser*. Quantum Electron. **45** (9) (2015), p. 797. 1

[34] A. V. Bogachev, S. G. Garanin, A. M. Dudov, V. A. Eroshenko, S. M. Kulikov, G. T. Mikaelian, V. A. Panarin, V. O. Pautov, A. V. Rus, and S. A. Sukharev. *Diode-pumped caesium vapour laser with closed-cycle laser-active medium circulation*. Quantum Electron. **42** (2) (2012), p. 95. 1

[35] R. J. Beach, W. F. Krupke, V. K. Kanz, S. A. Payne, M. A. Dubinskii, and L. D. Merkle. *End-pumped continuous-wave alkali vapor lasers: experiment, model, and power scaling*. JOSA B **21** (12) (2004), pp. 2151–2163. 1

[36] Y.-W. Cho, G. T. Campbell, J. L. Everett, J. Bernu, D. B. Higginbottom, M. T. Cao, J. Geng, N. P. Robins, P. K. Lam, and B. C. Buchler. *Highly efficient optical quantum memory with long coherence time in cold atoms*. Optica **3** (1) (2016), pp. 100–107. 1

[37] M. Hosseini, B. M. Sparkes, G. Campbell, P. K. Lam, and B. C. Buchler. *High efficiency coherent optical memory with warm rubidium vapour*. Nat. Commun. **2** (1) (2011), p. 174. 1

[38] R. B. Li, L. Deng, and E. W. Hagley. *Fast, all-optical logic gates and transistor functionalities using a room-temperature atomic controlled Kerr gate*. Phys. Rev. A **90** (6) (2014), p. 063806. 1

[39] R. J. Knize. *Optical NOR gate using cesium vapor*. Opt. Lett. **17** (4) (1992), pp. 244–246. 1

[40] M. Saffman, T. G. Walker, and K. Mølmer. *Quantum information with Rydberg atoms*. Rev. Mod. Phys. **82** (3) (2010), pp. 2313–2363. 1

[41] C. Carr, R. Ritter, C. G. Wade, C. S. Adams, and K. J. Weatherill. *Nonequilibrium Phase Transition in a Dilute Rydberg Ensemble*. Phys. Rev. Lett. **111** (11) (2013), p. 113901. 1

[42] J. J. Maki, M. S. Malcuit, J. E. Sipe, and R. W. Boyd. *Linear and nonlinear optical measurements of the Lorentz local field*. Phys. Rev. Lett. **67** (8) (1991), pp. 972–975. 1

[43] J. Keaveney, A. Sargsyan, U. Krohn, I. G. Hughes, D. Sarkisyan, and C. S. Adams. *Cooperative Lamb Shift in an Atomic Vapor Layer of Nanometer Thickness.* Phys. Rev. Lett. **108** (17) (2012), p. 173601. 1

[44] K. Whittaker, J. Keaveney, I. Hughes, A. Sargsyan, D. Sarkisyan, and C. Adams. *Optical Response of Gas-Phase Atoms at Less than* $\lambda/80$ *from a Dielectric Surface.* Phys. Rev. Lett. **112** (25) (2014), p. 253201. 1, 11, 23, 80

[45] M. Marinescu, H. R. Sadeghpour, and A. Dalgarno. *Dispersion coefficients for alkali-metal dimers.* Phys. Rev. A **49** (2) (1994), pp. 982–988. 1

[46] S. Vdović, D. Sarkisyan, and G. Pichler. *Absorption spectrum of rubidium and cesium dimers by compact computer operated spectrometer.* Opt. Commun. **268** (1) (2006), pp. 58–63. 1

[47] M. H. Anderson, J. R. Ensher, M. R. Matthews, C. E. Wieman, and E. A. Cornell. *Observation of Bose-Einstein Condensation in a Dilute Atomic Vapor.* Science **269** (5221) (1995), pp. 198–201. 1

[48] K. B. Davis, M. O. Mewes, M. R. Andrews, N. J. van Druten, D. S. Durfee, D. M. Kurn, and W. Ketterle. *Bose-Einstein Condensation in a Gas of Sodium Atoms.* Phys. Rev. Lett. **75** (22) (1995), pp. 3969–3973. 1

[49] P. Zeeman. *Over de invloed eener magnetisatie op den aard van het door een stof uitgezonden licht.* Verslagen en Mededeelingen der Kon. Acad. van Wetenschappen, Afd. Natuurkunde **5** (1896), pp. 181–184. 1

[50] F. Paschen and E. Back. *Liniengruppen magnetisch vervollständigt.* Physica **1** (1921), pp. 261–273. 1, 75

[51] J. Stark. *Beobachtungen über den Effekt des elektrischen Feldes auf Spektrallinien. I. Quereffekt.* Ann. der Physik **348** (1914), pp. 965–982. 1

[52] C. Alcock, V. Itkin, and M. Horrigan. *Vapour Pressure Equations for the Metallic Elements: 298–2500K.* Can. Metall. Q. **23** (3) (1984), pp. 309–313. 2

[53] W. Demtröder. *Atoms, Molecules and Photons: An Introduction to Atomic-, Molecular- and Quantum Physics.* Graduate Texts in Physics (2010). 1, 40, 103

[54] D. Sarkisyan, D. Bloch, A. Papoyan, and M. Ducloy. *Sub-Doppler spectroscopy by sub-micron thin Cs vapour layer.* Opt. Comm. **200** (1-6) (2001), pp. 201–208. 1, 3, 7, 8, 9, 10

[55] A. Sargsyan, G. Hakhumyan, A. Papoyan, D. Sarkisyan, A. Atvars, and M. Auzinsh. *A novel approach to quantitative spectroscopy of atoms in a magnetic field and applications based on an atomic vapor cell with* $L = \lambda$. Appl. Phys. Lett. **93** (021119) (2008). 1, 11, 87, 93

[56] A. Sargsyan, A. Papoyan, I. G. Hughes, C. S. Adams, and D. Sarkisyan. *Selective reflection from an Rb layer with a thickness below* $\lambda/12$ *and applications.* Opt. Lett. **42** (8) (2017), p. 1476. 1, 23, 25, 76, 80

[57] P. Tremblay, A. Michaud, M. Levesque, S. Thériault, M. Breton, J. Beaubien, and N. Cyr. *Absorption profiles of alkali-metal D lines in the presence of a static magnetic field.* Phys. Rev. A. **42** (1990), 2766–2773. 1, 3, 29, 77, 83, 87, 88

[58] A. Tonoyan, A. Sargsyan, E. Klinger, G. Hakhumyan, C. Leroy, M. Auzinsh, A. Papoyan, and D. Sarkisyan. *Circular dichroism of magnetically induced transitions for D2 lines of alkali atoms.* EPL **121** (53001) (2018). 1, 49, 53, 87, 88

[59] A. Sargsyan, A. Amiryan, A. Tonoyan, E. Klinger, and D. Sarkisyan. *Circular dichroism in atomic vapors: Magnetically induced transitions responsible for two distinct behaviors.* Phys. Lett. A **390** (127114) (2021). 1, 50, 51, 78, 87, 88

[60] A. Sargsyan, E. Klinger, G. Hakhumyan, A. Tonoyan, A. Papoyan, C. Leroy, and D. Sarkisyan. *Decoupling of hyperfine structure of Cs* D_1 *line in strong magnetic field studied by selective reflection from a nanocell.* JOSA B **34** (4) (2017), pp. 776–784. 1, 9, 10, 55

[61] A. Sargsyan, A. Amiryan, Y. Pashayan-Leroy, C. Leroy, A. Papoyan, and D. Sarkisyan. *Approach to quantitative spectroscopy of atomic vapor in optical nanocells.* Opt. Lett. **44** (22) (2019), pp. 5533–5536. 1, 11, 24, 51, 75, 78, 82, 88

[62] A. Sargsyan, A. Amiryan, and D. Sarkisyan. *Coherent Dicke Narrowing of Absorption Spectra, Collapse and Revival: Second-Derivative Processing.* J. Exp. Theor. Phys. **131** (37) (2020), pp. 220–226. 1, 40

[63] C. Umfer, L. Windholz, and M. Musso. *Investigation of the sodium and lithium D-lines in strong magnetic fields.* Z. Phys. D: At. Mol. Clust. **25** (1992), pp. 23–29. 2

[64] H. Hidenobu, M. Masaharu, and D. Muneyuki. *Paschen-Back Effect of D-Lines in Sodium under a High Magnetic Field.* J. Phys. Soc. Jpn. **51** (5) (1982), pp. 1566–1570. 2

[65] R. González-Férez and P. Schmelcher. *Sodium in a strong magnetic field.* Eur. Phys. J. D **23** (2003), 189–199. 2

[66] W. A. Davis, H. J. Metcalf, and W. D. Phillips. *Vanishing electric dipole transition moment.* Phys. Rev. A **19** (2) (1979), pp. 700–703. 2

[67] B. A. Olsen, B. Patton, Y. Y. Jau, and W. Happer. *Optical pumping and spectroscopy of Cs vapor at high magnetic field.* Phys. Rev. A **84** (2011), p. 063410. 2, 75, 76, 100

[68] A. Sargsyan, A. Tonoyan, G. Hakhumyan, C. Leroy, Y. Pashayan-Leroy, and D. Sarkisyan. *Complete hyperfine Paschen-Back regime at relatively small magnetic fields realized in potassium nano-cell.* EPL (Europhysics Lett. **110** (2) (2015), p. 23001. 2, 10, 51, 75, 76, 77, 78

[69] A. Sargsyan, G. Hakhumyan, C. Leroy, Y. Pashayan-Leroy, A. Papoyan, and D. Sarkisyan. *Hyperfine Paschen–Back regime realized in Rb nanocell.* Opt. Lett. **37** (8) (2012), p. 1379. 2, 8, 10, 75, 76, 80, 84

[70] L. Weller, K. Kleinbach, M. Zentile, S. Knappe, C. Adams, and I. Hughes. *Absolute absorption and dispersion of a rubidium vapour in the hyperfine Paschen–Back regime.* J. Phys. B: At. Mol. Opt. Phys. **45** (2012), p. 215005. 2, 76

[71] A. Sargsyan, A. Tonoyan, J. Keaveney, I. G. Hughes, C. S. Adams, and D. Sarkisyan. *Selective Reflection of Potassium Vapor Nanolayers in a Magnetic Field.* J. Exp. Theor. Phys. **153** (2018), pp. 355–365. 2, 76

[72] J. Kitching. *Chip-scale atomic devices.* Appl. Phys. Rev. **5** (3) (2018), p. 031302. 2, 81, 86, 97

[73] K.-M. Fu, G. Iwata, A. Wickenbrock, and D. Budker. *Sensitive magnetometry in challenging environments.* AVS Quantum Sci. **2** (2020), p. 044702. 2, 81, 86

[74] R. Wynands and A. Nagel. *Precision spectroscopy with coherent dark states.* Appl. Phys. B **68** (1) (1999), pp. 1–25. 3, 95, 96, 99, 100, 102, 104

[75] M. Fleischhauer, A. Imamoglu, and J. P. Marangos. *Electromagnetically induced transparency: Optics in coherent media.* Rev. Mod. Phys. **77** (2) (2005), pp. 633–673. 3, 87, 90, 91, 95, 96, 102, 104, 126

[76] R. Finkelstein, S. Bali, O. Firstenberg, and I. Novikova. *A practical guide to electromagnetically induced transparency in atomic vapor.* New J. Phys. **25** (3) (2023), p. 035001. 3, 95, 96, 103, 104

[77] T. Vartanyan and D. Lin. *Enhanced selective reflection from a thin layer of a dilute gaseous medium.* Phys. Rev. A **51** (3) (1995), 1959–1964. 3, 7, 76

[78] B. Zambon and G. Nienhuis. *Reflection and transmission of light by thin vapor layers.* Opt. Comm. **143** (4) (1997), pp. 308–314. 3, 7, 8, 20

[79] G. Dutier, S. Saltiel, D. Bloch, and M. Ducloy. *Revisiting optical spectroscopy in a thin vapor cell: mixing of reflection and transmission as a Fabry–Perot microcavity effect.* J. Opt. Soc. Am. B **20** (5) (2003), 793–800. 3, 7, 8, 18, 55, 76, 78, 83

[80] J. C. d. A. Carvalho, P. Pedri, M. Ducloy, and A. Laliotis. *Retardation effects in spectroscopic measurements of the Casimir-Polder interaction*. Phys. Rev. A **97** (2) (2018), p. 023806. 3, 8, 22, 27, 28, 105

[81] A. Laliotis, B.-S. Lu, M. Ducloy, and D. Wilkowski. *Atom-surface physics: A review*. AVS Quantum Sci. **3** (4) (2021), p. 043501. 3, 8, 22, 27, 105

[82] R. Momier, A. Aleksanyan, E. Gazazyan, A. Papoyan, and C. Leroy. *New standard magnetic field values determined by cancellations of ^{85}Rb and ^{87}Rb atomic vapors $5^2S_{1/2} \rightarrow 6^2P_{1/2,3/2}$ transitions*. J. Quant. Spectrosc. Radiat. Transf. **257** (2020), p. 107371. 5, 56

[83] A. Aleksanyan, R. Momier, E. Gazazyan, A. Papoyan, and C. Leroy. *Transition cancellations of ^{87}Rb and ^{85}Rb atoms in a magnetic field*. J. Opt. Soc. Am. B **37** (11) (2020), 3504–3514. 5, 56

[84] R. Momier, A. V. Papoyan, and C. Leroy. *Sub-Doppler spectra of sodium D lines in a wide range of magnetic field: Theoretical study*. J. Quant. Spectrosc. Radiat. Transf. **272** (2021), p. 107780. 5, 35

[85] A. Sargsyan, R. Momier, A. Papoyan, and D. Sarkisyan. *Sub-Doppler Spectroscopy of Room-Temperature Cs Atomic Vapor in a 400-nm-Thick Nanocell*. J. Exp. Theor. Phys. **133** (4) (2021), pp. 404–410. 5

[86] A. Sargsyan, A. Tonoyan, R. Momier, C. Leroy, and D. Sarkisyan. *Dominant magnetically induced transitions in alkali metal atoms with nuclear spin 3/2*. J. Opt. Soc. Am. B **39** (4) (2022), p. 973. 5, 39, 44, 49, 78

[87] M. Auzinsh, A. Sargsyan, A. Tonoyan, C. Leroy, R. Momier, D. Sarkisyan, and A. Papoyan. *Wide range linear magnetometer based on a sub-microsized K vapor cell*. Appl. Opt. **61** (19) (2022), p. 5749. 5, 76

[88] A. Sargsyan, R. Momier, C. Leroy, and D. Sarkisyan. *Saturated absorption technique used in potassium microcells for magnetic field sensing*. Laser Phys. **32** (10) (2022), p. 105701. 5, 76

[89] A. Aleksanyan, R. Momier, E. Gazazyan, A. Papoyan, and C. Leroy. *Cancellation of D_1 line transitions of alkali-metal atoms by magnetic-field values*. Phys. Rev. A **105** (4) (2022), p. 042810. 5, 56

[90] A. Sargsyan, A. Tonoyan, R. Momier, C. Leroy, and D. Sarkisyan. *Formation of strongly shifted EIT resonances using "forbidden" transitions of Cesium*. J. Quant. Spectrosc. Radiat. Transf. **303** (2023), p. 108582. 5, 88

[91] A. Sargsyan, R. Momier, C. Leroy, and D. Sarkisyan. *Competing van der Waals and dipole-dipole interactions in optical nanocells at thicknesses below 100 nm*. Phys. Lett. A **483** (2023), p. 129069. 5, 22

[92] A. Tonoyan, A. Sargsyan, R. Momier, C. Leroy, and D. Sarkisyan. *Formation of Narrow Atomic Lines of Rb in the UV Region Using a Magnetic Field*. Opt. Mem. Neural Networks **32** (S3) (2023), S343–S348. 5, 103

[93] R. Momier, A. Sargsyan, A. Tonoyan, C. Leroy, and D. Sarkisyan. *Micrometric-Thin Cell Filled with Rb Vapor for High-Resolution Atomic Spectroscopy*. Opt. Mem. Neural Networks **32** (3) (2023), S349–S355. 5

[94] A. Sargsyan, R. Momier, C. Leroy, and D. Sarkisyan. *Influence of buffer gas on the formation of N-resonances in rubidium vapors*. 2024. DOI: `10.48550/arXiv.2402.09184`. arXiv: `2402.09184 [physics]`. Pre-published. 6, 88.

[95] R. H. Romer and R. H. Dicke. *New Technique for High-Resolution Microwave Spectroscopy*. Phys. Rev. **99** (2) (1955), 532–536. 7, 20

[96] J.-M. Hartmann, X. Landsheere, C. Boulet, D. Sarkisyan, A. S. Sarkisyan, C. Leroy, and E. Pangui. *Infrared look at the spectral effects of submicron confinements of CO_2*. Phys. Rev. A **93** (1) (2016), p. 012516. 8, 10

[97] J. W. Wheeldon. *Absorption of sodium and argon by glass.* Br. J. Appl. Phys. **10** (6) (1959), p. 295. 9

[98] D. Sarkisyan, U. Hinze, L. Meyer, and B. Wellegehausen. *Efficient cw sodium dimer Raman laser operation in a high-temperature sapphire cell.* Appl. Phys. B **70** (3) (2000), pp. 351–354. 10

[99] E. Klinger. "Selective reflection spectroscopy of alkali vapors confined in nanocells and emerging sensing applications". PhD thesis. Université Bourgogne Franche-Comté ; Institute for Physical Research, 2019. URL: `https://tel.archives-ouvertes.fr/tel-02317761`. 10, 83.

[100] T. Peyrot, Y. Sortais, A. Browaeys, A. Sargsyan, D. Sarkisyan, J. Keaveney, I. Hughes, and C. Adams. *Collective Lamb Shift of a Nanoscale Atomic Vapor Layer within a Sapphire Cavity.* Phys. Rev. Lett. **120** (24) (2018), p. 243401. 11, 23, 25

[101] K. A. Whittaker, J. Keaveney, I. G. Hughes, A. Sargsyan, D. Sarkisyan, and C. S. Adams. *Spectroscopic detection of atom-surface interactions in an atomic-vapor layer with nanoscale thickness.* Phys. Rev. A **92** (5) (2015), p. 052706. 11, 23

[102] T. Peyrot, N. Šibalić, Y. R. P. Sortais, A. Browaeys, A. Sargsyan, D. Sarkisyan, I. G. Hughes, and C. S. Adams. *Measurement of the atom-surface van der Waals interaction by transmission spectroscopy in a wedged nanocell.* Phys. Rev. A **100** (2) (2019), p. 022503. 11, 23

[103] G. Nienhuis, F. Schuller, and M. Ducloy. *Nonlinear selective reflection from an atomic vapor at arbitrary incidence angle.* Phys. Rev. A **38** (10) (1988), pp. 5197–5205. 12

[104] M. F. H. Schuurmans. *Spectral narrowing of selective reflection.* J. de Physique **37** (5) (1976), pp. 469–485. 12

[105] G. Dutier. "Cavité nanométrique de vapeur de Césium : spectroscopie à haute résolution et interaction de surface de type van der Waals". PhD thesis. Université Paris-Nord - Paris XIII, 2003. URL: `https://theses.hal.science/tel-00583452`. 14.

[106] B. W. Shore. *The Theory of Coherent Atomic Excitation, Simple Atoms and Fields* (1990). 15, 90, 123, 125, 127

[107] A. V. Ermolaev and T. A. Vartanyan. *Theory of thin-vapor-layer linear-optical properties: The case of quenching of atomic polarization upon collisions of atoms with dielectric walls.* Phys. Rev. A **105** (1) (2022), p. 013518. 20, 23

[108] M. Oria, M. Chevrollier, D. Bloch, M. Fichet, and M. Ducloy. *Spectral Observation of Surface-Induced Van der Waals Attraction on Atomic Vapour.* Europhys. Lett. **14** (6) (1991), p. 527. 23

[109] H. Failache, S. Saltiel, M. Fichet, D. Bloch, and M. Ducloy. *Resonant van der Waals Repulsion between Excited Cs Atoms and Sapphire Surface.* Phys. Rev. Lett. **83** (26) (1999), pp. 5467–5470. 23

[110] D. Bloch and M. Ducloy. "Atom-wall interaction". In: *Advances In Atomic, Molecular, and Optical Physics.* Ed. by B. Bederson and H. Walther. Vol. 50. 2005, pp. 91–154. DOI: `10.1016/S1049-250X(05)80008-4`. 23, 27, 80.

[111] A. Sargsyan, G. Pichler, and D. Sarkisyan. *Study of the Interaction of Potassium Atoms with the Sapphire Surface with the Use of an Ultrathin Spectroscopic Cell.* JETP Lett. **115** (6) (2022), pp. 312–317. 23, 27

[112] A. Sargsyan. *Study of the Interaction of Rubidium Atoms with Sapphire Surface Using Spectroscopic Nanocells.* J. Appl. Spectrosc. **90** (4) (2023), pp. 731–735. 23

[113] A. Sargsyan, E. Klinger, C. Leroy, I. G. Hughes, D. Sarkisyan, and C. S. Adams. *Selective reflection from a potassium atomic layer with a thickness as small as $\lambda/13$.* J. Phys. B: At. Mol. Opt. Phys. **52** (19) (2019), p. 195001. 23, 25, 27

[114] J. Keaveney. "Collective Atom Light Interactions in Dense Atomic Vapours". In: 2014. 23.

[115] V. V. Vassiliev, S. A. Zibrov, and V. L. Velichansky. *Compact extended-cavity diode laser for atomic spectroscopy and metrology.* Rev. Sci. Instruments **77** (1) (2006), p. 013102. 24, 78, 82, 85, 91, 96

[116] W. D. Phillips. *Nobel Lecture: Laser cooling and trapping of neutral atoms.* Rev. Mod. Phys. **70** (3) (1998), pp. 721–741. 29

[117] K. L. Corwin, Z.-T. Lu, C. F. Hand, R. J. Epstein, and C. E. Wieman. *Frequency-stabilized diode laser with the Zeeman shift in an atomic vapor.* Appl. Opt. **37** (15) (1998), pp. 3295–3298. 29

[118] G. E. Santyr, R. M. Henkelman, and M. J. Bronskill. *Spin locking for magnetic resonance imaging with application to human breast.* Magn. Reson. Med. **12** (1) (1989), pp. 25–37. 29

[119] W. P. Aue, E. Bartholdi, and R. R. Ernst. *Two-dimensional spectroscopy. Application to nuclear magnetic resonance.* The J. Chem. Phys. **64** (5) (1976), pp. 2229–2246. 29

[120] T. D. Barrett, D. Stuart, O. Barter, and A. Kuhn. *Nonlinear Zeeman effects in the cavity-enhanced emission of polarised photons.* New J. Phys. **20** (7) (2018), p. 073030. 29

[121] E. U. Condon and G. H. Shortley. *The Theory of Atomic Spectra* (1935). 31

[122] M. L. Sánchez, B. Moreno, and A. López Piñeiro. *Matrix-element calculations for hydrogenlike atoms.* Phys. Rev. A **46** (11) (1992), pp. 6908–6913. 31

[123] H Marxer. *Off-diagonal matrix elements $< nl|r^k|nl' >$ for hydrogen-like states: an exact correspondence relationship in terms of orthogonal polynomials and the WKB approximation.* J. Phys. B: At. Mol. Opt. Phys. **28** (3) (1995), pp. 341–355. 31

[124] J. J. Sakurai and J. Napolitano. *Modern Quantum Mechanics* (2020). 32

[125] W. R. Johnson and G. Soff. *The lamb shift in hydrogen-like atoms,* $1 \leq Z \leq 110$. At. Data Nucl. Data Tables **33** (3) (1985), pp. 405–446. 32

[126] D. Hanneke, S. Fogwell, and G. Gabrielse. *New Measurement of the Electron Magnetic Moment and the Fine Structure Constant.* Phys. Rev. Lett. **100** (12) (2008), p. 120801. 32

[127] B. émile. *Spectroscopie atomique: instrumentation et structures atomiques.* LMD Physique (2006). 33

[128] V. K. Khersonskii, A. N. Moskalev, and D. A. Varshalovich. *Quantum Theory Of Angular Momentum* (1988). 33, 113

[129] V. Gerginov, A. Derevianko, and C. E. Tanner. *Observation of the Nuclear Magnetic Octupole Moment of* ^{133}*Cs.* Phys. Rev. Lett. **91** (7) (2003), p. 072501. 34

[130] G. Breit and I. I. Rabi. *Measurement of Nuclear Spin.* Phys. Rev. **38** (11) (1931), 2082–2083. 36

[131] E. De Clercq, M. De Labachellerie, G. Avila, P. Cerez, and M. Tetu. *Laser diode optically pumped caesium beam.* J. de Physique **45** (2) (1984), pp. 239–247. 37

[132] A. Sargsyan, G. Hakhumyan, A. Papoyan, and D. Sarkisyan. *Alkali metal atoms in strong magnetic fields: "Guiding" atomic transitions foretell the characteristics of all transitions of the* D_1 *line.* JETP Lett. **101** (5) (2015), pp. 303–307. 39

[133] A. Sargsyan, A. Tonoyan, G. Hakhumyan, C. Leroy, Y. Pashayan-Leroy, and D. Sarkisyan. *Atomic transitions of Rb,* D_2 *line in strong magnetic fields: Hyperfine Paschen–Back regime.* Opt. Comm. **334** (2015), pp. 208–213. 40

[134] T. G. Tiecke. *Properties of Potassium.* (2019). 40, 61

[135] A. Sargsyan, A. Tonoyan, and D. Sarkisyan. *Strongest Magnetically Induced Transitions in Alkali Metal Atoms.* JETP Lett. **113** (10) (2021), pp. 605–610. 50, 51

[136] A. Sargsyan, G. Hakhumyan, C. Leroy, Y. Pashayan-Leroy, A. Papoyan, D. Sarkisyan, and M. Auzinsh. *Hyperfine Paschen–Back regime in alkali metal atoms: consistency of two theoretical considerations and experiment.* JOSA B **31** (5) (2014), pp. 1046–1053. 50

[137] A. Sargsyan, A. Tonoyan, A. Papoyan, and D. Sarkisyan. *Dark resonance formation with magnetically induced transitions: extension of spectral range and giant circular dichroism.* Opt. Lett. **44** (6) (2019), p. 1391. 54, 87, 92

[138] A. Sargsyan, D. Sarkisyan, and A. Papoyan. *Electromagnetically Induced Transparency with Magnetically Induced $\Delta F = 0, m_F = 0 \rightarrow m_F = 0$ Probe Transition.* Laser Phys. **34** (8) (2024), p. 085701. 54

[139] A. Sargsyan, A. Tonoyan, and D. Sarkisyan. *Application of Magnetically Induced $F_g=4\rightarrow F_e=2$ Atomic Transitions of Cesium Atoms in Strong Magnetic Fields.* Opt. Commun. **537** (2023), p. 129464. 54

[140] A. Sargsyan, E. Klinger, Y. Pashayan-Leroy, C. Leroy, A. Papoyan, and D. Sarkisyan. *Selective reflection from Rb vapor in half- and quarter-wave cells: Features and possible applications.* JETP Lett. **104** (2016), pp. 224–230. 55, 67, 76

[141] G. Hakhumyan, C. Leroy, R. Mirzoyan, Y. Pashayan-Leroy, and D. Sarkisyan. *Study of "forbidden" atomic transitions on D_2 line using Rb nano-cell placed in external magnetic field.* The Eur. Phys. J. D **66** (5) (2012), p. 119. 55

[142] K. A. Khanbekyan, E. Mariotti, A. A. Khanbekyan, L. Moi, and A. M. Khanbekyan. *Sub-doppler spectroscopy of sodium vapor in an ultrathin cell.* Opt. Spectrosc. **120** (5) (2016), pp. 701–705. 55

[143] A. V. Papoyan, G. G. Grigoryan, S. V. Shmavonyan, D. Sarkisyan, J. Guéna, M. Lintz, and M. A. Bouchiat. *New feature in selective reflection with a highly parallel window: phase-tunable homodyne detection of the radiated atomic field.* The Eur. Phys. J. D - At. Mol. Opt. Plasma Phys. **30** (2) (2004), pp. 265–273. 55, 67

[144] D. Das and V. Natarajan. *High-precision measurement of hyperfine structure in the D lines of alkali atoms.* J. Phys. B: At. Mol. Opt. Phys. **41** (3) (2008), p. 035001. 61

[145] W. van Wijngaarden and J. Li. *Measurement of hyperfine structure of sodium $3P_{1/2,3/2}$ states using optical spectroscopy.* Zeitschrift für Physik D **32** (1994), 67–71. 61, 121

[146] S. Falke, E. Tiemann, C. Lisdat, H. Schnatz, and G. Grosche. *Transition frequencies of the D lines of ^{39}K, ^{40}K, and ^{41}K measured with a femtosecond laser frequency comb.* Phys. Rev. A **74** (3) (2006), p. 032503. 61, 121

[147] D. Budker, D. F. Kimball, S. M. Rochester, V. V. Yashchuk, and M. Zolotorev. *Sensitive magnetometry based on nonlinear magneto-optical rotation.* Phys. Rev. A **62** (4) (2000), p. 043403. 61

[148] A. Banerjee, D. Das, and V. Natarajan. *Absolute frequency measurements of the D_1 lines in ^{39}K, ^{85}Rb, and ^{87}Rb with ~ 0.1 ppb uncertainty.* Europhys. Lett. **65** (2) (2004), p. 172. 61, 68, 122

[149] G. P. Barwood, P. Gill, and W. R. C. Rowley. *Frequency measurements on optically narrowed Rb-stabilised laser diodes at 780 nm and 795 nm.* Appl. Phys. B **53** (3) (1991), pp. 142–147. 61, 122

[150] C. Glaser, F. Karlewski, J. Kluge, J. Grimmel, M. Kaiser, A. Günther, H. Hattermann, M. Krutzik, and J. Fortágh. *Absolute frequency measurement of rubidium $5S$ - $6P$ transitions.* Phys. Rev. A **102** (1) (2020), p. 012804. 61, 68

[151] S Bize, Y Sortais, M. S Santos, C Mandache, A Clairon, and C Salomon. *High-accuracy measurement of the ^{87} Rb ground-state hyperfine splitting in an atomic fountain.* Europhys. Lett. (EPL) **45** (5) (1999), pp. 558–564. 61, 122

[152] T. Udem, J. Reichert, R. Holzwarth, and T. W. Hänsch. *Absolute Optical Frequency Measurement of the Cesium D_1 Line with a Mode-Locked Laser.* Phys. Rev. Lett. **82** (18) (1999), pp. 3568–3571. 61, 120

[153] R. Rafac and C. Tanner. *Measurement of the ^{133} Cs $6p^2P_{1/2}$ state hyperfine structure.* Phys. Rev. A **56** (1) (1997), 1027–1030. 61, 120

[154] M. Phillips. *The Effect of Nuclear Motion on Atomic Magnetic Moments.* Phys. Rev. **76** (12) (1949), pp. 1803–1804. 61

[155] G. Audi, A. Wapstra, and C. Thibault. *The Ame2003 atomic mass evaluation.* Nucl. Phys. A **729** (1) (2003), pp. 337–676. 61, 121

[156] E. A. Gazazyan, A. V. Papoyan, D. Sarkisyan, and A. Weis. *Laser frequency stabilization using selective reflection from a vapor cell with a half-wavelength thickness.* Laser Phys. Lett. **4** (11) (2007), p. 801. 67

[157] A. Papoyan, S. Shmavonyan, A. Khanbekyan, K. Khanbekyan, C. Marinelli, and E. Mariotti. *Magnetic-field-compensation optical vector magnetometer.* Appl. Opt. **55** (4) (2016), pp. 892–895. 67

[158] J. Ye, S. Swartz, P. Jungner, and J. L. Hall. *Hyperfine structure and absolute frequency of the* ^{87}Rb $5P_{3/2}$ *state.* Opt. Lett. **21** (16) (1996), pp. 1280–1282. 68, 122

[159] D. Budker, W. Gawlik, D. F. Kimball, S. M. Rochester, V. V. Yashchuk, and A. Weis. *Resonant nonlinear magneto-optical effects in atoms.* Rev. Mod. Phys. **74** (4) (2002), 1153–1201. 75

[160] E. Klinger, H. Azizbekyan, A. Sargsyan, C. Leroy, D. Sarkisyan, and A. Papoyan. *Proof of the feasibility of a nanocell-based wide-range optical magnetometer.* Appl. Opt. **59** (8) (2020), 2231–2237. 75, 106

[161] A. Sargsyan, E. Klinger, A. Tonoyan, and D. Sarkisyan. *Observation of Magnetically-Induced Transition Intensity Redistribution in the Onset of the Hyperfine Paschen–Back Regime.* Optik **303** (2024), p. 171757. 75

[162] M. Zentile, J. Keaveney, L. Weller, D. J. Whiting, C. S. Adams, and I. G. Hughes. *ElecSus: A program to calculate the electric susceptibility of an atomic ensemble.* Comput. Phys. Commun. **189** (2015), pp. 162–174. 75, 105

[163] E. Tiesinga, P. Mohr, D. Newell, and B. Taylor. *The 2018 CODATA Recommended Values of the Fundamental Physical Constants.* (2020). 75, 120, 121, 122

[164] G. Talsky. *Derivative Spectrophotometry* (1994). 75

[165] A. Sargsyan, A. Amiryan, A. Tonoyan, E. Klinger, and D. Sarkisyan. *Coherent optical processes on Cs* D_2 *line magnetically induced transitions.* Phys. Lett. A **434** (2022), p. 128043. 75, 78, 87

[166] L. Weller, K. S. Kleinbach, M. A. Zentile, S. Knappe, I. G. Hughes, and C. S. Adams. *Optical isolator using an atomic vapor in the hyperfine Paschen–Back regime.* Opt. Lett. **37** (2012), p. 3405. 75

[167] S. Scotto, D. Ciampini, C. Rizzo, and E. Arimondo. *Four-level* N*-scheme crossover resonances in Rb saturation spectroscopy in magnetic fields.* Phys. Rev. A **92** (6) (2015), p. 063810. 75, 87

[168] D. J. Whiting, R. S. Matthew, J. Keaveney, C. S. Adams, and I. G. Hughes. *Four-wave mixing in a non-degenerate four-level diamond configuration in the hyperfine Paschen–Back regime.* J. Mod. Opt. **65** (2018), pp. 713–722. 75

[169] G. Hakhumyan, C. Leroy, Y. Pashayan-Leroy, D. Sarkisyan, and M. Auzinsh. *High-spatial-resolution monitoring of strong magnetic field using Rb vapor nanometric-thin cell.* Opt. Comm. **284** (2011), pp. 4007–4012. 75

[170] A. Sargsyan, A. Tonoyan, R. Mirzoyan, D. Sarkisyan, A. M. Wojciechowski, A. Stabrawa, and W. Gawlik. *Saturated-absorption spectroscopy revisited: atomic transitions in strong magnetic fields* (≥ 20 *mT) with a micrometer-thin cell.* Opt. Lett. **39** (8) (2014), p. 2270. 75, 83, 87, 95, 103, 105

[171] D. Bloch, M. Ducloy, N. Senkov, V. Velichansky, and V. Yudin. *Doppler-Free Spectroscopy of the* D_1 *Line of Potassium.* Laser Phys. **6** (1996), pp. 670–678. 75, 78

[172] A. Sargsyan, E. Klinger, C. Leroy, T. A. Vartanyan, and D. Sarkisyan. *Magnetically Induced Atomic Transitions of the Potassium D2 Line.* Opt. Spectrosc. **127** (3) (2019), pp. 411–417. 75

[173] K. Pahwa, L. Mudarikwa, and J. Goldwin. *Polarization spectroscopy and magnetically-induced dichroism of the potassium* D_2 *lines.* Opt. Express **20** (2012), p. 17456. 76

[174] A. Lampis, R. Culver, B. Megyeri, and J. Goldwin. *Coherent control of group index and magneto-optical anisotropy in a multilevel atomic vapor.* Opt. Express **24** (2016), p. 15494. 76

[175] B. Zlatković, A. Krmpot, N. Šibalić, M. Radonjić, and B. Jelenković. *Efficient parametric non-degenerate four-wave mixing in hot potassium vapor.* Laser Phys. Lett. **13** (2016), p. 015205. 76

[176] A. Sargsyan. *Formation of Narrow-Band N-Type Optical Resonance in Vapors of Potassium Atoms.* J. Appl. Spectrosc. **89** (2022), p. 12. 76, 95

[177] A. D. Sargsyan. *Investigations of Atomic Transitions of the D2 Line of Potassium in Strong Magnetic Fields Using Saturated Absorption Technique in a Microcell.* J. Contemp. Phys. (Armenian Acad. Sci. **58** (1) (2023), pp. 45–51. 76

[178] S. Nakayama. *Doppler-free laser spectroscopic techniques with optical pumping in D_1 lines of alkali atoms.* J. Opt. Soc. Am. B **2** (1985), pp. 1431–1437. 78

[179] D. W. Preston. *Doppler-free saturated absorption: Laser spectroscopy.* Am. J. Phys. **64** (1996), p. 1432. 78

[180] E. Jahier, J. Guéna, P. Jacquier, M. Lintz, A. V. Papoyan, and M. A. Bouchiat. *Temperature-tunable sapphire windows for reflection loss-free operation of vapor cells.* Appl. Phys. B **71** (2000), pp. 561–565. 78

[181] W. T. Silvfast. “Laser Fundamentals”. In: 2nd ed. 2004. 78.

[182] A. Krasteva, P. N. Gosh, S. Gateva, S. Tsvetkov, D. Sarkisyan, A. Sargsyan, T. Vartanyan, and S. Cartaleva. *Observation and theoretical simulation of N-resonances in Cs D_2 lines.* Phys. Scripta **95** (1) (2019), p. 015404. 79, 95, 102

[183] A. Sargsyan, B. Glushko, and D. Sarkisyan. *Micron-Thick Spectroscopic Cells for Studying the Paschen–Back Regime on the Hyperfine Structure of Cesium Atoms.* J. Exp. Theor. Phys. **120** (2015), pp. 579–586. 80, 82, 85

[184] J. Liang, T. M. Fuchs, R. Schäfer, and V. V. Kresin. *Strong permanent magnet gradient deflector for Stern–Gerlach-type experiments on molecular beams.* Rev. Sci. Instrum. **91** (2020), p. 053202. 81

[185] A. Wickenbrock, H. Zheng, L. Bougas, N. Leefer, S. Afach, A. Jarmola, V. Acosta, and D. Budker. *Microwave-free magnetometry with nitrogen-vacancy centers in diamond.* Appl. Phys. Lett **109** (2016), p. 053505. 81, 86

[186] T. Baluktsian, C. Urban, T. Bublat, H. Giessen, R. Low, and T. Pfau. *Fabrication method for microscopic vapor cells for alkali atoms.* Opt. Lett. **35** (2010), p. 1950. 82

[187] K. Whittaker, J. Keaveney, I. Hughes, A. Sargsyan, D. Sarkisyan, and B. Gmeiner. *Interrogation and fabrication of nm scale hot alkali vapour cells.* J. Phys.: Conf. Ser. **635** (2015), p. 122006. 82

[188] J. Zielinska, F. Beduini, N. Godbout, and M. Mitchell. *Ultranarrow Faraday rotation filter at the Rb D_1 line.* Opt. Lett. **37** (2012), p. 524. 84

[189] A. Sargsyan, A. Tonoyan, G. Hakhumyan, A. Papoyan, E. Mariotti, and D. Sarkisyan. *Giant modification of atomic transition probabilities induced by a magnetic field: forbidden transitions become predominant.* Laser Phys. Lett. **11** (055701) (2014). 87, 88

[190] D. Pizzey, J. D. Briscoe, F. D. Logue, F. S. Ponciano-Ojeda, S. A. Wrathmall, and I. G. Hughes. *Laser spectroscopy of hot atomic vapours: from ’scope to theoretical fit.* New J. Phys. **24** (12) (2022), p. 125001. 87, 88

[191] A. Sargsyan, A. Tonoyan, and D. Sarkisyan. *Application of Magnetically Induced Transitions of the 85Rb D2 Line in Coherent Processes.* J. Exp. Theor. Phys. **133** (1) (2021), pp. 16–25. 87, 88, 92, 93

[192] A. S. Zibrov, C. Y. Ye, Y. V. Rostovtsev, A. B. Matsko, and M. O. Scully. *Observation of a three-photon electromagnetically induced transparency in hot atomic vapor.* Phys. Rev. A **65** (4) (2002), p. 043817. 87, 95, 99

[193] D. Slavov, A. Sargsyan, D. Sarkisyan, R. Mirzoyan, A. Krasteva, A. D. Wilson-Gordon, and S. Cartaleva. *Sub-natural width N-type resonance in cesium atomic vapour: splitting in magnetic fields.* J. Phys. B: At. Mol. Opt. Phys. **47** (3) (2014), p. 035001. 88, 95, 96

[194] N. Hayashi, R. Sugizono, K. Harimaya, K. Shijo, K. Tsubota, and M. Mitsunaga. *Interference between electromagnetically induced transparency and N-type resonances in Na vapor.* JOSA B **32** (8) (2015), pp. 1754–1760. 88, 95, 96

[195] I. Novikova, D. F. Phillips, A. S. Zibrov, R. L. Walsworth, A. V. Taichenachev, and V. I. Yudin. *Cancellation of light shifts in an N-resonance clock.* Opt. Lett. **31** (5) (2006), pp. 622–624. 88, 96

[196] Y. Pashayan-Leroy, C. Leroy, A. Sargsyan, A. Papoyan, and D. Sarkisyan. *Electromagnetically induced transparency: the thickness of the vapor column is of the order of a light wavelength.* JOSA B **24** (8) (2007), pp. 1829–1838. 90, 91

[197] G. Nikogosyan, D. Sarkisyan, and Y. Malakyan. *Absorption of resonance radiation and fluorescence of a layer of an atomic gas with thickness of the order of a wavelength.* J. Opt. Technol. **71** (9) (2004), 602–607. 90

[198] T. T. Grove, V Sanchez-Villicana, B. C. Duncan, S Maleki, and P. L. Gould. *Two-photon two-color diode laser spectroscopy of the Rb* $5D_{5/2}$. Phys. Scripta **52** (3) (1995), pp. 271–276. 91

[199] V. V. Yashchuk, D. Budker, and J. R. Davis. *Laser frequency stabilization using linear magneto-optics.* Rev. Sci. Instruments **71** (2) (2000), pp. 341–346. 92, 96

[200] A. Sargsyan, C. Leroy, Y. Pashayan-Leroy, S. Cartaleva, and D. Sarkisyan. *High-contrast dark resonances on the* D_1 *line in cesium nanocell: the advantages compared with the other alkali D lines.* J. Mod. Opt. **62** (10) (2015), pp. 769–777. 92, 93

[201] J. Vanier. *Atomic clocks based on coherent population trapping: a review.* Appl. Phys. B **81** (4) (2005), pp. 421–442. 93

[202] H. Staerkind, K. Jensen, J. H. Müller, V. O. Boer, E. T. Petersen, and E. S. Polzik. *Precision Measurement of the Excited State Landé g-factor and Diamagnetic Shift of the Cesium* D_2 *Line.* Phys. Rev. X **13** (2) (2023), p. 021036. 94, 103

[203] Z. S. Xu, M. H. Cai, S. H. You, S. S. Zhang, and H. P. Liu. *Optical-optical double resonance spectroscopy of Rb* $5D_{3/2,5/2}$ *in magnetic fields.* Spectrochimica Acta Part B: At. Spectrosc. **193** (2022), p. 106453. 95, 96

[204] A. Lezama, S. Barreiro, and A. M. Akulshin. *Electromagnetically induced absorption.* Phys. Rev. A **59** (6) (1999), pp. 4732–4735. 95

[205] D. Sarkisyan, A. Papoyan, A. Sarkisyan, G. Grigoryan, A. Sargsyan, and Y. Malakyan. *Narrow and contrast resonance of increased absorption in Lambda- system observed in Rb cell with buffer gas.* (2009). 95, 97, 102, 103

[206] M. G. Bason, A. K. Mohapatra, K. J. Weatherill, and C. S. Adams. *Narrow absorptive resonances in a four-level atomic system.* J. Phys. B: At. Mol. Opt. Phys. **42** (7) (2009), p. 075503. 95

[207] C. Hancox, M. Hohensee, M. Crescimanno, D. F. Phillips, and R. L. Walsworth. *Lineshape asymmetry for joint coherent population trapping and three-photon N resonances.* Opt. Lett. **33** (13) (2008), pp. 1536–1538. 95

[208] A. Sargsyan, R. Mirzoyan, A. Papoyan, and D. Sarkisyan. *N-type resonances in a buffered micrometric Rb cell: splitting in a strong magnetic field.* Opt. Lett. **37** (23) (2012), pp. 4871–4873. 95, 96, 102

[209] D. Brazhnikov, S. Ignatovich, V. Vishnyakov, R. Boudot, and M. Skvortsov. *Electromagnetically induced absorption scheme for vapor-cell atomic clock.* Opt. Express **27** (25) (2019), pp. 36034–36045. 95

[210] J. A. McKelvy, I. Novikova, E. E. Mikhailov, M. A. Maldonado, I. Fan, Y. Li, Y.-J. Wang, J. Kitching, and A. B. Matsko. *Application of kernel principal component analysis for optical vector atomic magnetometry.* Mach. Learn. Sci. Technol. **4** (4) (2023), p. 045048. 95

[211] W. HAPPER. *Optical Pumping.* Rev. Mod. Phys. **44** (2) (1972), pp. 169–249. 97

[212] W. Demtröder. *Laser Spectroscopy: Basic Concepts and Instrumentation* (2002). 100

[213] D. E. Thornton, G. T. Phillips, and G. P. Perram. *Velocity changing collisions in the laser saturation spectra of* ^{87}*Rb* D_2 $F'' = 2$. Opt. Commun. **284** (12) (2011), pp. 2890–2894. 100

[214] X.-G. Wei, J.-H. Wu, G.-X. Sun, Z. Shao, Z.-H. Kang, Y. Jiang, and J.-Y. Gao. *Splitting of an electromagnetically induced transparency window of rubidium atoms in a static magnetic field.* Phys. Rev. A **72** (2) (2005), p. 023806. 100

[215] R. Mottola, G. Buser, and P. Treutlein. *Electromagnetically induced transparency and optical pumping in the hyperfine Paschen-Back regime.* Phys. Rev. A **108** (6) (2023), p. 062820. 100

[216] G. A. Pitz, A. J. Sandoval, T. B. Tafoya, W. L. Klennert, and D. A. Hostutler. *Pressure broadening and shift of the rubidium D1 transition and potassium D2 transitions by various gases with comparison to other alkali rates.* J. Quant. Spectrosc. Radiat. Transf. **140** (2014), pp. 18–29. 102, 103

[217] A. J. Krmpot, M. M. Mijailović, B. M. Panić, D. V. Lukić, A. G. Kovačević, D. V. Pantelić, and B. M. Jelenković. *Sub-Doppler absorption narrowing in atomic vapor at two intense laser fields.* Opt. Express **13** (5) (2005), pp. 1448–1456. 102

[218] A. Sargsyan, D. Sarkisyan, L. Margalit, and A. D. Wilson-Gordon. *Comparison of three EIT-type resonances formed in Rb nanocell.* J. Mod. Opt. **63** (17) (2016), pp. 1713–1718. 103

[219] D. Sarkisyan, A. Sargsyan, A. D. Wilson-Gordon, and S. Cartaleva. "Conversion between electromagnetically induced absorption and transparency in a four-level system". In: *18th International School on Quantum Electronics: Laser Physics and Applications.* 18th International School on Quantum Electronics: Laser Physics and Applications. Vol. 9447. 2015, pp. 51–56. DOI: `10.1117/12.2177887`. 103.

[220] L. Downes. *Simple Python tools for modelling few-level atom-light interactions.* J. Phys. B: At. Mol. Opt. Phys. **56** (22) (2023), p. 223001. 106, 126

[221] G. Racah. *Theory of Complex Spectra. II.* Phys. Rev. **62** (9-10) (1942), pp. 438–462. 113

[222] A. Messiah. *Quantum Mechanics, Vol. 2* (1961). 113

[223] D. R. Lide. *CRC Handbook of Chemistry and Physics* (2023). 120, 121, 122

[224] M. P. Bradley, J. V. Porto, S. Rainville, J. K. Thompson, and D. E. Pritchard. *Penning Trap Measurements of the Masses of* ^{133}*Cs,* ^{87,85}*Rb, and* ^{23}*Na with Uncertainties* ≤ 0.2 *ppb.* Phys. Rev. Lett. **83** (22) (1999), pp. 4510–4513. 120, 121, 122

[225] C. Tanner and C. Wieman. *Precision measurement of the hyperfine structure of the* $^{133}Cs\ 6P_3/2$ *state.* Phys. Rev. A **38** (3) (1988), 1616–1617. 120

[226] T. Udem, J. Reichert, T. W. Hänsch, and M. Kourogi. *Absolute optical frequency measurement of the cesium* D_2 *line.* Phys. Rev. A **62** (3) (2000), p. 031801. 120

[227] R. J. Rafac and C. E. Tanner. *Measurement of the ratio of the cesium D-line transition strengths.* Phys. Rev. A **58** (2) (1998), pp. 1087–1097. 120

[228] R. J. Rafac, C. E. Tanner, A. E. Livingston, and H. G. Berry. *Fast-beam laser lifetime measurements of the cesium* $6p\ ^2P_{1/2,3/2}$ *states.* Phys. Rev. A **60** (5) (1999), pp. 3648–3662. 120

[229] L. Young, W. T. Hill, S. J. Sibener, S. D. Price, C. E. Tanner, C. E. Wieman, and S. R. Leone. *Precision lifetime measurements of Cs* $6p\ ^2P_{1/2}$ *and* $6p\ ^2P_{3/2}$ *levels by single-photon counting.* Phys. Rev. A **50** (3) (1994), pp. 2174–2181. 120

[230] W. Yei, A. Sieradzan, and M. Havey. *Delayed–detection measurement of atomic Na* $3p\ ^2P_{3/2}$ *hyperfine structure using polarization quantum-beat spectroscopy.* Phys. Rev. A. **48** (1993), 1909–1. 121

[231] H. Wang, P. L. Gould, and W. C. Stwalley. *Long-range interaction of the* $^{39}K(4s)+^{39}K(4p)$ *asymptote by photoassociative spectroscopy. I. The g- pure long-range state and the long-range potential constants.* The J. Chem. Phys. **106** (19) (1997), pp. 7899–7912. 121

[232] U. Volz and H. Schmoranzer. *Precision lifetime measurements on alkali atoms and on helium by beam–gas–laser spectroscopy.* Phys. Scripta **1996** (T65) (1996), p. 48. 122

[233] J. E. Simsarian, L. A. Orozco, G. D. Sprouse, and W. Z. Zhao. *Lifetime measurements of the* $7p$ *levels of atomic francium.* Phys. Rev. A **57** (4) (1998), pp. 2448–2458. 122

[234] H. M. J. M. Boesten, C. C. Tsai, J. R. Gardner, D. J. Heinzen, and B. J. Verhaar. *Observation of a shape resonance in the collision of two cold* ^{87}*Rb atoms.* Phys. Rev. A **55** (1) (1997), pp. 636–640. 122

[235] R. F. Gutterres, C. Amiot, A. Fioretti, C. Gabbanini, M. Mazzoni, and O. Dulieu. *Determination of the* ^{87}*Rb* $5p$ *state dipole matrix element and radiative lifetime from the photoassociation spectroscopy of the* $Rb_2\ 0_g^-(P_{3/2})$ *long-range state.* Phys. Rev. A **66** (2) (2002), p. 024502. 122

[236] C. Cohen-Tannoudji, J. Dupont-Roc, and G. Grynberg. *Atom-Photon Interactions: Basic Processes and Applications* (1998). 123, 126

[237] R. Loudon and R. Loudon. *The Quantum Theory of Light* (2000). 123

[238] C. Aslangul. *Mécanique quantique Tome 2, Développements et applications à basse énergie.* Licence maîtrise doctorat (2008). 125

[239] F. Bloch and A. Siegert. *Magnetic Resonance for Nonrotating Fields.* Phys. Rev. **57** (6) (1940), pp. 522–527. 126

[240] R. Mirzoyan. “Study of the coherent effects in rubidium atomic vapor under bi-chromatic laser radiation”. These de doctorat. Dijon, 2013. URL: `https://theses.fr/2013DIJOS015`. 128.

ECOLE DOCTORALE
CARNOT - PASTEUR

Titre : Spectroscopie sous-Doppler de vapeurs alcalines confinées dans ces cellules minces nanométriques et micrométriques

Mots-clés : spectroscopie atomique ; alcalins ; effet Zeeman ; magnétométrie ; procédés magnéto-optiques

Résumé : Cette thèse explore divers aspects de la spectroscopie sous-Doppler, allant des études fondamentales de l'effet Zeeman aux processus de pompage cohérent. Elle offre une vue d'ensemble des avancées antérieures et actuelles en utilisant des cellules spectroscopiques fines d'épaisseur nanométrique et micrométrique. Du point de vue théorique, nous rappelons le modèle décrivant l'interaction entre un laser et une vapeur confinée dans une cellule fine. Nous présentons une description théorique complète du comportement d'une vapeur de sodium dans un champ magnétique allant jusqu'à 10 000 G. De plus, nous développons un cadre théorique complet pour l'annulation du moment dipolaire et calculons les valeurs de champ magnétique pour lesquelles les transitions Zeeman des atomes alcalins sont annulées. Ces valeurs dépendent uniquement de constantes physiques et peuvent servir de références pour l'étalonnage de magnétomètres. Nous présentons également un schéma de magnétomètre utilisant de fines cellules de potassium permettant de mesurer les champs magnétiques avec une haute résolution spatiale, potentiellement bénéfique pour la magnétométrie dans des environnements difficiles. La formation de résonances EIT dans des champs magnétiques forts est étudiée théoriquement et expérimentalement, montrant une faisabilité pour le verrouillage de la fréquence laser sur des fréquences fortement décalées. Enfin, nous explorons la formation de résonances N étroites et examinons l'effet d'un gaz tampon supplémentaire sur leur largeur et leur contraste. Les résonances N sont des candidates prometteuses pour des étalons de fréquence atomique pouvant être réalisés avec des lasers à diode disponibles dans le commerce.

Title: Sub-Doppler spectroscopy of alkali vapors confined in nanometric and micrometric thin cells

Keywords: atomic spectroscopy ; alkali ; Zeeman effect ; magnetometry ; magneto-optical processes

Abstract: This thesis explores various aspects of sub-Doppler spectroscopy, ranging from fundamental studies of the Zeeman effect to coherent pumping processes. It provides a general overview of past and present advancements using thin spectroscopic cells of nanometric and micrometric thickness. From a theoretical perspective, we recall the model describing the interaction between a laser and a vapor confined in a thin cell. We present a comprehensive theoretical description of the behavior of a sodium vapor under magnetic fields up to 10 000 G. Additionally, we develop a complete theoretical framework for dipole moment cancellation and calculate the magnetic field values at which Zeeman transitions of alkali atoms are canceled. These values depend solely on physical constants and can serve as standards for calibrating magnetometers. We also present a magnetometer scheme utilizing thin potassium cells allowing to measure magnetic fields with high spatial resolution, potentially beneficial for magnetometry in challenging environments. The formation of EIT resonances in strong magnetic fields is investigated both theoretically and experimentally, showing promise for laser frequency locking on strongly detuned frequencies. Lastly, we explore the formation of narrow N-resonances and examine the effect of additional buffer gas on their width and contrast. N-resonances are promising candidates for atomic frequency standards that can be achieved with commercially available diode lasers.

UBFC
UNIVERSITÉ
BOURGOGNE FRANCHE-COMTÉ

Université Bourgogne Franche-Comté
32 avenue de l'Observatoire
21000 Besançon